# Various Aspects of Polymer Induced Drag Reduction in Turbulent Flow

Ing. Ivan Zadražil

March 2011

A dissertation submitted in partial fulfillment of the requirements for
the degree of Doctor of Philosophy of the University of London
and the Diploma of Imperial College London

Department of Chemical Engineering and Chemical Technology
Imperial College London
London, SW7 2AZ, UK

# Abstract

High molecular weight polymers dissolved at very low concentrations - in the order of few wppm - in a solvent lead to a reduction of mechanical drag in turbulent flow when compared to a pure solvent. This phenomenon, known as drag reduction (DR), is of great industrial relevance. The applications include oil pipeline systems, secondary oil well operations, field irrigation or fire fighting.

This PhD thesis is focused on the study of DR from different perspectives. Firstly, drag reducing polymers - polyethylene oxide (PEO) and polyacrylamide (PAAm) - were thoroughly characterised in quiescent flow conditions using nuclear magnetic resonance, multi-angle laser light scattering, gel permeation chromatography, intrinsic viscosity and rheological techniques. Then, an experimental method for fast DR characterisation was developed based on the use of a commercially available rheometer equipped with a double gap sample holder. This method, which enables quantification of $DR$ under turbulent-Taylor flow conditions, was applied to investigate the degradation dynamics of PEO and PAAm and its effect on the level of $DR$. The role played by polymer aggregates, which composition was altered by changing a solvent quality, on the DR phenomenon was also ascertained. The main finding is that the level of $DR$, as measured by a commercial rheometer, can increase over time even though the molecular weight of the polymer decreases. Based on these results, a new mechanism of flow-induced polymer disaggregation-degradation and their effect on DR was proposed. An important achievement of this work was the design, construction and commissioning of a pilot plant-scale flow facility for studying DR at high Reynolds numbers, $Re$. Both homogeneous and heterogeneous DR can be tested, for $Re$ ranging between 10,000 and 1,000,000. For the purposes of this study, $Re$ up to 210,000 were applied to investigate DR using a non-intrusive flow field measuring technique, the particle image velocimetry. Based on the investigation of a broad range of polymer molecular weights, polymer concentrations and $Re$, a relationship between the observed level of $DR$ and the turbulent flow intensities and structure was found. Finally, a new mechanism of DR, a layer mechanism, based on the interaction of elongated polymer molecules in the inner near-wall region was proposed. Well known effects related to DR were explained within the framework of this mechanism. Predictions were also made accordingly to test its applicability.

# Contents

# List of Figures

# List of Tables

# Nomenclature

**Italic Symbols**

| | |
|---|---|
| $A_2$ | Second virial coefficient [mol·ml·g$^{-2}$] |
| a | Stiffness factor in Mark-Houwink equation [-] |
| $\mathrm{a}_{\dot{\gamma}}$ | Rheometer constant used to calculate shear rate [-] |
| $\mathrm{a}_{\tau}$ | Rheometer constant used to calculate shear stress [-] |
| B | Universal constant in the log-law velocity profile [-] |
| $c^*$ | Polymer overlap concentration [wppm] |
| c | Polymer concentration [wppm] |
| $c_{opt}$ | Optimum polymer concentration for max DR [wppm] |
| d | Pipe diameter [m] |
| dn/dc | Refractive index increment [cm$^3$·g$^{-1}$] |
| DR | Drag reduction [%] |
| f | Fanning friction factor [-] |
| H | Height [m] |
| $k_H$ | Huggins coefficient [-] |
| K | Optical constant [-] |
| k | Arbitrary constant used for visualisation of Zimm plot [-] |
| $\mathrm{K}^*$ | Constant in Mark-Houwink equation [ml·g$^{-1}$] |
| l | Length [m] |
| $M_n$ | Number average molecular weight [g·mol$^{-1}$] |

| | |
|---|---|
| $M_v$ | Viscosity based average molecular weight [g·mol$^{-1}$] |
| $M_w$ | Weight average molecular weight [g·mol$^{-1}$] |
| $N_A$ | Avogadro constant [mol$^{-1}$] |
| N | Number of polymer molecules [-] |
| n | Number fraction or number of data points [-] |
| $\mathrm{n}_0$ | Refractive index of a solvent [-] |
| PDI | Polydispersity index [-] |
| p | Pressure [Pa] |
| q | Scattering vector [cm$^{-1}$] |
| Re | Reynolds number [-] |
| $R_g$ | Radius of gyration [nm] |
| $R_h$ | Hydrodynamic radius [nm] |
| r | Radius [m] |
| $R_\theta$ | Rayleigh ratio [-] |
| Ta | Taylor number [-] |
| T | Torque [N·m] |
| t | Time [s] |
| $U_{bulk}$ | Bulk velocity [m·s$^{-1}$] |
| $\mathrm{U}_\tau$ | Frictional velocity [-] |
| u | Streamwise velocity [m·s$^{-1}$] |
| v | Spanwise velocity [m·s$^{-1}$] |
| w | Weight fraction [-] |
| x | Streamwise direction in a pipe flow |
| y | Spanwise direction in a pipe flow or distance from the pipe wall [m] |

**Greek Symbols**

| | |
|---|---|
| $\delta$ | Ratio between the radius of rotor and stator [-] |

| | |
|---|---|
| $\Delta$B | Shift factor of the universal constant in the log-law velocity profile [-] |
| $\Delta$p | Differential pressure [Pa] |
| $\Delta$s | Particle displacement between a PIV image pair [m] |
| $\delta^*$ | Gap between the rotor and the stator [mm] |
| $\Delta$t | Time between a PIV image pair [s] |
| $\eta$ | Apparent shear viscosity [Pa·s] |
| $\eta_{coil}$ | Extensional viscosity parameter [-] |
| $\dot{\eta}$ | Apparent viscosity in Taylor flow [Pa·s] |
| $[\eta]$ | Intrinsic viscosity [dl·g$^{-1}$] |
| $\eta_{red}$ | Reduced viscosity [cm$^3$·g$^{-1}$] |
| $\eta_{sp}$ | Specific viscosity [-] |
| $\Gamma$ | Aspect ratio of the double gap cell [-] |
| $\dot{\gamma}$ | Shear rate [s$^{-1}$] |
| $\gamma_{xx}$ | Streamwise compression strain rate [s$^{-1}$] |
| $\gamma_{xy}$ | Streamwise shear strain rate [s$^{-1}$] |
| $\gamma_{yx}$ | Spanwise shear strain rate [s$^{-1}$] |
| $\gamma_{yy}$ | Spanwise compression strain rate [s$^{-1}$] |
| $\kappa$ | von Kármán constant [-] |
| $\lambda$ | Wavelength of monochromatic light [nm] |
| $\nu$ | Kinematic viscosity [m$^2$·s$^{-1}$] |
| $\omega$ | Angular frequency [rad·s$^{-1}$] |
| $\omega_{cyc}$ | Rotational speed [rpm] |
| $\omega_z$ | 2D vorticity [s$^{-1}$] |
| $\rho$ | Density [kg·m$^{-3}$] |
| $\rho_t$ | Topology factor [-] |
| $\tau$ | Shear stress [Pa] |

| | |
|---|---|
| $\theta$ | Scattering angle [°] |
| $\tau_w$ | Wall shear stress [Pa] |
| $\tau_{xy}^{'}$ | Reynolds stress [$\mathrm{m}^2 \cdot \mathrm{s}^{-2}$] |
| $\varepsilon$ | Pipe roughness [m] |

**Miscellaneous**

| | |
|---|---|
| $(...)^+$ | Friction velocity normalised quantity |
| $(...)_a$ | Polymer additive related quantity |
| $(...)_N$ | Normalised quantity |
| $(...)^{'}$ | Fluctuating quantity |
| $(\bar{...})$ | Mean quantity |
| $(...)_{rms}$ | Root mean square |
| $(...)_s$ | Solvent related quantity |

**Abbreviations**

| | |
|---|---|
| 2D | 2-dimensional |
| 3D | 3-dimensional |
| DNS | Direct numerical simulation |
| DR | Drag reduction |
| GPC | Gel permeation chromatography |
| LDV | Laser Doppler velocimetry |
| MALLS | Multi-angle laser light scattering |
| PAAm | Polyacrylamide |
| PEO | Polyethylene oxide |
| PIV | Particle image velocimetry |
| RDA | Rotating disk apparatus |
| rms | Root mean square |
| wppm | Weight parts per million |

# Declaration

This dissertation is a description of the work carried by the author in the Department of Chemical Engineering and Chemical Technology, Imperial College London. No portion of the work referred to in the thesis has been submitted in support of an application for another degree or qualification of this or any other university or other institute of learning.

Ing. Ivan Zadražil
London $4^{th}$ March 2011

# Acknowledgments

I would like to begin by thanking my supervisors Professor Alexander Bismarck, Professor Geoffrey Hewitt and Professor Christos Vassilicos for their guidance throughout the course of the work. Especially Alexander whose help in my difficult beginnings and patience throughout the years is much appreciated. I also need to express my sincere gratitude to Dr Christos Markides who opened the Pandora's box of turbulence for me. The guidance, advice and discussions he has provided me with respect to the turbulent flow measurements are very much valued. I think I became a coffee addict that time. I obviously would like to thank Halliburton Energy Services for sponsoring the project and Dr Lewis Norman, Dr Ian Robb and Dr Peng Tonmukayakul for valuable discussions. Peng's explanation of the mechanism of polymer unraveling in turbulent flow makes me laugh even now. I also offer my thanks to Professor Paul Luckham and Professor Witold Brostow for agreeing to examine this work.

My thanks go to Globalservice a.s. and in particularly Ing. Peter Voborník for the production of the flow facility. Thanks also to Mr Richard Wallington who advised me during the modifications of the flow facility and during the construction of the visualisation cells in the chemical engineering student workshop. Also I would like to thank Dr Colin Hale for all the help he provided. The flow facility would never have worked properly without them.

I would like to continue thanking people that I met at Imperial and that made my stay in London joyful: Dr Steven Lamoriniere, Dr Alexander Malijevsky, Dr. Juntaro Julasak, Dr Kingsley Ho, Dr Charnwit Tridech, Ing. Vladimír Novák, Dr Lukáš Shrbený, Dr Zdeněk Groff, Dr Jonny Blaker, Anthony Abbot, Dr Ryo Murakami, Dr Emilia Kot, Jerzy Pental, Dr Francisco Garcia Garcia, Dr Giulia Soloperto, Matthew Laffan, Daniele Sileri, Dr Francesco Coletti, Edyta Lam, Nadine Graeber, Dr Natasha Shirshova,... and so on. I would like to apologise to those I forgot to mention, is was not on purpose. I also would like to thank the staff of Ealing hospital, Section 8 South, and Matthias Toth. It would sounds weird but I enjoyed the stay.

Most importantly I would like to thank my parents, Ing. Libuše Zadražilová and Ing. Milan Zadražil, for their love, support and inspiration. Of course the biggest thanks belongs also to my brother Dr Aleš Zadražil who introduced me to Imperial College London and without whom I would not have survived my first year. Finally, I thank to Dr Francesca Palombo for her love, support, encouragement and the time we spent in Perugia where this PhD thesis was written.

# Chapter 1

# Introduction

Objectives of the work described in this thesis is to get better understanding of the effect called drag reduction. The overall picture of the effect can only be obtained by detailed characterisation of polymer solutions in quiescent conditions but also in turbulent flow environment. Such comprehensive work is important not only for the fundamental questions associated with the drag reduction phenomenon, but also can find direct use in the industry.

The main aspects of the drag reduction effect are introduced in Section 1.1 and the aims of the project are presented in Section 1.2. The strategy for achieving the project aims and the structure of the thesis are summarised in Section 1.3.

## 1.1 Drag Reduction

In 1948 Toms [7] reported that the friction between a wall and a flowing liquid caused by turbulent flow can be reduced by addition of small amounts of polymers. He observed that poly methyl methacrylate dissolved in monochlorobenzene reduced the pressure drop necessary to pump the fluid through the pipe at a constant flow rate below that of pure solvent. This phenomenon is known as drag reduction (DR) and as a result of his pioneering work it is sometimes referred as "Toms effect". Toms observation was confirmed by Mysels in 1949 [8]. Nowadays the DR effect is defined as follows: "The addition of small quantities of high–molecular weight polymers to flowing liquids can produce profound effects on a wide variety of flow phenomena that appear incommensurate with the small concentration of polymers added to solution. This is most evident in turbulent boundary layers, in which dissolving parts-per-million quantities of long-chain flexible polymers into solution can reduce turbulent friction losses by as much as 80% compared with that of the solvent alone." [9]. The DR phenomenon is specific by a vortex intensity reduction in turbulent flow which can be seen on the images obtained by laser induced fluorescence [1] (see Figure 1.1).

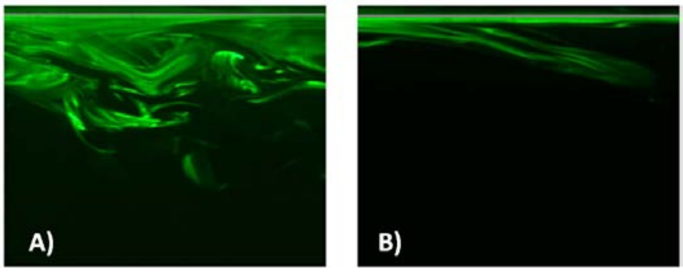

Figure 1.1: Planar Laser Induced Fluorescence images showing decrease in turbulence intensity next to the wall which is situated at the top of the images. A) water, B) polymer solution (polyethylene oxide, 100 wppm, $M_w = 4.5 \cdot 10^6\,\mathrm{g} \cdot \mathrm{mol}^{-1}$) [1].

The reduction of the friction between the fluid and the walls can be achieved by either active or passive techniques [10]. Active DR is the ability of certain additives, such as polymers, surfactants or air bubbles to reduce the frictional resistance in turbulent flow. It is noteworthy that in the case of polymer induced DR the effective concentration of additive could be as low as few parts per million. Even with such a low concentration the pumping pressure can be reduced by 80% at the same flow rates or the flow rate can be increased by 40% at the same pressure loss along the pipe. The passive techniques use compliant coatings and riblets on the pipe or channel wall. However, passive techniques are not as effective as the active ones [11]. Further in the text the emphasis will be given to polymer induced DR.

The breakthrough in this field was the discovery that polymer induced DR can also be achieved in water flows. The most DR effective water soluble polymer, namely polyethylene oxide (PEO), can reduce drag by more than 80%. In 1975 Virk in his review discovered the maximum DR asymptote [12]. He stated that the maximum DR that can be obtained is independent of the polymer structure but depends only on the physical properties of the flow.

The main drawback for polymer induced DR was identified in the beginning of 70's by Paterson et al. [13]. Their work showed the vulnerability of polymers to mechanical degradation causing a decrease in the level of $DR$. Even today this problem is still a common subject of current research [14, 15] and it is a matter of discussion whether mechanical degradation of polymer molecules or the break up of polymer aggregates is responsible for the decrease in the level of $DR$ [16, 17, 18]. Work in this area also focuses on synthesis of novel polymers that are more resistant to mechanical degradation [19] but also on the effect of naturally occurring polymer aggregates on the DR effect [20]. Despite the mentioned disadvantages drag reducing polymers have been successfully used in industrial applications; such as:

- Transport of liquids - Trans-Alaska Pipeline system where 1 wppm of drag reducer increased the flow rate of crude oil by 33 per cent [21].
- Oil well operations - DR additives are commonly used for hydraulic fracturing [22, 23].
- Irrigation - The use of drag reducers resulted in reduced energy requirements of sprinkler irrigation systems [24, 25].
- Urban sewage network - Drag reducing polymers were used to increase the capacity of sewerage pipes and storm-water drains during heavy storms [26, 27].
- Fire-fighting - Polymers were used to increase the range and coherence of water jets from fire-fighting water hoses [28, 29] .

Finally, it is interesting to mention that DR is not an unknown phenomenon even to the nature. It is believed, for example, that some sea creatures such as dolphins and eels do excrete a drag reducing substances so they can swim faster than predicted by hydrodynamic theory [30, 31].

## 1.2 Project Aim

The overall aim is to understand the DR phenomenon and the effect of polymer mechanical degradation on the level of measured $DR$. Understanding DR can help us to develop novel polymer systems that would be more efficient and less vulnerable to mechanical degradation. The primary aim of this project is to introduce and develop characterisation techniques for polymer induced DR. The main task was to prepare a quick analytical procedure for testing the $DR$ efficiency of novel polymers [32]. Experimentally obtained results should help us to choose the best polymer type at optimal concentration for testing in a pilot-plant scale flow facility. Next step was to design, manufacture and commission a pilot-plant scale flow facility for testing both homogeneous and heterogeneous DR and for the characterisation of turbulent flow at hydraulic fracturing conditions. The combination of both DR techniques can help us to clarify the DR mechanism and will provide key input for the synthesis of novel polymers.

The aim of this project was a detailed characterisation of a few selected polymer drag reducing agents and develop techniques for their characterisation in flow conditions. The main aims were as follows:

- Identify and develop techniques for characterisation polymer-solvent systems in quiescent conditions.
- Develop a quick, cheep and simple DR characterisation technique.
- Give an insight in the DR degradation mechanism using a quick DR characterisation technique.
- Design, develop and manufacture a flow facility in order to test DR under real application conditions.
- Investigate the effect of polymer drag reducers on the intensity and structure of turbulent pipe flow.

In order to achieve the aims, the work was divided in following steps:

- Detailed polymer characterisation in quiescent conditions.
- Development of a quick DR characterisation method to test and quantify $DR$.
- Study of DR behaviour of two polymer types using a quick DR characterisation method.
- Design, building and commissioning a flow facility capable of measuring $DR$ in real application conditions.
- Integrating a non-intrusive flow field characterisation technique into the flow facility.
- Study of DR effect using the flow facility.

## 1.3 Thesis Structure

This thesis presents work on various aspects of polymer induced DR in turbulent flow. Chapter 2 reviews the background literature. In Chapter 3 the materials and characterisation techniques used in both quiescent and flow conditions are described. Moreover, pilot-plant scale flow facility designed by the author is presented. Chapter 4 deals with detailed characterisation of the polymers used in a quiescent conditions and Chapters 5 and 6 examines the $DR$ efficiency of studied polymers using the quick DR characterisation technique and pilot-plant scale flow facility, respectively. Additionally, the influence of polymer aggregates on DR is described in Chapter 5. Chapter 6 also presents the results of non-intrusive measurement of turbulent flow intensity and structure. Also a new DR mechanism is suggested in the Chapter 6. Finally, Chapter 7 draws conclusions of the work and makes suggestions for future work.

# Chapter 2

# Background

DR research involves many subjects of research interest such as polymer science, fluid mechanics and mathematical modeling. The complexity of the subject can be seen in the number of publications. The last bibliography compiled by Nadolink et al. [33], covering the years from 1922 to 1994, contained over 4900 references. The topic was also summarised in several comprehensive reviews: Lumley [34], Virk [12], Pazwash [35] and lately Bismarck et al. [36] and Brostow [37]. The polymer part of the DR phenomenon was discussed by Berman [38] and Morgan [39] and various techniques to reduce drag were summarised by Truong [10]. The modification of turbulent flow due to the presence of polymer additives were reviewed by White et al. [9]. The application of DR additives was summarised by Lumley et al. [40]. Finally, a chapter about DR was published in Encyclopedia of Polymer Science and Technology [41].

## 2.1 Drag Reducing Polymers

It is well known that the DR phenomenon can be achieved in organic solvents as well as in water. The crucial polymer parameters are i) a long linear chain structure with no or few side branches, ii) chain flexibility, iii) high molecular weight ($5 \cdot 10^5\,\mathrm{g \cdot mol^{-1}}$ and more), and iv) good solubility in the fluid [22]. A list of the most common polymer drag reducers can be found in Table 2.1. Previous studies on polymer induced DR indicate that almost all polymers fulfilling the above mentioned criteria are able to reduce frictional drag in turbulent flow.

Even very small polymer concentrations can lead to significant reduction in frictional drag. Oliver et al. [48] used polyacrylamide (PAAm) of very high molecular weight and proved that DR can be achieved with polymer concentrations smaller than 0.02 wppm. Experimental work showed that $DR$ has its maximum at a certain polymer concentration, so called optimum concentration

Table 2.1: List of polymers soluble in water and organic solvents that are known to reduce the frictional drag.

| Water soluble polymers | Hydrocarbon soluble polymers |
|---|---|
| Polyethylene oxide [15] | Poly methyl methacrylate [7] |
| Polyacrylamide [42] | Poly styrene [43] |
| Hydrolyzed polyacrylamide [18] | Poly isobutylene [44] |
| Xanthan gum [45] | |
| Guar gum [46] | |
| Cellulose derivatives [47] | |

$c_{\text{opt}}$, for a given Reynolds number, *Re* (see Figure 2.1) [49]. Further increase of polymer concentration does not lead to the increase in *DR*. It was observed that the optimum concentration increases with temperature [50] and decreases with increasing polymer molecular weight [51]. The increase of the optimum concentration with temperature was ascribed to the change of polymer solubility and the reduced anisotropy of viscosity upon reduced size of the polymer molecules. Litte [52] studied the influence of polymer concentration and molecular weight on the level of *DR* and proposed an empirical relation between polymer concentration and *DR* for a certain *Re* value.

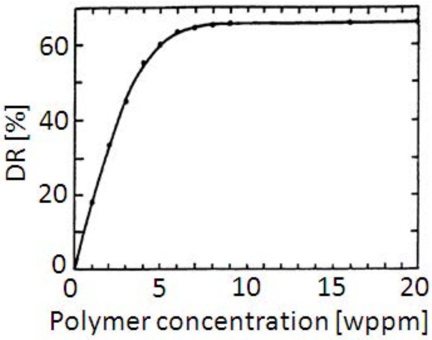

Figure 2.1: Percentage *DR* as a function of polymer concentration for PEO in water at a $Re = 14,000$ (59).

The strong effect of polymer molecular weight on the *DR* efficiency was recognised in 60's [53]. Virk [12] showed that increasing polymer molecular weight shifts the onset of *DR* to lower *Re* values, which in general implies higher *DR* efficiency. It was shown by Gampert et al. [54] that the highest molecular weight fraction of PEO contributes the most to the DR effect for a mixture of highly fractionated polymers. As stated by Hunston et al. [55] the highest polymer molecular weight fractions are able to interact with bigger vortices and are therefore responsible for higher levels of $DR$. The decrease in the overall turbulent dissipation of energy leads to higher values of $DR$. Vlachogiannis et al. [18] found that measured $DR$ differs even if the overall polymer molecular weight distribution is the same for PAAm polymers. They stated that not only individual polymer molecules of the highest polymer molecular weight tail are responsible for the DR effect but that also polymer aggregates play a key role in the DR mechanism.

The relationship between the polymer chemical structure and $DR$ efficiency has been widely studied by the group around McCormick [39, 56, 57, 58, 59, 60]. They showed that even minor modification of polymer chemical composition can alter $DR$ efficiency with the important parameters being: copolymer structure, composition and solvation of the polymer molecules. They stated that measured $DR$ can be linked to the hydrodynamic volume, $[\eta]\, c$, with a relationship: increasing polymer hydrodynamic volume results in higher $DR$. The exceptions were associating copolymers where the DR effect was related to the hydrophobic content rather than to the hydrodynamic volume. It was also noted that the polymer-solvent interactions and the polymer molecular associations, aggregates, have a strong effect on the resulting $DR$. Experiments performed by Cowan et al. [61] on wide scale of acrylamido polymers and PEO of different molecular weights showed that measured $DR$ can be universally correlated with $[\eta]\, c\eta_{\text{coil}}$ at constant $Re$ where $\eta_{\text{coil}}$ is the extensional viscosity parameter. The extensional viscosity parameter was related to the flexibility of a polymer molecule. They stated that the turbulent flow profile can be predicted from well characterised polymer-solvent systems.

## 2.2 Degradation and Aggregation

High molecular weight polymers are very efficient in reducing frictional drag but they are vulnerable to flow induced mechanical degradation. One of the symptoms of mechanical degradation is the loss of the $DR$ efficiency, which is a major drawback that does not allow drag reducing polymers to be broadly used in the industry [22]. Polymers in drag reducing applications are subjected to mechanical energy produced by flow passing through a pipe, pipe inlets or pumps which causes mechanical degradation resulting in a considerable decrease in their drag reducing capabilities [62]. Degradation is inevitably linked to the supposed mechanism of DR, where polymer molecules in a random coil conformation are stretched due to the fluctuating strains in the inner near-wall region. A polymer molecule in turbulent flow is subjected to stretching and rotation due to interaction with the vortices [63]. When the strain applied to a polymer molecule exceeds a characteristic threshold value, a polymer molecule is broken apart [64]. Generally the vulnerability of polymer molecules to the mechanical degradation depends on:

- Polymer type (chemical structure)
- Polymer concentration
- Polymer molecular weight and molecular weight distribution
- Polymer-solvent interaction
- Turbulent flow structure and intensity
- Other parameters such as temperature, pH or salinity

Experimental results did not unequivocally prove that polymer molecules degrade along a pipe in turbulent flow. The first observation of polymer degradation was attributed to the turbulent forces in a pipe flow [13]. Howbeit, Moussa et al. [65] showed that polymer solutions subjected to turbulent flow at the same $Re$ have similar $DR$ effectiveness, irrespective of the length of the pipe. Their findings suggest that the polymer degradation occurs at the contraction pipe inlets where the maximum extensional strain is generated. The effect of solvent quality on polymer degradation was until recently ambiguous. Nakano [66] stated that polymer molecules degrade faster in a good solvent but Zakin [67] found the opposite. An explanation was provided by Moussa et al. [68] who showed that in turbulent flow the polymer molecules degrade more rapidly in a poor solvent at low $Re$; whereas an opposite effect was observed at high $Re$. The difference in the polymer degradation dynamics in good and poor solvents was attributed to the existence of two possible sources: polymer stretching and intra-molecular entanglements. Detailed molecular weight distribution analysis showed that the intra-molecular entanglements dominated at low $Re$ in poor solvents. As $Re$ is increased the contribution of the polymer molecules stretching mechanism increases. However, in good solvents, the polymer stretching mechanism dominates independently on $Re$. Polymer degradation can be expressed using an exponential expression. A model of polymer mechanical degradation was introduced by Brostow [69]. The model was adopted by many research groups [17, 19, 70] who found an excellent agreement with experimental data. The findings on the flow induced polymer degradation can be summarised as follows [41]:

- The higher the molecular weight and the length of a polymer molecule the more the polymer molecule is susceptible to flow induced degradation

- Rate of mechanical degradation increases with increasing polymer molecular weight
- Degradation is higher in poor solvents at low $Re$
- Degradation is lower in poor solvents at high $Re$
- For a constant wall shear stress and a pipe diameter, the degradation rate is directly proportional to a polymer molecular weight
- For a constant wall shear stress and a polymer concentration, the degradation rate is inversely related to a pipe diameter
- For a constant wall shear stress and a pipe diameter, the degradation rate is inversely related to a polymer concentration
- For a constant polymer concentration and a pipe diameter the degradation rate increases with a wall shear stress
- The shear stability is an increasing function of the solubility of polymer molecules in a given solvent (its solvation number is the parameter to take into account)
- The higher the ratio of total length to the width of a polymer molecule, the faster will be the degradation

It is not even clear what is the basic nature of the loss of polymer molecules ability to reduce frictional drag in turbulent flow. Some researchers observed polymer backbone scission [17, 71, 72] others the breakup of polymer aggregates [16, 18, 73]. The contradicting conclusions of various researchers could be explained by different values of strain in the testing apparatus. An experiment carried out under sufficiently low strains may reveal the presence only of aggregates while at high strains both aggregates and molecules may manifest themselves in reducing drag [16]. This is in agreement with findings of Liberatore et al. [42] who found polymer aggregate breakup and Gampert et al. [54] who attributed the loss in $DR$ efficiency to the polymer scission. Their contrary results may be explained by different strains used in their experimental set-up. For example molecule scission could be the dominant factor in flows through smaller passages, for which the wall shear stress would be much higher [54] when compared to the experiments performed in big square conduits which can show no molecular scission at all [42]. Cox et al. [16] assumed that aggregates might play an important role in polymer induced DR. From their review and experiments, using a rotating disk apparatus, they concluded that polymer aggregates are common in polymer solutions even at high dilution. Additionally, they inferred from their results that polymer aggregates might be more efficient in reducing drag when compared to individual polymer molecules.

Aggregates may, in principle, be detected by the same methods as are available for the determination of polymer molecular weight and size. It was found that water soluble polymers (PEO and PAAm) can contain aggregates even in a dilute solution [16]. Polymer aggregation is currently extensively investigated by gel permeation chromatography (GPC) [42], viscosimetry [74], dynamic and static light scattering [75] and spectroscopic techniques [76]. The presence of aggregates can be for example inferred from the time dependent intrinsic viscosity behaviour of PAAm-water solutions. It is expected that the solution intrinsic viscosity would increase with time during polymer dissolution. However, an unusual effect was observed by Gardner et al. [77] who found that PAAm solution intrinsic viscosity rapidly increased in the first 5 - 24 h followed by a decrease with a minimum at approximately 160 – 180 h. The initial increase of intrinsic viscosity can be attributed to the polymer conformation change derived from intra-molecular hydrogen bonding between amide groups [78]. Muller et al. [79] suggested that the decrease in the intrinsic viscosity over time could be ascribed to the agglomeration of multiple polymer chains. Another indication of polymer aggregation can be seen from rheo-optical studies [80]. It was found that PAAm undergoes large scale structure formation and pseudo-reversible turbidity patterns in simple shearing flows at shear rates above $1,000\,s^{-1}$. Aggregates can be therefore formed by the flow itself when the flow is strong enough to increase the possibility of flow induced collision of two or more polymer molecules. Hecker et al. [81] used static and dynamic light scattering and verified that the time dependent intrinsic viscosity of PAAm solutions is a function of the number of micrometre sized aggregates. They observed form the dynamic light scattering measurements that the number of polymer microgels increases with aging time of the polymer solutions. They also demonstrated that in the case of PAAm the aggregate population can be altered by the modification of the solvent quality. Similar conclusion was drawn for PEO solutions by Shetty et al. [20] who demonstrated that the measured values of $DR$ are indeed altered by the presence of polymer aggregates.

## 2.3 Flow Characterisation

The DR effect was mainly studied experimentally in channels and pipes. As it was noted before the main manifestation of DR is the decrease of pressure drop over a pipe or channel length ${}^{\Delta p}/_{l}$ at a constant $Re$ in turbulent flow conditions. Reynolds was the first who discovered that the transition from laminar to turbulent flow for a hydraulically smooth pipe takes place at a certain value of dimensionless parameter named in his honour Reynolds number which is defined as:

$$Re = \frac{\rho d U_{\text{bulk}}}{\eta} \tag{2.1}$$

where $d$ is the pipe diameter, $U_{\text{bulk}}$ is the mean fluid velocity and $\rho$, $\eta$ are the density and the dynamic viscosity of the fluid, respectively. The pressure drop along a pipe is caused by fluid frictional resistance that can be expressed by Fanning friction factor $f$ which is defined as follows:

$$f = \frac{\Delta p}{l} \frac{d}{2\rho U_{\text{bulk}}^2} \tag{2.2}$$

Fanning friction factor is directly proportional to the pressure drop along the pipe at constant $Re$. The measurements where the relationship between Fanning friction factor and $Re$ are investigated are usually referred to "gross flow measurements". The results of the gross flow measurements, presented in the semi-logarithmic Prandtl - von Kármán coordinates $1/\sqrt{f}$ and $Re\sqrt{f}$, prove that the addition of polymers does not influence the laminar flow which is described by Poiseuille law:

$$\frac{1}{\sqrt{f}} = \frac{Re\sqrt{f}}{16} \tag{2.3}$$

The flow is usually laminar when $Re$ is smaller than $2,300$. When $Re$ is increased over the threshold a transition to turbulent flow occurs. A Newtonian solvent, in the turbulent flow region ($Re > 2,400$), follows an empirical Prandtl - von Kármán law:

$$\frac{1}{\sqrt{f}} = 4.0 \log_{10} Re\sqrt{f} - 0.4 \tag{2.4}$$

When drag reducing polymers are added to the flow, a deviation from the Prandtl - von Kármán law occurs at a given $Re$ which is called "DR onset". For higher $Re$ the polymeric solution $1/\sqrt{f}$ value is increased, which signify $DR$. A remarkable feature is that there exists a maximum level of $DR$ independent on polymer type and polymer-solvent system. The maximum DR asymptote was for the first time described by Virk [53], hence sometimes refer as "Virk's asymptote", and it is expressed by:

$$\frac{1}{\sqrt{f}} = 19.0 \log_{10} Re\sqrt{f} - 32.4 \tag{2.5}$$

The polymer DR regime is therefore strictly demarcated by Equations 2.4 and 2.5. Figure 2.2 shows described behaviour where 1 represents Poiseuille law

(Equation 2.3), 2 is the empirical Prandtl - von Kármán law (Equation 2.4) and 3 is the maximum DR asymptote (Equation 2.5).

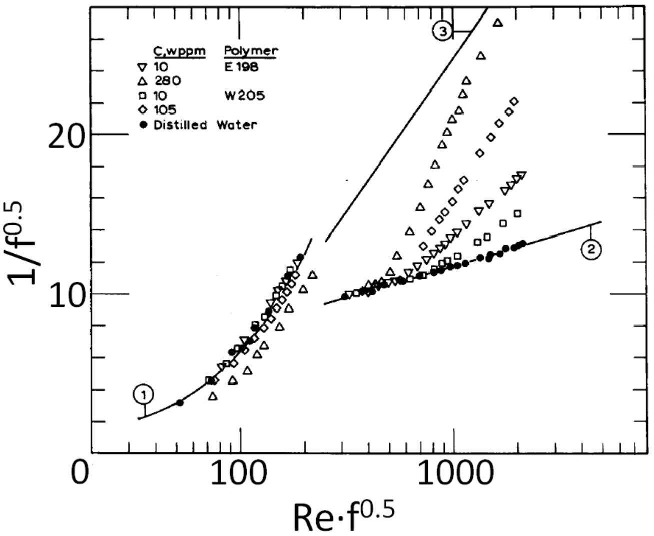

Figure 2.2: DR effect in semi-log Prandtl - von Kármán coordinates. Solid lines stand for: 1 - laminar flow (Equation 2.3), 2 - turbulent flow of a Newtonian solvent (Equation 2.4) and 3 - maximum DR asymptote (Equation 2.5) [2].

The gross flow measurements, however, cannot provide information on the modification of the turbulent flow intensity and structure which is imposed by polymer additives. Early studies utilised intrusive measuring techniques such as hot-wire anemometers [82]. However, problems with hot-wire probe calibration were reported by White [83]. The problem is in the interactions between the measuring device and the non-Newtonian turbulent flow where large extensional viscosities can be present [84]. McComb [85] did not recommend this method for the turbulent flow characteristics at all. He stated that the non-Newtonian polymer solution behaviour can affect the results in unpredictable ways and he suggests the use of non-intrusive optical methods. The development of laser Doppler velocimetry (LDV), which is a one point measuring technique, provided a tool in analysing the change of the turbulent flow intensity and structure with the addition of polymeric drag reducers [4, 86, 87, 88]. However, LDV is able to measure only turbulent velocity statistics and the instantaneous chaotic structures of turbulent flow remained undiscovered. Only the arrival of digital particle image velocimetry (PIV) allowed to measure the velocity at multiple points in a plane simultaneously [89].

The measurements of the mean velocity profiles in channel or pipes are usually showed in universal non-dimensional coordinates $U^+$ and $y^+$ that are defined as follows:

$$U^+ = \frac{\overline{u}}{U_\tau} \tag{2.6}$$

$$y^+ = \frac{U_\tau y \rho}{\eta} \tag{2.7}$$

where $y$ is the distance from the wall, $\overline{u}$ the mean streamwise velocity and $U_\tau$ is the frictional velocity which is based on the wall shear stress $\tau_w$. Both variables are defined accordingly:

$$U_\tau = \sqrt{\frac{\tau_w}{\rho}} \tag{2.8}$$

$$\tau_{\mathrm{w}} = \frac{\Delta p}{l}\frac{d}{2U_{\mathrm{bulk}}} = \nu\rho\frac{d\overline{u}}{dy}_{y=0} \tag{2.9}$$

The viscous sublayer which is situated at $y^+ < 5$ is not affected by the polymer additives. The viscous sublayer is defined as follows:

$$U^+ = y^+ \tag{2.10}$$

The viscous sublayer is followed by the so called log-law region, or the Newtonian law of the wall, that extends from $y^+ > 30$ to $y/D \sim 0.3$. The characteristic log-law logarithmic velocity profile is:

$$U^+ = \frac{1}{\kappa}\ln y^+ + B \tag{2.11}$$

where $\kappa$ is the von Kármán constant and it has a value of $\kappa \approx 0.39$. Different values of the universal constant $B$ appear in the literature ranging from 4 to 5.5 [90]. The region between the viscosity dominated and turbulence dominated areas, $5 < y^+ < 30$, is the so-called buffer layer. It is thickened by the polymer additives and therefore the log-law profile is shifted by a factor $\Delta B$ above the Newtonian law of the wall. It should be noted that the most vigorous turbulent activity is situated to $y^+ \sim 20$. The parallel shift depends on polymer type, pipe and flow characteristics. The higher the level of $DR$ the higher the upward shift $\Delta B$ [12]:

$$U^+ = \frac{1}{\kappa}\ln y^+ + B + \Delta B \tag{2.12}$$

In the case of maximum DR, that is defined by Equation 2.5, the log-law profile disappears and new ultimate profile of maximum DR emerges [12]:

$$U^+ = 11.7\ln y^+ - 17.0 \tag{2.13}$$

The inner near-wall region (the viscous sublayer and the buffer layer) bears a key role in maintaining the turbulent character of the flow and it is populated by many turbulent structures. The turbulent structures are very difficult or almost impossible to capture by means of turbulent flow measuring techniques such as LDV and PIV. Based on flow visualisation the low- and high-speed streaks, sweeps and ejections were identified [91]. The majority of the turbulent energy production is ascribed to the intermittent outward ejection of low speed fluid that take place in the buffer layer and high-speed ejections at a small angle towards the wall [92]. The longitudinal vortices that direct from the outer velocity-defect region towards the wall, sweeps, are responsible for the regions in the inner near-wall region with higher and lower velocities than the average, streaks. Described processes play a dominant role in the production of the turbulences, in the transport of turbulences from the inner near-wall region to the outer velocity-defect region and in the regeneration cycle of the near-wall turbulence. The turbulent structures are nevertheless not studied, at least not directly, in the presented work. Interested reader should look for additional information elsewhere [93, 94].

The measurements of the root-mean-square, rms, streamwise velocity fluctuations, $u^{'}_{\mathrm{rms}}$, indicate that the $u^{'}_{\mathrm{rms}}$ peak value is shifted to higher values of $y^+$ when polymer additives are present. The influence of polymer additives on the absolute height of the $u^{'}_{\mathrm{rms}}$ peak is somehow ambiguous. Smaller [95] and higher values [86] of the $u^{'}_{\mathrm{rms}}$ peak were reported when the polymer solutions were compared to a Newtonian solvent. Recent measurements showed higher $u^{'}_{\mathrm{rms}}$ peak values for the polymer additives [4, 87, 5]. The spanwise rms velocity fluctuations, $v^{'}_{\mathrm{rms}}$, measurements are more uniform in the results. They show shift of the near-wall $v^{'}_{\mathrm{rms}}$ peak away from the wall and lower $v^{'}_{rms}$ peak values when the drag reducing additives are present in the flow [4, 5, 87, 96].

One of the remarkable features of polymer induced DR in turbulent flow is the evolution of Reynolds stress with increasing DR. The Reynolds stress was observed to decrease with increasing $DR$ [87]. It should be noted that Warholic et al. [97] found almost zero Reynolds stress for a maximum DR in a channel flow across the entire channel. The zero values of Reynolds stress suggest that the wall is no more producing turbulences and therefore the typical self sustaining mechanism of vortex regeneration cycle does not exist. It was discussed that the polymer molecules are introducing additional stresses into the flow. They concluded that at maximum DR the turbulences are produced by fluctuating polymer stresses and that the vortices are produced by the interaction of polymers with fluctuating flow field [97]. However, similar results were not observed for a pipe flow where Reynolds stress was lowered but never close to zero [4, 87]. The comparison of LDV and PIV data made on heterogeneous

DR where concentrated polymer solution is injected into the Newtonian turbulent flow showed good agreement [98]. Additional statistics of turbulent flow measured for heterogeneous DR can be found elsewhere [42, 99, 100].

The measurements of higher order statistics of turbulent flow, skewness and kurtosis, that describe the structure of turbulent flow fluctuations are very rare in the literature. Wei et al. [101] showed that polymer additives decrease the streamwise skewness in the log-law region, where streamwise direction refers to the flow direction. The spanwise skewness was altered by the polymer additives only in the inner near-wall region, where spanwise direction refers to the direction which is radial to the flow. Den Toonder et al. [4] confirmed the measurements on streamwise skewness but they did not see almost any influence of the polymer additives on the spanwise skewness profiles. They additionally calculated the streamwise and spanwise kurtosis and showed that the former is increased in $y^+ \sim 100$ and the latter is decreased in the inner near-wall region when the drag reducing additives were present.

Warholic et al. [98] used PIV technique to identify turbulent structures close to the wall typical for Newtonian solvents. They were characteristic by the ejection of low momentum fluid to the outer velocity-defect region and quasi-streamwise vortices. Such structures were recognised as locations of large Reynolds stresses. For high measured $DR$ they observed reduction or elimination of the ejections from the wall [98]. Liberatore et al. [42] also observed that the frequency and the intensity of large scales ejections also decreased when compared to a Newtonian solvent. The polymer induced DR effect was also found to reduce the small scale fluctuations, as it was determined from spectral functions [98], and to reduce the magnitude and frequency of the small scale swirls [42]. Additionally, large regions of almost unidirectional fluctuating velocity vectors were observed for solutions exhibiting high levels of $DR$ [42, 98]. This observation was linked to the decrease of spanwise velocity fluctuations.

## 2.4 Mechanism of Drag Reduction

A comprehensive mechanism for DR should be able to specify and explain the interaction between polymer molecules and turbulent flow. The theory should persist when confronted with macro- and micro-scale DR observations such as i) reduction of a specific energy requirement during pumping when compared to a pure solvent, ii) modifications of the turbulent flow intensity and structure, iii) the effect of polymer concentration and molecular weight on measured $DR$, iv) DR onset and maximum DR asymptote and v) polymer degradation in turbulent flow.

Early explanations of the DR effect linked the phenomenon to a pipe or channel wall. They include slip at the wall [102] or a layer of adsorbed macromolecules on the wall [103]. These theories have been either disproved or they have no experimental support [22].

Later explanations tried to find a link between vortices and polymer molecules. The relationship between polymer molecules and vortices is for example demonstrated by the existence of DR onset at a specific $Re$. The first complex explanation of DR was proposed by Virk [12] who linked the DR effect to a macromolecular deformation in the buffer region. Virk supposed that the DR onset occurs when the ratio of polymer and turbulence length scales attain specific value. The interaction of polymer molecules with vortexes is situated in the vicinity of $y^+ \sim 15$ which means, according to Virk, that the drag reducing effect is connected to the interaction of polymer molecules with the turbulent bursting process.

Lumley [34] stated that polymer molecules are elongated due to the elongation component of turbulent flow. Additionally, the extent of polymer elongation is lowered by flow vorticity thanks to randomly fluctuating strain fields decreasing the polymer residual time when it is aligned with the strain field. Therefore, the elongation should take place in the buffer region, but not in the viscous sublayer where polymer molecules are not subjected to elongation. He also postulated that the elongated polymer molecules lead to an increase in effective viscosity which enhances the dissipation of turbulent fluctuations. This effect consequently leads to an increase of the thickness of the buffer region. Lumley in his theory explains the onset phenomenon by linking the time scale ratio of eddies to the polymer relaxation time, which is in direct contradiction to Virk's theory who based the DR onset on the ratio of polymer and turbulence length scales. He also explained the maximum DR by a feedback saturation mechanism between eddies causing polymer molecules elongation, which at the same time suppress the turbulent character of the flow. The disadvantage of the theory is that it is qualitative rather than quantitative. However, Lumley's analysis showed that his theory, which operates with increase of effective viscosity in regions with high strains, can produce reduction in frictional drag [84].

Ryskin [104] proposed a yo-yo model of polymer dynamics in transient extensional flows and using this idea, he constructed a quantitative theory of DR [105]. The yo-yo model states that when the strain rate exceeds a critical value the polymer chain unravels. The central part is elongated first and grows at the expense of the coiled ends. When the flow becomes weaker the straightened polymer molecule flocks back into the coiled conformation.

Tabor et al. [106] introduced their cascade theory of DR, which is based on the well known Kolmogorov cascade theory of turbulences. The DR theory was lately improved and summarised by de Gennes [107]. They assumed that each coil behaves like a small spring and that the flow characteristic is altered when the elastic energy of elongated polymer molecules becomes equal to the kinetic energy of the flow domain. When these two become comparable the turbulence is truncated at certain length scale. The novelty of the theory is that it is based on the elastic properties of the dissolved polymers and it accounts for moderately stretched polymer molecules. The cascade theory predicts both minimum and maximum polymer concentration in DR effect. Minimum polymer concentration is defined from a polymer elastic energy which has to be higher than the lowest Reynolds stresses of the flow defined by Kolmogorov vortices. Maximum polymer concentration where the level of $DR$ does not increase with increasing polymer concentration is related, according to de Gennes, to the polymer overlap concentration.

A mechanism which is based on polymer-solvent interactions was introduced by Brostow [69]. He suggested that polymer molecules should be viewed as polymer-solvent domains that are shaped by vortices. The DR effect should be caused by solvent molecules (solvated and entrapped inside the domain) that are protected from turbulent flow eddies. The larger the protected solvent volume inside the polymer domain is the higher is measured $DR$. He also stated that the polymer DR efficiency can be directly linked and estimated from the solvation number. Brostow, using his model, explains several effects observed during DR experiments such as: the effect of polymer molecular weight, polymer concentration, solvent quality as well as polymer degradation [37].

L'Vov et al. [108] described the mechanism of DR effect as a suppression of the Reynolds stresses in the buffer region, which leads to a decrease in the momentum flux to the wall and therefore increase in the mean velocity in the channel. The theory is based on boundary layer turbulent models which consist of a momentum balance and an approximate turbulent energy equation.

The latest attempt to describe DR phenomenon was made by Sher et al. [109] who suggested a new mechanistic model. Their model consists of a force balance of polymer molecules in turbulent flow where the main forces exhibited on a polymer molecule are elastic and centrifugal. In the model the eddy kinetic energy is converted to elastic energy stored in a polymer molecule by means of centrifugal elongation. Such an excited polymer molecule is viscously damped by the surrounding solvent molecules when the polymer molecule relaxes. They used their model to simulate Virk's experiments and found good agreement, without using empirical constants, in prediction of: i) velocity profiles, ii) maximum DR asymptote, iii) onset of DR and iv) dependency of measured $DR$ on polymer concentration and radius of gyration.

## 2.5 Measurement of Drag Reduction

Various techniques for DR quantification have emerged since the discovery of the DR phenomenon. Each of them is suitable for different exploration of the DR phenomenon and all of them have advantages and disadvantages that are discussed below. An appropriate combination of measuring techniques can help in better understanding of the subject and clarifying the DR mechanism or the polymer degradation mechanism.

An emerging technique to study turbulent DR is based on rotating disk apparatuses (RDA) of various constructions that simulate external flow. They are widely used for measuring polymer DR effectiveness, mechanical shear degradation, molecular weight and solvent effects [17, 44, 110, 111, 112]. However, the mechanism of pipe/channel turbulent DR is different when compared to the flow in RDA. The flow in RDA is a drag flow with no given pressure gradients, thus the origin of the turbulent boundary layer is different than in the pressure-driven flow case. RDA flow is generally described as external flow while pipe/channel flows are internal flows. External flow studies the total drag (frictional plus form drag), whereas internal flows are subjected only to frictional drag. The DR phenomena is only related to the frictional drag. The difference in the ratio between the frictional drag and the total drag stands for maximum $DR$ for internal flows of $\sim 80\%$ while for external flows reachable maximum $DR$ is $\sim 50\%$, which complicates the comparison of results. On the other hand RDAs are easy to use, thermally controlled and provide stable and highly accurate results for long period of time, thus they are very suitable for the investigation of the mechanical stability of novel polymers. A manual for constructing RDA was published by Kim et al. [113]. The advantages and drawbacks are summarised in Table 2.2.

Table 2.2: Advantages and disadvantages of rotating disk apparatus.

| Advantages | Disadvantages |
|---|---|
| Easy to use | Different nature of turbulent pipe flow |
| Quick $DR$ characterisation | Turbulent flow is not fully understood |
| Polymer degradation studies are possible | |
| Flow visualisation studies are possible | |

Couette flow refers to a non-turbulent circular flow between two long concentric cylinders where the outer cylinder is a stator and the inner a rotor. When the rotor speed exceeds a critical value the stable flow between rotating cylinders starts to exhibit toroidal instabilities known as Taylor vortices. In general Taylor vortices emerge when the centrifugal forces become large enough to overcome the stabilising viscous forces. Further increase of the rotor speed leads to wavy vortex flow, the appearance of modulated waves and finally turbulent Taylor flow [114]. It was proved that the addition of DR active polymers decreases the intensity and the onset of Taylor vortices [115, 116]. The advantage of DR studies performed in Taylor-Couette flow is that the nature of the instabilities is better understood and does not vary with time in contrast to fully chaotic turbulent pipe flow. The advantages and drawbacks are summarised in Table 2.3. A recent study showed that a commercial rheometer can be used for the characterisation of polymer induced DR [117]. The authors used special double-gap sample holder having axial symmetry as a substitute for the standard concentric cylinder measuring system. Using a similar setup a fully developed turbulent Taylor flow, that still contains the Taylor cells, can be obtained at higher rotational speeds [118]. An accurate polymer $DR$ characterisation in the sense of the effect of polymer molecular weight, polymer concentration and temperature was obtained [43, 119].

Table 2.3: Advantages and disadvantages of Couette-Taylor cell.

| Advantages | Disadvantages |
|---|---|
| Easy to use<br>Quick $DR$ characterisation<br>Polymer degradation studies possible<br>Flow visualisation studies possible<br>Known nature of Taylor vortices | Taylor flow is not the same as turbulent pipe flow |

DR effect is mostly utilised in applications dealing with pipe flow e.g. pipeline systems, hydraulic fracturing and irrigation systems. Pilot-plant scale flow facilities were developed to obtain realistic and quantitative testing method for polymer induced DR in turbulent pipe flow. The pilot-plant scale experimental systems are voluminous and measurements are both time and sample consuming. The level of $DR$ in turbulent pipe/channel flow is defined as follows:

$$DR = \frac{f_{\mathrm{s}} - f_{\mathrm{a}}}{f_{\mathrm{s}}} \cdot 100_{Re=\mathrm{const.}} \tag{2.14}$$

where the subscript s stands for the pure solvent and a for a solvent containing a drag reducing additive. Generally three different methods for introducing a polymer into turbulent flow have been used (see Figure 2.3) [3]. A homogeneous pre-mixed DR (case A) occurs when a polymer is mixed into the solvent and dispersed uniformly before it is allowed to flow through the pipe. It is obvious that in the turbulent flow regime there is no polymer concentration gradient. Homogeneous DR is affected by following factors: $DR = f\,(Re, d, c, P, O)$ where $c$ designates the polymer concentration in the pipe, $d$ the pipe diameter, $P$ summarises the physical and chemical properties of the polymer, and $O$ stands for other parameters such as temperature, $pH$ or salinity. During homogeneous diffusing DR (case B) a concentrated polymer solution is injected into the centreline or at the wall of the pipe at concentrations where the polymer is completely dispersed by turbulent mixing. This leads to uniform homogeneous polymer concentration distribution at a specific distance downstream from the injector, which depends on the injector type and turbulent flow intensity. In the case C, known as heterogeneous or polymer thread DR, a concentrated polymer solution is injected into the centreline, wall or inner near-wall region of turbulent flow so a coherent unbroken polymer thread is formed that continues several hundred pipe diameters downstream the injector. Diffusing DR and heterogeneous DR depends on: $DR = f\left(Re, d, {}^{x}\!/\!{}_{d}, I, c_{\mathrm{r}}, c_{\mathrm{p}}, u^{*}, P, O\right)$ where $I$ describes the injector type, $c_{\mathrm{r}}$ the polymer concentration averaged over the cross section of the tube, $c_{\mathrm{p}}$ the polymer concentration of the injected polymer solution, $u^{*}$ the ratio between injected and mean flow velocity and ${}^{x}\!/\!{}_{d}$ is the downstream distance from the injector. The advantages and drawbacks of the pilot plant flow facility systems are summarised in Table 2.4.

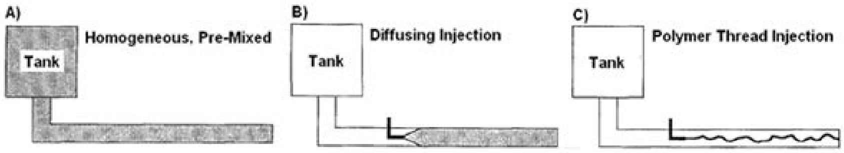

Figure 2.3: Different methods of introduction polymer drag reducers into pipe flow [3].

Most of the DR studies have focused on various aspects of homogeneous DR, such as polymer testing [12], effect of pipe diameter [120], measurements of turbulent flow velocity fields [100], the DR onset [121] and maximum DR [122]. A typical homogeneous DR test apparatus is shown in Figure 2.4 [123]. As can be seen the system consists of a closed-loop circuit where the flow is driven by a pump. It is well known fact that common polymeric DR agents are vulnerable to mechanical degradation [17, 65, 124] so the flow facility configuration has strong influence on the polymer stability and thus the experimental error. The mechanical degradation of the drag reducing polymers is caused by the mechanical energy that the polymer solution obtains by passing through pumps or the pipe/channel system. It has been shown by den Toonder et al. [62] that the choice of a pump is crucial for polymer stability. They found that the use or centrifugal pumps substantially decrease measured $DR$ and they suggested the use of different pumps e.g. disk pump or screw pump in order to minimise the polymer degradation. Another way of avoiding the mechanical polymer degradation is to use a one-pass system with a pneumatic driven flow. This set-up was successfully used for studying the effect of pipe diameter on $DR$ [125]. In the case of pneumatic pressure driven flow the polymer degradation takes place at the pipe inlet where high extensional strain is developed [65]. The DR effectiveness is measured via pressure drop along the pipe test section. It is worth noting that all the equipments used in a flow facilities require to minimise contact with tested polymer solution to avoid mechanical degradation of the polymer.

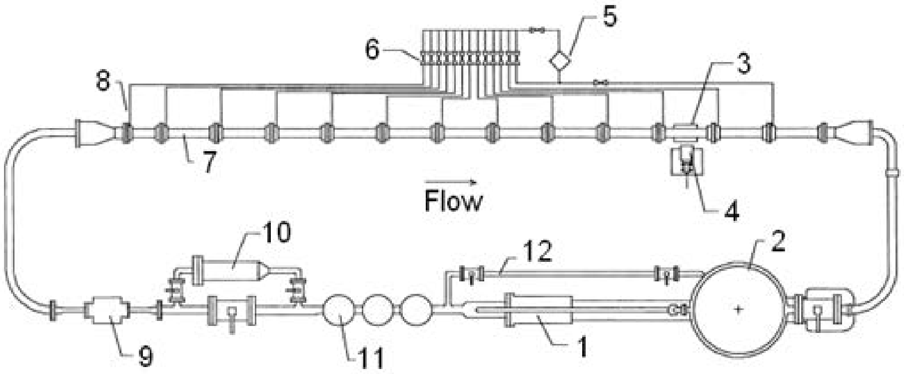

Figure 2.4: Typical pilot plant scale flow facility to test homogeneous DR (40) where 1 – screw pump, 2 – storage tank, 3 – optical window, 4 – LDV instrumentation, 5 – differential pressure transducer, 6 – valves, 7 – pipe test section, 8 – pressure taps, 9 – flow meter, 10 – water filter, 11 – pump pulse dampers, 12 – mixing loop.

Heterogeneous DR was firstly described by Vleggaar and Tels [126] in 1973 and was widely studied in the following years. The heterogeneous DR facilities contain a polymer injector that is usually flanged into the test section after the pump and it is constructed in one-pass flow order while homogeneous DR facility is constructed in recycle loop order. The construction of the heterogeneous DR flow facility allows to minimise the risk of polymer being degraded in the pump. The polymer can be injected into the mean flow by means of different injectors. The most common technique is centreline injection [127, 128, 129]. Bewersdorff [95] found that centreline polymer injection of PAAm is more efficient in the terms of $DR$ when compared to a homogeneous polymer solution with the same mean concentration. His results were confirmed by Frings [130]. However, experiments performed by Hoyt and Sellin [127] showed opposite results. They found that at low $Re$ the efficiency of heterogeneous DR is almost the same as when using a homogeneous polymer solution, but at higher Re the outcome of premixed polymer solution was better. The wall injector was only used in channel turbulent flow. The comparison between wall and central line injector using a rectangular channel flow facility was made by Kim et al. [129]. An annular injector was used in the pipe turbulent flow experiments preformed by Frings [130]. His results indicated that the polymer injection into the inner near-wall region provides better DR efficiency than centreline injection or using a premixed polymer solution. According to Smith et al. [3], who performed detailed measurements of the streamwise $DR$ and polymer concentration in the inner near-wall region, the mechanism of heterogeneous DR can be explained by small concentrations of polymer additives in the vicinity of the wall that are removed from a polymer thread.

Table 2.4: Advantages and disadvantages of pilot-plant scale flow facilities used to test polymer DR.

| Advantages | Disadvantages |
|---|---|
| Can simulate real applications | Turbulent flow is not fully understood |
| Flow visualisation studies possible | Expensive |
| Homogeneous and heterogeneous DR can be tested | Experiments are time consuming |

# Chapter 3

# Experimental Methods

This chapter describes the experimental work on polymer solution preparation and characterisation in quiescent and flow conditions. The characterisation techniques in quiescent conditions such as intrinsic viscosity, gel permeation chromatography, multi-angle laser light scattering and rheology are explained including the parameters used for the calculation of measured variables. Flow characterisation techniques including author developed DR characterisation using a rheometer, design and operation parameters of author designed pilot plant scale flow facility and particle image velocimetry measuring principles are described.

## 3.1 Materials

Typical water soluble polymers with a linear structure, namely polyethylene oxide (PEO) and polyacrylamide (PAAm), were chosen for this work. Both polymers are non-ionic and the chemical structure is shown in Figure 3.1. The details of the polymers as given by manufacturers and the abbreviations of the polymers used throughout the thesis are summarised in Table 3.1.

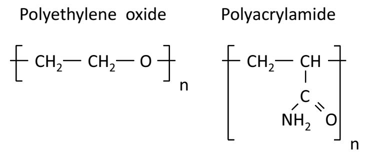

Figure 3.1: Chemical structure of polyethylene oxide and polyacrylamide.

Table 3.1: Polymers and the corresponding abbreviations used in this study with the weight average molecular weigh as stated by the supplier.

| Polymer type | Manufacturer | Molecular weight $\left[\mathrm{g}\cdot\mathrm{mol}^{-1}\right]$ | Abbreviation |
|---|---|---|---|
| PEO | Sigma-Aldrich, Inc. | 200,000 | PEO0.2 |
| PEO | Sigma-Aldrich, Inc. | 2,000,000 | PEO2 |
| PEO | Sigma-Aldrich, Inc. | 4,000,000 | PEO4 |
| PEO | Sigma-Aldrich, Inc. | 8,000,000 | PEO8 |
| PAAm | Polyscience, Inc. | 5,000,000-6,000,000 | PAAm5 |

The solvents used in the study are: DI water (purified by: Option 4 Water Purifier, ELGA), 2-propanol (purity 99.7%; VWR International Ltd.) and formamide (purity 99%; Sigma-Aldrich). All solvents and solvent mixtures were filtered through $0.22\,\mu$m cellulose acetate Millipore filters (Millipore Co.) prior use. Tap water was used for the experiments employing flow facility.

The preparation of aqueous polymer solutions for characterisation in quiescent conditions and for $DR$ characterisation using a commercial rheometer requires great care. Contamination of dust or any other impurities as well as mechanical or chemical polymer degradation have to be avoided. It is known that polymer aggregation can be triggered by a presence of organic or inorganic impurities [131]. To avoid contamination, all glassware was cleaned using a detergent and sonicated twice in DI water for 20 min. Afterwards it was rinsed with DI water filtered through $0.22\,\mu$m filter and dried at 80°C in an oven for 4 h. During the dissolution, care was taken that the polymer powder would not clump together on the solvent surface. All solutions were prepared gravimetrically. Polymer powder was weighted with accuracy $\pm 0.1$ mg and solvents were weighted with accuracy $\pm 10$ mg. The error for the preparation of the polymer stock solution was 0.18% and 0.01% for polymer powder and solvent, respectively. After the starting $\approx 1$ h interval in which the polymer powder was allowed to hydrate in quiescent conditions, the polymer solution was subjected to mechanical shaking ($\approx 200\,\mathrm{oscilation}\cdot\mathrm{min}^{-1}$) for 12 to 24 h (KS 260 basic, IKA, Staufen, Germady). No magnetic stirrer was used to avoid mechanical polymer degradation. The homogeneity of the polymer samples was checked visually. Only samples that did not contain visible impurities or undissolved polymer microgels were used for the analysis. Solutions prepared by this procedure were kept at ambient temperature and were analysed within 3 days. Stock solutions with a concentration of 550 wppm were prepared and then diluted to lower polymer concentrations. This procedure should minimise the weighting error while preparing very diluted polymer solutions.

Crystaline guanine platelets (Kalliroscope Corporation, Massachusetts, USA) were used for Taylor flow visualisation experiments. The average size of an platelet is $6 \times 30 \times 0.07\,\mu$m and the density is $1,620$ kg $\cdot$ m$^{-3}$. The platelets orient according to the direction of a local shear stress so that only those platelets with their faces oriented toward the observer reflect light.

The preparation of polymer solutions for experiments using flow facility is described in Section 3.2.6.

## 3.2 Methods

### 3.2.1 Intrinsic Viscosity

Intrinsic viscosity measurements were performed using an Ubbelohde capillary viscosimeter. All measurements were performed at $25.0 \pm 0.1$°C using a Schott CT 150 water bath (Mainz, Germany). Efflux times were measured for a solvent and polymer solutions of various concentrations. These times were converted to specific $\eta_{\mathrm{sp}}$ and reduced $\eta_{\mathrm{red}}$ viscosities using the following equations:

$$\eta_{\mathrm{sp}} = \frac{t_{\mathrm{a}} - t_{\mathrm{s}}}{t_{\mathrm{s}}} \tag{3.1}$$

$$\eta_{\mathrm{red}} = \frac{\eta_{\mathrm{sp}}}{c} \tag{3.2}$$

where $c$ is the polymer concentration, $t_{\mathrm{a}}$ and $t_{\mathrm{s}}$ are the efflux times of the polymer solution and the solvent, respectively. The intrinsic viscosity $[\eta]$ is defined as the reduced viscosity extrapolated to zero concentration:

$$[\eta] = \lim_{c \to 0} \frac{\eta_{\mathrm{sp}}}{c} \tag{3.3}$$

The Huggins coefficient $k_H$ can be determined from the linear relationship between the reduced viscosity and the polymer concentration:

$$\eta_{\mathrm{red}} = [\eta] + k_H \, [\eta]^2 \, c \tag{3.4}$$

where $k_H \, [\eta]^2$ is the slope and $[\eta]$ is the intercept. The dimensionless Huggins coefficient $k_H$ describes the interaction between a polymer molecule and a solvent; high $k_H$ values indicate that polymer-polymer interactions are favoured over polymer-solvent interactions, which usually is the case in poor solvents [132]. Cluster formation in a solution can further change the value of $k_H$. The Huggins coefficient ranges between $0.5 - 0.7$ in a good solvent. Higher $k_H$ values than for a good solvent indicate poor polymer dissolution and the presence of polymer clusters [132]. The polymer overlap concentration $c^*$ can be estimated using following relation:

$$c^* \approx \frac{1}{[\eta]} \tag{3.5}$$

Finally, the molecular weight was estimated using Mark-Houwing equation:

$$[\eta] = K^* M^a \tag{3.6}$$

where $K^*$ and $a$ are parameters depending on the particular polymer-solvent system. The parameter $a$ is the so called stiffness factor and it reaches values of 0.5 and 0.8 for a theta solvent and a good solvent, respectively. Semi-flexible polymers have $a \geq 0.8$. The values of $K^*$ and $a$ parameters used in this work were obtained from Polymer Handbook [133] and they are: $K^*_{\mathrm{PEO}} = 12.50 \cdot 10^{-3}\,\mathrm{ml} \cdot \mathrm{g}^{-1}$; $a_{\mathrm{PEO}} = 0.78$; $K^*{}_{\mathrm{PAAm}} = 6.31 \cdot 10^{-3}\,\mathrm{ml} \cdot \mathrm{g}^{-1}$; $a_{\mathrm{PAAm}} = 0.80$.

### 3.2.2 Gel Permeation Chromatography

GPC-50+ system (Polymer Laboratories Ltd) was used to analyse the molecular weight of the polymers. The system was equipped with a triple detector assembly: refractive index, viscosity and light scattering (15° and 90°) detectors. A guard column (PL aquagel-OH Guard 15 $\mu$m) and two columns (PL aquagel-OH 60 15 $\mu$m) for analysing high molecular weight polymers were used in series to separate the polymer molecules based on their hydrodynamic volume. The detectable molecular weight range is $1 \cdot 10^5 - 1 \cdot 10^7\,\mathrm{g} \cdot \mathrm{mol}^{-1}$. The mobile phase was 0.1 M $NaNO_3$ and 0.01% w/w $NaN_3$ in DI water, the flow rate of $0.7\,\mathrm{ml} \cdot \mathrm{min}^{-1}$ was constant for all measurements which are similar conditions as used by Liberatore et al. [42]. The eluent was filtered three times through 0.1 $\mu$m anodisc Millipore filters (Millipore Co.) prior use in order to remove any contamination that would interfere with the light scattering detector. A PEO standard of $M_w = 124,700\,\mathrm{g} \cdot \mathrm{mol}^{-1}$ (Polymer Laboratories Ltd) was used to calibrate all three detectors. All measurements were performed at 25°C in an air conditioned room. The chromatographs were analysed using commercial GPC software PL Cirrus Multi (Polymer Laboratories Ltd).

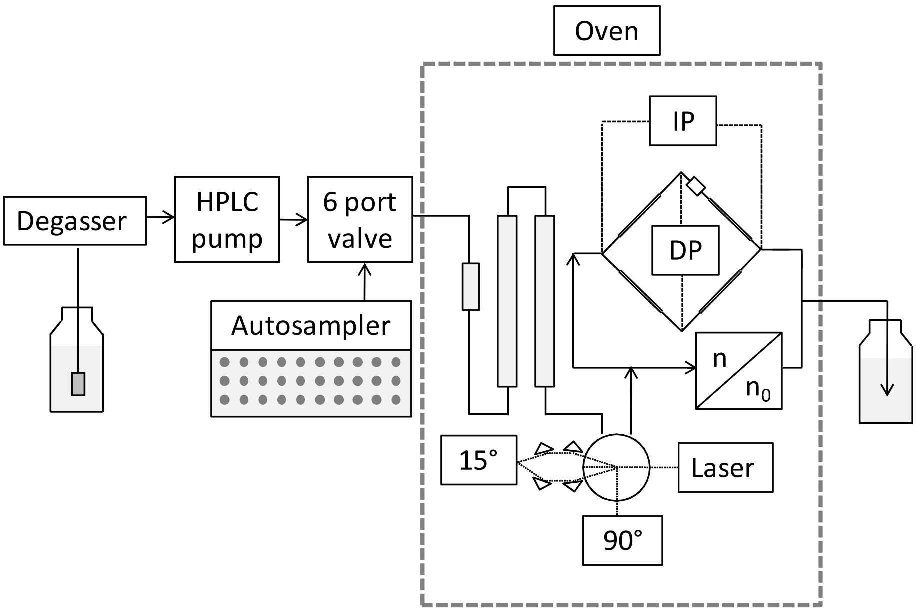

Figure 3.2: Schematic illustration of the GPC system.

A schematic illustration of the GPC system is shown in Figure 3.2. The mobile phase is stored in a sealed reservoir and it is degassed before pumping through the system by a low oscillation 2 piston pump. The polymer samples are injected into the mobile phase flow from the autosampler through a 6-port valve and then are carried to the separation columns. Polymer is detected in 3 different detectors and the molecular weight calculation mechanism is described below. The molecular weight calculation utilises the simplified Rayleigh equation, which states that the intensity of scattered light at 0 degree angle is proportional to the molecular weight:

$$R\left(\theta\right)_{\theta\rightarrow 0}\cong KcM \tag{3.7}$$

where $K$ is the optical constant, $c$ is the polymer concentration and $M$ is the polymer molecular weight. Our system detects the scattered light at 15° and 90°. Combination of the intensities of scattered light from both angles allows the extrapolation of the scattered light to zero angle. Polymer concentration is directly obtained from the refractive index detector. The optical constant $K$ is defined as follows:

$$K=\frac{4\left(\pi n_0\frac{dn}{dc}\right)^2}{N_A\lambda_0^4} \tag{3.8}$$

where $n_0$ is the refractive index of the solvent, $\frac{dn}{dc}$ is the refractive index increment of the polymer-solvent pair, $N_A$ is Avogadro's number and $\lambda_0$ is the wavelength of the incident light in vacuum. The $n_0$ and $\frac{dn}{dc}$ values necessary for the calculation were obtained from the Polymer Handbook [133].

The molecular weight distributions are represented in the terms of number and weight molecular weight averages. For a sample with $N$ polymer molecules with number $n_i$ or mass $w_i$ of molecular masses $M_i$, the number-average molecular weight is defined as:

$$M_n = \frac{\sum\limits_i n_i M_i}{\sum\limits_i n_i} = \frac{\sum\limits_i n_i M_i}{N} = \frac{\sum\limits_i c_i}{\sum\limits_i \frac{c_i}{M_i}} \sim \frac{RI\,peak\,area}{Molar\,concentration\,peak\,area} \tag{3.9}$$

The molar concentration peak is a derived function which is not directly detected by any used detector. Therefore the determined values are often of higher error than the weight-average molecular weight. The weight-average molecular weight is defined as:

$$M_w = \frac{\sum\limits_i n_i M_i^2}{\sum\limits_i n_i M_i} = \frac{\sum\limits_i w_i M_i}{\sum\limits_i w_i} = \frac{\sum\limits_i c_i M_i}{\sum\limits_i c_i} \sim \frac{LS\,peak\,area}{RI\,peak\,area} \tag{3.10}$$

A monodisperse sample has $M_n = M_w$. The deviation from the monodisperse state, polydispersity, is often shown as a ratio of weight to number molecular weight averages:

$$PDI = \frac{M_w}{M_n} \tag{3.11}$$

The intrinsic viscosity is calculated from the viscosity detector using following relation:

$$[\eta] = \frac{\sum \eta_{\mathrm{sp},i}}{\sum c_i} = \frac{\frac{4DP}{IP-2DP}}{RI\,peak\,area} \tag{3.12}$$

where $\eta_{\mathrm{sp},i}$ is the specific viscosity of the $i^{th}$ fraction, $DP$ is the differential pressure and $IP$ is the pressure drop in the viscometer (see Figure 3.2). The hydrodynamic radius $R_h$ is calculated from the intrinsic viscosity and the weight average molecular weight using the following expression which is valid for random coils:

$$[\eta]\,M_w = \frac{10}{3}\pi R_h^3 \tag{3.13}$$

The $\rho_{\mathrm{t}}$-ratio that is an estimate of the molecule topology is defined as follows:

$$\rho_{\mathrm{t}} = \frac{R_g}{R_h} \tag{3.14}$$

The $\rho_{\mathrm{t}}$-ratio gives following the values: $1/\sqrt{3} ln\left(l/D - 0.5\right)$; 0.775; 1; 0.775-4; 1.505 for a rod with a length $l$ and diameter $D$, a homogeneous sphere, a hollow sphere, an ellipsoid and a random polymer coil, respectively. Please note that the $\rho_{\mathrm{t}}$-ratio has only little informative importance since the hydrodynamic radius was calculated using the expression which is only valid for random coils. Experimentally the hydrodynamic radius should be measured using dynamic light scattering employing Stokes-Einstein equation.

### Calibration

Gel permeation chromatography is an analytical method for the determination of polymer molecular weight distribution. In this work the triple detection is used which provides not only the information on polymer molecular weight distribution but also information on the radius of gyration and intrinsic viscosity. The GPC was calibrated using a PEO standard $M_w = 124,700\,\mathrm{g}\cdot\mathrm{mol}^{-1}$ and the system constants obtained from the calibration are shown in Table 3.2. The $IDD$ constants in Table 3.2 refer to the inter-detector shift. The $K$ constant refers to the area of the signal. A typical chromatograph containing signals from refractive index, viscosity and laser scattering at 15 and 90 degrees detectors is shown in Figure 3.3.

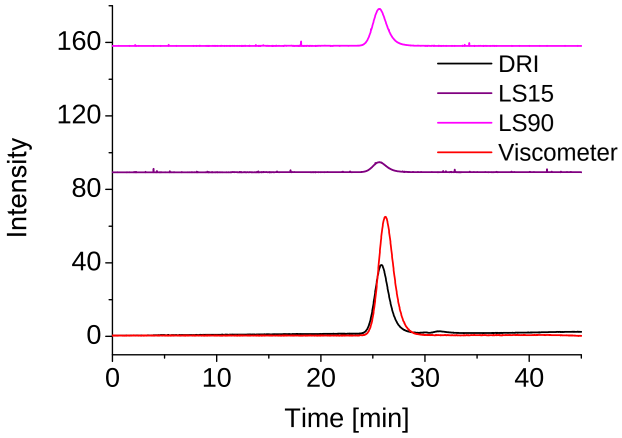

Figure 3.3: Example of GPC chromatograph with traces for differential refractive index detector, light scattering at 15° and 90° and viscometer. The example is PEO standard with $M_w = 124,700\,\mathrm{g}\cdot\mathrm{mol}^{-1}$.

Table 3.2: GPC system calibration constants used for the evaluation of multi-detector response from GPC.

| $IDD_{\text{vis.}}$ [min] | $IDD_{\text{LS}}$ [min] | $K_{\text{conc.}}$ | $K_{\text{LS}\,15^o}$ | $K_{\text{LS}\,90^o}$ | $K_{\text{diff. press.}}$ | IP [kPa] |
|---|---|---|---|---|---|---|
| -0.3667 | 0.2167 | 4568.75 | 197429 | 52542.4 | 1.09887 | 25.5 |

### 3.2.3 Multi-Angle Laser Light Scattering

Multi-angle laser light scattering (MALLS) is analysing the elastic scattering of monochromatic light from polymer molecules in order to asses the absolute molecular weight, radius of gyration and second virial coefficient. The static light scattering measurements were carried out using the Goniometer SLS-2 PC104 (SLS-Systemtechnik, Denzlingen, Germany). The incident laser light was vertically polarised and the wavelength was 543.5 nm. The scattered light was measured between $15^\circ < \theta < 145^\circ$ in 5° increments. Each time 6 polymer concentrations were prepared. The polymer samples were purified by centrifuging (centrifuge: Accu Spin 400, Fisher Scientific) at 3,000 rpm for 15 min. All the measurements were performed at room temperature.

A schematic illustration of the MALLS technique is shown in Figure 3.4. Scattering intensities were analysed utilising the Zimm extrapolation method using Rayleigh equation:

$$\frac{Kc}{R_\theta} = \left(\frac{1}{M_w} + 2A_2c\right)\left(1 + \frac{1}{3}R_g^2q^2\right) \tag{3.15}$$

where $K$ is the optical constant defined by Equation 3.8, $R_\theta$ the Rayleigh ratio, $\theta$ the scattered angle, $A_2$ the second virial coefficient, $R_g$ the radius of gyration and $q$ the scattering vector. The second virial coefficient $A_2$ expresses the deviation of a solvent from an ideal solvent, $\theta$-solvent, for a given polymer-solvent pair. In good, theta and poor solvent the $A_2$ yields $> 0$; 0 and $> 0$ values, respectively. The scattering vector is defined as follows:

$$q = \frac{4\pi \sin\left(\frac{\theta}{2}\right)}{\lambda_0} \tag{3.16}$$

where $\lambda_0$ is the laser wavelength. The typical Zimm analysis is based on plotting the light scattering results in the coordinates $Kc/R_\theta$ as a function of $q^2 + kc$ where $k$ is an arbitrary selected constant. The $M_w$, $R_g$ and $A_2$ values are obtained by extrapolation of the scattered light intensity to zero concentration and zero angle:

$$\lim_{\theta\to 0}\frac{Kc}{R_\theta} = \frac{1}{M_w} + 2A_2c \tag{3.17}$$

$$\lim_{c \to 0} \frac{Kc}{R_\theta} = \frac{1}{M_w} \left[ 1 + \frac{q^2}{3} R_g^2 \right] \tag{3.18}$$

The molecular weight and the radius of gyration can be used to estimate the polymer overlap concentration $c^*$. Ying et al. [134] stated that for a polymer molecule having a random coil conformation in a good solvent the overlap concentration can be ranged by:

$$\frac{M_w}{N_A R_g^3} \sim c^* \sim \frac{3M_w}{4\pi N_A R_g^3} \tag{3.19}$$

It should be noted that the equations described above provide meaningful results only for polymer solutions that do not contain aggregates. The presence of aggregates demonstrates itself by a curved dependence of $\frac{Kc}{R_\theta}$ vs. $q^2$, whereas molecularly dissolved polymers exhibit liner dependence. As discussed by Kratochvíl [135], the information of individual polymer molecules can be obtained by analysing the intensity of scattered light at large angles which exhibit a linear dependency of scattered light on the scattering angle. The analysis of the whole angular range of the scattered light revels the additional information on the aggregates.

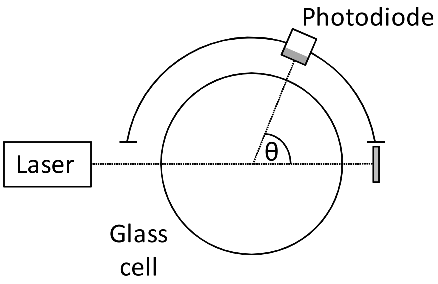

Figure 3.4: Schematic representation of multi-angle laser light scattering.

### 3.2.4 Nuclear Magnetic Resonance

The nuclear magnetic resonance is a common method to analyse and characterise the chemical structure of chemicals. NMR spectra of the polymers used in this work dissolved in $D_2O$ were obtained using 2-channel DRX-400 spectrometer (Bruker, Germany). Chemical shifts are shown in weight parts per million.

### 3.2.5 Rheology and Quick Drag Reduction Measurement

A Physica USD 200 rheometer (Physica Messtechnik GmBH, Stuttgart, Germany) equipped with a double gap sample holder having an axial symmetry (see

Figure 3.5) was used for rheological and DR measurements. The sample was located in interconnected stationary cylinder shaped stators between which a thin walled tube shaped rotor was placed. The sample loading procedure is crucial for obtaining correct and meaningful DR results. Care was taken to avoid the presence of air bubbles in the measuring cell. Air bubbles cause sample foaming during a measurement, which leads to chaotic increase of the measured rheological variables.

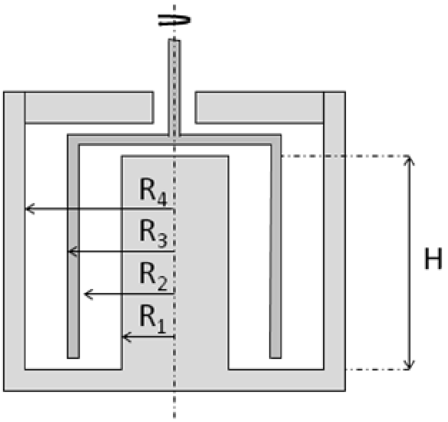

Figure 3.5: Schematic representation of the double gap cell with axial symmetry used for DR characterisation. The measuring cell active rotor height is $H = 111.00\,\mathrm{mm}$ and the radii are $r_1 = 22.25\,\mathrm{mm}$, $r_2 = 22.75\,\mathrm{mm}$, $r_3 = 23.50\,\mathrm{mm}$ and $r_4 = 24.00\,\mathrm{mm}$. The sample volume: 17 mm. The perspex cell used for Taylor flow visualisation has $r_4 = 63.33\,\mathrm{mm}$.

The measuring cell active rotor height is $H = 111.00\,\mathrm{mm}$ and the radii are $r_1 = 22.25\,\mathrm{mm}$, $r_2 = 22.75\,\mathrm{mm}$, $r_3 = 23.50\,\mathrm{mm}$ and $r_4 = 24.00\,\mathrm{mm}$. The aspect ratio $\Gamma = \frac{H}{\delta^*}$ is 222, where $\delta^*$ is the gap between the rotor and the stator. Such a big aspect ratio means that the measuring geometry could be considered as indefinitely long cylinders and rotor end effects can be neglected. The rotational speed $\omega_{\mathrm{cyc}}$ and torque $T$ exerted on the rotor were recorded and transformed into shear rate $\dot{\gamma}$ and shear stress $\tau$:

$$\dot{\gamma} = a_{\dot{\gamma}} \omega_{\mathrm{cyc}} \tag{3.20}$$

$$\tau = a_{\tau} T \tag{3.21}$$

where $a_{\dot{\gamma}}$ and $a_{\tau}$ are instrument constants (just for curiosity the parameters are: $a_{\dot{\gamma}} = 4.98$ and $a_{\tau} = 1,217.20$). It should be noted that the constants are valid only for used rheometer equipped with the described measuring cell. The temperature was controlled by a water circulatory thermostat (Julabo Series MV) and was fixed to $25.0 \pm 0.5$°C.

#### 3.2.5.1 Rheological Measurements

Two rheological parameters were measured. The solution apparent viscosity was measured at $\dot{\gamma} = 1,000\,\mathrm{s}^{-1}$. Prior the measurement the samples were pre-sheared at $\dot{\gamma} = 200\,\mathrm{s}^{-1}$ for 30 s. The apparent viscosity was calculated as follows:

$$\eta = \frac{\tau}{\dot{\gamma}} \tag{3.22}$$

The apparent viscosity at the Taylor flow onset was determined by increasing the shear rate from 750 to $3,500\,\mathrm{s}^{-1}$. The apparent viscosity at the Taylor flow onset is defined as an abrupt change of the slope of the function $\eta = f\left(\dot{\gamma}\right)$ (see Figure 5.3). The shear rate span should cover the apparent viscosity at the Taylor onset for pure solvents as well as for polymer solutions. The onset of Taylor vortex formation depends on the fluid properties and the geometry of the measuring cell, which is described by the empirical relation [117]:

$$\left(\frac{\rho\omega_{\mathrm{crit}}}{\eta}\right)^2 = \frac{\pi^4\left(\delta+1\right)}{2\left(\delta-1\right)^3 r_3^4} \cdot \frac{1-0.652\left(\delta-1\right)}{0.00056+0.0571\left[1-0.652\left(\delta-1\right)\right]^2} \tag{3.23}$$

where $\omega_{\mathrm{crit}}$ is the critical angular frequency, $\rho$ is the density, $\eta$ is the apparent viscosity, $\delta$ is the ratio of the distance between rotor and stator ${}^{r_2}/_{r_1} \approx {}^{r_4}/_{r_3}$.

#### 3.2.5.2 Drag Reduction Measurements

It should be noted that the apparent viscosity as defined by Equation 3.22 is valid only for Couette flow, or more generally for flow with no vortices. Hence, we introduce the term nominal shear viscosity $\dot{\eta}$ which is viscosity calculated in Taylor flow region using Equation 3.22.

It was found that the onset of Taylor vortices appears at different apparent viscosities for pure solvents and polymer solutions. Therefore, to make the $DR$ calculation possible the nominal shear viscosity was normalised as follows:

$$\dot{\eta}_N = \dot{\eta}_T - \eta_{T.o} \tag{3.24}$$

where $\dot{\eta}_T$ is the nominal shear viscosity in the Taylor flow region and $\eta_{T,o}$ the apparent viscosity at the onset of Taylor vortices. The normalisation procedure is applied to account for the polymer induced viscosity change which is a function of the polymer concentration. Finally, the level of $DR$ is defined as follows:

$$DR = \frac{\dot{\eta}_{N,\mathrm{s}} - \dot{\eta}_{N,\mathrm{a}}}{\dot{\eta}_{N,\mathrm{s}}} \cdot 100 \,_{\dot{\gamma}=\mathrm{const.}} \tag{3.25}$$

where the subscript s stands for the pure solvent and a for a solvent containing a drag reducing agent.

### 3.2.6 Flow Facility

The $DR$ measurements in a pipe were done using a pilot plant scale flow facility (see Figure 3.6). The author was the person who designed and negotiated the manufacturing of the flow facility (the flow facility was manufactured by G.S. s.r.o., Chotěboř, Czech Republic). The author was also responsible for the modification of the flow facility to a loop configuration and responsible for commissioning the apparatus. The main design specifications for the flow facility were as follows:

- Ability to reach high $Re$ ($Re \sim 1,000,000$) in order to simulate the hydraulic fracturing environment
- Minimisation of polymer degradation before the test section
- Hydrodynamically smooth test section
- Easy to be modified

The flow facility (see Figure 3.6) consists of three tanks of which one is a pressure vessel. The tanks specifications are summarised in Table 3.3. The tank number I is the stirring tank equipped with a low speed stirrer. The maximum stirring speed is set to 200 rpm. The tank allows the preparation of homogeneously dissolved polymer solution for homogeneous DR tests. The two outlets from the tank contain ball valves that prevent polymer from settling in the take out or drain pipe. The main driving pump in the set-up is substituted by pressure vessel labeled II. The pressure driven set-up minimises the risk of polymer degradation that would be inevitable if a centrifugal pump would have been used. The liquid is driven instead by compressed air. The valve system and a pressure sensor on the head of the tank II, connected to the control panel, ensure a constant flow rate during an experiment. The set pressure can be kept constant within 0.01 bar. Tank III is the drain tank and contains an outlet that can either be connected to a sewage or a recycle loop using a pump $\mathrm{Q}_{\mathrm{r/d}}$ (March May Ltd., Huntingdon, UK).

The feed pipe with a diameter of 2 inch is situated before the test section and contains a magneto-inductive flowmeter (Sitrans F M Magflo MAG5000, Siemens, Denmark), a flow straightening device and a smooth contraction from

2 inch to 1 inch pipe diameter. The magneto-inductive flowmeter has no protrusions into the pipe and thus can measure the flow rate of liquids without interfering with the flow. Before entering the pipe, the fluid passes through a flow straightening device which contains a honeycomb screen. The flow straightener function is to eliminate any flow turbulence history that could be present after the fluid passes through the pressure vessel II outlet pipe elbow and pressure vessel closing pneumatic valve.

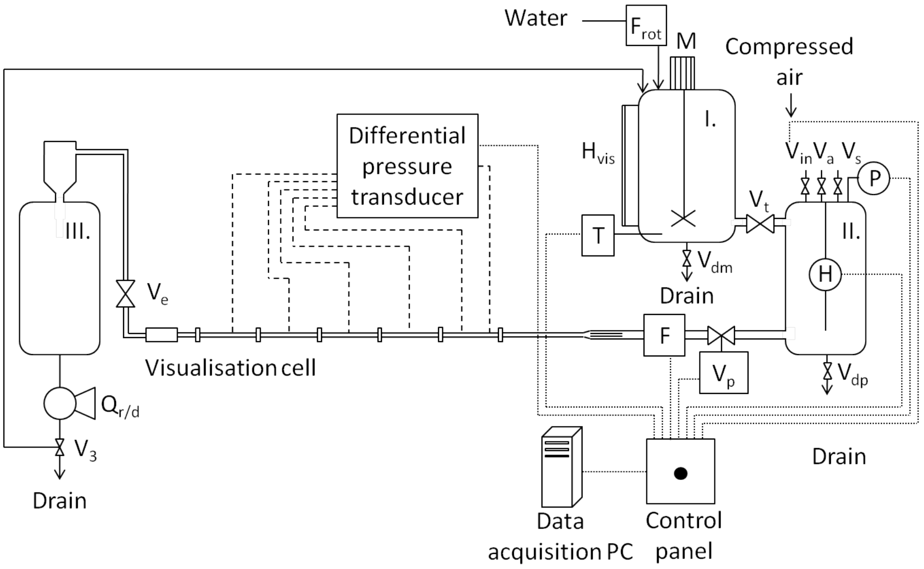

Figure 3.6: Schematic representation of the flow facility. Tanks: I. the mixing tank, II. the pressure vessel, III. the drain tank. Valves: $V_{in}$ the pneumatic valve controlling the pressure in the pressure vessel II, $V_a$ the relief valve, $V_s$ the safety valve, $V_{dm}$ the mixing tank drain valve, $V_{dp}$ the pressure tank drain valve, $V_p$ the pneumatic valve, $V_t$ the transfer valve, $V_e$ the experimental valve, $V_3$ the 3-way valve. Sensors: $F_{rot}$ is the rotor flowmeter, $H_{vis}$ the visual level meter, T the thermometer, P the absolute pressure sensor, H the digital level meter, F the magneto-inductive flowmeter. Other instrumentation: $Q_{r/d}$ the recycle/drain pump, M the low speed stirrer.

The test section consists of a pipe with an internal diameter of 1 inch, pressure taps and flow visualisation cell (see Figure 3.9). The test pipe is made of stainless steel that has short time resistance to the presence of salts (artificial sea water). The test pipe inlet is situated at the distance of 200 pipe diameters from the flow straightening device. The inlet distance is required to allow full development of the turbulent flow. In order to determine the pressure drop, the test pipe is equipped with 6 pressure taps. The distances between which the pressure drop is measured are: 0.2, 1.2, 2.2, 3.2, 4.2 and 5.2 m. It should be noted that the obtained test section was not manufactured accordingly to the design criteria. The test section was not polished and the flange joins were not machined in order to achieve a smooth transition. However, the flow facility was used for DR experiments without re-machining the test section due to time restrictions.

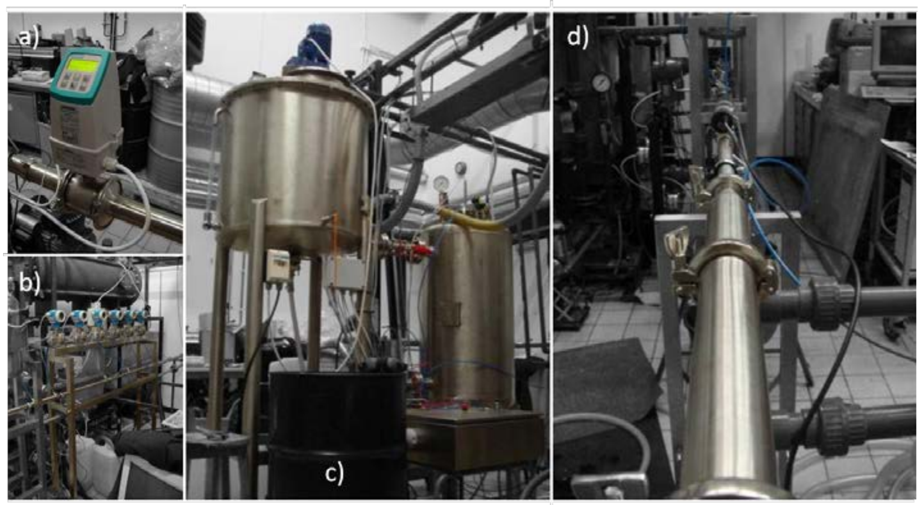

Figure 3.7: Images of the flow facility: a) the magneto-inductive flowmeter, b) the rack containing differential pressure transducers, c) the stirring tank, the pressure vessel and the control panel and d) the entrance to the test section with flow straightening device and the test section with the pressure taps.

The pressure drop between the reference and the measuring taps is recorded using 6 differential pressure transducers (Deltabar S, Endress+Hauser, Germany). A transparent pipe screen is situated at the downstream end of the test section and enables flow velocity profile measurements via a PIV system (see Section 3.2.7). The whole system was designed to be able to reach as high $Re$ in the test section as possible. The maximum pressure in the pressure vessel 20 bar allows for $Re \simeq 1,000,000$. This was however not possible to achieve during the experiments due to the use of a pressurised air from the mains (max pressure: 6 bar). The level of $DR$ was calculated using Equation 2.14. The images of the flow facility are shown in Figure 3.7. The main feature of the flow facility is that it can easily be modified. Here is a list of possible studies that can be performed:

- Fluid flow at very high $Re$ ($Re \simeq 1,000,000$). It would, however, be necessary to connect a rack with pressure cylinders.
- Heterogeneous DR. An additional pressure vessel would have to be con-

nected prior the test section. The pressure vessel was manufactured but was never used.

- Study of the influence of a pipe diameter and artificial roughness on DR effect. The main test section can be relatively easily replaced with a test section with different diameter or with artificial pipe roughness.
- Stability of polymer solutions in centrifugal pumps. The mixing tank I. and pressure vessel II. can be completely bypassed so the system will be closed in a loop.

Table 3.3: Tanks used in the flow facility.

| Parameter | Unit | Tank I | Tank II | Tank III |
|---|---|---|---|---|
| Diameter | [m] | 800 | 600 | 800 |
| Height | [m] | 700 | 1000 | 700 |
| Volume | [$m^3$] | 0.35 | 0.3 | 0.35 |
| Max working pressure | [barg] | 0 | 20 | 0 |
| Min working pressure | [barg] | 0 | 0 | 0 |
| Max temperature | [°C] | 30 | 30 | 30 |
| Min temperature | [°C] | 10 | 10 | 10 |

The operating procedure for the flow facility is as follows (see Figure 3.6 for details):

- Preparation of the experiment
    - Fill the mixing tank I. with water - volume is known from flowmeter $\mathrm{F_{rot}}$ (the level indicator in Tank I is only for visual inspection)
    - Add desired amount of polymer (weighted on analytical balance)
    - Stirring for $\sim 12\,\mathrm{h}$
    - Transfer the polymer solution to the pressure vessel I. by opening valves $\mathrm{V_t}$ and $\mathrm{V_a}$ (the pressure sensor P has to show zero pressure!)
    - Close valves $\mathrm{V_t}$ and $\mathrm{V_a}$ and open the pneumatic valve $\mathrm{V_p}$ and the experimental valve $\mathrm{V_e}$
    - Close valve $\mathrm{V_e}$, pressurise the pressure vessel and set the program to keep the head pressure in the pressere vessel II.
    - Flood the pressure transducers
- Experiment

  - Open/close the experimental valve $\mathrm{V_e}$ (the data are recorded automatically)

- Refiling the pressure vessel
  - Close the pneumatic valve $\mathrm{V_p}$ and open the relief valve $\mathrm{V_a}$
  - Set the 3-way valve $\mathrm{V_3}$ to the direction of the mixing tank I.
  - Switch on/off pump $\mathrm{Q_{r/d}}$
  - Transfer the polymer solution to the pressure vessel II. by opening valves $\mathrm{V_t}$ and $\mathrm{V_a}$ (the pressure sensor P has to show zero pressure!)

- Cleaning
  - Open the valve $\mathrm{V_{dm}}$ and drain the mixing tank
  - Open the valve $\mathrm{V_{dp}}$ and drain the pressure vessel
  - Drain the test section by pressurising the pressure vessel II. and open valves $\mathrm{V_p}$ and $\mathrm{V_e}$
  - Drain the drain tank III. by setting the 3-way valve $\mathrm{V_3}$ to the drain direction and switch on/off pump $\mathrm{Q_{r/d}}$
  - Fill the mixing tank I. with water
  - Transfer water to the pressure vessel II. by opening valves $\mathrm{V_t}$ and $\mathrm{V_a}$ (the pressure sensor P has to show zero pressure!)
  - Pressurise the pressure vessel
  - Flush the test section by opening valves $\mathrm{V_p}$ and $\mathrm{V_e}$ (check the readings of the pressure drop)
  - Drain the drain tank
  - If the pressure drop during flushing the test section was equal to pressure drop for water then the cleaning procedure is over. If not then repeat from the beginning.

### 3.2.7 Particle Image Velocimetry

Particle image velocimetry is a non-intrusive technique used to measure flow velocity. During a PIV measurement the flow is seeded with inert particles, called seeding or tracer particles. These particles are illuminated usually by a laser and the scattered light is recorded on a digital camera. The vector field can be then calculated by comparing the displacement of the particles between a pair of images. A schematic illustration of the PIV system used is shown in Figure 3.8. The system consists of the following parts:

- Flow visualisation cell - Two different cells were used (see Figure 3.9). The visualisation cell used for the flow measurements of the half cross-section of the pipe (where the half is defined as a line symmetry) was designed to minimise the light distortions caused by the curved profile of the pipe. A visualisation cell utilising a refractive index matching technique was used for the near-wall measurements. Such a cell almost completely suppresses the optical differences caused by the differences in the refractive indexes of the studied liquid, the material of the visualisation cell and air.

- Image acquisition consisting of a CMOS camera, camera lenses and a computer for a camera control, image data acquisition and storage.

- Flow illumination consisting of Nd:YAG double pulsed laser, sheet optics, energy attenuation system for control of the intensity of the laser light and timing and synchronisation unit, which controls the laser pulse intensity, laser pulse delay and synchronisation of the emission of the laser light with the CMOS camera.

- Data evaluation software - DaVis supplied by LaVision GMBH (Göettingen, Germany).

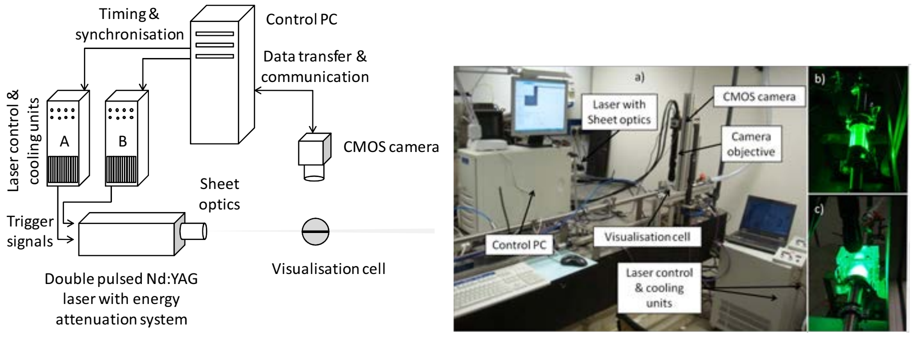

Figure 3.8: Schematic illustration of particle image velocimetry and images of the experimental set-up: a) the overall view on the experimental set-up, b) visualisation cell used for flow measurements at the half cross-section of the pipe and c) visualisation cell used for near-wall measurements.

Figure 3.9 shows two different cells used in this work. Perspex with refractive index $n = 1.48$ was used exclusively as a construction material. Cell A) was used for the flow visualisation of the half cross-section of the pipe. The sides of the visualisation cell through which the light passed from the laser and to camera were flattened and polished to minimise the refraction from the curved surface and to alleviate the differences between the refractive indexes of the cell material and air. Cell B) was used for near-wall measurements and a refractive matching approach was used during the manufacturing. A thin walled perspex pipe with a thickness of 1 mm was enclosed in a perspex box which was filled with water. Thanks to the very thin wall an assumption can be made that the distortions caused by the different refractive indexes can be neglected and the whole cell behaves as an optically homogeneous material.

The image acquisition system consists of a high speed CMOS camera and a framegrabber board which was installed in the control PC. The 100 Hz monochromatic camera VC-Imager Pro HS 500 (LaVision GMBH, Göettingen, Germany) has resolution of $1280 \times 1024$ pixels. Two different lenses were used, EX Sigma DG Marco 105 mm f/2.8 (Nikon, Japan) for imaging of the half cross-section of the pipe and VZ-Image Objektiv Zoom Navitar 12x (LaVision GMBH, Göettingen, Germany) for the near-wall measurements. The viewing windows were: $16.0 \times 12.8$ mm and $5.5 \times 4.4$ mm for the half cross-section of the pipe and for the near-wall measurements, respectively. The corresponding pixel-to-pixel spacing was 25 and 8 $\mu$m. The time difference between an image pair was estimated using the following equation:

$$\Delta t = \frac{(\Delta n \cdot (x_{\mathrm{m}}; y_{\mathrm{m}})}{(U_{\mathrm{bulk}} \cdot (x; y))} \tag{3.26}$$

where $\Delta n$ is the pixel shift. $(x_{\mathrm{m}}; y_{\mathrm{m}})$ is the field of view in mm, $U_{\mathrm{bulk}}$ is the bulk velocity and $(x; y)$ is the field of view in pixels. A pixel shift of $\Delta n = 5$ pixels was chosen, with respect to the calculation method and a size of an interrogation window (see below for details), for all $\Delta t$ estimations.

The flow illumination was performed using double pulsed Nd:YAG laser (Nano-L-50-100PV ,Litron Lasers Ltd, Rugby, UK) with an emission wavelength of 532 nm. The laser pulse duration was 4 ns, the energy of the pulse 50 mJ and the frequency 100 Hz. The sheet optics divergence angle was 20°.

General requirements for the seeding particles in order to realistically follow the fluid flow are i) small diameter, ii) narrow size distribution and iii) density closely matching the density of the visualised fluid. In this study the hollow borosilicate glass spheres were used with a mean diameter $9 - 13\,\mu$m and density $1100 \pm 50\,\mathrm{kg} \cdot \mathrm{m}^{-3}$, as supplied by LaVision GMBH (Göettingen, Germany).

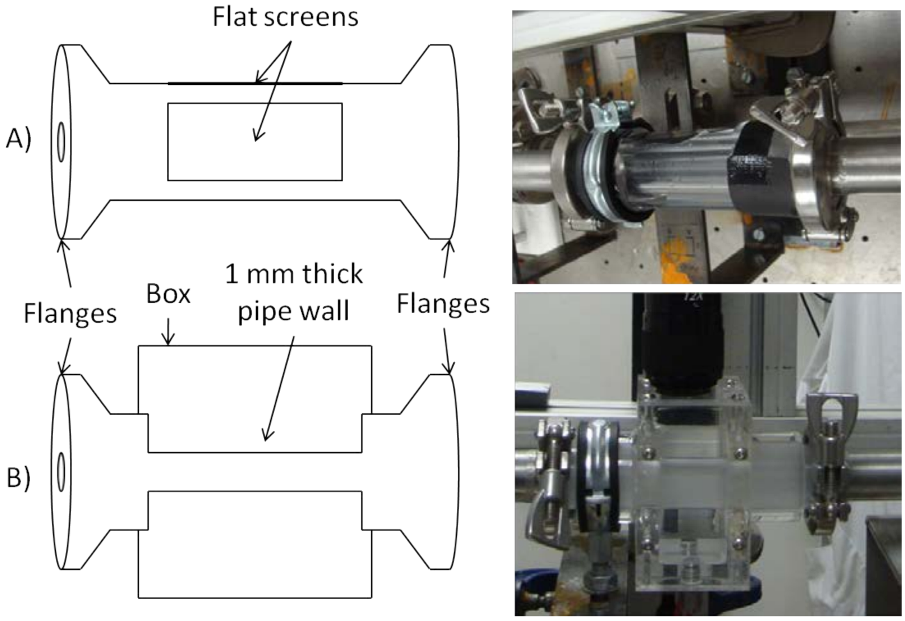

Figure 3.9: Schematic illustration and images of the used visualisation cells: A) cell used for the half cross-section of the pipe measurements and B) cell used for the near-wall measurements.

PIV is a non-intrusive measurement technique where the velocity vectors are calculated from the displacement of seeding particles during a defined time interval $\Delta t$. Considering a single particle in an imaging window the principle of the technique is illustrated in Figure 3.10. The position of the particle (x,y) is captured in two different times separated by a short interval.

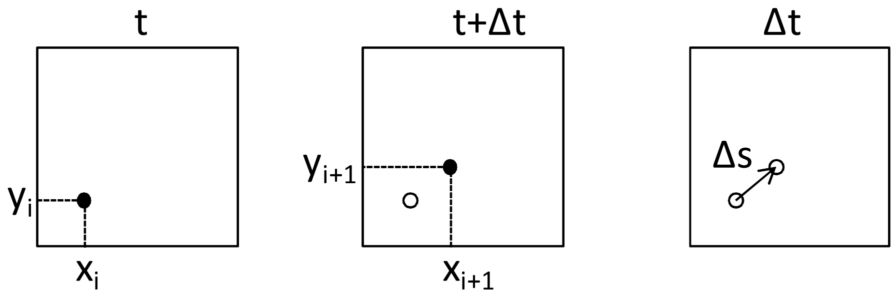

Figure 3.10: PIV technique is based on comparing the displacement of particle patterns between an image pair. The displacement vector $\Delta s$ is calculated from the position of the particle pattern between times: $t$ and $t + \Delta t$.

For short time intervals $\Delta t$ the fluid velocity can be calculated as:

$$u \approx \frac{(x_{i+1}, y_{i+1}) - (x_i, y_i)}{(t + \Delta t) - t} = \frac{\Delta s}{\Delta t} \tag{3.27}$$

In the real applications the imaging window contains thousands of seeding particles and it is difficult to follow each particle. For this, and also in order to improve the spatial resolution of the measurement, the imaging window is subdivided into smaller interrogation windows and a pattern of seeding particles within one interrogation window is tracked between a pair of images. The particle pattern displacement is calculated utilising a cross-correlation function. An overlap function is used to increase the spatial quality of the calculated vector field (see Figure 3.11).

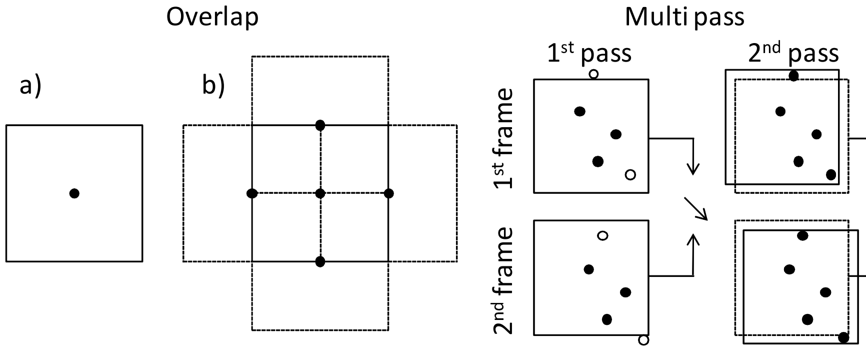

Figure 3.11: The spatial quality of the calculated vector field can be increased by using an overlap function and the quality of the vectors by multipass algorithm with decreasing interrogation window size. Overlap function: a) 0% overlap yields 1 vector, b) 50% overlap yields 5 vectors. Multipass: 3 particles are correlated during the first pass which indicates poor correlation while 5 particles are correlated in the second pass.

The overlap function is defined as the overlap among neighboring interrogation windows. The vector quality can be increased by calculating the vector field using a multipass approach with decreasing interrogation window size (see Figure 3.11). The initial calculation of the vector field using a large interrogation window gives a highly accurate reference vector. Then the interrogation window is downsized and the calculation repeated giving a larger number of vectors whose average is the reference vector. During the multipass the reference vector is calculated in the first pass. The reference vector information is then used in the following pass when the interrogation window is shifted accordingly to the reference vector. The multipass technique improves the signal to noise ratio by correlating the correct particles.

The visualisation of the flow close to the wall is associated with a problem of excess of scattered light from the wall of the visualisation cell. This can lead to a calculation of spurious vectors in the vicinity of the background light fluctuations. To increase the signal to noise ratio the raw images are often pre-processed using various techniques. One of them is subtract a sliding minimum over time where the intensity of pixels in a PIV window is compared over time which is a parameter for the method. The minimum intensity is then subtracted from the reference pixel and therefore artificial reflections but not those from the seeding particles are erased.

During each measurement a set of $500 - 600$ image pairs was taken. The PIV processing parameters of the raw image pairs for the half cross-section of the pipe measurements were as follows:

- Pre-processing
    - Subtract sliding minimum over 3 images
- Processing
    - Multipass iterations with decreasing interrogation window size
        - Window size: 32 x 32; window weight: 1:1; overlap: 25%, number of passes:1
        - Window size: 16 x 16; window weight: 1:1; overlap 50%, number of passes: 2
- Post-processing
    - Median filter, parameter: remove/replace if difference to average $>$ 1.5×rms of neighbours
    - Remove groups with $< 15$ vectors
    - Fill-up the area that does not contain vectors by interpolation

Near-wall measurements:

- Pre-processing
    - Subtract sliding minimum over 3 images
- Processing
    - Multipass iterations with decreasing interrogation window size
        - Window size: 64 x 64; window weight: 1:1; overlap: 25%, number of passes:1

- Window size: 32 x 32; window weight: 1:1; overlap 50%, number of passes: 2

- Post-processing
  - Median filter, parameter: remove/replace if difference to average > 1.5×rms of neighbours
  - Remove groups with < 15 vectors
  - Fill-up empty spaces by interpolation

**Scaling and Calibration**

PIV as an optical method requires calibration in order to asses the pixel to pixel distance as well as to minimise the optical distortions caused by the visualisation cell. During the calibration procedure, a half-cylinder shaped calibration target (see Figure 3.12) was inserted into the visualisation cell and 100 images were taken after the calibration setup was flooded with water. Care was taken to position the calibration plate parallel with the top flat screen of the visualisation cell and the camera. Crosses or dots were printed on the top of the calibration plate (see Figure 3.12). The calibration calculation consisted of locating the reference points and assessing their pixel coordinates with respect to their true dimensions. The fit models, rms of the fits and pixel dimensions of the de-warped calibrated images can be found in Table 3.4.

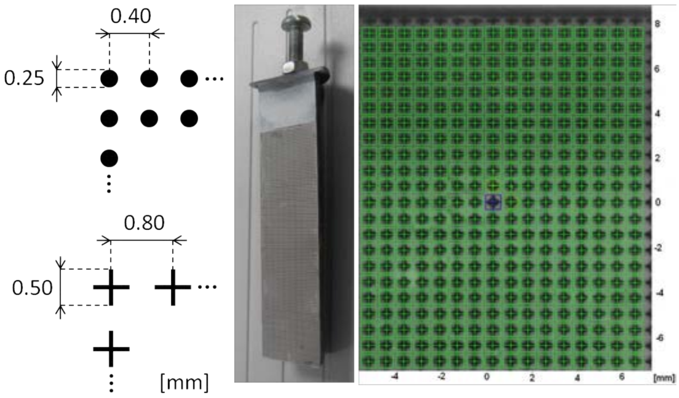

Figure 3.12: Calibration of PIV

Table 3.4: Calibration parameters of the PIV measurements

| Measurement | Fit model | rms of the fit | Size of de-warped image |
|---|---|---|---|
| Half cross-section of the pipe | $3^{rd}$order polynomial | 1.3 | $1406 \times 998$ |
| Near-wall | Pinhole | 1.5 | $1280 \times 1024$ |

### Image pre-processing

During each measurement $500 - 600$ image pairs were taken. An example of raw and pre-processed image pairs is shown in Figure 3.13. A subtract sliding minimum over time algorithm was used for pre-processing of the raw images in order to increase the overall image quality (the signal-to-noise ratio and the contrast between the particles and the background) and to suppress artificial reflections.

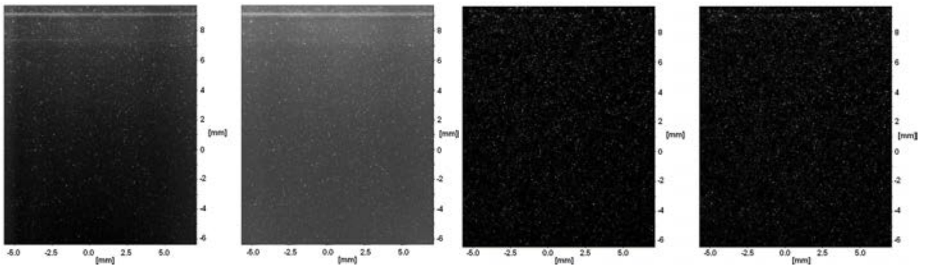

Figure 3.13: Raw image pair and corrected image pair using subtract sliding minimum over time algorithm.

### Instantaneous Images

Figure 3.14 shows an example of a processed corrected image pair. The vectors were calculated according to the procedure described above. To make the image clearer the number of vectors was decreased in the horizontal and in the vertical direction by a factor of 4×, the length of the vectors was increased by a factor of 4× and, therefore, the length of the vectors is not in agreement with the scales of the image. The vectors are coloured according to magnitude of the local velocity (flow speed). The most important feature is that the vectors correctly point in the direction of the flow which is from the left to the right. Also the absolute value of the velocity increases from the pipe wall towards the outer velocity-defect region which is in qualitative agreement with theory as expected.

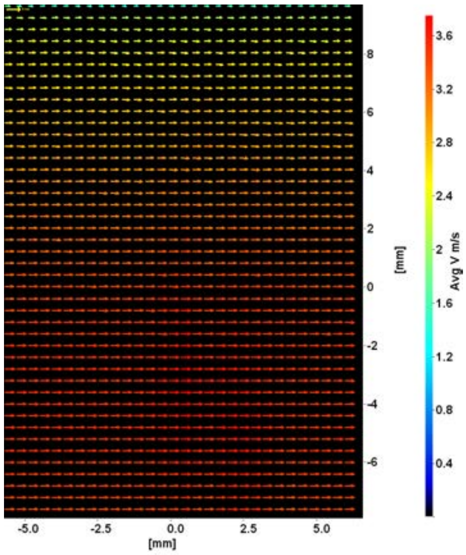

Figure 3.14: Example of instantaneous velocity vector map. A reference vector of $U = 5\,\mathrm{m}\cdot\mathrm{s}^{-1}$ is shown in the top left corner of the image. The number of vectors was decreased in the horizontal and in the vertical direction by a factor of 4×, the length of the vectors was increased by a factor of 4 × . The example is measurement of water at $Re = 70,000$.

### Definitions

The absolute value of the instantaneous velocity is extracted from an instantaneous velocity vector field using the following equation:

$$U\left(x,y\right) = \sqrt{u\left(x,y\right)^2 + v\left(x,y\right)^2} \tag{3.28}$$

where $u$ and $v$ are the streamwise and spanwise instantaneous velocity components, respectively. The streamwise $u^{'}_{rms}$ velocity fluctuations and spanwise velocity fluctuations $v^{'}_{rms}$ are defined by:

$$u\left(x,y\right) = \overline{u}\left(x,y\right) + u^{'}\left(x,y\right) \tag{3.29}$$

$$v\left(x,y\right) = \overline{v}\left(x,y\right) + v^{'}\left(x,y\right) \tag{3.30}$$

where $\overline{u}$ and $\overline{v}$ are the mean streamwise and spanwise velocities, respectively. The definitions show that $U$, $u$, $v$, $u^{'}$ and $v^{'}$ are dependent on a position as well as on time, but $\overline{u}$ and $\overline{v}$ are dependent only on position. In this thesis the units with a bar or a prime are used to refer to mean time-averaged values or time dependent fluctuations, respectively. The root-mean-square (rms) of the streamwise component of velocity fluctuations $u^{'}_{\text{rms}}$was calculated as follows:

$$u^{'}_{\text{rms}} = \sqrt{\overline{u^{'2}}} = \sqrt{\frac{1}{n-1}\sum_{i=1}^{n}\left(u_i - \overline{u}\right)^2} \tag{3.31}$$

where $n$ is the number of instantaneous images and $u_i$, $\overline{u}$ are the streamwise instantaneous and mean velocities, respectively. The rms of the spanwise component of velocity fluctuations was calculated as follows:

$$v^{'}_{\text{rms}} = \sqrt{\overline{v^{'2}}} = \sqrt{\frac{1}{n-1}\sum_{i=1}^{n}\left(v_i - \overline{v}\right)^2} \tag{3.32}$$

where $v_i$ and $\overline{v}$ are the spanwise instantaneous and mean velocities, respectively. Additional stresses of the turbulent flow when compared to the laminar flow are expressed in term of Reynolds stresses. The xy component of the Reynolds stress $\tau^{'}_{xy}$ is defined as follows:

$$\tau^{'}_{xy} = -\overline{u^{'}v^{'}} = -\frac{1}{n}\sum_{i=1}^{n}\left(\left(u_i - \overline{u}\right)\left(v_i - \overline{v}\right)\right) \tag{3.33}$$

The instantaneous streamwise shear strain rate is defined as:

$$\gamma_{xy} = \overline{\gamma}_{xy} + \gamma^{'}_{xy} = \frac{d\overline{u}}{dy} + \frac{du^{'}}{dy} \tag{3.34}$$

Additionally in few cases instantaneous spanwise shear strain rate, streamwise and spanwise compression strain rates will be shown. The definitions of the strain rates are:

$$\gamma_{yx} = \overline{\gamma}_{yx} + \gamma^{'}_{yx} = \frac{d\overline{v}}{dx} + \frac{dv^{'}}{dx} \tag{3.35}$$

$$\gamma_{xx} = \overline{\gamma}_{xx} + \gamma^{'}_{xx} = \frac{d\overline{u}}{dx} + \frac{du^{'}}{dx} \tag{3.36}$$

$$\gamma_{yy} = \overline{\gamma}_{yy} + \gamma^{'}_{yy} = \frac{d\overline{v}}{dy} + \frac{dv^{'}}{dy} \tag{3.37}$$

The definition of instantaneous 2D vorticity is:

$$\omega_z = \overline{\omega}_z + \omega^{'}_z = \left(\frac{d\overline{v}}{dx} - \frac{d\overline{u}}{dy}\right) + \left(\frac{dv^{'}}{dx} - \frac{du^{'}}{dy}\right) \tag{3.38}$$

The streamwise and spanwise skewness were calculated as follows:

$$S = \frac{1}{n}\sum_{i=1}^{n}\left(\frac{u_i - \overline{u}}{u'_{\text{rms}}}\right)^3 \tag{3.39}$$

$$S = \frac{1}{n}\sum_{i=1}^{n}\left(\frac{v_i - \overline{v}}{v'_{\text{rms}}}\right)^3 \tag{3.40}$$

Finally, the definitions of streamwise and spanwise kurtosis, sometimes called flatness, are:

$$K = \frac{1}{n}\sum_{i=1}^{n}\left(\frac{u_i - \overline{u}}{u'_{\text{rms}}}\right)^4 - 3 \tag{3.41}$$

$$K = \frac{1}{n}\sum_{i=1}^{n}\left(\frac{v_i - \overline{v}}{v'_{\text{rms}}}\right)^4 - 3 \tag{3.42}$$

where $n$ is the number of used data points. $n$ equals to $67,650$ for 550 images and for the PIV calculation method described above.

# Chapter 4

# Polymer Characterisation in Quiescent Conditions

In this Chapter the results on the physical properties of polymer solutions in quiescent conditions are presented and discussed. A detailed polymer characterisation is necessary in order to be able to understand the mechanism by which polymers are interacting with vortices in turbulent flow. The chemical composition and structure of the polymers used was verified using NMR. The polymer molecule shape, size in solution and polymer-solvent interactions was investigated using intrinsic viscosity measurements, GPC, static light scattering and rheology techniques.

## 4.1 Nuclear Magnetic Resonance Measurements

The $H^1-$NMR spectra of PEO4 and PAAm5 are shown in Figure 4.1. In the case of PEO4 the peak at 3.6 ppm (a) can be assigned to the methylene protons of the polyethylene oxide units. The spectra of PEO2 and PEO8 were identical to presented PEO4 $H^1-$NMR spectrum. In the spectrum of PAAm5 the peaks observed in the range $1.4 - 1.8\,\text{ppm}$ and $2.0 - 2.4\,\text{ppm}$ correspond to the protons of the methylene (a) and methine (b) groups of polyacrylamide molecule, respectively.

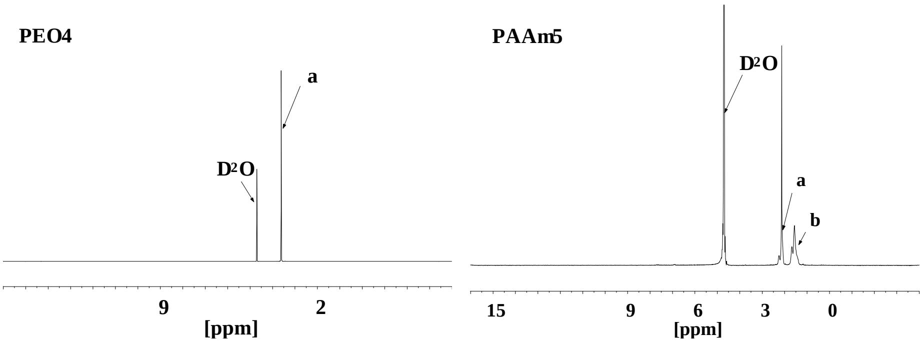

Figure 4.1: $H^1$−NMR spectra for PEO4 and PAAm5.

## 4.2 Intrinsic Viscosity Measurements

The intrinsic viscosity of the polymers studied, which were analysed using Equations 3.1 and 3.2 are shown in Figure 4.2. The dependence of the reduced viscosity on polymer concentration is linear, which indicates that polymers are present in the form of individual molecules. The presence of aggregated structures demonstrates itself by an upward curved relationship of reduced viscosity on concentration [74], however, it should be noted that the intrinsic viscosity technique is not as sensitive to the presence of aggregates as multi-angle laser light scattering (see Section 4.4). The values of intrinsic viscosity increase as follows: PEO0.2<PEO2<PAAm5<PEO4<PEO8.

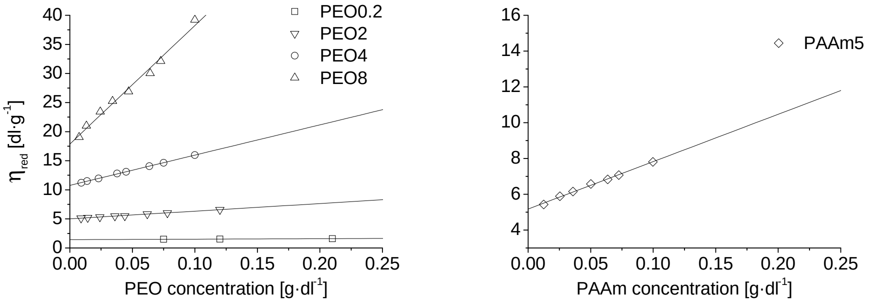

Figure 4.2: Huggins plot of the reduced viscosity $\eta_{\text{red}}$ as a function of polymer concentration.

The regressions were processed in order to obtain polymer overlap concentration, Huggins coefficient and molecular weight using Equations 3.5, 3.4 and 3.6, respectively and the results are shown in Table 4.1. Polymer overlap concentration $c^*$ is a measure of dilution of a polymer solution. Any concentrations below $c^*$ are generally called dilute solutions and concentrations above $c^*$ as concentrated polymer solutions. This work is dealing with polymer induced DR which is usually defined for diluted polymer concentrations. Therefore, the span of polymer concentrations investigated in terms of DR was limited by $c^*$ and the polymer concentrations used were always in the dilute region. Maximum polymer concentration used in this thesis was $c = 550\,\text{wppm}$.

The dimensionless Huggins coefficient describes the interaction between a polymer molecule and a solvent. High $k_H$ values indicate that polymer-polymer interactions are favoured over polymer-solvent interactions. The Huggins coefficient ranges between $0.5 - 0.7$ in a good solvent. Huggins coefficient lower than 0.5 indicate relative inability of the polymer molecule to interact with the solvent, which indicates that polymer-polymer interactions are favoured over polymer-solvent interactions. Polymer in a non-solvent would yield zero $k_H$ value. On the other hand Huggins coefficients larger than 0.7 indicate a very strong increase of viscosity with increasing polymer concentration. This is usually the case when large macromolecule clusters are present in a solution. The values of Huggins coefficients in Table 4.1 show that water is a good solvent for PEO2, PEO4 and PEO8, however, PEO0.2 has a slightly lower $k_H$ value indicating weaker polymer solvent interactions. PAAm5 on the other hand shows $k_H$ value larger than 0.7 indicating that some polymer clusters are present in a solution.

There is significant inconsistency in the values of molecular weight of the polymers given by the manufacturer and the molecular weights calculated from the intrinsic viscosity (see Tables 3.1 and 4.1). Nevertheless, the range of the molecular weight allows us to conduct a systematic study of the influence of molecular weight on the $DR$ efficiency. Note also, that molecular weight was measured using two other independent techniques namely gel permeation chromatography and multi-angle laser light scattering . The results will be compared and discussed at the end of this chapter.

Table 4.1: Intrinsic viscosity $[\eta]$, overlap concentration $c^*$, Huggins coefficient $k_H$ and molecular weight $M_v$ obtained from the Huggins plots in Figure 4.2 with the standard error of the measurements.

| | $[\eta]\,[\text{dl}\cdot\text{g}^{-1}]$ | $k_H$ | $c^*$ [wppm] | $M_v\,[\text{g}\cdot\text{mol}^{-1}]$ |
|---|---|---|---|---|
| PEO0.2 | 1.43 ±0.01 | 0.40 | 6,990 | 160,000 |
| PEO2 | 5.02 ±0.02 | 0.52 | 1,990 | 800,000 |
| PEO4 | 10.77 ±0.02 | 0.45 | 930 | 2,120,000 |
| PEO8 | 17.87 ±0.47 | 0.64 | 560 | 4,070,000 |
| PAAm5 | 5.18 ±0.04 | 0.99 | 1,930 | 1,390,000 |

## 4.3 Gel Permeation Chromatography Measurements

The molecular weight distributions of the fresh polymers are shown in Figure 4.3. The four high molecular weight polymers (PEO2, PEO4, PEO8 and PAAm5) had a narrow molecular weight distribution. The molecular weight distributions exhibit asymmetry. The low molecular weight tail contains a higher number of molecules when compared to the high molecular weight part of the distribution. It is possible that the low molecular weight tail observed for these polymers can be artificially caused by the band broadening effect which is inevitable for multi-detector systems. The low molecular weight PEO0.2 had a broad distribution of molecular weights. It can be noted that PEO0.2 exhibits a more symmetrical molecular weight distribution when compared to the high molecular weight polymers.

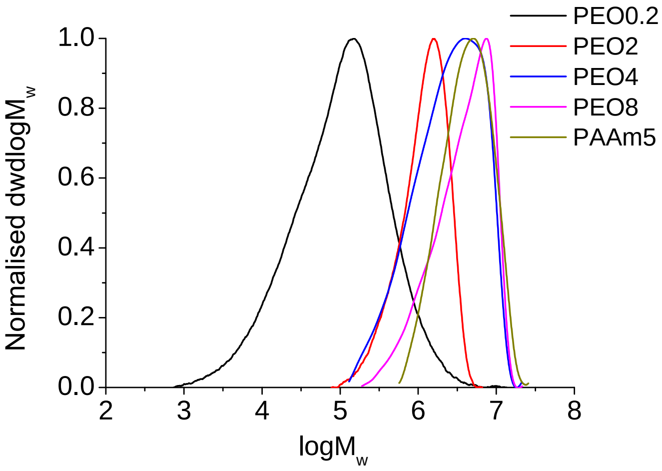

Figure 4.3: Molecular weight distribution of fresh polymers PEO0.2; PEO2; PEO4; PEO8 and PAAm5.

The results obtained from the chromatographs in Figure 4.3 are shown in Table 4.2. The weight average molecular weights for PEOs are similar to the ones obtained from the intrinsic viscosity measurements, however, the PAAm weight average molecular weight is higher for the GPC measurements. The polydispersity, which can be inferred from the broadness of the molecular weight distribution functions (see Figure 4.3 and Equation 3.11 for definition), showed that only PEO0.2 has polydisperse character. If we take in account the possibility of artificial low molecular weight tails then PEO4 and PEO8 can be considered as quasi-monodisperse and PEO2 and PAAm5 as monodisperse polymers. The radius of gyration increases with increasing molecular weight for the PEO family. If the radius of gyration results of PEO8 and PAAm5, which have similar molecular weight, are compared then it can be concluded that PEO8 is more expanded in aqueous solution than PAAm5. In other words PAAm5 molecules are more tightly packed in solution.

The hydrodynamic radius and the topology factor were calculated from Equations 3.13 and 3.14, respectively. All studied polymers should be in a random coil conformation. However, only the low molecular weight polymer, PEO0.2, has the topology factor that corresponds to the random coil conformation (see description under Equation 3.14). The conformations of high molecular weight polymers can be almost anything from hollow spheres to ellipsoids but not random coils. It might seem as error until we realise that $R_H$ is not directly measured by GPC and that the molecules were subjected to strong shear fields in the columns. High molecular weight polymers are more prone to be elongated in strong shear fields when compared to low molecular weight polymers. Therefore, it is possible that the polymer molecules were stretched to an ellipsoid conformation which was indeed observed. Based on this finding it would not be recommend to use GPC data as a reliable source for assessing topological data of flexible polymers. An independent technique should be used in order to asses the hydrodynamic radius, such as dynamic light scattering.

Table 4.2: Molecular parameters of fresh polymer solutions obtained from the GPC analysis. The molecular parameters are: number average molecular weight $M_n$ (Eq. 3.9), weight average molecular weight $M_w$ (Eq. 3.10), polydispersity index $PDI$ (Eq. 3.11), intrinsic viscosity $[\eta]$ (Eq. 3.12), radius of gyration $R_g$ (Eq. 3.18), hydrodynamic radius $R_h$ (Eq. 3.13) and molecule topology $\rho_t$ (Eq. 3.14).

| | PEO0.2 | PEO2 | PEO4 | PEO8 | PAAm5 |
|---|---|---|---|---|---|
| $M_n$ $\left[\mathrm{g \cdot mol^{-1}}\right]$ | 35,000 | 885,000 | 1,350,000 | 2,340,000 | 3,210,000 |
| $M_w$ $\left[\mathrm{g \cdot mol^{-1}}\right]$ | 230,000 | 1,430,000 | 3,500,000 | 4,850,000 | 5,160,000 |
| $PDI$ | 6.7 | 1.6 | 2.6 | 2.1 | 1.6 |
| $[\eta]$ $\left[\mathrm{dl \cdot g^{-1}}\right]$ | 1.65 | 7.44 | 12.64 | 15.22 | 7.17 |
| $R_g$ [nm] | 50 | 71 | 103 | 136 | 99 |
| $R_h$ [nm] | 33 | 101 | 162 | 192 | 152 |
| $\rho_t$ | 1.5 | 0.7 | 1.0 | 0.7 | 0.7 |

## 4.4 Multi-Angle Laser Light Scattering Measurements

The dependency of the scattering intensity on the squared scattering vector is shown in Figure 4.4. The scattering vector is defined by Equation 3.16 and is related to the scattering angle. All polymer solutions show different trends at small and large angles. As discussed by Kratochvíl [135], large particles scatter light intensively at small angles but the intra-particle interference of scattered light decreases the scattering intensities at larger angles. Individual polymer molecules, on the other hand, usually exhibit a linear angular dependency on scattered light intensity [136]. The downturn trends in normalised plots of ${}^{Kc}/_{R_\theta}$ as a function of $q^2$ at small angles indicate the presence of large aggregated polymer structures [137].

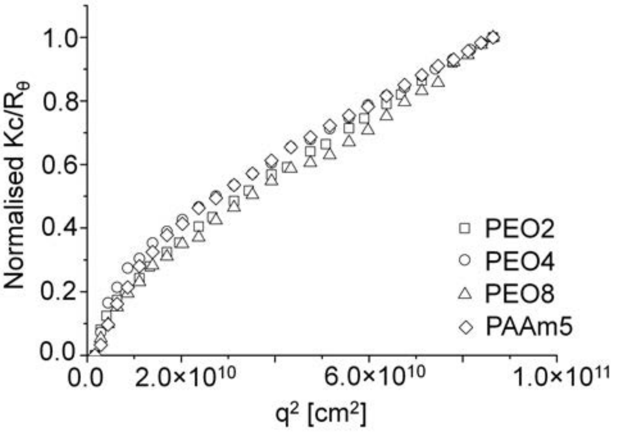

Figure 4.4: Normalised intensities of scattered light from high molecular weight polymers as a function of scattering vector.

The contribution to the scattered light intensity of aggregates at large angles is relatively low, therefore, an extrapolation of large angles to zero angle can reveal physical properties of individual polymer molecules. On the other hand the analysis of the whole angular dependency can reveal approximate information on physical properties of aggregates [135]. An example of a Zimm plot for PAAm5 where large angles and the whole angular dependency were analysed is shown in Figure 4.5. Zimm plots constructed for PEO2, PEO4 and PEO8 exhibited similar trends. The results of the data interpolation to zero concentration (Equation 3.18) and zero angle (Equation 3.17) for PEO2, PEO4, PEO8 and PAAm5 are summarised in Table 4.3. Two values of molecular weight were obtained for each analysis, one from the zero concentration extrapolation and one from the zero angle extrapolation. Values shown in Table 4.3 represent their average value. The difference between them was up to 5% and 25% for the analysis of large angles and the whole angular dependency, respectively.

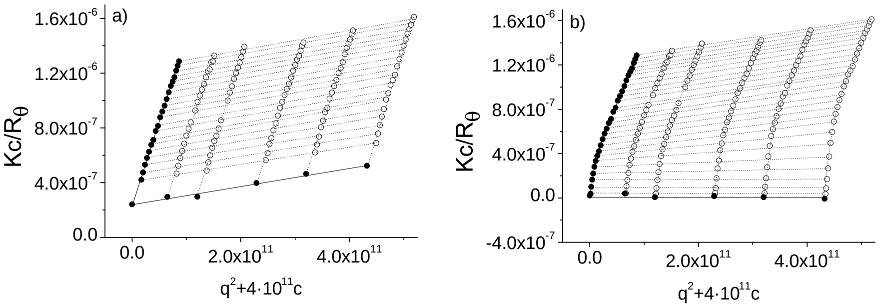

Figure 4.5: Zimm plot of PAAm5. The physical polymer properties were calculated a) for the individual molecules from angles higher than 45° and b) for the aggregates from the whole angle range 15°-145°.

The weight average molecular weight $M_w$ obtained from the large angles showed good agreement with the data provided by the manufacturer of the polymers. However, the analysis of the whole angular dependency showed the presence of aggregated structures in all samples. The trends of the radius of gyration, $R_g$, showed a similar picture where the $R_g$ increased with increasing $M_w$. Also $R_g$ of the aggregates increased as a function of molecular weight. The second virial coefficient $A_2$, describing the interaction between the polymer molecules and the solvent, verify the intrinsic viscosity results that water is a good solvent for the studied polymers. In the case of aggregates the $A_2$ become negative for PEO4 and PAAm5 which suggests that the polymer-polymer interactions in aggregates are favoured over polymer-solvent interactions. The $A_2$ value of PEO8 aggregates is also substantially lower when compared to individual polymer molecules. The decrease can be be explained by the collapsed, or more tightly packed, character of the polymer aggregates and highly swollen character of individual polymer molecules. The estimation of the range in which the polymer overlap concentration should be located (see Equation 3.19) indicate that the presence of polymer aggregates has strong effect on the spatial restrictions. However, the concentration of the aggregated polymers is possibly very low compared to individual polymer molecules. It should be noted that all calculated values are estimates and not absolute values. The reason is the heterogeneous character of the solutions and unknown concentrations of individual molecules and aggregates in the mixtures. More detailed analysis would be necessary, such as two-component decomposition [138], in order to obtain absolute values.

Table 4.3: Weight average molecular weight $M_w$, z-averaged radius of gyration $R_g$, second virial coefficient $A_2$ and overlap concentration $c^*$ for PEO2, PEO4, PEO8 and PAAm5.

| | $M_w$ $[\mathrm{g} \cdot \mathrm{mol}^{-1}]$ | $R_g$ [nm] | $A_2$ $[\mathrm{mol} \cdot \mathrm{ml} \cdot \mathrm{g}^{-2}]$ | $c^*$ [wppm] |
|---|---|---|---|---|
| $\mathrm{PEO2}_{\mathrm{Large\,angles}}$ | 2,200,000 | 138 | $8.32 \cdot 10^{-4}$ | $332 \sim c^* \sim 1,390$ |
| $\mathrm{PEO2}_{\mathrm{All\,angles}}$ | 2,810,000 | 171 | $6.49 \cdot 10^{-4}$ | $223 \sim c^* \sim 933$ |
| $\mathrm{PEO4}_{\mathrm{Large\,angles}}$ | 5,540,000 | 173 | $1.95 \cdot 10^{-4}$ | $424 \sim c^* \sim 1,777$ |
| $\mathrm{PEO4}_{\mathrm{All\,angles}}$ | 23,100,000 | 421 | $-1.10 \cdot 10^{-5}$ | $123 \sim c^* \sim 514$ |
| $\mathrm{PEO8}_{\mathrm{Large\,angles}}$ | 9,050,000 | 275 | $7.05 \cdot 10^{-4}$ | $173 \sim c^* \sim 723$ |
| $\mathrm{PEO8}_{\mathrm{All\,angles}}$ | 33,350,000 | 684 | $7.05 \cdot 10^{-6}$ | $41 \sim c^* \sim 173$ |
| $\mathrm{PAAm5}_{\mathrm{Large\,angle}s}$ | 4,160,000 | 123 | $1.34 \cdot 10^{-4}$ | $886 \sim c^* \sim 3,712$ |
| $\mathrm{PAAm5}_{\mathrm{All\,angles}}$ | 43,500,000 | 547 | $-2.43 \cdot 10^{-6}$ | $105 \sim c^* \sim 441$ |

## 4.5 Rheology Measurements

The dependence of the apparent shear viscosity on polymer concentration at shear rate of $\dot{\gamma} = 1,000\,\mathrm{s}^{-1}$ is shown in Figure 4.6. DR effect is resulting in a decrease of the fluid friction in a pipe even at polymer concentrations where the viscosity is almost equal to that of the solvent. As expected, the polymer solution viscosity increases with increasing polymer concentration and increasing polymer molecular weight. However, even for the polymer with the highest molecular weight, the solution viscosity is almost equal to that of the solvent up to 75 wppm. This indicates that up to 75 wppm the polymer solutions are dilute and the polymer molecules do not or little contribute to the internal friction of the solution.

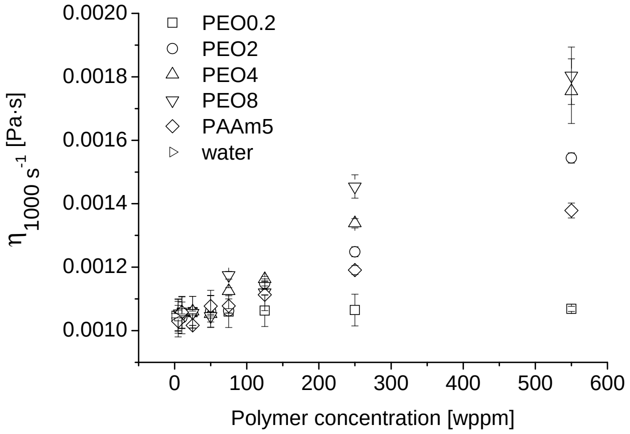

Figure 4.6: Dependence of apparent shear viscosity at $\dot{\gamma} = 1,000\,\mathrm{s}^{-1}$ on the polymer concentration.

## 4.6 Summary

The $H^1$−NMR spectra verified the chemical structure of used polymers and no impurities could be identified. The analysis of intrinsic viscosity, GPC and MALLS results showed a substantial scatter in the measured molecular weight. The differences might be explained by different polymer properties that each technique is measuring. Intrinsic viscosity measures the increase in resistance to flow in a capillary, which can be related to viscosity. GPC, which is sometimes called gel filtration chromatography, separates polymer molecules based on their hydrodynamic volume but the subsequent analysis uses mass, viscosity and scattered light detection. MALLS determines the molecular weight from a scattering function of non-fractionated polymer molecules. Molecular weight based on intrinsic viscosity refers to viscosity molecular weight and it is not the same molecular weight as determined by GPC and MALLS. Additionally, a range of values of Mark-Houwing parameters, that are necessary in order to calculate the viscosity molecular weight, is very common in the literature [133]. The difference between molecular weight measured by GPC and MALLS techniques was previously reported for different polymer systems [139, 140, 141]. Three different theories explain the discrepancy: i) The highest molecular weight fraction is filtered out inside the GPC system, ii) the highest molecular weight fraction is extremely diluted hence undetectable by the classical GPC detectors and iii) polymer degradation occurs in the GPC columns due to high shears [142, 143]. Even though special GPC columns suitable for high molecular weight polymers (void channel size $15\,\mu$m) were used during the analysis it is possible that the highest polymer molecular weight fractions might be filtered out or degraded inside the columns. Also several inline filters, that are necessary to increase the signal to noise ratio of the light scattering detector, are present in the GPC system. Therefore, all three explanations might play a role in the difference between molecular weight measured by GPC and MALLS. With the knowledge of the GPC problems it should be stated that the MALLS molecular weight results are the most precise. However, GPC technique will be used in this work to assess the evolution of molecular weight during polymer degradation experiments as only one sample is needed to obtain $M_w$ information using GPC technique but several samples of different concentrations are necessary for MALLS measurements, which is almost impossible to achieve.

The MALLS measurements proved that polymer aggregates are present in water solutions of studied polymers. The size of the aggregates increases with increasing polymer molecular weight. The influence of aggregates on measured $DR$ is investigated in Chapter 5 - Section 5.5.

Finally, the polymer apparent viscosity measurements at $\dot{\gamma} = 1,000\,\mathrm{s}^{-1}$ proved that the solution viscosity is almost identical for polymer concentrations up to 75 wppm when compared to the Newtonian solvent. An increase in measured apparent viscosity was observed for more concentrated polymer solutions. Higher molecular weight of a polymer yield to higher apparent viscosities. However, the polymer overlap concentration, as calculated from intrinsic viscosity (Table 4.1) and MALLS results (Table 4.3), indicated that all studied polymer solutions can be still assumed to be dilute.

# Chapter 5

# Drag Reduction Characterisation in Taylor Flow

Typically DR is quantified by measuring the pressure drop over a length of a pipe. This technique provides very good approximation of real applications, however, it is necessary to design and build a flow facility. The construction of a flow facility is expensive and time demanding. Additionally, large amounts of solvents as well as polymer is needed for the experiments. It is therefore desirable to be able to test DR in a cheaper and faster way. Custom made instruments emerged in the past, such as rotating disks apparatus, however, they do not solve the problem since the design and manufacturing is required as well as programing driving software [144, 113]. Therefore, it was decided to investigate the possibility of using standard laboratory equipment to quantify DR. The motivation behind this approach comes from the works of several authors who were investigating the influence of polymer additives on the flow behaviour between rotating cylinders [115, 145, 116, 146]. The idea of using a commercial rheometer for DR characterisation was for the first time introduced by Nakken et al. [117]. In this Chapter, the flow between rotating cylinders will be investigated by flow visualisation (Section 5.1) and the quantification of DR will be explained (Section 5.2). The instantaneous and time dependent DR characterisation of polymers will be presented in Sections 5.3 and 5.4. Finally, the possibilities of enhancing the sustainability of DR in vigorous shear flows due to the presence of polymer aggregates will be presented in section 5.5.

## 5.1 Flow Visualisation

The effect of drag reducing polymers on the structure and intensity of Taylor flow can be seen in Figure 5.2. The different gap between the rotor and the stator of the visualisation cell and the double gap cell, used for DR measurements, requires the use of Taylor number, $Ta$, in order to compare the flow intensities in different cell geometries (see Section 3.2.5). It should be noted that there are numerous definitions of $Ta$ in the literature [145, 146]. Here $Ta$ is defined as follows:

$$Ta = \frac{r_3 \omega^2 d^3}{\nu^2} \tag{5.1}$$

where $r_3$ is the outer wall rotor radius, $\omega$ the rotor angular frequency, $d = r_4 - r_3$ is the gap width (see Figure 3.5) and $\nu$ is the kinematic viscosity of a solution. Figure 5.1 provides an easy tool for the comparison of $Ta$ used during the flow visualisation and DR measurements.

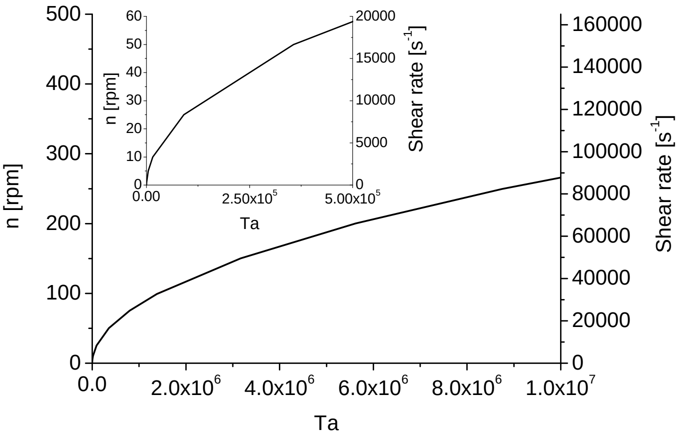

Figure 5.1: Taylor numbers of the visualisation and DR measurements. The rotational speed and shear rate values refer to the visualisation and DR measurements, respectively.

At the lowest recorded velocity, 5 rpm, the Newtonian solvent already starts to form contra rotating toroidal vortices, Taylor vortices. However, the drag reducing polymer delayed the onset of Taylor vortices formation and the Couette flow remains stable even for 10 rpm for PEO8 550 wppm. The flow further evolved with increasing rotor velocity and several different flow patterns can be observed: wavy vortex flow (e.g. water 25 rpm), onset of turbulence (e.g. water 50 rpm) and turbulent Taylor flow (e.g. water 100 rpm). Similar observations with additional analysis and image post-processing can be also found in the literature [145, 146, 118]. The flow visualisation experiments indicate that fully developed turbulent flow cannot be obtained during the $DR$ measurements using a commercial rheometer equipped with double gap sample holder having the described geometry (see Figure 3.5). In order to be able to quantify $DR$ in fully developed turbulent flow, the gap between the stator and the rotor would have to be larger or the rotational speed should be increased. None of that was possible in the presented measurements since a commercial rheometer, with all its limitations, was used for the characterisation of $DR$. However, the geometries of double gap sample holders vary between each rheometer manufacturer and even between different rheometer models within one company. Hence it might be possible to quantify DR in turbulent flow even using a commercial rheometer if an adequate system is identified.

## 5.2 Calculation of Drag Reduction Efficiency

The DR effect takes place exclusively in turbulent flow, which is almost impossible to achieve in measuring geometries of commercial rheometers. It was therefore necessary to asses, in the first place, the flow behaviour in the used geometry (see Figure 3.5). Figure 5.3 reports the nominal shear viscosity for water as a function of increasing shear rate $\dot{\gamma}$. It should be kept in mind that the nominal shear viscosity and the shear rate were calculated using expressions valid only for Couette flow (see Equations 3.24 and 3.20). Three flow regimes can be identified in Figure 5.3: i) Couette flow ; ii) Taylor flow and iii) onset of turbulent Taylor flow (see also Figure 5.2). When centrifugal forces become large enough to overcome the stabilizing viscous forces the circular Couette flow starts to exhibit toroidal roll vortexes - Taylor flow. These vortices are aligned in the circumferential direction and span across the entire gap. The onset of Taylor flow can be seen in Figure 5.3 as an abrupt increase in Newtonian plateau viscosity located at $\dot{\gamma} = 1,100\,\mathrm{s}^{-1}$ ($\omega_{cyc} = 220\,\mathrm{rpm}$), which is in agreement with Nakken et al. [117] who found the onset of Taylor flow for water using a similar experimental setup at 215 rpm. The predicted onset of Taylor flow based on Equation 3.23 is 210 rpm which in good agreement with the experimental data. The values used to calculate the onset of Taylor flow for water in Equation 3.23 are: $\rho = 997.04\,\mathrm{kg} \cdot \mathrm{m}^{-3}$ and $\eta = 8.905 \cdot 10^{-4}\,\mathrm{Pa} \cdot \mathrm{s}$. Further increase of the rotational speed leads to a second onset which was defined by Andereck et al. [114] as the onset of turbulent Taylor flow. The onset of turbulent Taylor flow is located at $\dot{\gamma} = 6,000\,\mathrm{s}^{-1}$.

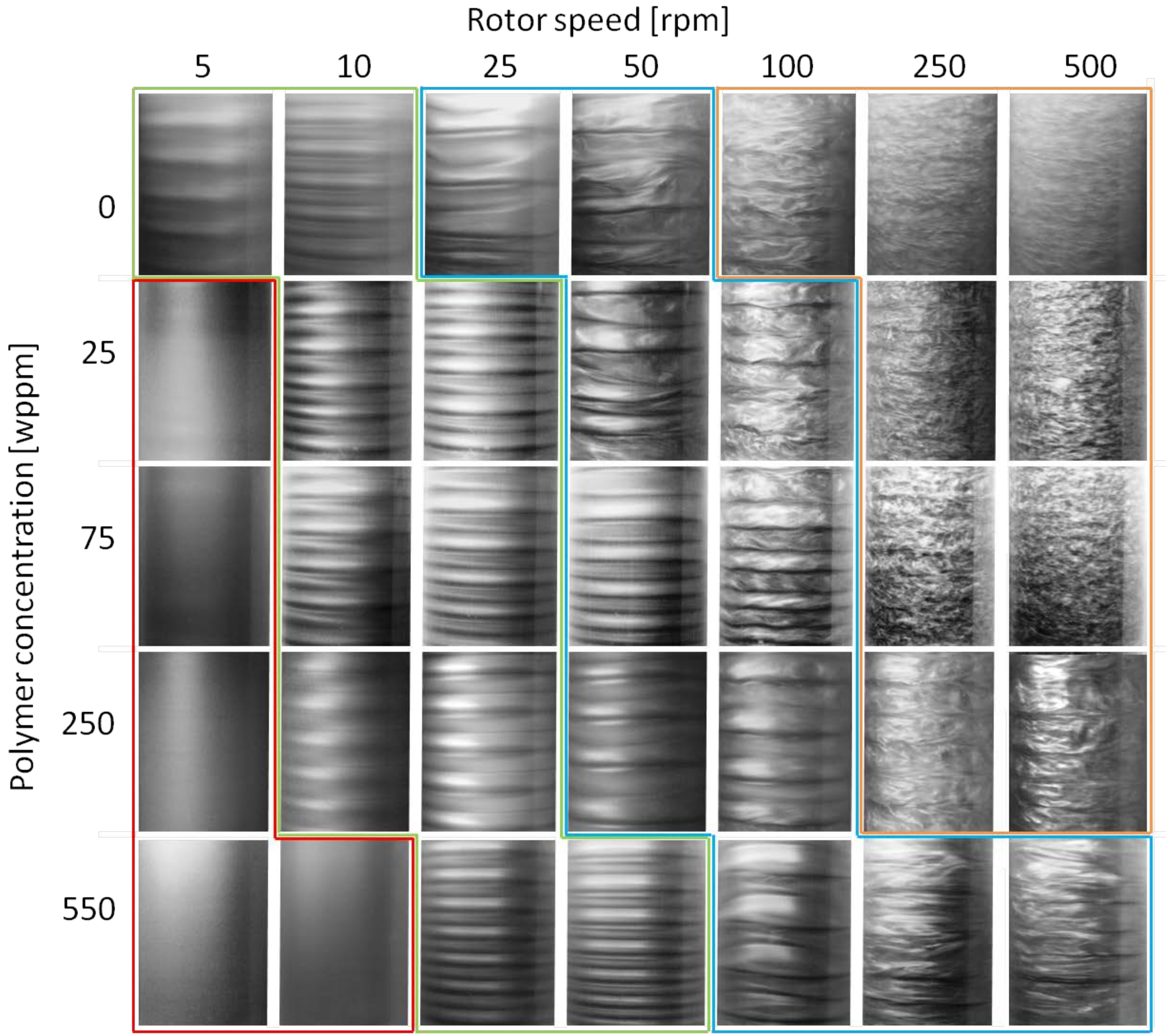

Figure 5.2: Guanine platelets visualisation photographs of the flow instabilities in a Couette cell for water and PEO8 at various rotor rotation speeds. Red, green, blue and orange areas refer to Couette flow, Taylor flow, the onset turbulent Taylor flow and turbulent Taylor flow, respectively.

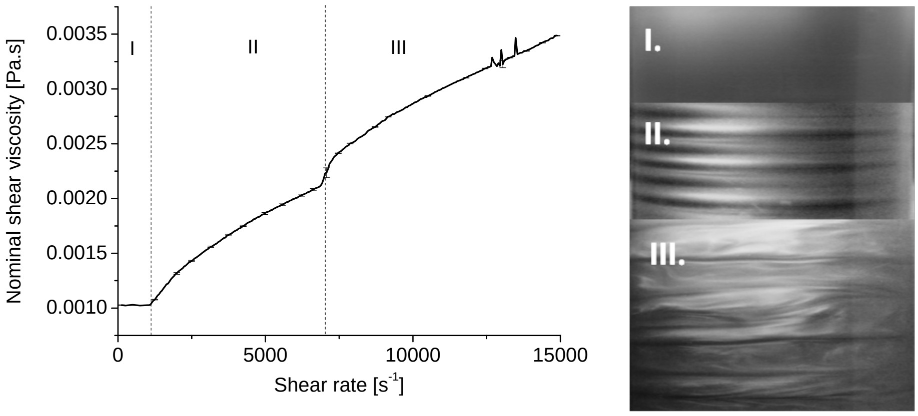

Figure 5.3: Plot of the nominal shear viscosity $\dot{\eta}$ for pure water as a function of shear rate $\dot{\gamma}$ representing an average of 6 measurements. 3 different flow regimes can be distinguished: I - Couette flow, II – Taylor flow and III – onset of turbulent Taylor flow. The flow was visualised in a Perspex visualization cell using guanine platelets.

Figure 5.3 shows that the standard error of the nominal shear viscosity for shear rates between $0-1,100\,\mathrm{s}^{-1}$ is about 1% for a steady Couette flow and 3% for the flow transition from Taylor to the onset of turbulent Taylor flow. The standard error was calculated from six discrete measurements using pure water. Therefore, the rheometer equipped with double gap sample holder having axial symmetry provides consistent data with reproducibility better than 3% even for a transition between two flow regimes. Random errors caused by high loads of the torque sensor occurred at shear rates above $12,000\,\mathrm{s}^{-1}$.

The dependence of the apparent shear viscosity at the onset of Taylor flow on the apparent viscosity at $\dot{\gamma} = 1,000\,\mathrm{s}^{-1}$ is shown in Figure 5.4. The relationship was investigated for a range of different polymer solutions varying by chemical structure, molecular weights, concentrations and solvent quality. It is obvious that the limit of the stability of Couette flow for a given system is directly proportional to the apparent shear viscosity at $\dot{\gamma} = 1,000\,\mathrm{s}^{-1}$ of the solution. The linear empirical relationship is as follows:

$$\eta_{\mathrm{Taylor\,flow\,onset}} = 9.312 \cdot 10^{-1}\eta_{1000\,s^{-1}} + 6.625 \cdot 10^{-5} \tag{5.2}$$

Equation 5.2 will be used in Section 5.4 in order to correct the $DR$ calculation to the flow induced decrease of apparent viscosity at the Taylor flow onset.

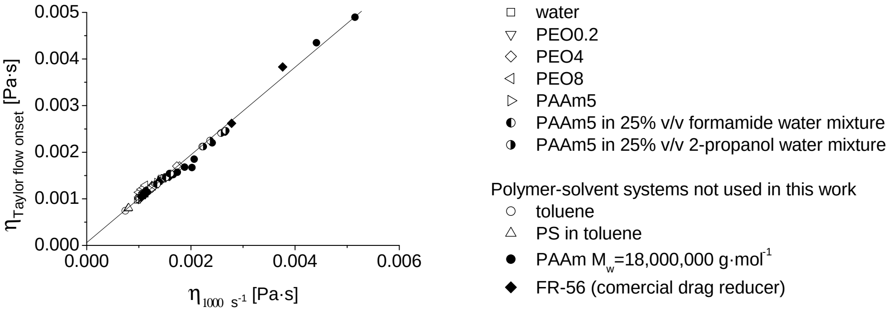

Figure 5.4: Dependence of the apparent shear viscosity at the onset of Taylor flow on the apparent shear viscosity at $\dot{\gamma} = 1,000\,\mathrm{s}^{-1}$.

The nominal shear viscosity $\dot{\eta}_N$ (see Equation 3.24), as a function of shear rate $\dot{\gamma}$ for PEO2, PEO4, PEO8 and PAAm5 is shown in Figure 5.5. If the polyethylene oxides are compared then few observations can be made: i) the $DR$ onset, which in this case is defined as the shear rate where the polymer solution profile departures from the water profile, does not occur at the onset of Taylor vortices but it is shifted to higher shear rates, ii) the $DR$ efficiency increases with increasing PEO concentration and molecular weight and iii) the onset of turbulent Taylor flow is delayed by the presence of polymer additives. A remarkable feature is observed when polyethylene oxides and PAAm5 profiles are compared. The PAAm5 solutions seems to be more efficient in reducing drag than polyethylene oxides. A similar conclusion regarding the efficiency of PEO and PAAm was made by Bizotto et al. [119]. However, previous studies acknowledge PEO to be the most efficient drag reducer among common polymers [147, 112, 15]. The contradicting results can be explained by the higher vulnerability of PEO molecules to mechanical degradation and subsequent loss of the ability to reduce drag. The degradation kinetics of polyethylene oxides and PAAm5 will be investigated in Sections 5.4 and 5.5, respectively.

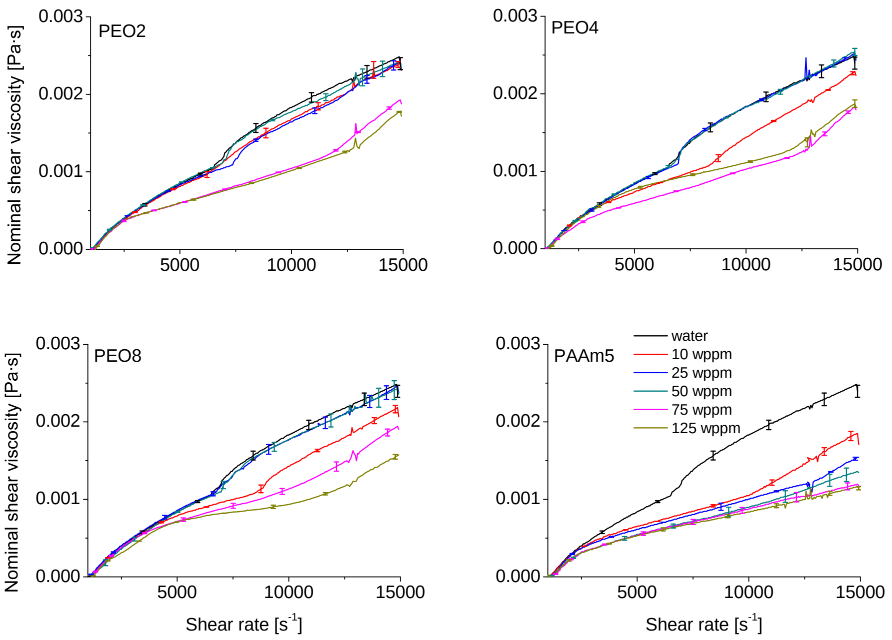

Figure 5.5: The dependence of nominal shear viscosity $\dot{\eta}_N$ on the shear rate $\dot{\gamma}$ for PEO2, PEO4, PEO8 and PAAm5.

## 5.3 Instantaneous Drag Reduction

Figure 5.6 compares the $DR$ efficiency, calculated by Equation 3.25, as a function of polymer concentration for PEO0.2, PEO2, PEO4 and PEO8 in water at shear rates $\dot{\gamma} = 6,000$; $11,000$; and $15,000\,\mathrm{s}^{-1}$. The level of $DR$ increases with increasing polymer molecular weight and with increasing shear rate. However, as can be seen from the $DR$ results of PEO0.2, a minimum molecular weight exists below which the DR effect does not occur. The dependency of $DR$ on the polymer concentration follows the classical trend; $DR$ increases with increasing polymer concentration until a maximum is reached at an optimum polymer concentration $c_{\mathrm{opt}}$. A further increase of polymer concentration beyond $c_{\mathrm{opt}}$ does not lead to a significant increase in $DR$. The constant level of $DR$ after $c_{\mathrm{opt}}$ is, however, in contradiction with observations made by Bizotto et al. [119] and Nakken et al. [43] who observed a sharp decline in $DR$ after $c_{\mathrm{opt}}$. The difference in the observed trends is caused by different calculation of $DR$. Bizotto et al. [119] and Nakken et al. [43] used $DR_{t=0\,\mathrm{s}}$ which is $DR$ value at beginning of the $DR$ measurement. Their choice of instantaneous $DR$ definition should minimise the effect of polymer degradation in Taylor flow on the obtained $DR$ value. However, we used $DR_{\mathrm{max}}$ for calculating $DR$ for a given system, which is the maximum $DR$ value obtained during the first 5 min of a measurement at a given shear rate. We believe that using $DR_{t=0\,\mathrm{s}}$ is not adequate to calculate the level of $DR$ since the behaviour of polymer solutions in turbulent Taylor flow as a function of time is more complex at $c > c_{\mathrm{opt}}$ than at $c < c_{\mathrm{opt}}$ (see Section 5.4).

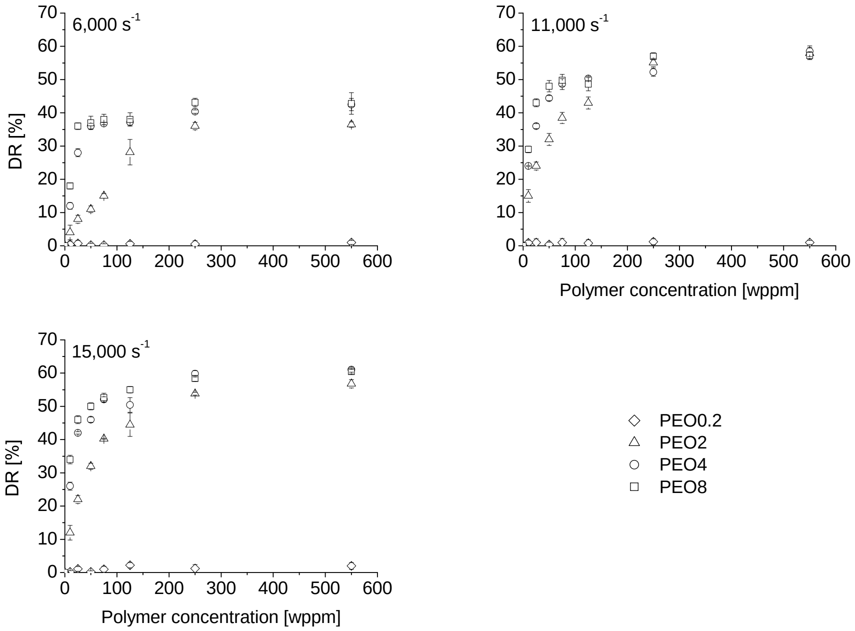

Figure 5.6: Maximum DR as a function of polymer concentration.

Tabor et al. [106] suggested that the optimum polymer concentration $c_{\mathrm{opt}}$ can be linked to the polymer overlap concentration $c^*$, defined as the concentration where random polymer coils begin to touch each other in a solution. The polymer overlap concentration in a quiescent condition can be estimated using Equations 3.5 or 3.19. The calculated polymer overlap concentrations from the results intrinsic viscosity measurements are $1,990$; 930 and 560 wppm for PEO2, PEO4 and PEO8, respectively. Since $c_{\mathrm{opt}} \ll c^*$ one can conclude that maximum DR is determined by a different mechanism than direct polymer-polymer spatial restrictions. All DR theories [12, 107, 148] link polymer molecule elongation in the inner near-wall region to the drag reducing effect. It is obvious that the spatial restrictions for a polymer molecule in a random coil conformation in quiescent conditions and for highly stretched polymer molecule in a flow are different. Therefore, we propose that $c_{\mathrm{opt}}$ should be understood as the polymer overlap concentration of elongated polymer molecules (see Figure 5.7).

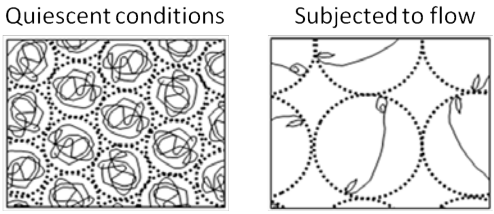

Figure 5.7: Schematic representation of the proposed stretched polymer overlapping concentration. It is assumed that stretched polymer spatial restrictions might be the reason for DR optimum concentration $c_{opt}$.

The optimal concentrations for PEO2, PEO4 and PEO8 as well as the ratio of the polymer overlap concentration to the polymer optimum concentration is shown in Table 5.1. The ratio can be considered as an extent of polymer molecule flow induced elongation if the flow induced polymer overlap concentration model is correct. Similar values of $^{c^*}/_{c_{\mathrm{opt}}}$ for most of the cases $\sim 10$ indicate that the spatial restrictions are driven by the same mechanism, most possibly elongation of polymer molecules. However, it is surprising that the ratio $^{c^*}/_{c_{\mathrm{opt}}}$ decreases with increasing Taylor flow intensity. In fact the opposite effect would be more understandable, since more intense flow fluctuations should be able to elongate polymer molecule to higher extent. Obviously more detailed measurements are required in order to asses the polymer optimum concentration with higher precision and to verify the trends observed.

Table 5.1: Comparison between polymer overlap concentration $c^*$ and polymer optimum concentration $c_{opt}$ at different shear rates.

| | | $c^*$ | $c_{\mathrm{opt}}$ | $^{c^*}/_{c_{\mathrm{opt}}}$ |
|---|---|---|---|---|
| PEO2 | $6,000\,\mathrm{s}^{-1}$ | 1990 | 200 | 10.0 |
| | $11,000\,\mathrm{s}^{-1}$ | 1990 | 200 | 10.0 |
| | $15,000\,\mathrm{s}^{-1}$ | 1990 | 200 | 10.0 |
| PEO4 | $6,000\,\mathrm{s}^{-1}$ | 930 | 50 | 18.6 |
| | $11,000\,\mathrm{s}^{-1}$ | 930 | 80 | 11.6 |
| | $15,000\,\mathrm{s}^{-1}$ | 930 | 100 | 9.3 |
| PEO8 | $6,000\,\mathrm{s}^{-1}$ | 560 | 40 | 14 |
| | $11,000\,\mathrm{s}^{-1}$ | 560 | 70 | 8 |
| | $15,000\,\mathrm{s}^{-1}$ | 560 | 80 | 7 |

## 5.4 Time Dependent Drag Reduction

The DR calculation as defined by Equation 3.25 is using the nominal shear viscosity $\dot{\eta}_N$ of the pure solvent and solutions containing polymer additives. The nominal shear viscosity is directly calculated from the apparent shear viscosity at the onset of Taylor vortices (see Equation 3.24). It was shown in Figure 4.6 that the apparent shear viscosity at $\dot{\gamma} = 1,000\,\mathrm{s}^{-1}$ of polymer solutions increases with increasing polymer concentration and molecular weight for concentrations $> 75\,\mathrm{wppm}$. Additionally, the relationship between the apparent viscosity at the onset of Taylor vortices and the apparent shear viscosity at $\dot{\gamma} = 1,000\,\mathrm{s}^{-1}$ was shown in Figure 5.4 and Equation 5.2. It is expected that the apparent shear viscosity at the onset of Taylor vortices of polymer solutions would be altered if flow induced polymer degradation occurs. Therefore the apparent shear viscosity at $\dot{\gamma} = 1,000\,\mathrm{s}^{-1}$ was measured before and after a polymer solution was subjected to Taylor flow of different intensities. The apparent shear viscosity at the onset of Taylor vortices can be then calculated by using Equation 5.2. The dependence of the apparent shear viscosity at $\dot{\gamma} = 1,000\,\mathrm{s}^{-1}$ on the shearing time for PEO2, PEO4 and PEO8 is shown in Figure 5.8. The rate of decrease of the apparent shear viscosity at $\dot{\gamma} = 1,000\,\mathrm{s}^{-1}$ over time is enhanced with increasing shear rates exerted on the polymer solutions, increasing polymer concentration and polymer molecular weight. As presented in Figure 4.6, the difference between the apparent shear viscosity of the solvent and polymer solutions with polymer concentrations $< 75\,\mathrm{wppm}$ were negligible. Also the observed decrease of the apparent shear viscosity as a function of time was indistinguishable from the error of the measurement. The presented data were used in order to correct the time dependent DR measurements of polyethylene oxides.

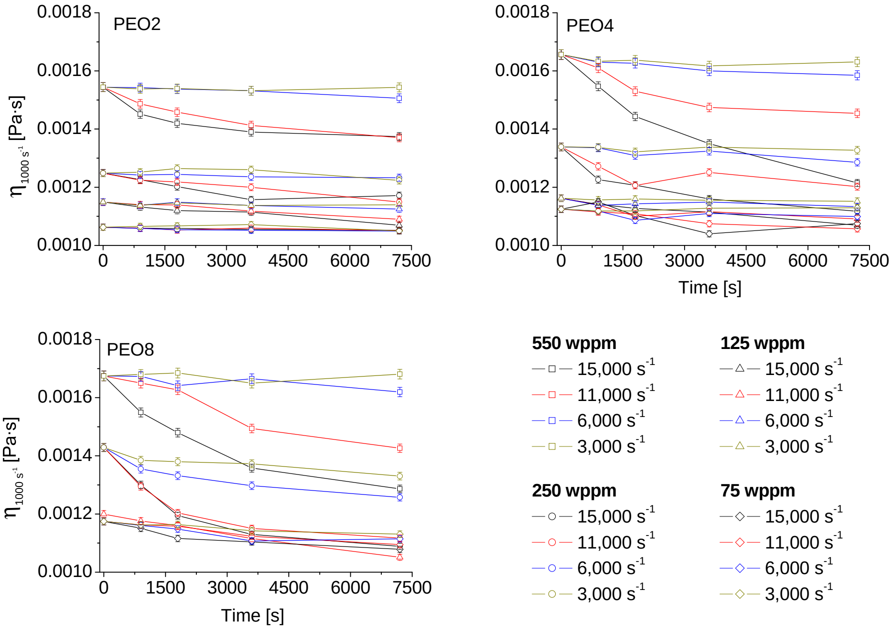

Figure 5.8: Dependence of the apparent shear viscosity at $1,000\,\mathrm{s}^{-1}$ on time. The apparent shear viscosity was measured after shearing at a given shear rate for a given time.

Figures 5.9, 5.10 and 5.11 show the $DR$ efficiency profiles of PEO2, PEO4 and PEO8, respectively for four different polymer concentrations of 75, 125, 250 and 550 wppm and three different intensities of Taylor flow at shear rates of $6,000$, $11,000$ and $15,000\,\mathrm{s}^{-1}$ as a function of time. It should be noted that the evolution of the apparent shear viscosity at $\dot{\gamma} = 1,000\,\mathrm{s}^{-1}$ with time, which was used to correct the time dependent DR effect, was also quantified for polymer solutions sheared at $3,000\,\mathrm{s}^{-1}$. However, the results of $DR$ efficiency as a function of time for Taylor flow intensity of $3,000\,\mathrm{s}^{-1}$ are not shown. The reason is that a huge scatter of the measured $DR$ was observed; the maximum standard error was $DR \pm 20\%$. The explanation of the inability to measure $DR$ at relatively low shear rates could be attributed to the dominating viscous effects, which were stronger than the forces exerted on the polymer molecules by Taylor vortices. Nevertheless, it seems evident from Figure 5.8 that no polymer degradation took place when the solutions were sheared at $\dot{\gamma} = 3,000\,\mathrm{s}^{-1}$ since the measured apparent shear viscosity at $\dot{\gamma} = 1,000\,\mathrm{s}^{-1}$ remained constant as a function of time.

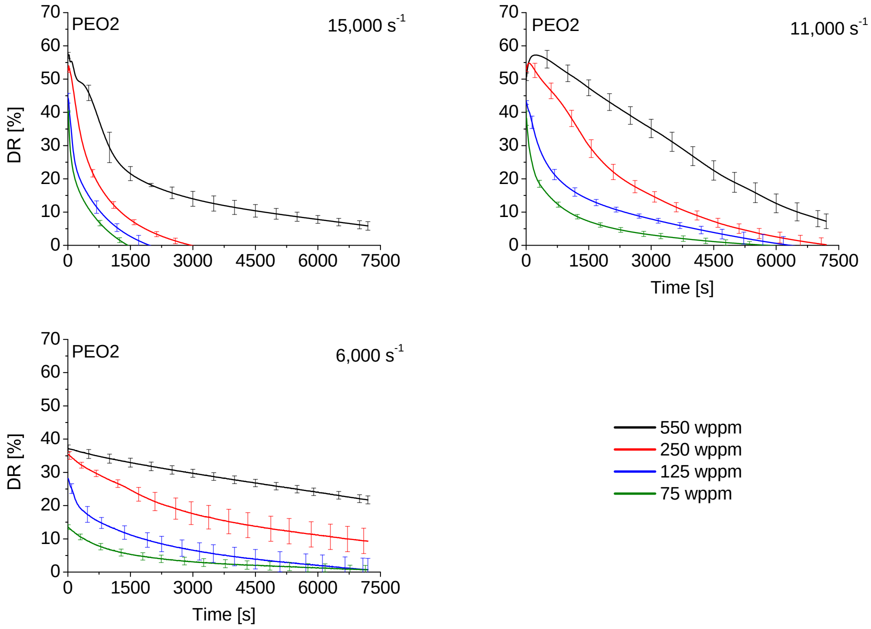

Figure 5.9: Evolution of $DR$ with a shearing time for PEO2 at shear rates $6,000$; $11,000$ and $15,000\,\mathrm{s}^{-1}$.

The influence of increasing intensity of Taylor flow, shown in the terms of shear rates, on the level of time dependent $DR$ is very strong. All polymer systems show significant decrease in the drag reducing ability at $\dot{\gamma} = 15,000\,\mathrm{s}^{-1}$ during the first 1 h of shearing. The rate of the decrease is dependent on the polymer concentration; a higher polymer concentrations led to slower decrease in the $DR$ efficiency over time. The decrease of the $DR$ efficiency is smaller for $\dot{\gamma} = 11,000\,\mathrm{s}^{-1}$. The highest polymer concentrations of PEO2, PEO4 and PEO8 show considerable level of $DR$ even after 2 h of shearing, however, lower concentrations exhibit almost zero ability to reduce drag after 2 h. Finally, at $\dot{\gamma} = 6,000\,\mathrm{s}^{-1}$ the level of $DR$ decreases for all concentrations only for PEO2. In the case of PEO4 and PEO8 the highest polymer concentration used, 550 wppm, exhibited stable $DR$ over the period of time studied. Such a behaviour demonstrated that increasing polymer concentration can have positive effect on the stability of drag reducing solutions. Polymer overdosing is commonly used in the industry, e.g. during hydraulic fracturing in the oil industry, in order to maintain maximum level of $DR$. Additionally, it can be seen that the increasing molecular weight also decreases the rate of the loss of $DR$ with time, especially at $\dot{\gamma} < 11,000\,\mathrm{s}^{-1}$. For the Taylor flow with the highest intensity, $\dot{\gamma} = 15,000\,\mathrm{s}^{-1}$, only the highest polymer concentration, 550 wppm, exhibits the described dependency of polymer molecular weight on the rate of the loss of $DR$. Polymer concentrations below 250 wppm with lower molecular weight seems to be more resistant to the shear induced loss of $DR$.

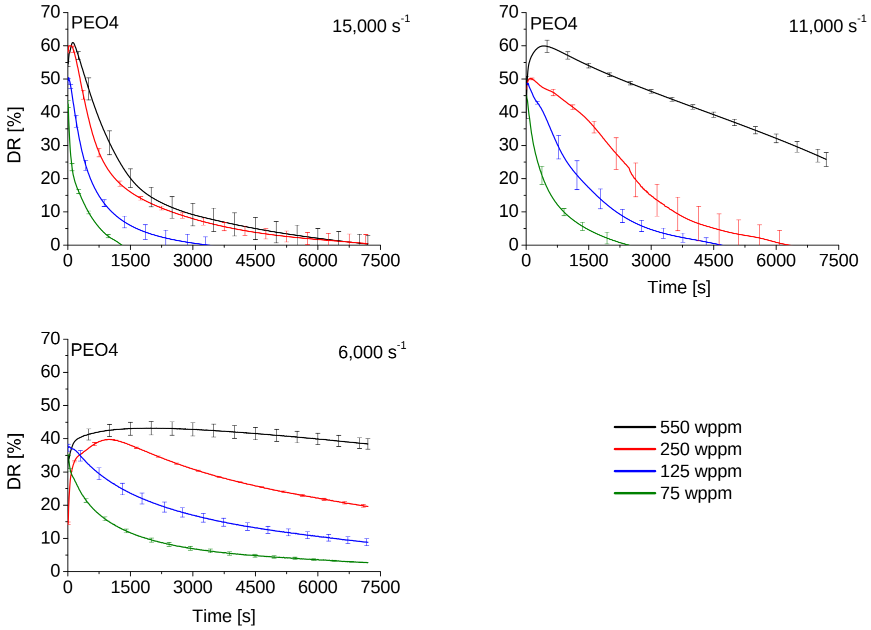

Figure 5.10: Evolution of $DR$ with a shearing time for PEO4 at shear rates $6,000$; $11,000$ and $15,000\,\mathrm{s}^{-1}$.

It is a typical practice to compare the results of time dependent $DR$ with one of the theoretical models that describe the polymer degradation mechanism [149, 150, 70]. However, the use of the theoretical models would be troublesome for the presented results. The reason is the observed increased $DR$ during the first few minutes of shearing for the highest polymer concentrations. The theoretical models are based on exponential decay functions and by definition they cannot predict or capture the initial increase of $DR$. Even the development of time dependent $DR$ after the maximum $DR$ is reached would be difficult to describe based on the theoretical degradation models. The reason for this lies in the irregularities of the time dependent $DR$ curves, which can be seen for example for PEO2 550 wppm $\dot{\gamma} = 15,000\,\mathrm{s}^{-1}$, PEO2 250 wppm $\dot{\gamma} = 11,000\,\mathrm{s}^{-1}$ or PEO4 250 wppm $\dot{\gamma} = 11,000\,\mathrm{s}^{-1}$, that can be related to the change of the vortex structure (see Figure 5.2).

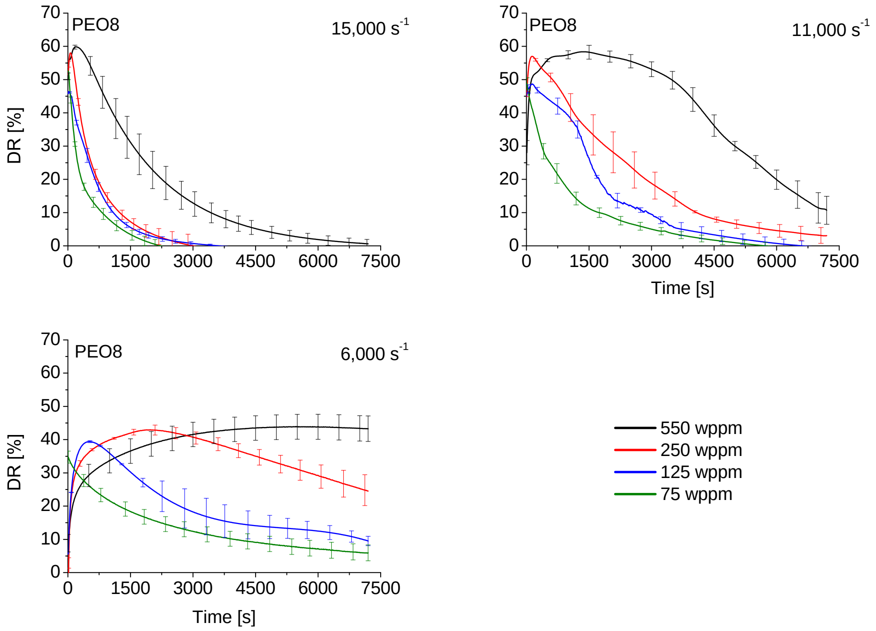

Figure 5.11: Evolution of $DR$ with a shearing time for PEO8 at shear rates $6,000$; $11,000$ and $15,000\,\mathrm{s}^{-1}$.

## 5.5 Influence of Aggregates on Drag Reduction

The effect of aggregates on polymer induced DR was investigated merely for PAAm5. The aggregate structure was modified by changing the solvent quality and therefore even polymer characterisation in quiescent conditions will be presented in this section in order to determine the presence and structure of polymer aggregates. Three solvent mixtures were used to alter the solvent quality: PAAm5 was dissolved in 25% v/v formamide water, water and 25% v/v 2-propanol water mixtures. The following denominations are used in the text for described solvent mixtures: very good, good and poor solvents, respectively.

The intrinsic viscosity results of PAAm5 in very good, good and poor solvents, which were calculated using Equations 3.1 and 3.2 are shown in Figure 5.12. A linear dependency between the reduced viscosity and polymer concentration was observed for PAAm5 in all solvents. The reduced viscosity decreases with decreasing quality of the solvent (see Table 5.2). As expected the intrinsic viscosity is the highest for PAAm5 dissolved in a very good solvent and the lowest for a poor solvent. The intrinsic viscosity can be seen as a measure of molecule size in a solution. We compare the same polymer in solvents with different qualities, therefore, we can link the differences in intrinsic viscosities to polymer chain solvation and extension in a particular solvent system. Based on this assumption it is suggested that the extension of PAAm5 in the solvents increases as follows: poor < good < very good solvent.

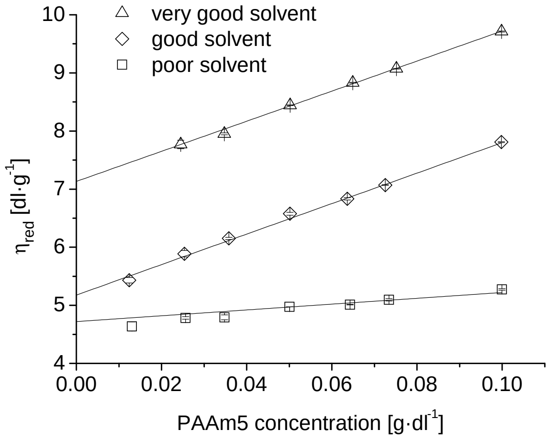

Figure 5.12: Huggins plot of the reduced viscosity $\eta_{red}$ as a function of PAAm concentration in 25% v/v formamide water (a very good solvent), water (a good solvent) and 25% v/v 2-propanol water (a poor solvent) mixtures. The vertical bars show the standard error of the measurements.

The $k_H$ value for PAAm5 in water is 0.95 (Table 5.2), which is in good agreement with the value reported by Wu et al. [151]. They noted that water is not a thermodynamically good solvent for high molecular weight PAAm. PAAm5 in 25% v/v formamide water shows $k_H$ values expected for a very good solvent. The low $k_H$ value and intrinsic viscosity for PAAm5 in 25% v/v 2-propanol water indicates its poor solvent quality, in which polymer molecules are collapsed or present in clusters that do little interact with the solvent.

Table 5.2: Intrinsic viscosity $[\eta]$, overlap concentration $c^*$ and Huggins coefficient $k_H$ obtained from the Huggins plot for PAAm5 in different solvents (see Figure 5.12) with the standard error of the measurements.

| | Very good solvent (25% v/v formamide water) | Good solvent (Water) | Poor solvent (25% v/v 2-propanol water) |
|---|---|---|---|
| $[\eta]$ $[\mathrm{dl} \cdot \mathrm{g}^{-1}]$ | 7.11 ± 0.05 | 5.18 ± 0.05 | 4.63 ± 0.02 |
| $c^*$ [wppm] | 1406 ± 10 | 1930 ± 18 | 2160 ± 10 |
| $k_H$ | 0.52 ± 0.02 | 0.95 ± 0.03 | 0.30 ± 0.01 |

It is known that the addition of a non-solvent to a solvent reduces the solvation of polymer molecules and promotes the formation of aggregates [152]. Hence PAAm molecules are less solvated in the water 2-propanol mixture when compared to pure water. Considering the dissolution mechanism of PAAm proposed by Owen et al. [153] it seems that polymer-polymer interactions might be favoured and that the stability of polymer aggregates is much enhanced in water 2-propanol mixtures. The reason of the higher stability of the polymer aggregates in water 2-propanol mixtures compared to the other studied solvent systems lies in the hydrogen bonding interactions between water and 2-propanol, which are much stronger than that between the amide group in PAAm and water. The aggregate structure can also be estimated from $[\eta]$ and $k_H$ values. It can be deduced from $[\eta]$ and $k_H$ values that PAAm5 is more solvated in water formamide mixtures then in water or water 2-propanol mixtures. From the intrinsic viscosities we can conclude that the aggregates in water 2-propanol mixtures occupy a much smaller volume than in the case of water. The high intrinsic viscosity value for the water formamide mixture suggests that PAAm5 molecules are very expanded. The Huggins parameter is in the range for a good solvent so it can be assumed that only polymer molecules are present in this solvent mixture.

Figure 5.13 shows a typical example of the dependency of the scattering intensity on the square of the scattering vector. A linear dependency was observed for PAAm5 in a very good (25% v/v formamide water) solvent, however, PAAm5 in good (water) and poor (25% v/v 2-propanol water) solvents showed different scattering trends at low and high angles. As it was discussed in Section 4.4 the downturn trends in ${}^{Kc}\!/_{R_\theta}$ as a function of $q^2$ for good and poor solvents indicate the presence of large aggregated polymer structures.

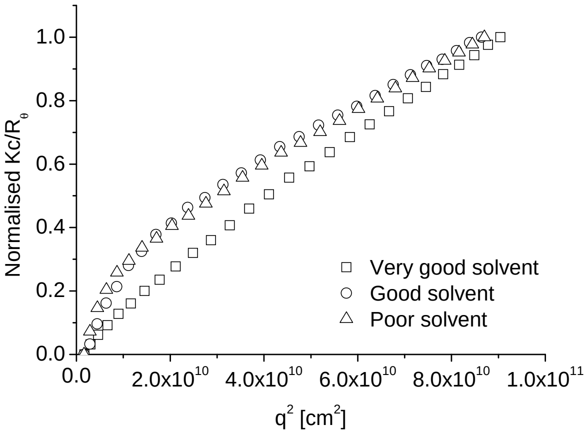

Figure 5.13: Normalised laser light scattering intensity as a function of scattering vector for PAAm5 in very good, good and poor solvents. The polymer concentration in a solution is approximately $0.5\,\mathrm{mg}\cdot\mathrm{ml}^{-1}$.

The results were processed in terms of Zimm analysis in a similar way as in Section 4.4. The results of the data interpolation to zero concentration and zero angle are summarised in Table 5.3. The second virial coefficient values $A_2$, verify the intrinsic viscosity results that the quality of the solvent increases as follows: 25% v/v 2-propanol water (a poor solvent) $<$ water (a good solvent) $<$ 25% v/v formamide water (a very good solvent). The quality of the solvent determines how swollen/collapsed a polymer molecule is in a solution. As expected the radius of gyration of individual molecules decreases with decreasing solvent quality.

The full angular dependency analysis of the Zimm plots showed that almost only individual molecules are present in a solution in the case of a very good solvent. The estimates of the z-average radius of gyration and the second virial coefficient for lower quality solvents showed the presence of aggregated structures in very good and good solvents. $R_g$ and $A_2$ indicate that the aggregates are highly swollen (flexible) in the case of a good solvent and collapsed (semi-rigid) in the case of a poor solvent. The polymer overlap concentration range as calculated using Equation 3.19 is in good agreement with the overlap concentration estimated from intrinsic viscosity measurements (see Table 4.1). Once again, as in Section 4.4, it should be noted that all calculated values for good and poor solvents are estimates and not absolute values. The reason is the heterogeneous character of the solutions and unknown concentrations of individual molecules and aggregates in the solutions.

Table 5.3: Weight average molecular weight $M_w$, z-averaged radius of gyration $R_g$, second virial coefficient $A_2$ and overlap concentration $c^*$ for PAAm in very good, good and poor solvents. 1st order fit of the high scattering angles corresponds to physical properties of individual molecules and the 2nd order fit of the full angular scattering dependency is estimation for physical properties aggregates present in the solution.

| | $M_w$ $[\mathrm{g \cdot mol^{-1}}]$ | $R_g$ [nm] | $A_2$ $[\mathrm{mol \cdot ml \cdot g^{-2}}]$ | $c^*$ [wppm] |
|---|---|---|---|---|
| Very good solvent - molecules | 3,315,000 | 126 | $2.66 \cdot 10^{-4}$ | $657 \sim c^* \sim 2572$ |
| Very good solvent - aggregates | 3,880,000 | 150 | $1.99 \cdot 10^{-4}$ | |
| Good solvent - molecules | 4,160,000 | 123 | $1.34 \cdot 10^{-4}$ | $886 \sim c^* \sim 3712$ |
| Good solvent - aggregates | 43,500,000 | 547 | $-2.43 \cdot 10^{-6}$ | |
| Poor solvent - molecules | 2,720,000 | 105 | $1.01 \cdot 10^{-4}$ | $931 \sim c^* \sim 3902$ |
| Poor solvent - aggregates | 17,450,000 | 327 | $-1.17 \cdot 10^{-5}$ | |

The apparent shear viscosity for polymer solutions with concentrations between 10 and 550 wppm at shear rate $1,000\,\mathrm{s}^{-1}$ are shown in Figure 5.14. The apparent shear viscosities at a constant polymer concentration increased as follows: good $<$ very good $<$ poor solvents and slightly increases with increasing polymer concentration, however, no abrupt upward trend is visible which means that polymer solutions are at $c < c^*$.

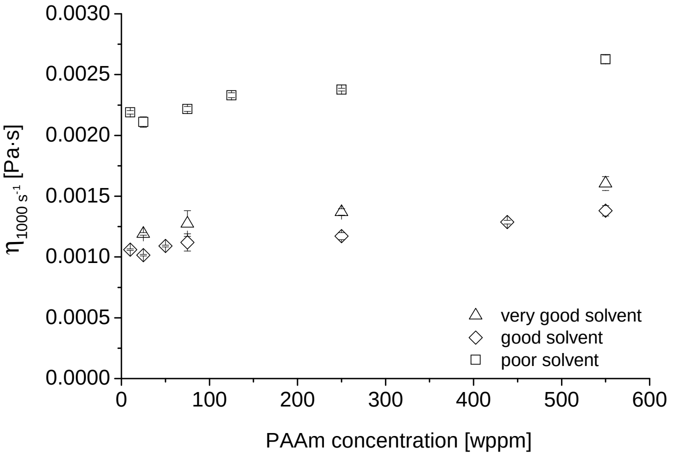

Figure 5.14: The apparent shear viscosity dependency on a polymer concentration at shear rate $\dot{\gamma} = 1,000\,\mathrm{s}^{-1}$.

Figure 5.15 compares the level of $DR$, calculated by Equation 3.25, at shear rate $\dot{\gamma} = 11,000\,\mathrm{s}^{-1}$ as a function of polymer concentration for PAAm5 in different solvents with varying qualities . The maximum $DR \sim 58\%$ is the same for very good and good solvents, however, the maximum $DR$ for a poor solvent reaches only $DR \sim 40\%$. The optimal concentrations of PAAm5 $c_{\mathrm{opt}}$ are $\sim$ 83 and 111 wppm for PAAm5 in very good and good solvents, respectively. After $c_{\mathrm{opt}}$ the level of $DR$ is constant. The $c_{\mathrm{opt}}$ for a poor solvent is unclear because of the upward trend of $DR = f\,(c)$. If the upward trend is neglected then the $c_{\mathrm{opt}}$ can be estimated to $\sim$ 62 wppm. The initial slope at low PAAm5 concentrations, $DR = f\,(c)$, is the highest for PAAm5 in a very good solvent and the lowest for PAAm5 in a poor solvent.

The extent of polymer molecule elongation was estimated by calculating the ratio of $^{c^*}/_{c_{\mathrm{opt}}}$. The $^{c^*}/_{c_{\mathrm{opt}}}$ values are $\sim$ 16, 17 and 34 for very good, good and poor solvents, respectively. The similar values for very good and good solvents indicate similar elongation of polymer molecules. In the case of a poor solvent the ratio $^{c^*}/_{c_{\mathrm{opt}}}$ is double when compared to the other studied systems, which is in agreement with the idea of semi-rigid aggregates that unravel in the flow.

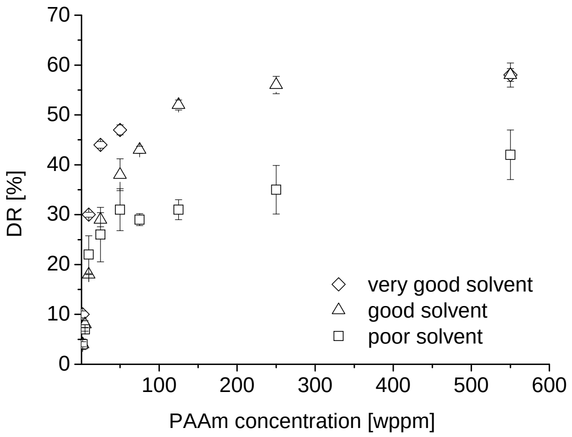

Figure 5.15: $DR$ measured at $\dot{\gamma} = 11,000\,\mathrm{s}^{-1}$ as a function of polymer concentration for PAAm5 in very good, good and poor solvents.

Several authors [75, 154] suggested that polymer aggregates are present even at dilute concentrations in quiescent conditions, however, the effect of polymer aggregates on DR is still poorly understood or has even been dismissed. Figure 5.16 shows $DR$ measurements as a function of time for PAAm5 with concentrations below $c_{\mathrm{opt}}$ in solvents of different quality, which were prepared following the procedure described in Chapter 3 Section 3.1. The experiments were repeated three times and the reproducibility is shown in the terms of standard error. Zero $DR$ refers to data obtained for the Newtonian pure solvents, namely 25% v/v formamide water (a very good solvent), water (a good solvent) and 25% v/v 2-propanol water (a poor solvent) mixtures. The PAAm5 solutions that contain flexible or no aggregates showed comparable initial levels of $DR$ which increase with increasing polymer concentration from 40 to 50% for polymer concentrations 25 and 75 wppm, respectively. It is interesting that PAAm5 in a very good solvent has virtually the same initial $DR$ when compared to a good solvent even if the polymer molecules are more swollen (see Figure 5.12). The initial level of $DR$ for polymer solutions in a poor solvent ranges from 20 to 25% for polymer concentrations 25 and 75 wppm, respectively.

Both polymer solutions in very good and good solvents show a significant decrease of $DR$ during the whole experiment. The rate of $DR$ decrease obtained from the slope in Figure 5.16 for 25 and 75 wppm are $-0.38$; $-0.42$ and $-0.35$; $-0.40\,{}^{DR(\%)}/_{\mathrm{min}}$ for very good and good solvents, respectively. The slightly higher decrease of $DR$ over time in a very good solvent when compared to a good solvent can be explained by the fact that i) polymer molecules are more

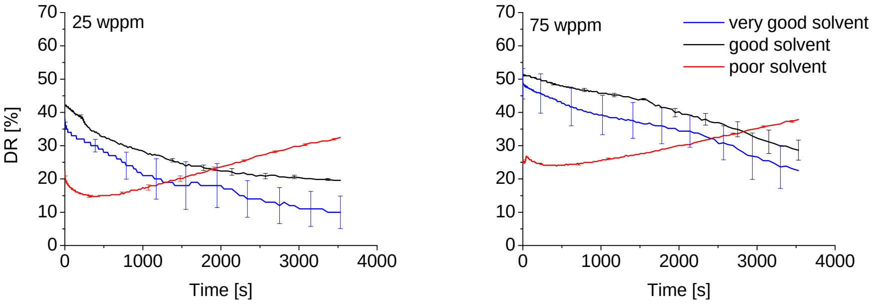

Figure 5.16: $DR$ as a function of time at constant shear rate $\dot{\gamma} = 11,000\,\mathrm{s}^{-1}$ for polymer concentrations below $c_{\mathrm{opt}}$ in very good, good and poor solvents.

extended in a very good solvent then in a good solvent and thus the elongation of polymer molecules can be more rapid which would result in faster polymer degradation but also in higher initial level of $DR$, ii) the different state of polymer molecules, such as the presence of aggregates, iii) experimental error. It was shown that individual polymer molecules are present in a very good solvent and flexible aggregates and molecules in a good solvent. Aggregates can prevent polymer molecules to be immediately stretched and degraded. A different trend is observed for a poor solvent, in which $DR$ initially decreases and then increases. The $DR$ minimum is reached after 400 s followed by a consecutive increase in $DR$. It is interesting that the level of $DR$ is higher after 1,300 s and 1,400 s then the initial $DR$ at time zero for PAAm5 at polymer concentrations 25 and 75 wppm in a poor solvent, respectively. The possible explanation for this behaviour is that individual polymer molecules are degraded during the first 400 s while semi-rigid aggregates are elongated and then unravel while releasing more individual polymer molecules that are continuously dosed into the flow.

Figure 5.17 shows the influence of polymer concentrations higher than $c_{\mathrm{opt}}$ on the level of $DR$ at shear rate $\dot{\gamma} = 11,000\,\mathrm{s}^{-1}$ as a function of time. It should be stated that even these (high) PAAm5 concentrations are far below the overlap concentration $c^*$ in quiescent conditions (see Table 5.2 and 5.3), so the solutions can still be considered as dilute. An increase in $DR$ can be seen in the first 120 s of the test. This effect occurs only for concentrations above $c_{\mathrm{opt}}$. It is possible that the initial increase of $DR$ is caused by the elongation of polymer molecules in Taylor flow. The effect of the elongation of polymer molecules is more obvious for polymer concentration $c > c_{\mathrm{opt}}$ because of higher spatial restriction when compared with $c < c_{\mathrm{opt}}$ (see Figure 5.7). Both polymer solutions in very good and good solvents exhibited similar levels of $DR$ within the error. It is interesting that at lower polymer concentration, 250 wppm,

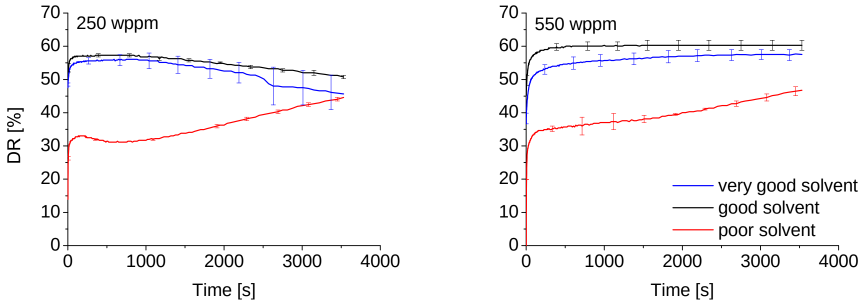

Figure 5.17: $DR$ as a function of time at shear rate $\dot{\gamma} = 11,000\,\mathrm{s}^{-1}$ for polymer concentrations above $c_{\mathrm{opt}}$ in very good, good and poor solvents.

the rate of $DR$ decrease over time is higher in a very good solvent then in a good solvent. It has been stated by Moussa et al. [68] that polymer molecules degrade faster in better solvents at high $Re$. The shear rate used during the experiments $\dot{\gamma} = 11,000\,\mathrm{s}^{-1}$, corresponding to a Reynolds number $Re = 2,500$, might seem low, however, the reader should note that $Re$ for Couette flow cannot be directly compared to those obtained for pipe flows. We prefer to compare Couette geometry and pipe results based on shear rates. In our system the shear rate is $\dot{\gamma} = 11,000\,\mathrm{s}^{-1}$. Such high shear rates can be found in pipe flows only if the Reynolds numbers approaches $Re \approx 1,000,000$.

The behaviour of PAAm5 in a poor solvent is, however, more complicated. As we proposed before, in a poor solvent PAAm5 exists in equilibrium between individual polymer coils and semi-rigid aggregates that initially do not or little contribute to the DR effect. The DR behaviour is very similar to the one observed for less concentrated polymer solutions. $DR$ increases as soon as semi-rigid aggregates are unraveled which takes place at 400 s and 750 s for 550 wppm and 250 wppm, respectively. Bizotto et al. [119] used a kinetic model to describe the mechanical degradation kinetics of flexible polymers in Taylor flow and stated that under high shear the degradation dynamics of highly elongated polymer molecules is independent of the polymer radius of gyration. This is obviously in contradiction with our observations; we see that the presence of aggregates is a key factor determining the time dependent DR. It is expected that the time dependent DR in a poor solvent would reach maximum at some point and then the level of $DR$ will steadily decrease once the polymer aggregates are completely unraveled. It was, however, not possible to obtain reasonable $DR$ data beyond 1 h of shearing using our rheometer. The reason was very high noise to signal ratio of the results caused by overheating of the torque sensor in the rheometer.

Figure 5.18 shows the evolution of the molecular weight distribution of

PAAm5 over time for samples subjected to turbulent Taylor flow. Figure 5.18 shows that polymer degradation occurs in all investigated solvent systems. All tested samples had the same PAAm5 concentration, 75 wppm, and were subjected to turbulent Taylor flow ($\dot{\gamma} = 11,000\,\mathrm{s}^{-1}$) for a given time (see Figure 5.18 legend). The molecular weight distribution gradually moves to lower molecular weights with increasing shearing time which is in agreement with the generally accepted degradation mechanism, which states that the highest molecular weight tail is preferentially degraded [17].

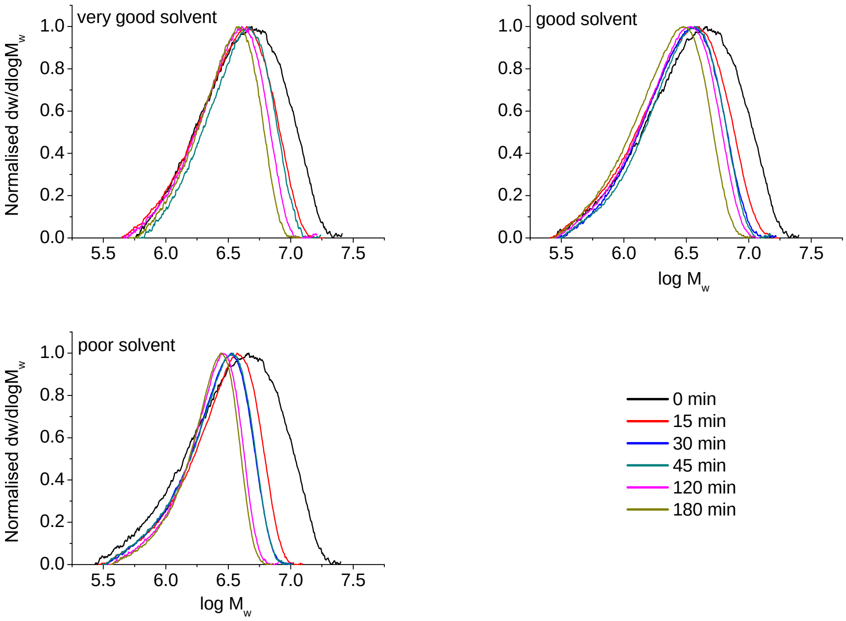

Figure 5.18: Evolution of molecular weight distribution with residence shearing time in a double gap cell $\left(\dot{\gamma} = 11,000\,\mathrm{s}^{-1}\right)$ for PAAm dissolved in good, poor and very good solvents.

PAAm5 dissolved in very good and good solvents behaved very similar in terms of $DR$ (see Figure 5.16 and 5.18) but also in terms of the polymer degradation, which is represented by the molecular weight. The weight average molecular weight decreases for all used solvent systems (see Figure 5.19). For PAAm5 in very good and good solvents, we have to conclude, that the decrease of $DR$ efficiency is caused by the flow induced polymer degradation which is in agreement with the literature [17, 155]. In the case of PAAm5 in a poor solvent, $M_w$ levels off after 2 h of shearing. However, it should be noted that despite of the decreasing $M_w$, the level of $DR$ steadily increases from $t = 700\,\mathrm{s}$ (see Figure 5.16). To our knowledge this is the first time when increasing $DR$ over time was accompanied with steady or decreasing average $M_w$.

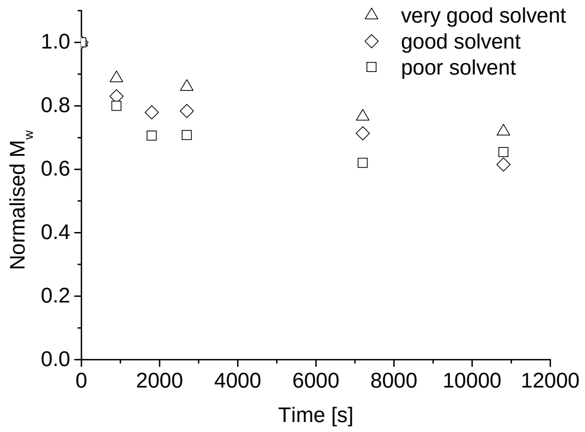

Figure 5.19: Weight average molecular weight as a function of time for which PAAm5 in very good, good and poor solvents was subjected to turbulent Taylor flow in the double gap cell.

Based on the results presented above, a mechanism can be proposed to explain the influence of aggregates on time dependent DR in turbulent Taylor flow. This can be described by the schematic shown in Figure 5.20. Solution I. represents homogeneously dissolved polymer molecules in a very good solvent in which only individual well hydrated polymer coils exist. Polymer molecules are subjected to high stresses in the flow that stretch the molecules. The stretching mechanism is believed to be crucial for DR [107]. When the elongation of polymer molecules reaches a critical value the polymer chain is subsequently ripped apart. The polymer molecular weight degradation mechanism has been observed for example by Kim et al. [17]. Solution II. shows the polymer state in a relatively good solvent where loose aggregates coexist in equilibrium with individual polymer chains. It can be assumed that the stresses necessary to unravel these flexible aggregates are much lower than those necessary to break a polymer backbone. It is possible that these aggregates could be important in flows with considerably lower fluctuating strain rates, e.g. pipe flow, then were used in current study. Solution III. represents a system in a relatively poor solvent where aggregates are composed of many tightly packed polymer molecules. These aggregates initially do not or contribute little to the DR effect, however, they are unraveled in the fluctuating strain rates and so release individual polymer molecules to the flow (see Figure 5.16). When the aggregates become flexible enough the level of $DR$ increases as can be seen in Figure 5.16. These aggregates act as a pool of fresh polymer molecules.

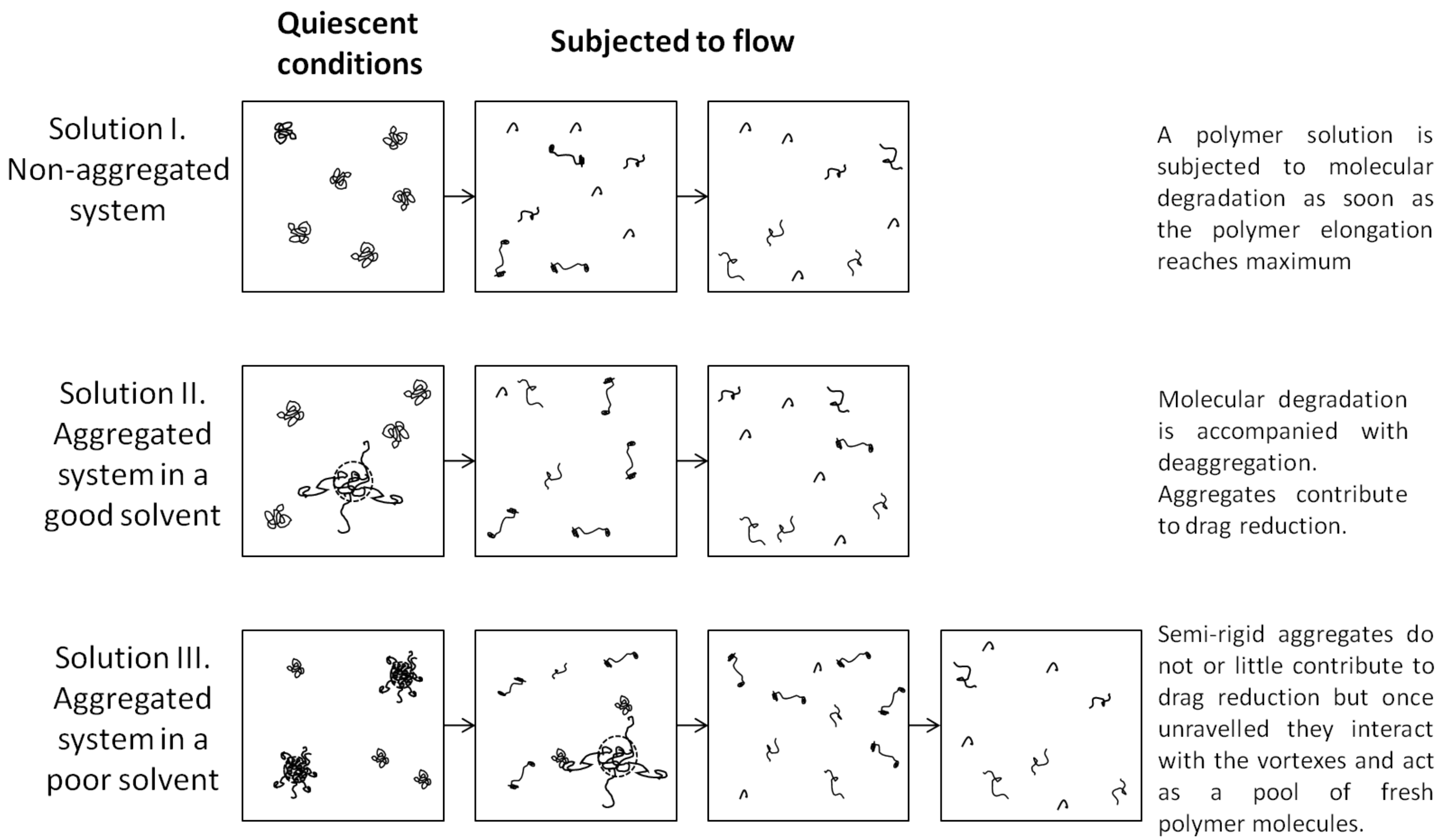

Figure 5.20: Schematic illustration of proposed mechanism of the influence of polymer aggregates on DR.

## 5.6 Summary

In this Chapter the DR characterisation using a commercial rheometer equipped with a double gap sample holder was investigated. The flow visualisation showed that the flow between two concentric cylinders is getting more complex when the rotational speed of the rotor is increased. Simple Couette flow, Taylor flow, the onset of turbulent Taylor flow and fully developed Taylor flow were observed in the visualisation cell. Additionally, it was shown that the polymer additives have a strong effect on the stability and structure of the flow between concentric cylinders. The flow visualisation data comparison with the double gap cell used for the DR characterisation indicated that the fully developed turbulent Taylor flow cannot be achieved during the DR measurements. However, an onset of turbulent Taylor flow was located in the DR measurement flow profiles (see Figure 5.3).

The $DR$ calculation requires the knowledge of the apparent shear viscosity at the onset of Taylor flow in order to correct the $DR$ results for increase of the apparent viscosity caused by the addition of polymer. An empirical relationship between the apparent shear viscosity and the apparent shear viscosity at Taylor flow onset was derived from a large number of polymer-solvent systems (see Figure 5.4). The measurements of instantaneous $DR$ as a function of polymer concentration showed the typical trends for drag reducing polymers: i) $DR$ increases with increasing polymer concentration until an optimum concentration is reached. Further increase of polymer concentration does not lead to a significant increase in $DR$, ii) $DR$ efficiency increases with increasing polymer molecular weight and iii) $DR$ increases with increasing intensity of the flow. Therefore, presented technique can be reliably used to measure the $DR$ efficiency. Also an explanation of the optimum polymer concentration was proposed which is based on spatial restrictions of elongated polymer molecules. However, more work is needed to clarify the real nature of the optimum concentration.

The time dependent measurements of $DR$ in Taylor flows with different shear rates showed that polymer induced DR decreases with increasing shearing time. Moreover, the magnitude of the decrease is proportional to the Taylor flow shear rate. It was also identified that an increased polymer concentration can be used in order to increase the sustainability of the drag reducing effect. The attempt to fit the degradation curves with one of the degradation models was not successful. There were two main reasons: i) DR increases in the first few minutes of the experiment, especially for polymer concentrations above $c_{\mathrm{opt}}$ and ii) change of the vortex structure during the degradation experiments. The classical models are based on an exponential decay functions that are unable to capture the two described effects.

The work on the influence of polymer aggregates on DR was stipulated by the earlier work of Hecker et al. [81] and Liberatore et al. [42]. The combination of static light scattering and intrinsic viscosity measurements was used to assess the presence of aggregates in a polymer solution. The presence of aggregates in PAAm5 solutions was proved by these techniques. Additionally, it was inferred from static light scattering and the intrinsic viscosity measurements that PAAm5 aggregates exist in flexible form in water (a good solvent) and semi-rigid form in the case of water 2-propanol mixtures (a poor solvent). Formamide water mixtures (a very good solvent) on the other hand ensure complete dissolution of PAAm5.

It was found that different aggregate structures influenced the initial level of $DR$ as well as the time dependent $DR$ in Taylor flow. The initial $DR$ increases as follows: semi-rigid aggregates $<$ individual molecules $\approx$ flexible aggregates. The measurements, using the double gap cell, in Taylor flow revealed that flexible aggregates have a small stabilising effect on the DR performance over time even if the rate of polymer chain mechanical degradation is comparable for PAAm5 dissolved in very good and good solvents. However, the main finding is that semi-rigid aggregates are slowly unraveled in turbulent Taylor flow and act as a pool of fresh polymer molecules. Such a polymer solution showed unprecedented time dependent $DR$ in high shear flows in which $DR$ increases over time even though molecular weight decreases.

# Chapter 6

# Drag Reduction Characterisation in a Turbulent Pipe Flow

The following Chapter is divided into two main section. The results of the differential pressure and velocity measurements in a turbulent pipe flow are presented in Section 6.1. The turbulent flow characterisation using particle image velocimetry is presented in Section 6.2.

## 6.1 Drag Reduction Measurements

The author designed a pilot-plant scale flow facility which was described in Section 3 Section 3.2.6. In this Section the commissioning and gross flow measurements are presented. In what follows, Section 6.1.1 deals with the verification of the flow facility measuring performance. Section 6.1.2 composes of gross flow measurements in terms of semi-log Prandtl - von Kármán coordinates and the classical DR efficiency dependency on polymer concentration. Additionally, degradation experiments where the polymer solution was allowed to pass the test section several times is also presented.

### 6.1.1 Verification

The friction reduction efficiency and the corresponding levels of $DR$ were measured using the flow facility which was primarily constructed to minimise the possibility of polymer degradation prior entering the test section (see Section 3.2.6). The usually used centrifugal or screw pumps were substituted with a pressure vessel and the driving force to pump the polymer solution or the Newtonian solvent through the test section was only the head pressure in the pressure vessel. The *Re* achievable in the test section is therefore function of the head pressure, length and quality of the pipe system and solution properties. The pressurised air from the Imperial College London mains was used to pressurise the pressure vessel. The maximum pressure in the mains was $p = 5 - 6\,\mathrm{bar}$. However, it should be noted that a pressure of 5 bar was not sustainable in the pressure vessel during the experiments. Figure 6.1 shows the evolution of water bulk velocity $U_{\mathrm{bulk}}$ in the test section and the head pressure in the pressure vessel over time. The flow facility allowed for velocities between 3 and $6\,\mathrm{m \cdot s^{-1}}$ without significant deviation. The minimum velocity used was $1.5\,\mathrm{m \cdot s^{-1}}$, but the flow oscillated slightly with time. The highest velocity $9\,\mathrm{m \cdot s^{-1}}$ showed decreasing trend over time, since the pressurised air from the mains was not able to maintain a constant pressure of $p \sim 4\,\mathrm{bar}$ in the head of the pressure vessel. Additional sources of pressurised air would be needed, such as pressure cylinders, in order to be able to perform measurements at the maximum design bulk velocities $U_{\mathrm{bulk}} \sim 30\,\mathrm{m \cdot s^{-1}}$. The instabilities for minimum and maximum velocity were minimised by averaging all the values over time. The time-averaged bulk velocity standard deviations were 1.7% and 1.9% for the 1.5 and $9\,\mathrm{m \cdot s^{-1}}$, respectively. Ten values from each pressure sensor and from the flowmeter were recorded per second, which gives 600 points per 1 min of measurement.

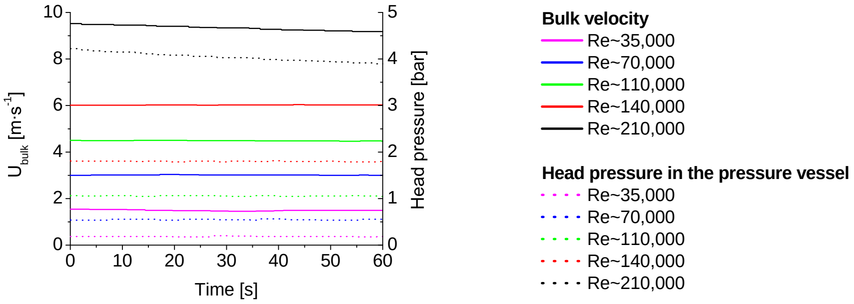

Figure 6.1: The evolution of the water bulk velocity $U_{\mathrm{bulk}}$ in the test section and of the air pressure in the pressure vessel as a function of time.

The flow facility contains six differential pressure transducers. It should be noted that only one pressure transducer is necessary to quantify homogeneous DR. The higher number of pressure transducers is needed to study heterogeneous DR. However, a higher number of pressure transducers, when homogeneous DR is tested, can be used to asses whether any polymer degradation occurs within the test section. The pressure drop of water at different velocities as a function of length from the reference pressure tap is shown in Figure 6.2. The

$\Delta p = f(l)$away from the reference pressure sensor increases linearly. Moreover, pressure drop increased with increasing velocity, which is in agreement with the theory. The standard deviation of the differential pressure measurements was $< 2\%$ in all cases.

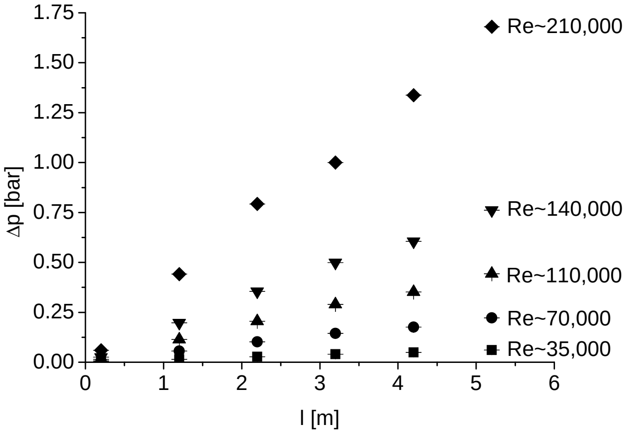

Figure 6.2: Dependence of a pressure drop on length of the test section for water.

### 6.1.2 Gross Flow Measurements

The gross flow results for the Newtonian solvent, water, can be verified when plotted in semi-log Prandtl - von Kármán coordinates $1/\sqrt{f}$ versus $\log Re\sqrt{f}$ (Figure 6.3). Following the measured data from low to high velocities unveiled that all data points are in the turbulent flow region. Reynolds numbers calculated using Equation 2.1 are $35,000$; $70,000$; $110,000$; $140,000$ and $210,000$ for velocities of 1.5; 3; 4.5; 6 and $9\,\mathrm{m \cdot s^{-1}}$, respectively.

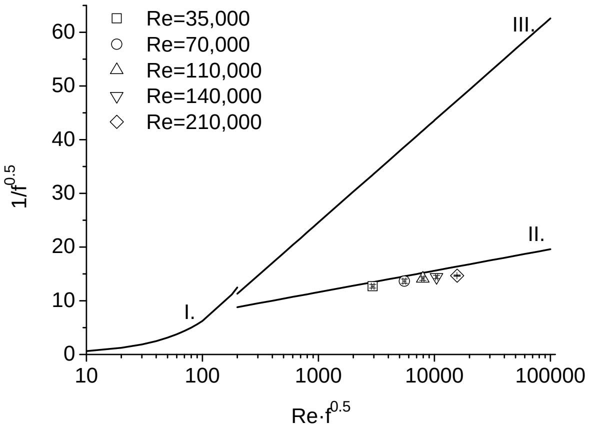

Figure 6.3: Gross flow measurements of water in semi-log Prandtl - von Kármán coordinates. Curves I., II. and III. represent laminar flow following Poiseuille's law (Equation 2.3), turbulent flow following the law for Newtonian turbulent flow (Equation 2.4) and Virk's maximum DR asymptote (Equation 2.5), respectively.

It should be noted that the data points do not lei exactly on the turbulent flow curve but they are shifted to lower $1/\sqrt{f}$ values indicating higher friction. The reason is that our pipe test section is not completely smooth as described in Section 3.2.6. The average pipe roughness can be estimated using following equation:

$$\frac{1}{2}\frac{1}{\sqrt{f}} = -2.0 \log\left(\frac{\varepsilon/D}{3.7} + \frac{2.51}{2Re\sqrt{f}}\right) \tag{6.1}$$

where $\epsilon/D$ is the absolute roughness relative to the pipe diameter. The relative roughness is: $\varepsilon/D = 0.0005$ which gives the absolute roughness: $\epsilon = 0.0125\,\mathrm{mm}$. The pipe roughness values indicate normal type of steel, although we wanted a hydrodynamically smooth test section. A hydrodynamically smooth test section could be obtained for howened (polished) stainless steel pipes. The presence of pipe roughness should be kept in mind throughout Chapters 6 and 6.2.

The gross flow results for PEO2, PEO4 and PEO8 solutions are shown in Figure 6.4 in semi-log Prandtl - von Kármán coordinates. It can be seen that the level of $DR$ increases with increasing polymer concentration for a fixed molecular weight and with increasing polymer molecular weight for a fixed polymer concentration. $DR$ increased with increasing $Re$ for PEO2 solutions. However, PEO4 and PEO8 solutions exhibit different behaviour for low and high $Re$. The difference is possibly caused by polymer degradation. The maximum DR was not achieved during the tests.

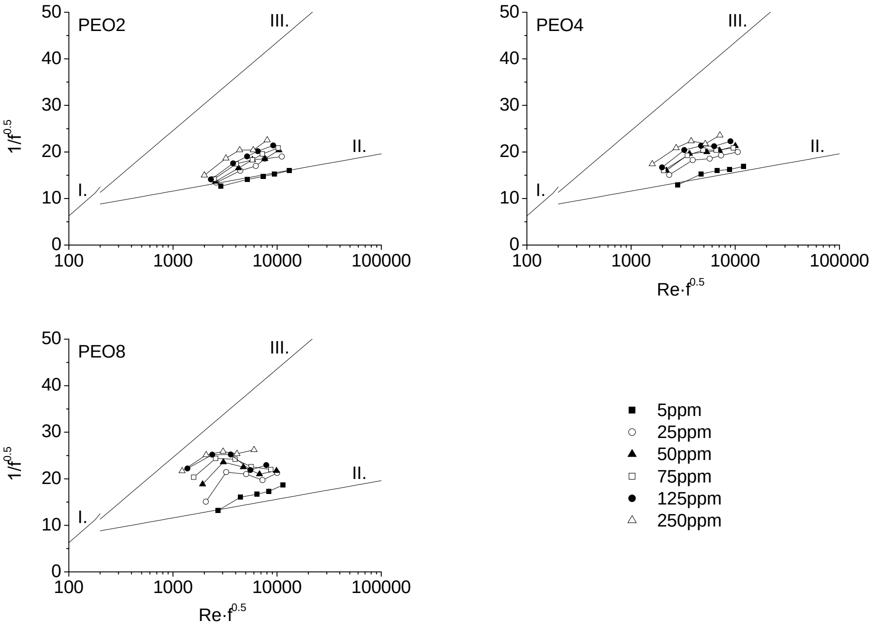

Figure 6.4: DR effect in semi-log Prandtl - von Kármán coordinates for PEO2, PEO4 and PEO8 solutions. Curves I., II. and III. represent laminar flow following Poiseuille's law (Equation 2.3), turbulent flow following the law for Newtonian turbulent flow (Equation 2.4) and Virk's maximum DR asymptote (Equation 2.5), respectively.

The dependence of $DR$ on polymer concentration for PEO2, PEO4 and PEO8 solutions at different $Re$ is shown in Figure 6.5. The level of $DR$ increases with increasing polymer concentration and polymer molecular weight. The biggest difference between the various polymer molecular weights can be seen for relatively low $Re$. With increasing $Re$ the difference of the ability of polymer molecules to decrease the frictional drag decreases with respect to their molecular weight. The flow $c^*$ concept (see Figure 5.7) can be used to explain such behaviour. As discussed by Sher [109] polymer molecules can be unraveled by centrifugal, elongational and shear forces in the fluctuating strains of turbulent flow. It is obvious that it is easier for longer molecules to get elongated compared to shorter molecules when subjected to small strain rates. However, when the strain rates become large enough then both long and short molecules can be completely unraveled.

In order to investigate the possibility of polymer degradation within the test section, the evolution of the level of $DR$ was monitored as a function of length of the test section (see Figure 6.6). If polymer degradation occurs then one would

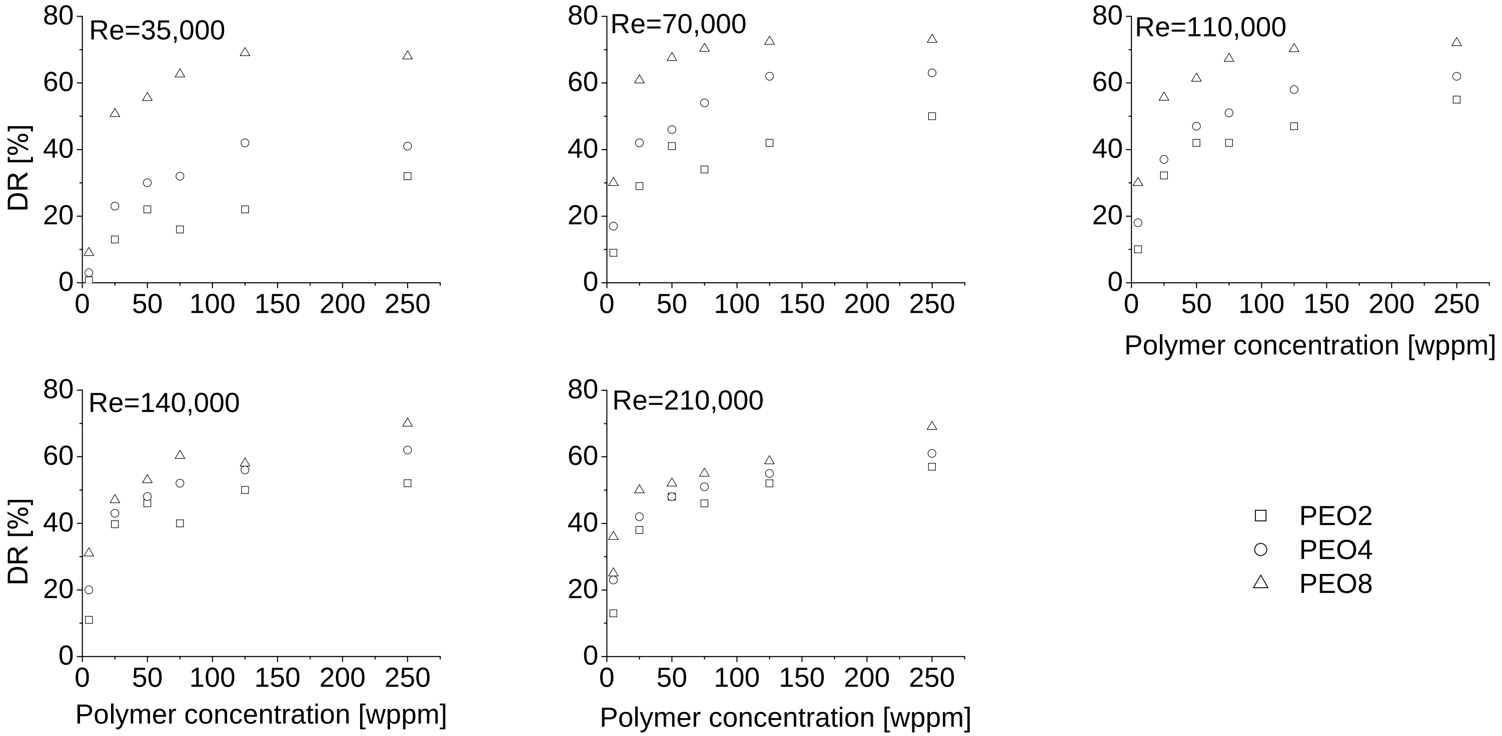

Figure 6.5: Drag reduction as a function of polymer concentration

expect a steady decrease of $DR$ with pipe length. For a relatively low $Re$, $Re < 70,000$, the level of $DR$ is steady over length within experimental error. Such a behaviour indicates that there is no flow induced polymer degradation. Small decrease can be seen between 0.2 and 1.2 m. However, the decrease should be attributed to the presence of a flange in the former case. The remarkable and unexpected trend starts to be visible for $Re > 70,000$. The level of $DR$ suddenly increases at $l = 2.2\,\mathrm{m}$ from the reference pressure tap. It should be noted that the differential pressure was measured between a reference pressure tap and a measuring pressure taps at distances of $l_i = 0.2$; 1.2; 2.2; 3.2; 4.2 and 5.2 m. Therefore, the sudden increase of $DR$ must happen somewhere between $1.2 - 2.2\,\mathrm{m}$ from the reference pressure tap. The $DR$ "peak" becomes more intense with increasing $Re$. The example shown in Figure 6.6 is for PEO2, however, the same trend was observed for two other studied polymers namely PEO4 and PEO8 (see Appendix A Figures A.1 and A.2).

The evolution of $DR$ for PEO2, PEO4 and PEO8 at $Re = 210,000$ for repeated runs through the test section is shown in Figure 6.7. It is clearly visible that the level of $DR$ decreases with the number of runs in the test section which suggests polymer degradation. As it was shown in Figure 6.6 the decrease cannot be unambiguously linked to the polymer degradation in the test section. Moussa et al. [65] discussed that the design of the inlet into the test section is crucial to avoid mechanical degradation of polymer molecules. Their statement can be generalised in a way that any part of the system that causes deviation in the flow profile can be responsible for polymer degradation. The reason are much larger elongation and shear strains present in a contraction and much larger vorticity present in a pipe elbow when compared to a straight pipe. The used flow facility setup consists of two contractions and three elbows prior the test section. Additionally a pump was used for recycling the polymer solutions which according to den Toonder et al. [62] has also strong influence on the degradation of polymer molecules. It is therefore hard to pinpoint the main cause of the polymer degradation and further work is necessary on this topic for our test facility. The continuous lines in Figure 6.7 are fits to the data using the model describing the relationship between $DR$ and polymer degradation developed by Brostow [69]:

$$\frac{DR\,(t)}{DR_{t=0}} = \frac{1}{1 + W\,(1 - e^{-ht})} \tag{6.2}$$

where $DR\,(t)$ is $DR$ at time $t$, $DR_{t=0\,\mathrm{s}}$ is the initial $DR$, $W$ is related to the number of points in a polymer molecule that are vulnerable to mechanical degradation and $h$ is the decay constant. The equation was recently updated by incorporating a linear and a quadratic term to the decay constant $h$ [19]. The

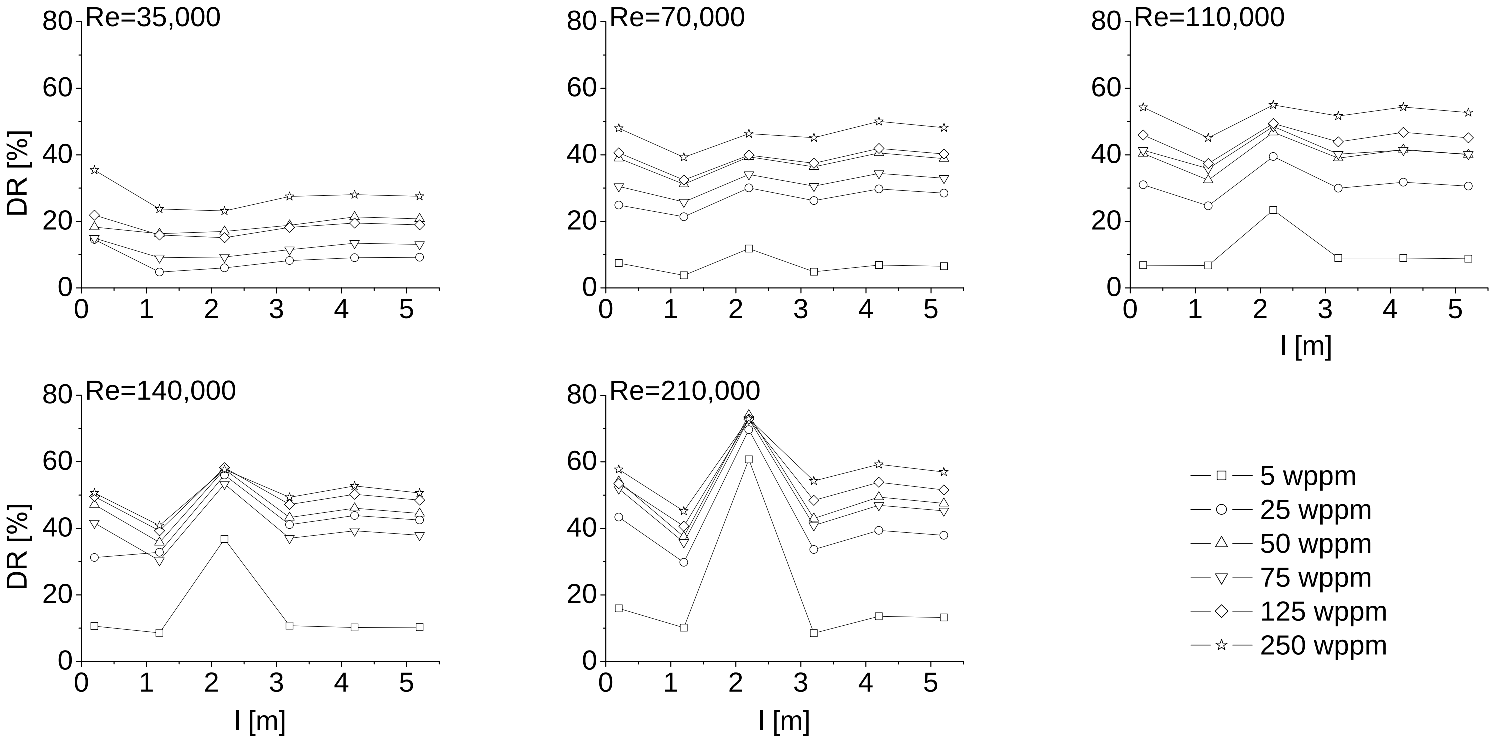

Figure 6.6: The evolution of the level of $DR$ with length for PEO2 solutions.

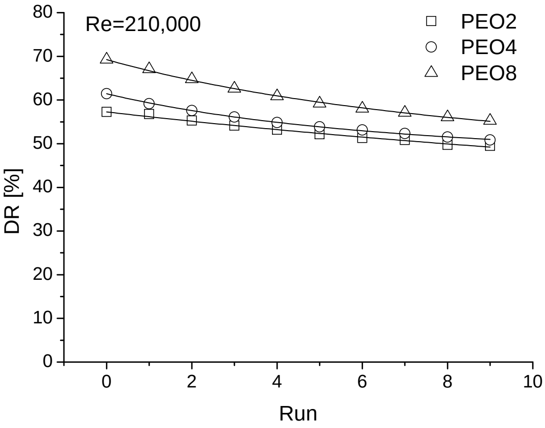

Figure 6.7: The decrease of the level of $DR$ as a function of number of runs through the test section.

new version of Equation 6.2 is taking in account the variation of $Re$, polymer-solvent pair and the overlap of polymer molecules. However, Equation 6.2 is more than sufficient to describe the degradation dynamics of polymer molecules in turbulent pipe flow. The parameter $W$ reaches values of 1.07; 0.30 and 0.51 for PEO2, PEO4 and PEO8, respectively. The values of $W$ mean that on average every polymer molecule, every third polymer molecule and every second polymer molecule is ripped apart in the turbulent flow. In other words the vulnerability to mechanical degradation at $c = 250\,\mathrm{wppm}$ increases as follows: PEO4 $<$ PEO8 $<$ PEO2.

### 6.1.3 Summary of the Section

The verification of the flow facility proved that precise pressure drop results along the pipe can be obtained for flow velocities between 1.5 and $9\,\mathrm{m \cdot s^{-1}}$. The velocities correspond to Reynolds numbers between $35,000$ and $210,000$. The gross flow measurements of water indicated that the test section is not hydrodynamically smooth. The absolute roughness of the test section was estimated by Equation 6.1 to be $\epsilon = 0.0125\,\mathrm{mm}$, which corresponds to that of a normal steel pipe.

The gross flow measurements of polymer solutions showed that the maximum level of $DR$ was not achieved during the tests. Additionally, the downward trends in the semi-log Prandtl - von Kármán plots for polymer solutions at high $Re$ indicate that polymer degradation did occur during the tests. However, the measurements of $DR$ over the length of the test section did not prove any degradation within the test section. Instead, an unusual $DR$ "peak" was observed. The author has to date no explanation for this observation.

A decrease $DR$ was observed when the polymer solutions were repeatedly pumped through the test section. The cause of the degradation was attributed to the pipe contractions and elbows as well as to the pump used for the recycling of polymer solutions. A model describing polymer degradation was used to fit the data and a perfect fit was obtained. The vulnerability of polymer molecules to mechanical degradation was estimated using the model. The vulnerability to mechanical degradation at $c = 250\,\text{wppm}$ increases as follows: PEO4 $<$ PEO8 $<$ PEO2.

## 6.2 Particle Image Velocimetry Measurements

In this Chapter results are presented non-intrusive measurements of the flow field, performed with Particle Image Velocimetry (PIV). The effect of polymer additives on instantaneous images of the turbulent flow is discussed (Section 6.2.1). A new DR mechanism is suggested based on the observations made from the instantaneous images of turbulent flow. The time-averaged flow images are presented in Section 6.2.4. The flow can be decomposed into four basic flow domain transformations (see Figure 6.8), which are translation, shear, elongation or compression and rotation.

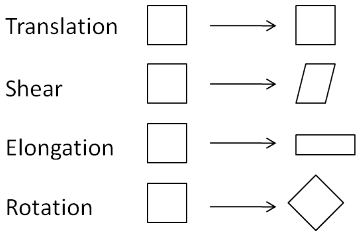

Figure 6.8: Schematic illustration of flow domain transformation in turbulent flow.

The effect of drag reducing agents on the translation and the fluctuation of the translation in the flow domain is described in Sections 6.2.5 and 6.2.6, respectively. The change of shear, elongation/compression and rotation of the flow domain transformation is discussed in Section 6.2.7. Finally, the structure of the turbulent flow is analysed in terms of higher order statistics of the stream- and spanwise velocity fluctuations, skewness and kurtosis, in Section 6.2.8, where the terms are also defined.

### 6.2.1 Instantaneous Images

Before turning to the statistical treatment of the PIV measurements, it is important to analyse the instantaneous images of pure solvent and polymer containing solutions. In particular, the effect of polymer additives will be investigated at $Re = 35,000$ in the terms of instantaneous i) velocity (see definition in Equation 3.28), ii) streamwise shear strain rate (see definition in Equation 3.34), iii) 2D vorticity (see definition in Equation 3.38) and iv) vector fields of velocity fluctuations (see definition in Equations 3.29 and 3.30). Additionally in few cases instantaneous spanwise shear strain rate (see definition in Equation 3.35), streamwise and spanwise compression strain rate (see definition in Equations 3.36 and 3.37) will be shown.

The axial size (16.0 mm) of the PIV window, the mean velocity $U_{\text{bulk}} = 1.5\,\text{m}\cdot\text{s}^{-1}$ which corresponds to $Re = 35,000$ and the sampling rate (100 Hz) of the PIV image pairs allows us to stitch together instantaneous images of the turbulent flow in order to track the evolution of possible patterns in the flow. Figures 6.9 and 6.10 show instantaneous flow velocity $U$, streamwise shear strain rate $\gamma_{xy}$, 2D vorticity $\omega_z$ and velocity fluctuation ($u^{'}$ and $v^{'}$) images for water and PEO8 5 wppm at $Re = 35,000$. The instantaneous velocity increases from zero wall velocity towards the centre of the pipe. The instantaneous streamwise strain rate and 2D vorticity show coherent values in the wall region where also the boundary between the viscous sublayer and the turbulent flow is located. Further from the wall towards the centre of the pipe the instantaneous streamwise strain rate and 2D vorticity maps show noisy pattern, without defining features. The vector field of the velocity fluctuations shows a high degree of fluctuation complexity ranging from the lowest resolved scales to structures that are larger than the radius of the pipe. The large scale velocity fluctuation structures were identified as large contributors to the Reynolds stress [156, 98]. The instantaneous spanwise strain rate, stream- and spanwise compression strain rate images are shown in Figures 6.10, 6.11, 6.12 and 6.13. The variables exhibit a high degree of scatter and no features are visible.

Features appear when the concentration of polymer additives increases (see Figures 6.11, 6.12, 6.13, 6.14 and 6.15). The most obvious feature is that the high velocity flow situated in the central region of the pipe is separated from the inner near-wall region. The separation is demonstrated by i) an abrupt change in the instantaneous velocities over short distance, ii) coherent layer of low values of instantaneous streamwise shear strain rate, iii) coherent layers of high values of instantaneous 2D vorticity and iv) continuous regions of coherent velocity fluctuations. The separation is similar to the viscous sublayer - turbulent flow layer separation which is visible for the Newtonian solvent as well as for polymer

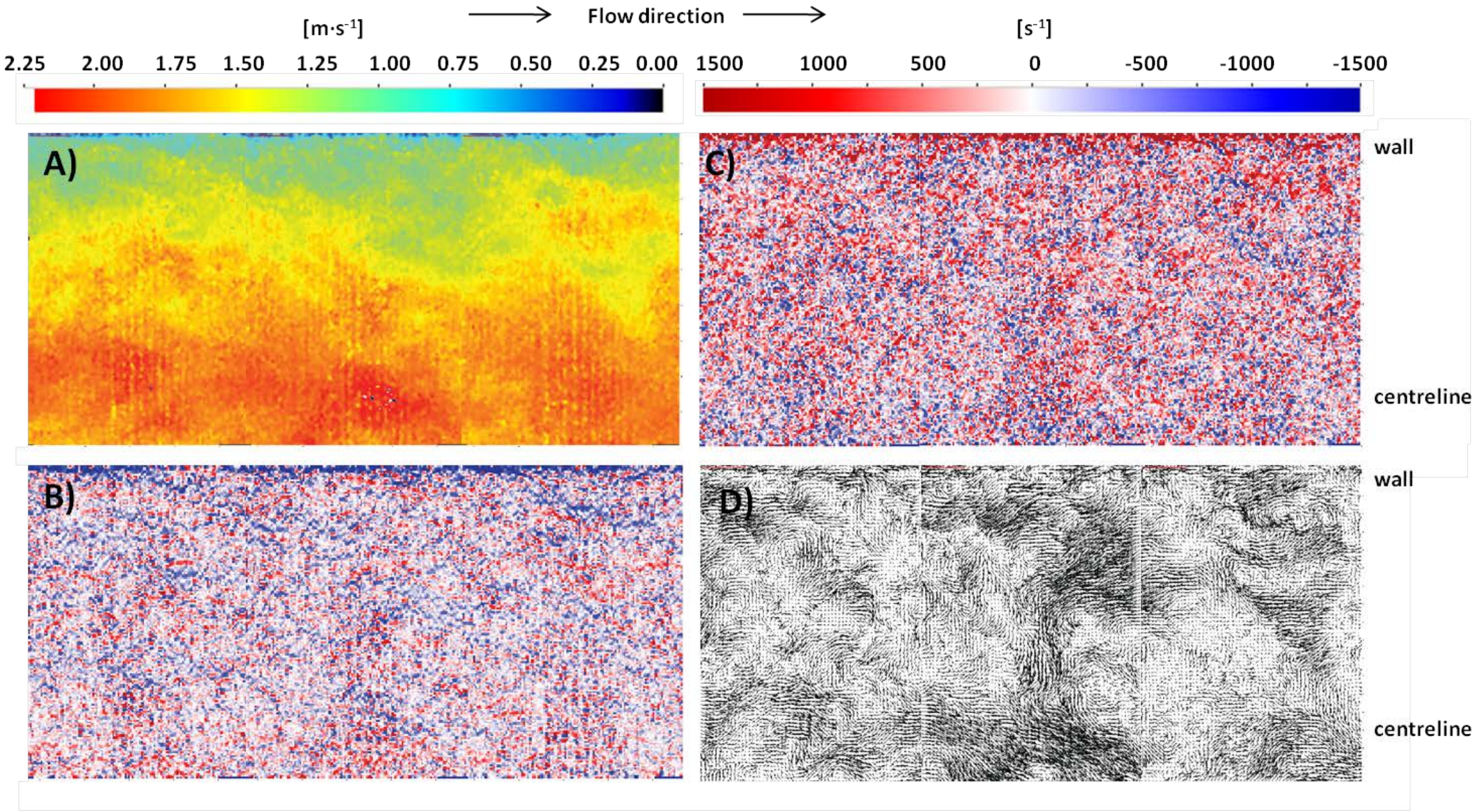

Figure 6.9: Instantaneous images of water at $Re = 35,000$. A) instantaneous velocity $U$, B) instantaneous streamwise shear strain rate $\gamma_{xy}$, C) instantaneous 2D vorticity $\omega_z$ and D) velocity fluctuations ($u^{'}$ and $v^{'}$). The wall is located at the top of the images and the flow direction is from the left to the right.

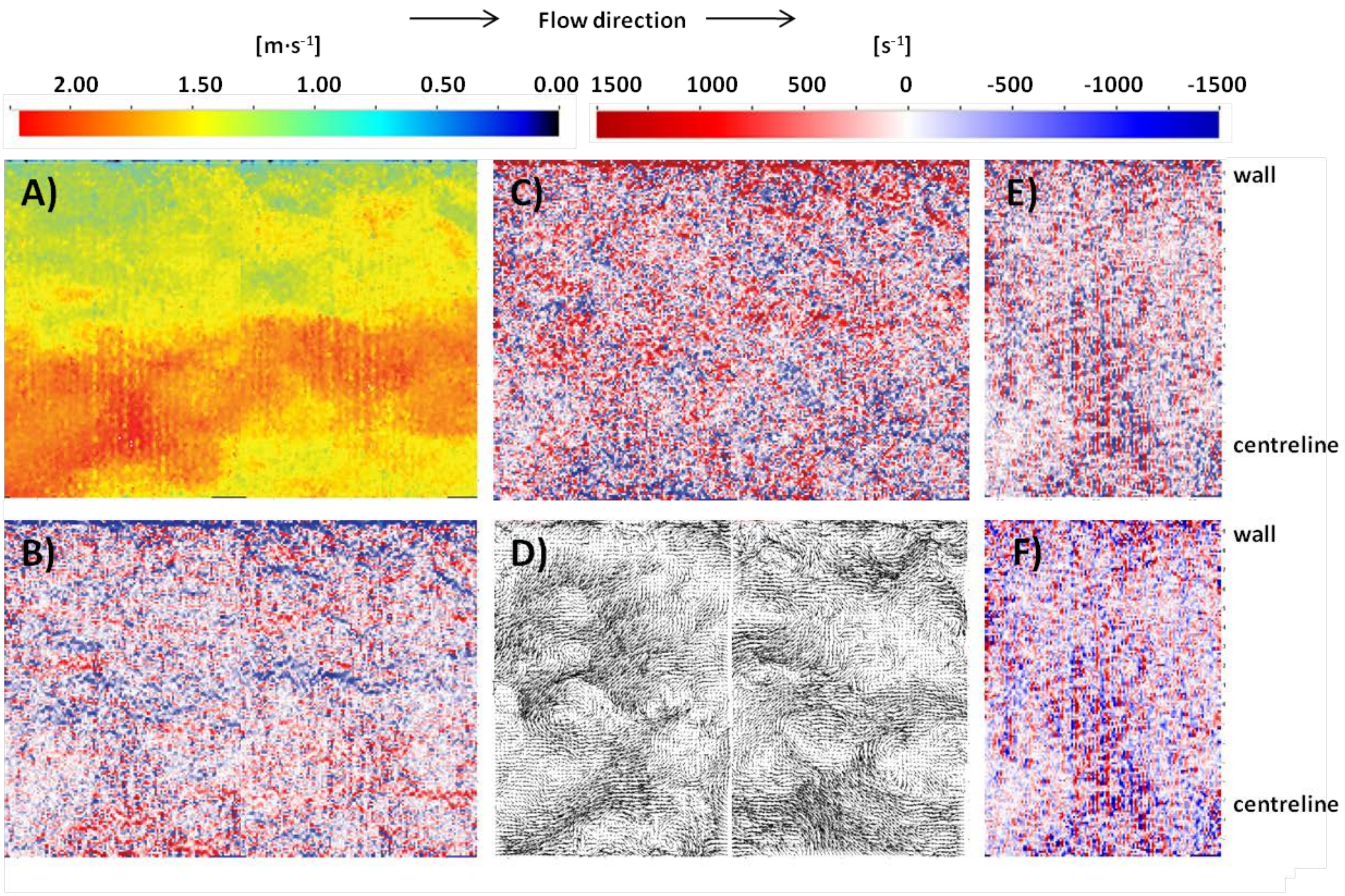

Figure 6.10: Instantaneous images of PEO8 5 wppm at $Re = 35,000$. A) instantaneous velocity $U$, B) instantaneous streamwise shear strain rate $\gamma_{xy}$, C) instantaneous 2D vorticity $\omega_z$, D) velocity fluctuations ($u^{'}$ and $v^{'}$), E) instantaneous spanwise shear strain rate $\gamma_{yx}$ and F) instantaneous streamwise compression strain rate $\gamma_{xx}$. The wall is located at the top of the images and the flow direction is from the left to the right.

solutions.

Another feature is visible when the vector fields of velocity fluctuations are compared. The magnitude of the spanwise fluctuations decreases with increasing polymer concentration. At the highest polymer concentrations the ejections, which are the intermittent outward vortices of the low speed fluid that take place in the boundary layer, of the liquid from the wall towards the outer velocity-defect region are almost completely suppressed. Also the small scale vortices are less common for the flows containing DR additives. On the other hand, an increase of the occurrence and the size of the continuous structures of the streamwise fluctuations in the vicinity of the wall can be observed with increasing polymer concentration. The continuous streamwise fluctuation structures seem to be caused by a region of low momentum fluid in the vicinity of the wall. The low momentum fluid does not contribute to the Reynolds stresses as much as the large scale velocity fluctuation structures observed for water. The reason is that the spanwise component of the velocity fluctuations is substantially lower for the low momentum fluid when compared to large scale velocity fluctuation structure. Therefore, the instantaneous images of velocity fluctuations reveal the mechanism by which the Reynolds stresses decrease and the streamwise fluctuations increase with increasing concentration of polymer additives. The decrease of Reynolds stress and increase of streamwise velocity fluctuations was previously reported [4, 87]. The low momentum fluid is separated from the outer velocity-defect region by the aforementioned layers of intense instantaneous streamwise shear strain rate and 2D vorticity. It should be noted that the layers of continuous values of instantaneous streamwise shear strain rate and 2D vorticity have not been previously reported in the literature, perhaps because: i) most of the turbulent flow characterisation was done using LDV which, although a very precise point measurement technique, cannot provide simultaneous spatially-resolved (planar) measurements as was done here with PIV. The instantaneous features of the turbulent flow would therefore remain undetectable. ii) Few investigations involved measurements with PIV. Most of the publications are for channel flow where the geometry and the flow structure is different from pipe flow [156, 98, 42]. No change of the instantaneous streamwise compression, and spanwise shear and compression strain rate can be detected for the instantaneous images that contain the low momentum flow layer.

The difference between the instantaneous velocities of the low momentum layer and the high-momentum core can be seen in Figure 6.16 where profiles of instantaneous velocity at three positions are shown for a) water, b) PEO8 50 wppm and c) PEO8 125 wppm at $Re = 35,000$. In the case of water the instantaneous velocity gradually increases from the wall towards the outer

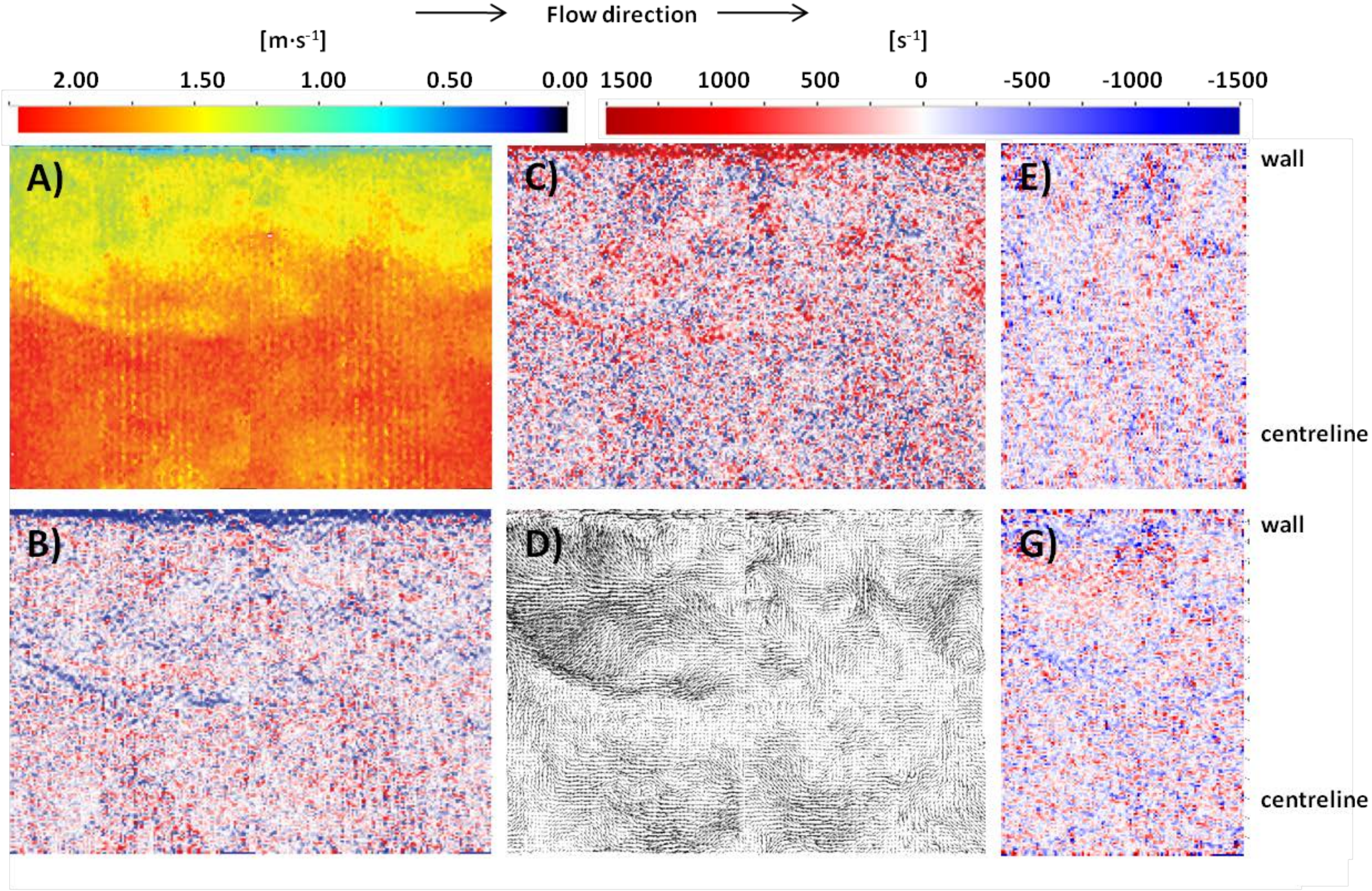

Figure 6.11: Instantaneous images of PEO8 25 wppm at $Re = 35,000$. A) instantaneous velocity $U$, B) instantaneous streamwise shear strain rate $\gamma_{xy}$, C) instantaneous 2D vorticity $\omega_z$, D) velocity fluctuations ($u^{'}$ and $v^{'}$), E) instantaneous spanwise shear strain rate $\gamma_{yx}$ and G) instantaneous spanwise compression strain rate $\gamma_{yy}$. The wall is located at the top of the images and the flow direction is from the left to the right.

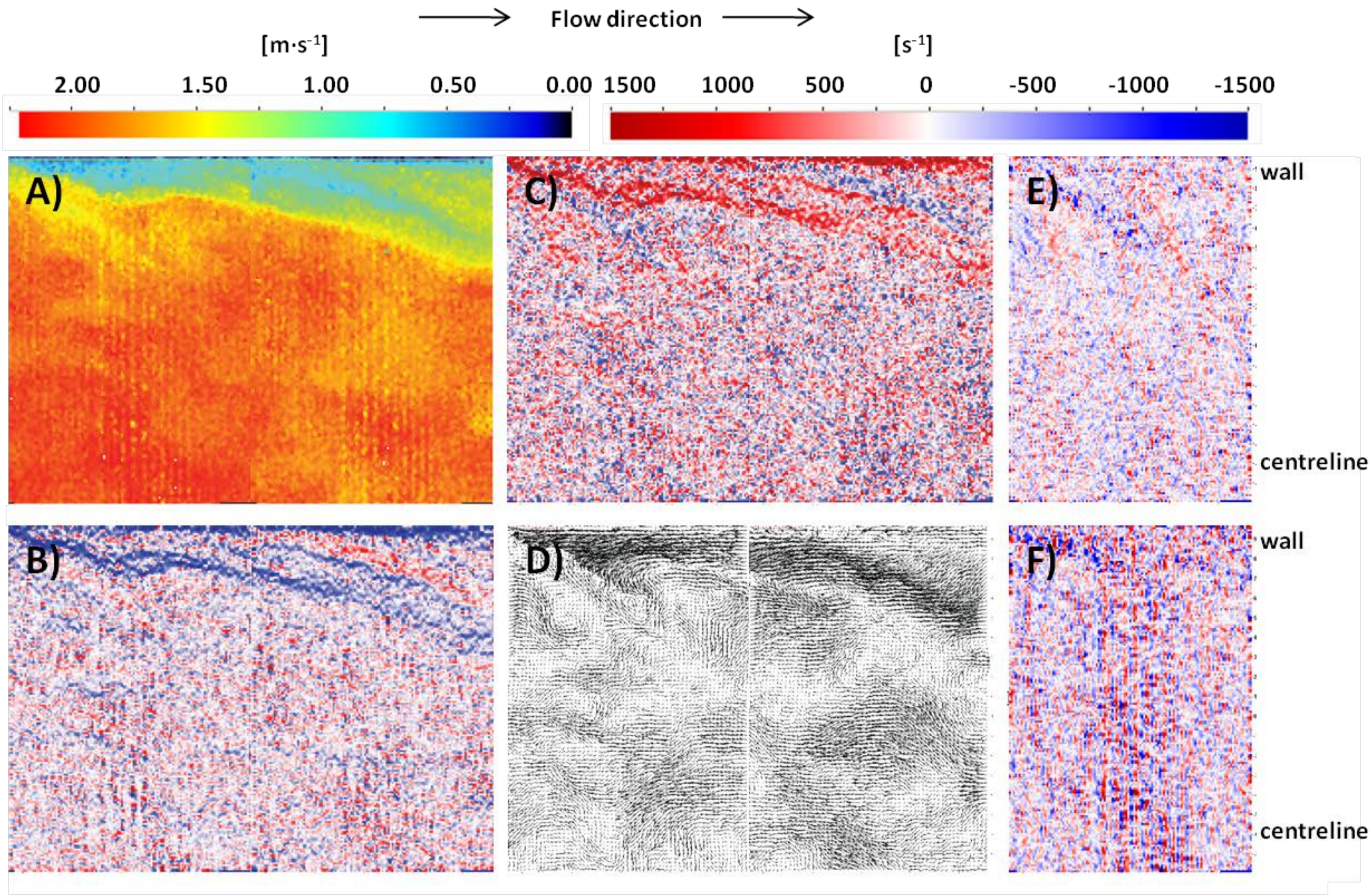

Figure 6.12: Instantaneous images of PEO8 50 wppm at $Re = 35,000$. A) instantaneous velocity $U$, B) instantaneous streamwise shear strain rate $\gamma_{xy}$, C) instantaneous 2D vorticity $\omega_z$, D) velocity fluctuations ($u^{'}$ and $v^{'}$), E) instantaneous spanwise shear strain rate $\gamma_{yx}$ and F) instantaneous streamwise compression strain rate $\gamma_{xx}$. The wall is located at the top of the images and the flow direction is from the left to the right.

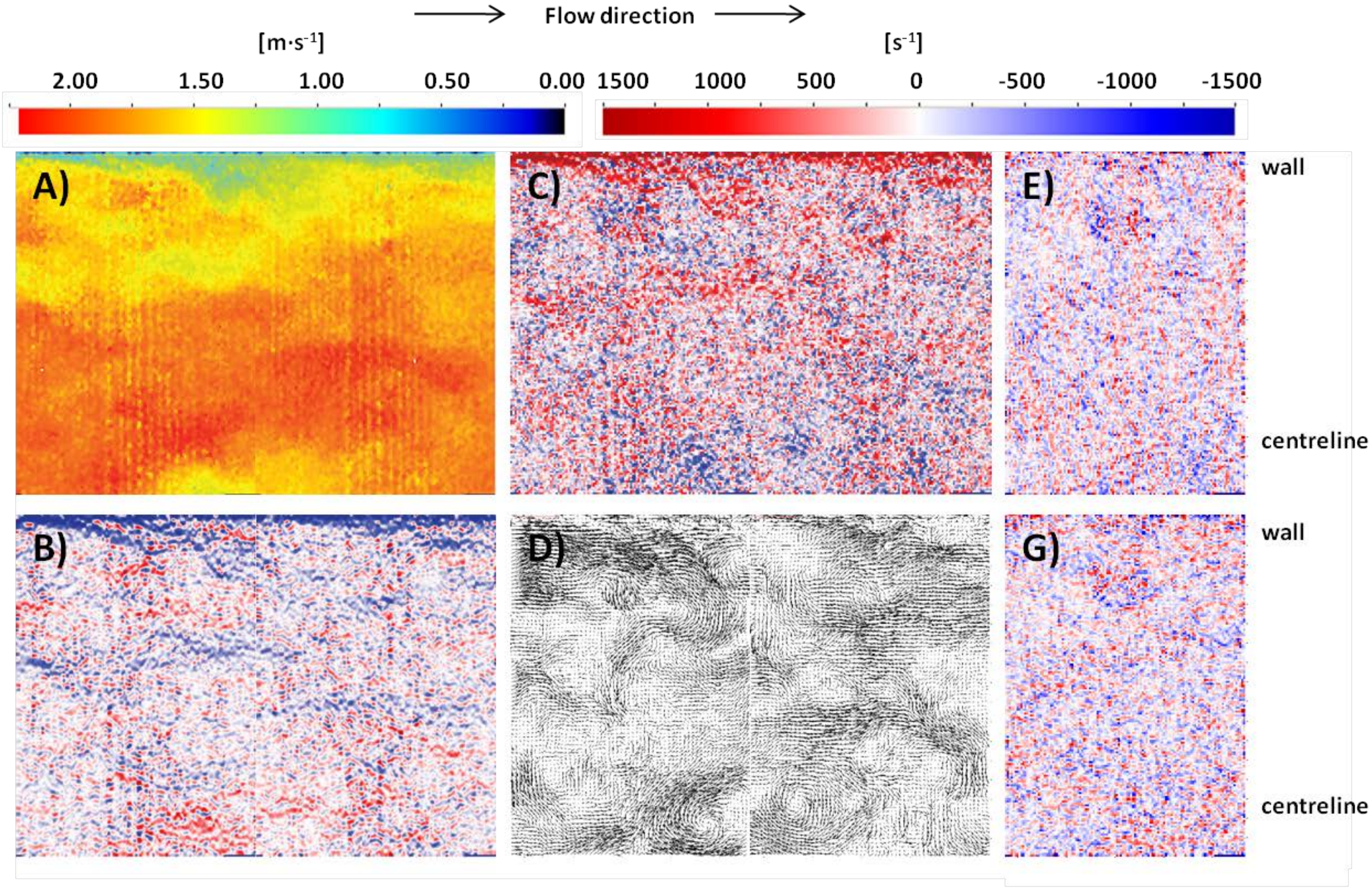

Figure 6.13: Instantaneous images of PEO8 75 wppm at $Re = 35,000$. A) instantaneous velocity $U$, B) instantaneous streamwise shear strain rate $\gamma_{xy}$, C) instantaneous 2D vorticity $\omega_z$, D) velocity fluctuations ($u^{'}$ and $v^{'}$), E) instantaneous spanwise shear strain rate $\gamma_{yx}$ and G) instantaneous spanwise compression strain rate $\gamma_{yy}$. The wall is located at the top of the images and the flow direction is from the left to the right.

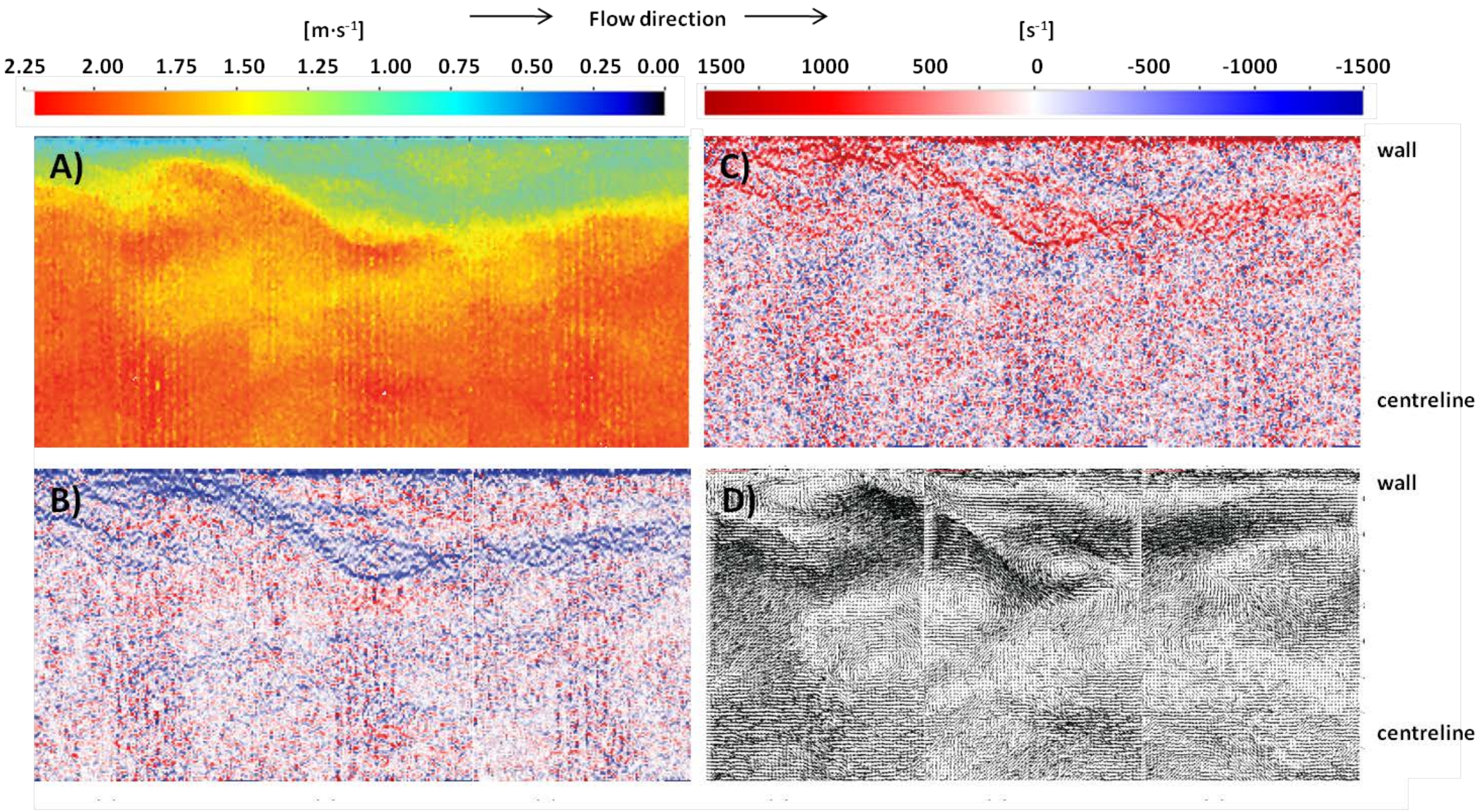

Figure 6.14: Instantaneous images of PEO8 125 wppm at $Re = 35,000$. A) instantaneous velocity $U$, B) instantaneous streamwise shear strain rate $\gamma_{xy}$, C) instantaneous 2D vorticity $\omega_z$ and D) velocity fluctuations ($u^{'}$ and $v^{'}$). The wall is located at the top of the images and the flow direction is from the left to the right.

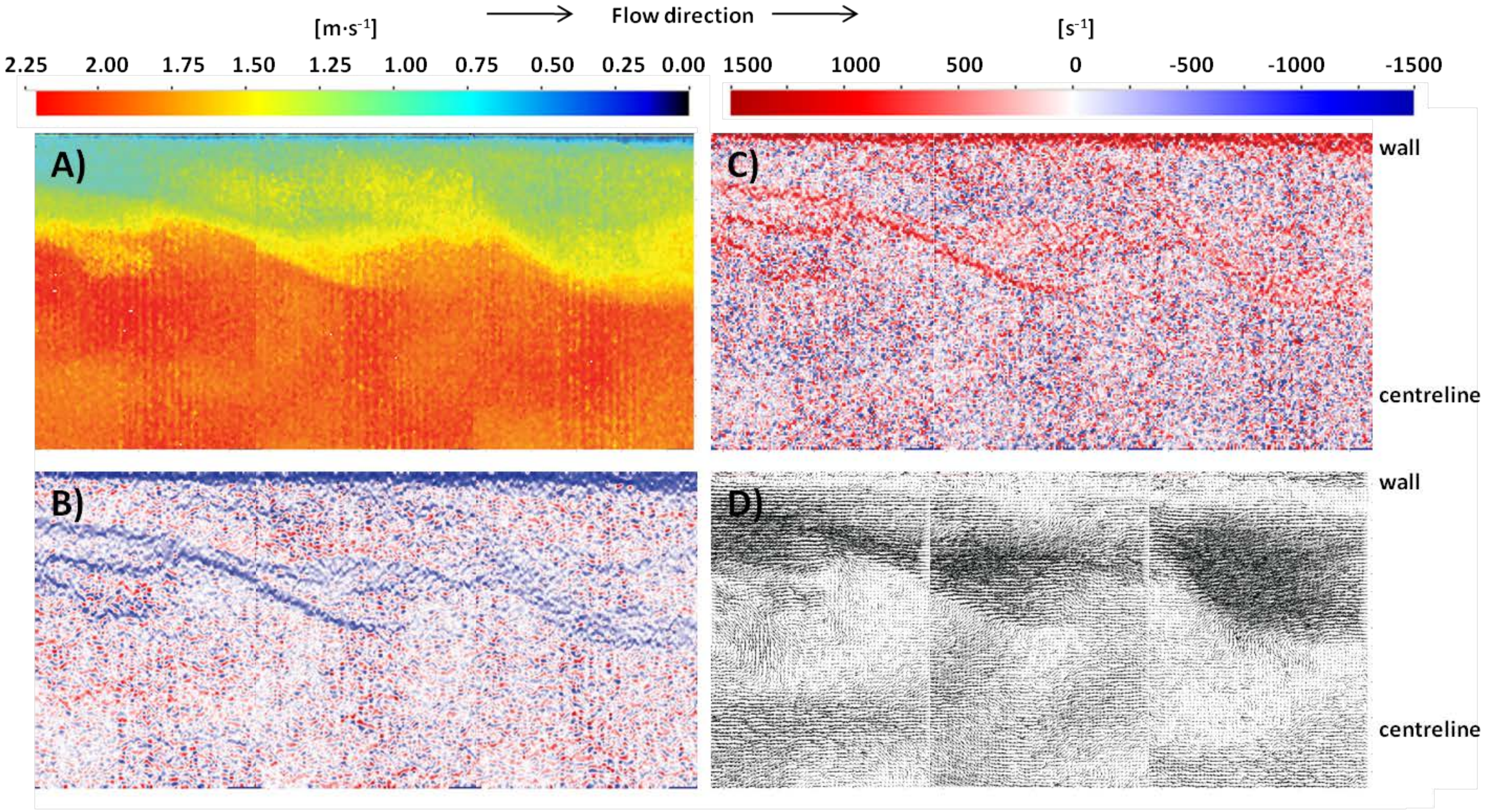

Figure 6.15: Instantaneous images of PEO8 250 wppm at $Re = 35,000$. A) instantaneous velocity $U$, B) instantaneous streamwise shear strain rate $\gamma_{xy}$, C) instantaneous 2D vorticity $\omega_z$ and D) velocity fluctuations ($u^{'}$ and $v^{'}$). The wall is located at the top of the images and the flow direction is from the left to the right.

velocity-defect region. However, a discontinuity in the instantaneous velocity profiles is observed when the polymer is introduced into the solution and the low momentum layer appears. The difference in the instantaneous velocities between the outer velocity-defect region and the low momentum layer for PEO8 125 wppm (see Figure 6.16) is $\sim 0.75\,\mathrm{m}\cdot\mathrm{s}^{-1}$over less than 1 mm. Nevertheless, the main indication of the presence of different layers in the turbulent flow with polymer additives are the coherent layers in the maps of instantaneous streamwise shear strain rate and 2D vorticity. The position of the coherent layers in the maps of instantaneous streamwise shear strain rate was used to measure the layer thickness for all studied flows. A Matlab algorithm written by the author was used to filter the salt and pepper noise and to detect the layer position (see Figure 6.17). The coherent layer position was defined as the most distant location of the the coherent layer in the maps of instantaneous streamwise shear strain rate from the wall. It should be noted that during the calculation the difference between the coherent layer and the viscous sublayer was neglected and, therefore, the Newtonian solvent has a positive value of the coherent layer position. The statistical values were obtained from $\sim$550 images and 105 layer positions were measured per image.

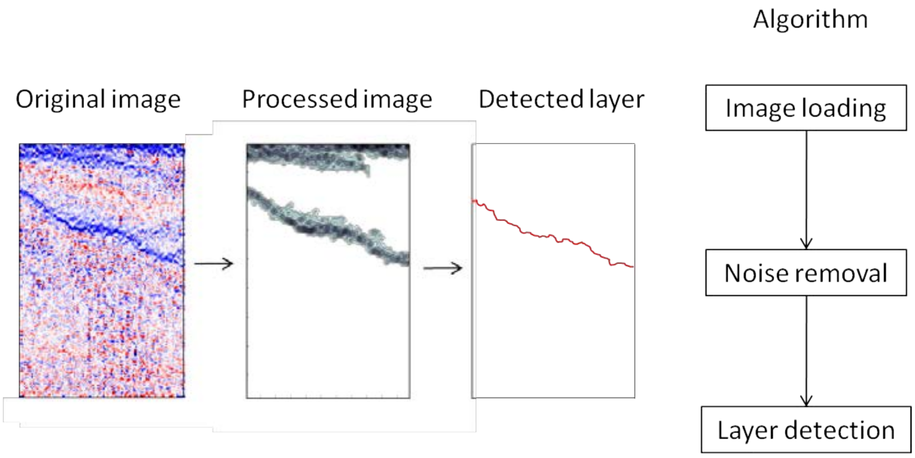

Figure 6.17: Description of the algorithm used for the layer detection.

Figures 6.18, 6.19 and 6.20 show the average position of the layer as a function of polymer concentration as well as probability functions of the layer position at different *Re* for PEO2, PEO4 and PEO8, respectively. Zero polymer concentration refers to the pure solvent - water. For each of these polymers the average distance of the coherent layer from the wall increases with increasing polymer concentration and decreases with increasing *Re*. Additionally, the coherent layer thickness increases with increasing polymer molecular weight for

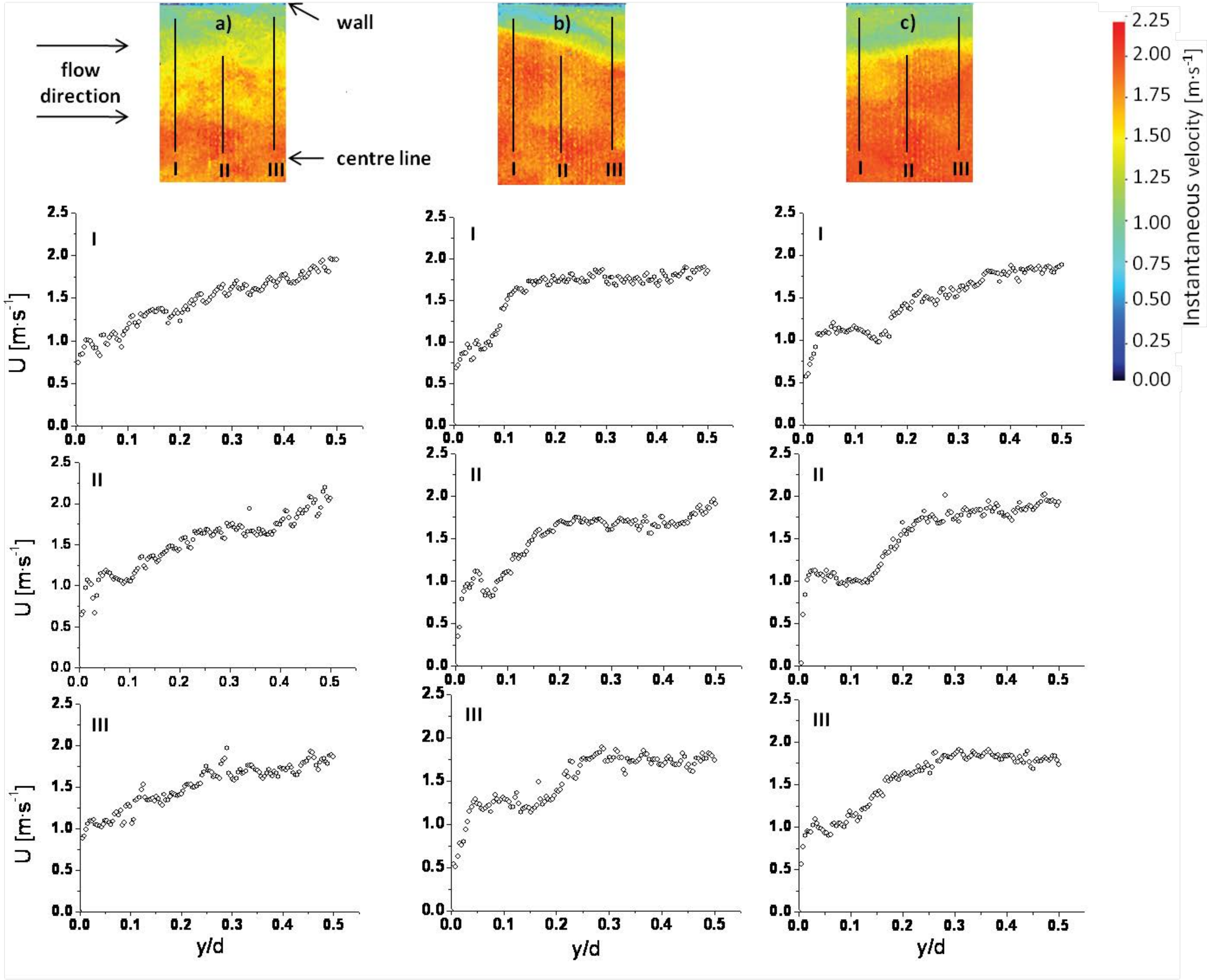

Figure 6.16: Instantaneous velocity profiles at 3 different positions of instantaneous velocity images for a) water, b) PEO8 50 wppm and c) PEO8 125 wppm at $Re = 35,000$.

a given polymer concentration and $Re$. The dependence of the coherent layer position on polymer concentration is very similar to the $DR$ dependence on polymer concentration (see Figure 6.5). The similarity suggests that the layer is perhaps linked to the DR phenomenon.

The probability functions of the coherent layer position (see Figures 6.18, 6.19 and 6.20) show that the position of the coherent layer is shifted towards the wall with increasing $Re$. The coherent layer appear in the vicinity of the wall for water and polymer solutions with low concentrations ($c < 25\,\text{wppm}$). It should be reminded that the viscous sublayer is also present in the inner near-wall region. With increasing polymer concentration and polymer molecular weight the probability of the appearance of the coherent layer is shifted towards the outer velocity-defect region. In the case of the highest concentration of PEO8 at low $Re$ the coherent layer cannot be found in the inner near-wall region.

The evolution of the average distance of the coherent layer from the wall for PEO2, PEO4 and PEO8 at $Re = 210,000$ with the number of passes of a polymer solution through the test section is shown in Figure 6.21. Similar to the previous comparison the dependence of the layer position on the number of runs is very similar to the dependence of $DR$ on the number of runs (see Figure 6.7).

### 6.2.2 A New Drag Reduction Mechanism

The presence of a region with a discontinuity in the instantaneous velocities which is associated with high values of instantaneous 2D vorticity and low values of instantaneous streamwise shear strain rate is a significant proof for the existence of two different flow layers. The question is what is the physical nature of the layer. The very low polymer concentrations employed in drag reducing solutions led scientists to explain DR based on the behaviour of individual polymer molecules [107, 105]. Classical DR theories always deal with i) the transfer of polymer molecules to the inner near-wall region with high fluctuating strains, ii) the elongation of polymer molecules in the inner near-wall region and iii) the relaxation of polymer molecules to random coil conformations in the more quiescent outer velocity-defect region (see Figure 6.22). Classical theories fail to explain the observed coherent layer.

Therefore, “a polymer layer mechanism” of DR is proposed here, which is based on the presence of physically entangled polymer molecules (see Figure 6.22). The new mechanism could not be proposed without the earlier DR theories. As was stated above (see Figure 5.7) an elongated polymer molecule has significantly lower polymer overlap concentration $c^*$ when compared with a polymer molecule in a random coil conformation. When polymer molecule

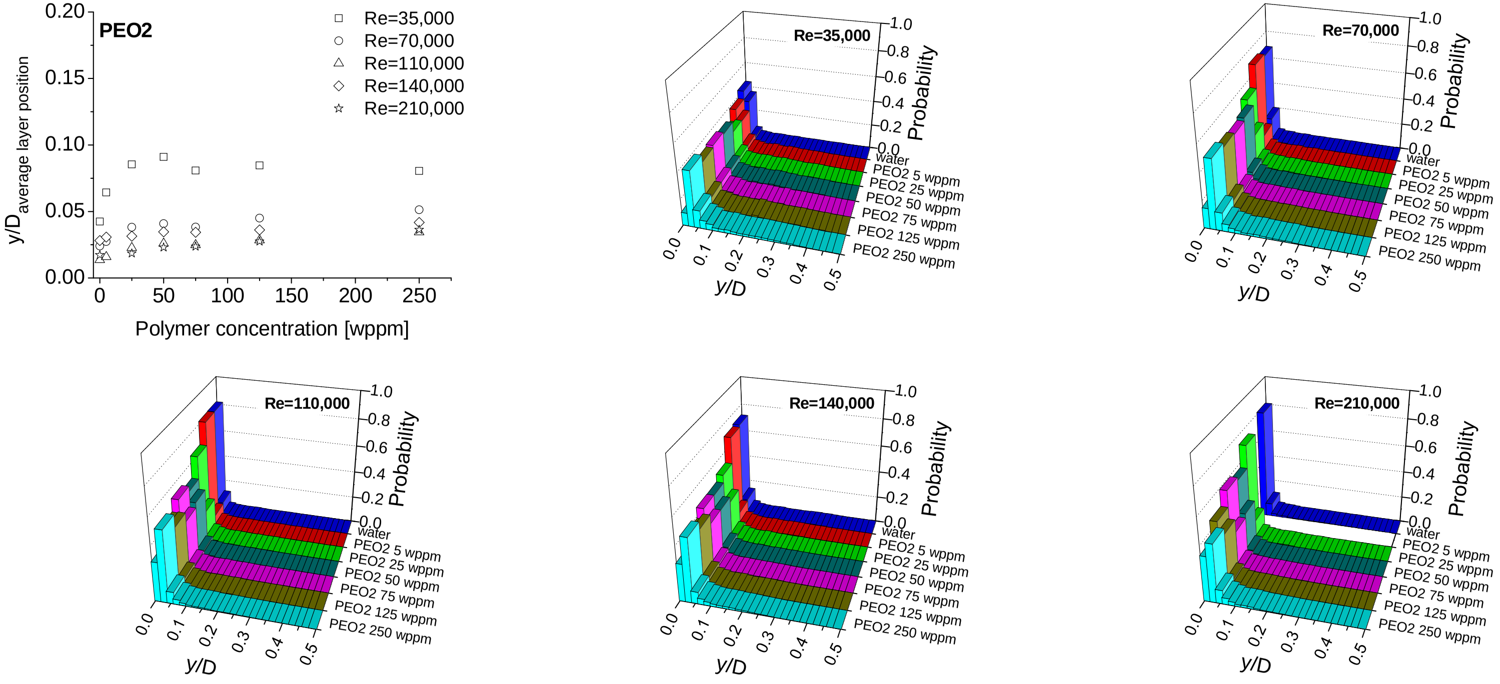

Figure 6.18: The dependence of the average layer distance from the wall on the polymer concentration for PEO2. The histograms show the probability of the occurrence of the layer position.

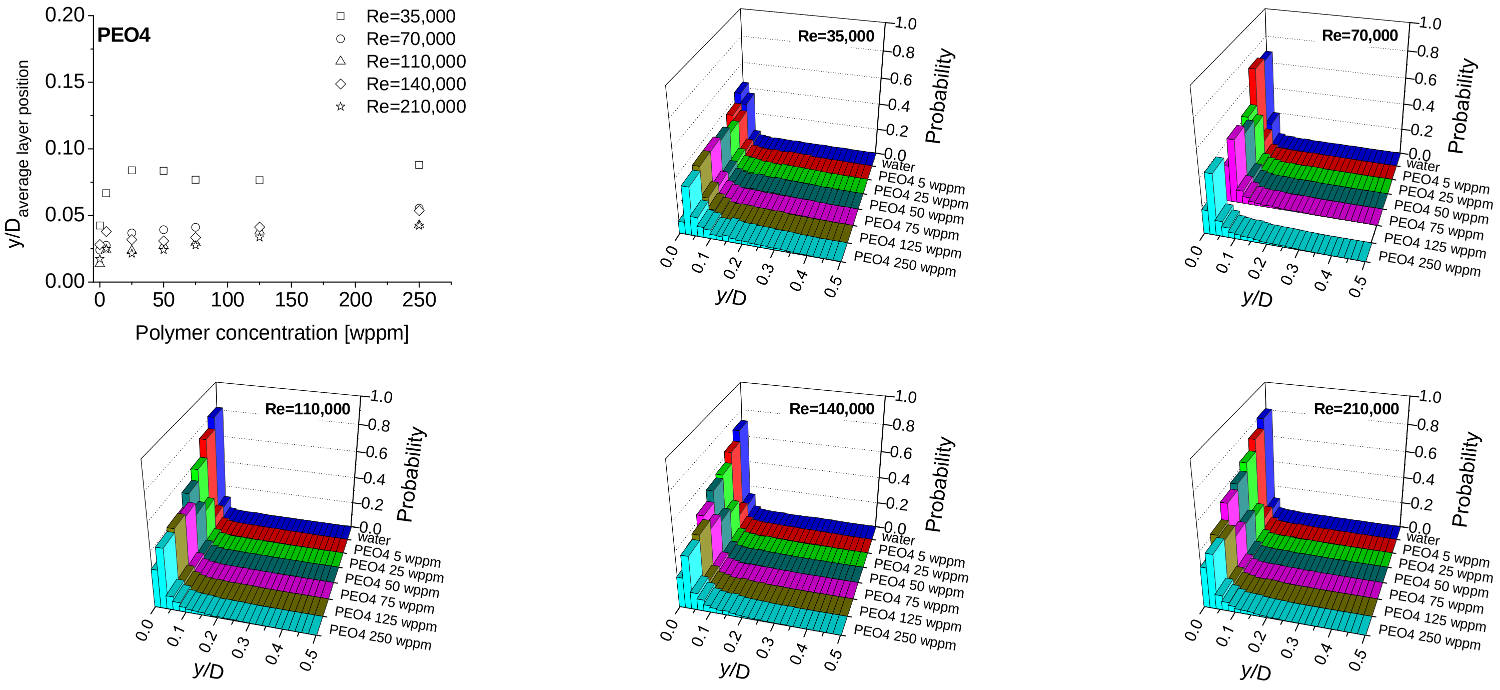

Figure 6.19: The dependence of the average layer distance from the wall on the polymer concentration for PEO4. The histograms show the probability of the occurrence of the layer position.

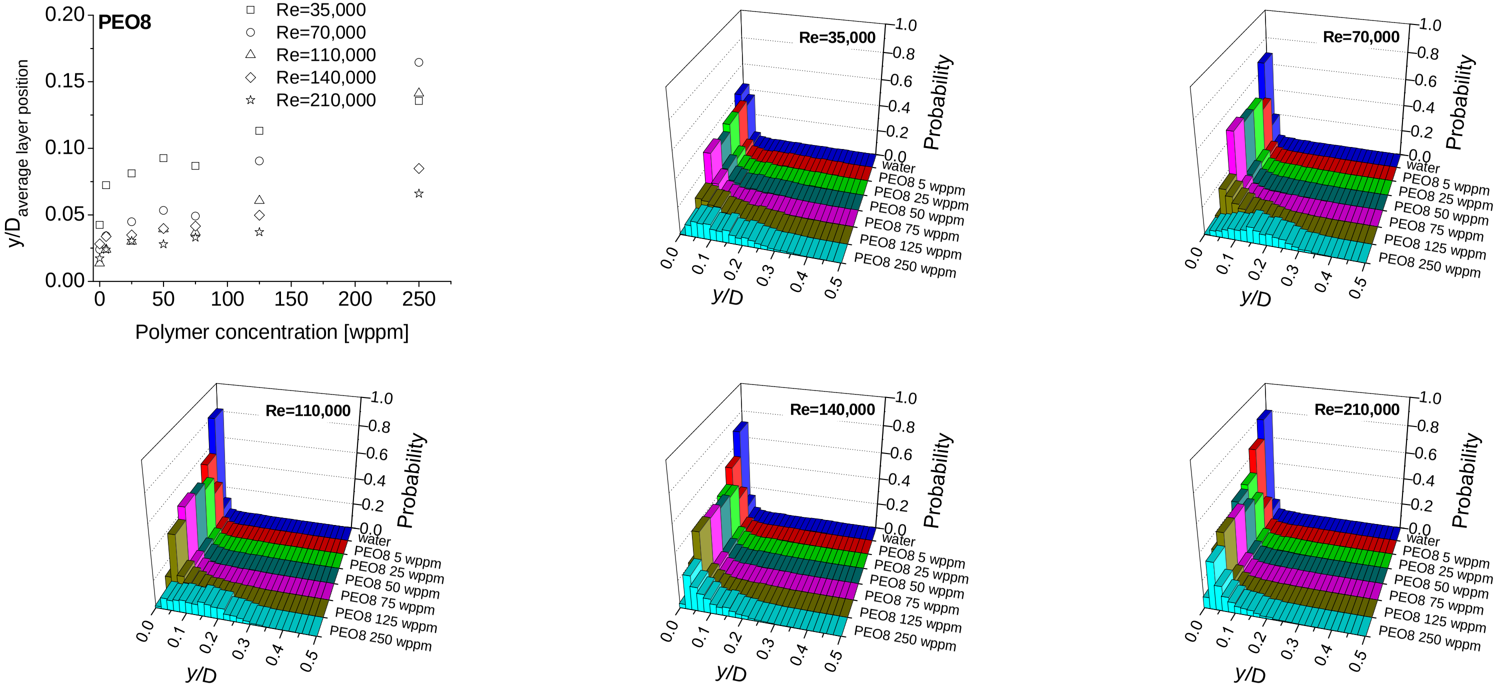

Figure 6.20: The dependence of the average layer distance from the wall on the polymer concentration for PEO8. The histograms show the probability of the occurrence of the layer position.

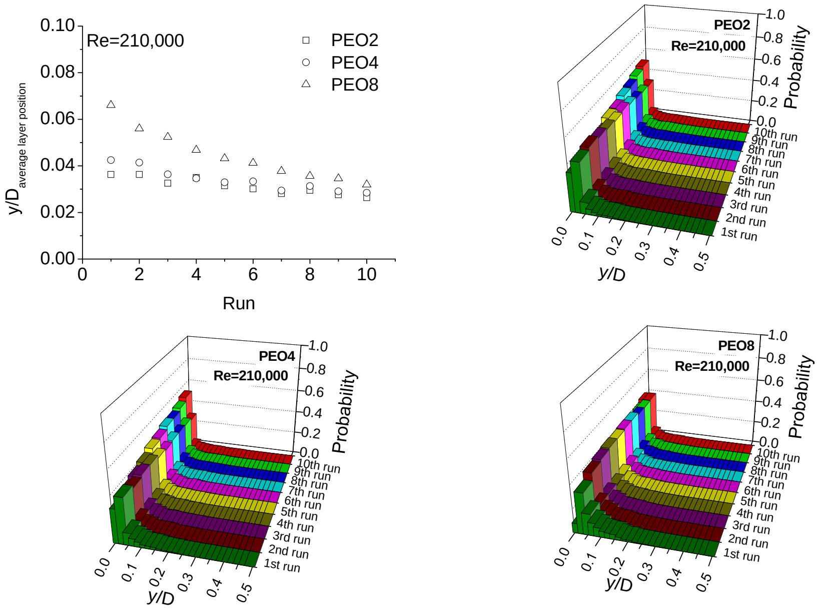

Figure 6.21: The dependence of the average layer distance from the wall on the polymer concentration for the degradation experiments. The histograms show the probability of the occurrence of the layer position.

elongation takes place in the inner near-wall region the local polymer dilution character also changes and the possibility of a collision of two or more polymer molecules significantly increases. Additionally, the presence of the wall decreases the freedom of movement of polymer molecules that can stay in the inner near-wall region or migrate to the outer velocity-defect region. It is, therefore, possible that polymer molecules could be captured in strong strain and vorticity fields. The described factors increase the possibility of collision of polymer molecules. The result of the collisions of elongated polymer molecules could be a formation of a 3D entangled polymer structure. A polymer network structure was observed for PEO solutions that were subjected to elongation flow in cross slot cell [157]. Such a network would not be stationary, but would be affected by the outer velocity-defect region environment. In Figure 6.22 a hypothetical example of the development of such a structure is shown, which would consist of the following steps: I. turbulent flow fluctuations in the far-wall region cause, II. pressing the polymer network structure which III. bounces to the outer velocity-defect region and IV. leaves exposed wall that can play a role in maintaining the turbulent nature of the turbulent flow.

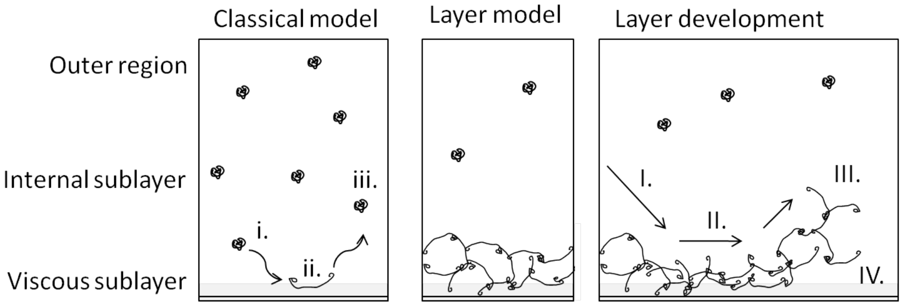

Figure 6.22: Polymer layer mechanism of drag reduction.

Such a layer mechanism would have following implications:

- $DR$ increases with increasing polymer concentration up to a limit $c_{\text{opt}}$. The limiting polymer concentration, after which the level of $DR$ does not increase, is governed by the inaccessibility of the inner near-wall region to polymer molecules in the random coil conformation. It should be reminded that the polymer elongation takes place in the inner near-wall region. The restricted accessability of the inner near-wall region is caused by the the presence of 3D polymer structures. A limiting concentration $c_{\text{opt}}$ was observed [49, 12, 158].

- The level of $DR$ decreases with increasing pipe diameter. An increased pipe diameter leads to an increase of the near wall area volume which decreases the possibility of a collision of two or more elongated polymer molecules for a given polymer concentration. Gasljevic et al. [120, 125] compared the level of $DR$ for a number of different pipe diameters at a constant $Re$. They found that $DR$ decreases with increasing pipe diameter at constant $Re$ and polymer concentration. Additionally, the optimum polymer concentration $c_{\text{opt}}$ should increase with increasing pipe diameter.

- Increasing the molecular weight of the selected polymer leads to an increase in $DR$ for a given polymer concentration. Polymer molecular weight is directly linked to the length of a polymer molecule for a given polymer type. With increasing polymer molecular weight the length of an elongated polymer molecule also increases and therefore a collision of two or more polymer molecules is more probable. The relationship between $M_w$ and $DR$ is well known [159, 12].

- Increased polymer concentration in the inner near-wall region when compared with the outer velocity-defect region. The mathematical models simulating DR are not able to produce experimentally observed levels of

$DR$ for a homogeneously distributed polymers in a solvent. However, the resulting $DR$ was reaching the expected values when it was assumed that a higher polymer concentration is present in the area of strongest turbulent activity, e.g. in the inner near-wall region [160]. A simple experiment performed by Hoyer et al. [161] demonstrated the existence of an inhomogeneous polymer concentration distribution in a diffusing turbulent vortical flow. The authors utilised a bottle-like diffuser with radial intake and analysed the polymer concentration of samples taken from the core of the vortex and from the outflow of the bottle chamber at the vortex periphery. They used homogeneously dissolved polymer solutions and found a much larger polymer concentration in the region associated with high turbulence activity.

- The existence of a coherent layer in the vicinity of the wall. Instantaneous images shown in this section prove the presence of a layer.

The definition of a scientific theory as described by Karl Popper [162] is that a theory must be falsifiable or have testable predictions. The predictions as well as measurement techniques to test them are as follows:

- The inner near-wall region should show an increase in viscosity. Polymer molecules usually show shear thinning behaviour. However, such a behaviour is observed in simple shear flows. The opposite trend, shear thickening, should be observed, according to the author, in a flow with fluctuating strain rates.
    - The PIV experiments are able to measure the streamwise strain rate. Additionally, a measurement of the streamwise stress is necessary to calculate the local viscosity, which can be done by using a shear stress probe.
- Heterogeneous polymer distribution in a pipe. Higher polymer concentration in the inner near-wall region should be detected when compared to the outer velocity-defect region, even if the experiment starts with homogeneously distributed polymer molecules in a solvent.
    - Smith et al. [3] used laser induced fluorescence utilising fluorescein dye as a tracer to measure polymer concentration in the inner near-wall region for heterogeneous DR. Clever design of the visualisation cell allowed them to detect polymer concentrations $c \sim 0.5\,\text{wppm}$ in the inner near-wall region, $y^+ = 50$. Similar measurements for homogeneous polymer DR should unequivocally prove or disprove the polymer layer mechanism.

- Birefringence in the inner near-wall region. Birefringence which is a measure of the anisotropy in the real component of the refractive index tensor provides information about the orientation, alignment and deformation of polymer molecules. The polymer layer in the inner near-wall region should show different values of birefringence than in the outer velocity-defect region.
    - The use of birefringence experimental technique to study the the dynamic behaviour of diluted polymer solutions is well known [163, 164, 155]. However, the use was limited to cross-jet channels and transient flows with rather high polymer concentration [163, 155] or to heterogeneous DR [164]. Obviously the limiting factor for the use of birefringence technique to verify the polymer layer theory might be in highly diluted character of polymer layers.

### 6.2.3 Implications of the Polymer Layer Mechanism for Polymer Design

Based on the polymer layer mechanism of DR, the author would like to propose novel polymer structures that should have higher drag reducing efficiency when compared with the well known polymeric drag reducers. The idea is based on the unraveling DR mechanism as well as on the author's polymer layer mechanism. Classical theories expect that polymers are unraveled in fluctuating shear fields next to the wall. Additionally, Sher et al. [109] predicts that polymer molecules can be unraveled by centrifugal forces. However, this statement is questionable when polymers, such as PEO, are taken in account because of the homogeneous weight distribution along the polymer. Fluctuating strain rate and 2D vorticity fields were indeed observed in the inner near-wall region (see Section 6.2.7). The novel polymers would be equipped with heavy anchors at each end to allow the polymer to unravel in all types of fluctuating fields. The anchor should have following properties: i) heavy enough to be able to unravel a polymer molecule in fluctuating vorticity fields, but not too heavy as to break the backbone chain, ii) higher affinity to the solvent then to the polymer backbone so the anchors are sticking outside the random coil. The main objective of the anchors would be to increase the possibility of collision and subsequent capturing of another polymer molecule. The overall effect should be, according to the author, a more stable polymer layer at lower polymer concentrations.

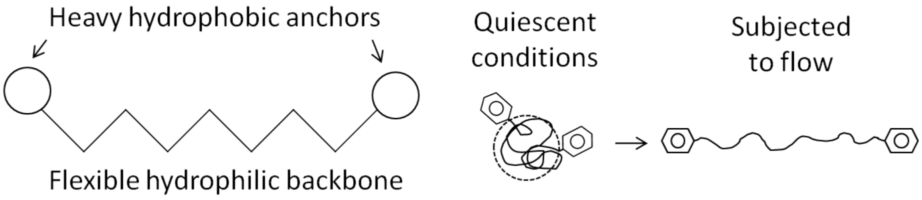

Figure 6.23: Proposed polymer structure with increased drag reduction efficiency.

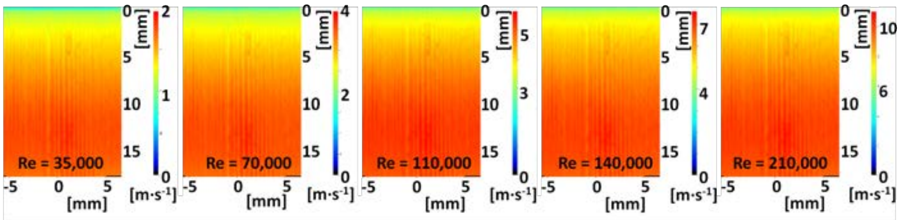

Figure 6.24: Images of mean velocity for water at $Re = 30,000$; $70,000$, $110,000$, $140,000$ and $210,000$.

### 6.2.4 Time Averaged Velocity Field

The time-averaged images for the mean velocity and for the root mean squares (rms) of the velocity fluctuations are shown in Figures 6.24 and 6.25, respectively. The time-averaged images were obtained from $500 - 600$ instantaneous images. The mean velocity images exhibit the expected features; the velocity continuously increases from the wall towards the outer velocity-defect region for all investigated cases and conditions ($Re$ and polymer concentrations). Similarly the rms of the velocity fluctuations continuously decrease from the wall towards the centreline for all $Re$. The only visible artifacts are the spanwise grooves which are most possibly caused by small size defects in the visualisation cell. Similar images, however with different groove structures, were obtained for the visualisation cell used for the zoomed experiments. The main feature is that the images do not contain any time dependent velocity or rms velocity fluctuation structures and, therefore, the results can be used for calculation of flow profiles described in Sections 6.2.5, 6.2.6, 6.2.7 and 6.2.8.

### 6.2.5 Statistics of the Mean Velocity and the Streamwise and Spanwise Velocity Components

Figure 6.26 shows the mean streamwise velocity profiles $\overline{u}$ for water, PEO2, PEO4 and PEO8 at different $Re$. The mean streamwise velocity profiles were

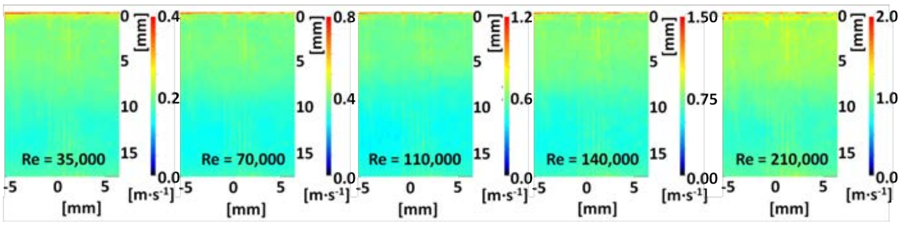

Figure 6.25: Images of rms velocity fluctuations $u'_{\mathrm{rms}}$ and $v'_{\mathrm{rms}}$ for water at $Re = 30,000$; $70,000$, $110,000$, $140,000$ and $210,000$.

obtained by time averaging of the $\sim 550$ instantaneous images and then spatial averaging the time mean images along the x-axis (streamwise direction). The mean velocity profiles $\overline{U}$ (not shown) follow exactly the same trends since the contribution of the mean spanwise velocity component to the mean velocity is negligible when compared to the mean streamwise velocity component. The $\overline{u}$ profiles have a typical logarithmic turbulent flow trend with the peak velocity at the centreline of the pipe $y/D = 0.5$. The highest concentration of PEO8, 125 and 250 wppm, significantly change the shape of the flow profile when compared with pure water or even other studied drag reducing solutions. The difference can be caused by the laminarisation of the flow at very high levels of $DR$.

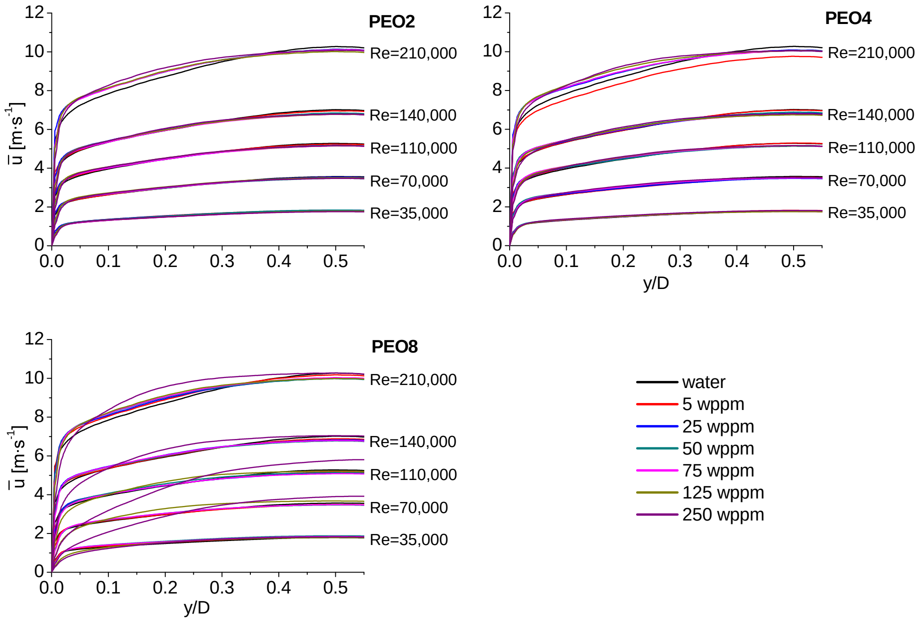

Figure 6.26: Mean streamwise velocity $\overline{u}$ as a function of normalised distance from the wall $y/D$ for PEO2, PEO4 and PEO8 solutions at various $Re$.

The correctness of the PIV measurements can be verified by comparing the bulk velocities $U_{\text{bulk}}$ measured by the magneto-inductive flowmeter with values calculated from the mean velocity profiles using following equation:

$$U_{\text{bulk}} = \frac{1}{\pi r^2} \int_0^r \overline{U}(y) 2\pi (r - y) dy \tag{6.3}$$

where $r$ is the pipe radius, $y$ is the distance from the wall and $\overline{U}$ is the mean velocity at $y$ distance from the wall. Additionally the wall shear stress $\tau_w$ obtained from the slope of the mean velocity profiles in the viscous sublayer, can be compared with the wall shear stress calculated from the pressure drop measurements (see Equation 2.9). The comparison of the bulk velocities is a measure of overall precision of the measurements and the comparison of the wall shear stress is a measure of the quality of the near-wall measurements. As can be seen in Table 6.1 the bulk velocities calculated from the PIV mean velocity profiles are very similar to the flowmeter readings with an average difference of -6.2%. The slightly under-estimated PIV values can have many different reasons such as: i) an error of the flow-meter, ii) slight deviation of the laser light sheet from the centreline plane or iii) the effect of gravity. However, the error is so small that the PIV measurements can be considered to be correct. The wall shear stress values are comparable for small velocities, with corresponding $Re = 35,000$ and $70,000$, however, the difference between the wall shear stress calculated from the mean velocity profiles and the pressure drop measurements becomes large for higher velocities. The reason is that the thickness of the viscous sublayer is a function of $Re$ and with increasing $Re$ the thickness of the viscous sublayer diminishes. The conclusion is that the near-wall measurements have to be taken with caution especially for high $Re$. A way of improving the quality of the near-wall measurements would be to use smaller seeding particles and a different visualisation cell design based on a true refractive index matching technique.

Table 6.1: Comparison between data measured by the flow facility (FF) and calculated from PIV measurements.

| half cross-section of the pipe | | | | | | zoomed near-wall | |
|---|---|---|---|---|---|---|---|
| $\overline{U}_{bulk\,FF}$ | $\overline{U}_{bulk\,PIV}$ | Difference | $\tau_{w\,FF}$ | $\tau_{w\,PIV}$ | Difference | $\tau_{w\,PIV}$ | Difference |
| $[\mathrm{m} \cdot \mathrm{s}^{-1}]$ | | [%] | [Pa] | | [%] | [Pa] | [%] |
| 1.5 | 1.4 | -6.7 | 6.2 | 6.4 | 3.2 | 5.8 | -6.5 |
| 3.0 | 2.8 | -6.7 | 21.5 | 16.6 | -22.8 | 20.9 | -2.8 |
| 4.5 | 4.2 | -6.7 | 45.8 | 27.9 | -39.1 | 30.1 | -34.3 |
| 6.0 | 5.6 | -6.7 | 79.7 | 39.5 | -50.4 | 39.3 | -50.7 |
| 8.9 | 8.5 | -4.7 | 152.3 | 60.6 | -60.2 | 66.6 | -56.3 |

The mean spanwise velocity profiles $\overline{v}$ are shown in Figure 6.27. The average spanwise velocity increases with increasing $Re$ and with increasing distance from the wall. No difference between water and water containing drag reducers can be observed. Also the effect of polymer concentration on the intensity and shape of the profiles seems to be negligible.

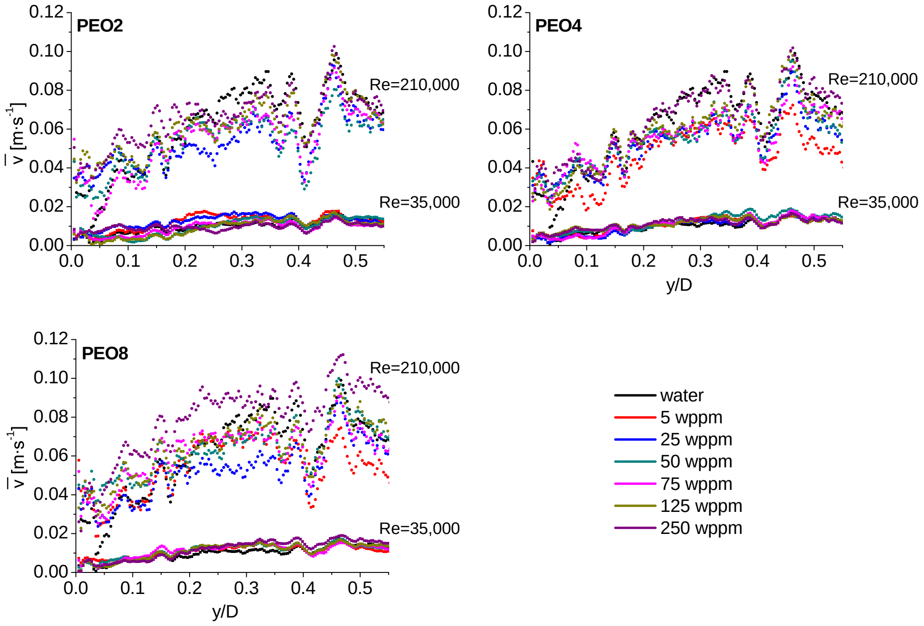

Figure 6.27: Mean spanwise velocity $\overline{v}$ as a function of normalised distance from the wall $y/D$ for PEO2, PEO4 and PEO8 solutions at $Re = 35,000$ and $210,000$.

The results of the mean velocity plotted in the classical semi-logarithmic coordinates of $U^+$ and $y^+$ for PEO2, PEO4 and PEO8 are shown in Figures 6.28, 6.29 and 6.30, respectively. The velocity and distance from the wall normalised by frictional velocity are defined in Equations 2.6 and 2.7. It should be noted that the centre of the pipe using $y^+$ variable varies with the frictional velocity, which is a function of $Re$ and the level of $DR$ and, therefore, it is not indicated to keep the graphs clear. The first feature to be noticed is that the data points in the viscous sublayer region do not exactly fall on the theoretical line given by Equation 2.10. The difference between the data points and the theoretical trend line increases with increasing $Re$. It is caused by the definition of the wall position which was determined by combination of visual inspection of the images and the extrapolation of the mean velocity profile to zero, which both have errors associated. The small error which is almost invisible for low $Re$ becomes large with increasing $Re$ due to the definition of $y^+$. Den Toonder [165] in order to overcome the problem in determining the wall position, fit the $U^+$ vs. $y^+$ measured data below $y^+ = 5$ to the theoretical equation of viscous sublayer. Close inspection of published literature reveals that either the data show considerable scatter in the inner near-wall region [96, 5, 166] or a correction of the near wall measurements to the viscous sublayer was made [4, 167]. Such a technique would be problematic for the presented data since the resolution the inner near-wall region is poor, especially at high $Re$. Also it should be noted that the wall shear stress data obtained from the deferential pressure measurements (see Table 6.1) were used for the calculation of frictional velocity.

The data points for water fall on the line which is expressed by the Newtonian law of the wall (see Equation 2.11). The good agreement between the measured and theoretical data is another proof of correctness of these measurements. The upward deviation that can be seen at high $y^+$ values is caused by the outer velocity-defect region where the Newtonian law of the wall is not valid. The polymer solutions follow the same trends as the Newtonian solvent in the region of the viscous sublayer, which is not surprising. All published data in the literature show that the viscous sublayer profile is not affected by polymer additives [4, 167, 123, 97]. The main deviation of polymer solutions from the Newtonian solvent occurs in so called buffer region, $5 < y^+ < 30$, which is thickened by the polymer additives and the onset of the Newtonian log-law is shifted to higher $y^+$ values and upwards to higher values of $U^+$. The polymer solution profiles can be well described by Equation 2.12 where $\Delta B$ is related to the upward shift. It could be tempting to link the $\Delta B$ parameter to the thickness of the polymeric layer which was identified in Section 6.2.1. However, no correlation between $\Delta B$ and the average position of the polymeric layer was found. The reason is that the absolute value of $\Delta B$ parameter increases increases with increasing $Re$ and $DR$ but the thickness of the polymeric layer decreases with increasing $Re$. The unusual behaviour of the highest polymer concentration of PEO8 was already mentioned few paragraphs above where the streamwise mean velocity profiles were described. The deviation also occurs for the $U^+$ dependence on $y^+$ especially for $Re \leq 110,000$. It might be possible that the highest concentrations of PEO8 are following the maximum DR profile but are shifted to higher $y^+$ values due to the error associated with the position of the wall. However, the gross flow measurements do not indicate that the maximum level of $DR$ was reached during the measurements.

### 6.2.6 Statistics of Velocity Fluctuations

The comparison between measured streamwise rms velocity fluctuations normalised with the friction velocity (Equation 2.8) as a function of wall normalised

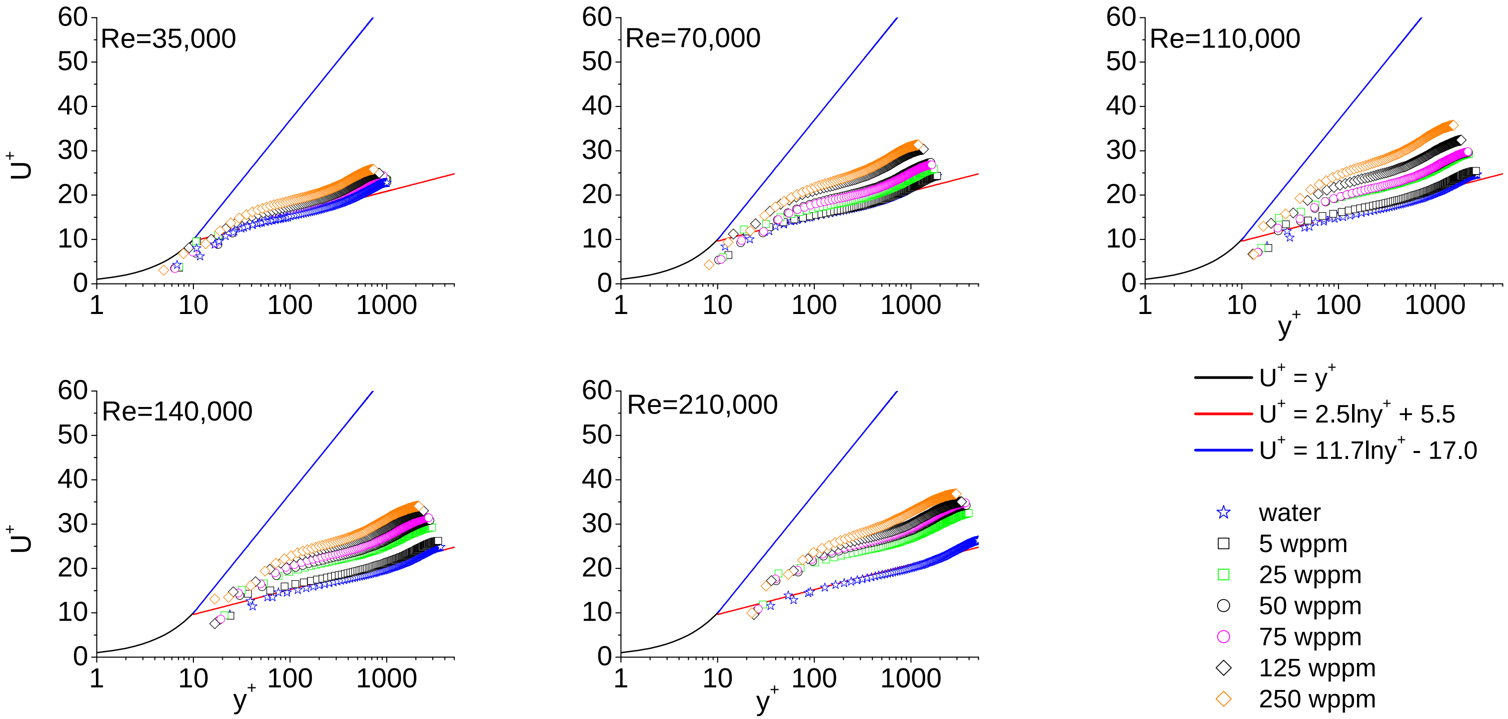

Figure 6.28: Dependency of normalised velocity $U^+$ on normalised distance from the wall $y^+$ for PEO2 solutions at various $Re$.

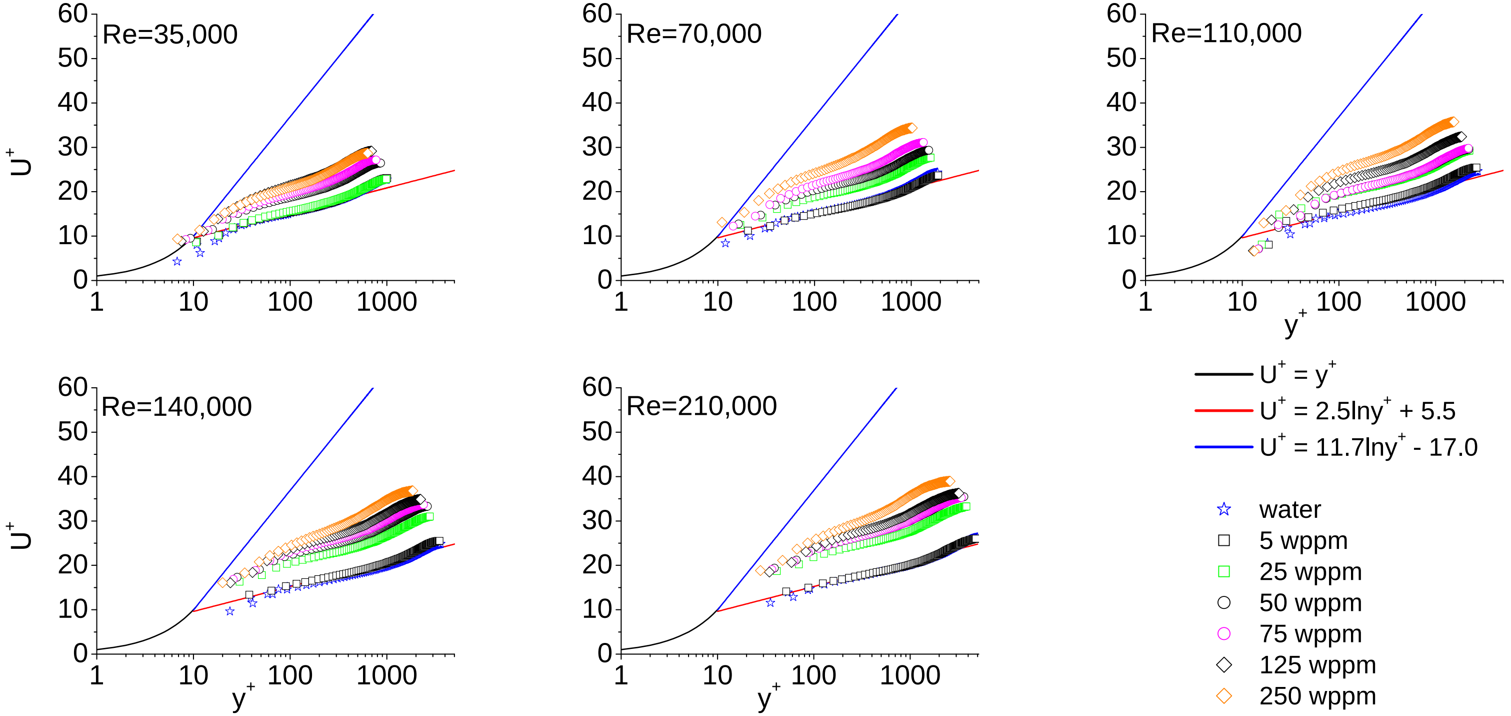

Figure 6.29: Dependency of normalised velocity $U^+$ on normalised distance from the wall $y^+$ for PEO4 solutions at various $Re$.

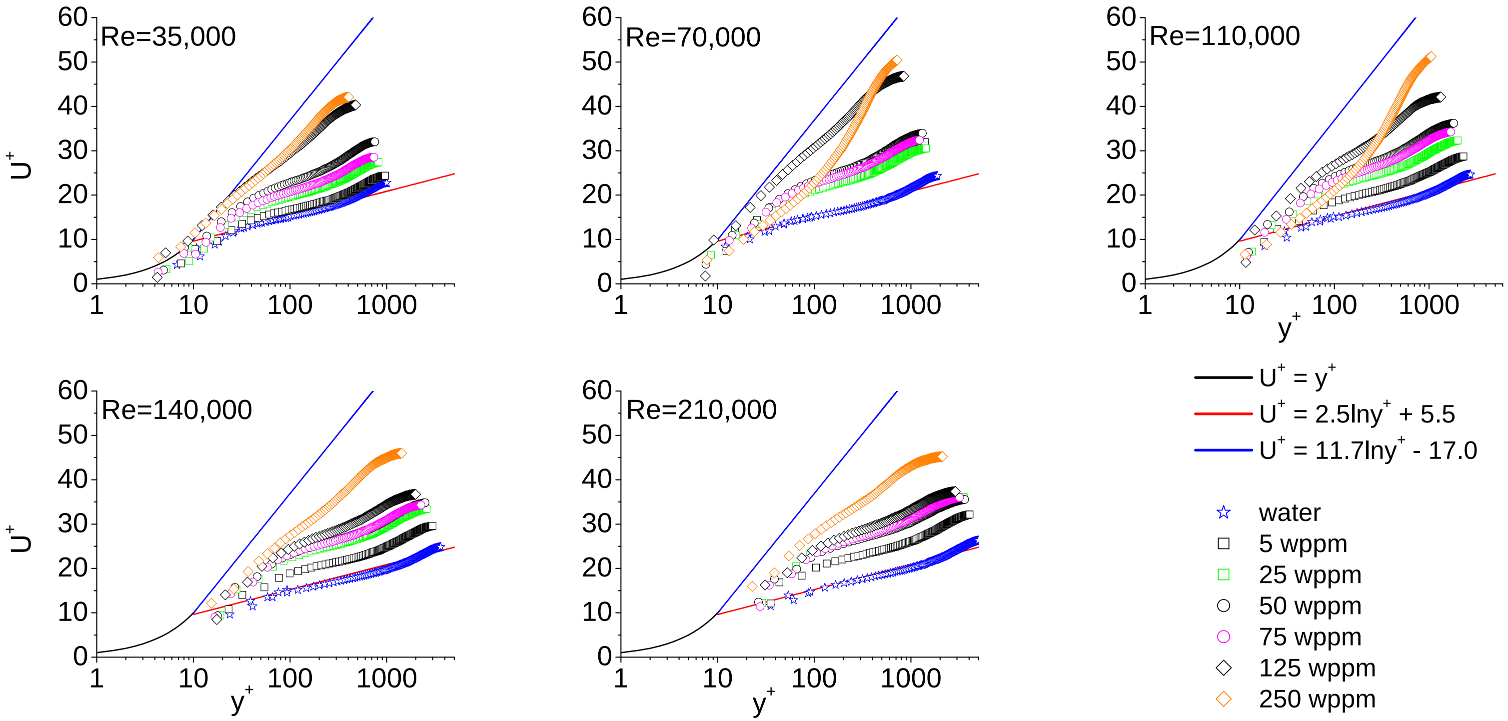

Figure 6.30: Dependency of normalised velocity $U^+$ on normalised distance from the wall $y^+$ for PEO8 solutions at various $Re$.

distance from the wall (Equation 2.7) for measured and published data is shown in Figure 6.31. The data obtained by den Toonder et al. [4] were measured using the LDV technique in a pipe with internal diameter $d = 40\,\text{mm}$. Den Toonder compared his results with DNS simulations for turbulent flow in a pipe performed by Eggels et al. [168] and found excellent agreement. The measurements of White et al. [5] were done in a channel with cross-sectional dimensions: $360 \times 130\,\text{mm}$. The data presented in this work show good agreement with the published data except for the closest point to the wall. Therefore, the first point will be neglected in the following results.

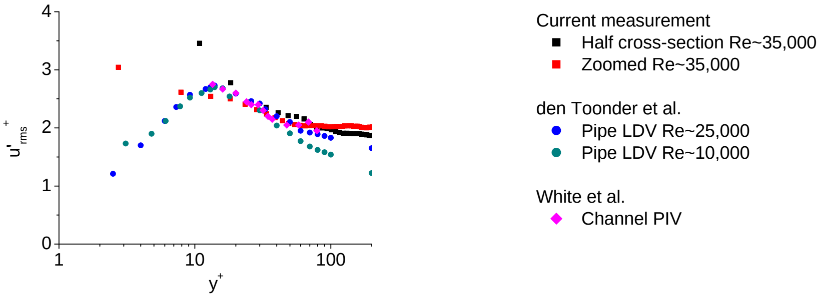

Figure 6.31: Comparison of measured normalised streamwise velocity fluctuations $u^{'+}_{\text{rms}} = f\left(y^{+}\right)$ with data published by den Toonder et al. [4] and White et al. [5].

The results of the streamwise rms velocity fluctuations $u^{'}_{\text{rm}s}$ (see Equation 3.31) for PEO4 and PEO8 are shown in Figures 6.32 and 6.33, respectively. The shape of the $u^{'}_{\text{rms}}$ fluctuation profiles for PEO2 is similar to PEO4 (see Appendix A Figures A.3, A.4 and A.5). The intensities of $u^{'}_{\text{rms}}$ increase with increasing $Re$. For a constant $Re$ the value of $u^{'}_{\text{rms}}$ profiles decreased over the entire pipe cross-section with a peak value in the inner near-wall region.

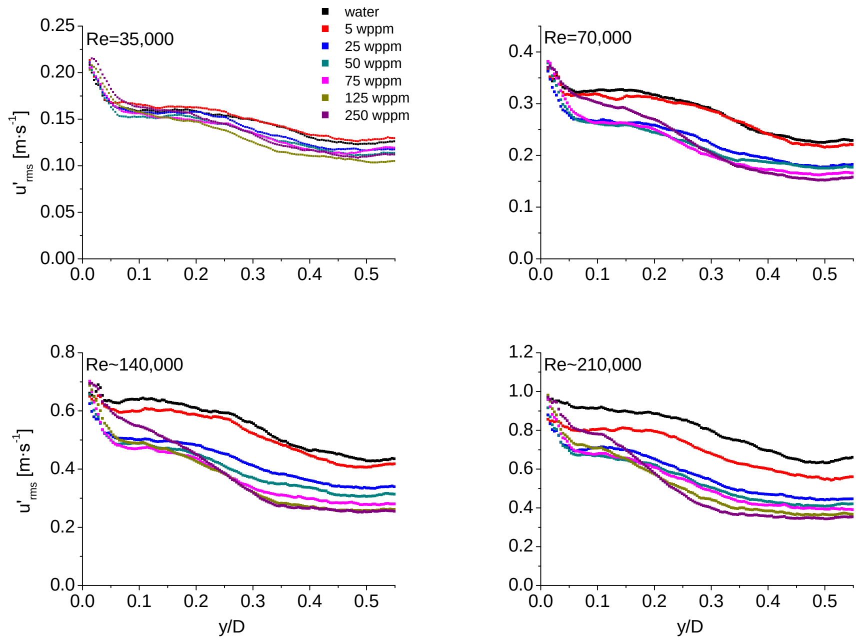

Figure 6.32: Dependence of rms streamwise velocity fluctuations ($u'_{rms}$) on the normalised distance from the wall for PEO4 solutions at various *Re*.

Due to the resolution in the inner near-wall region it is hard to say what the effect of polymer drag reducers is on the height and position of the peak. The influence of drag reducers on the shape of the $u'_{\mathrm{rms}}$ profiles is discussed in the next paragraph. A deviation from the observed trends can be seen for the two highest polymer concentrations of PEO8 especially at low *Re*. The near-wall peak of the two highest concentrations of PEO8 is shifted further away from the wall. A shift of the $u'_{\mathrm{rms}}$ peak values towards the outer velocity-defect region was also observed by Ptasinski et al. [87] who studied the turbulent flow profiles at maximum DR in pipe flow.

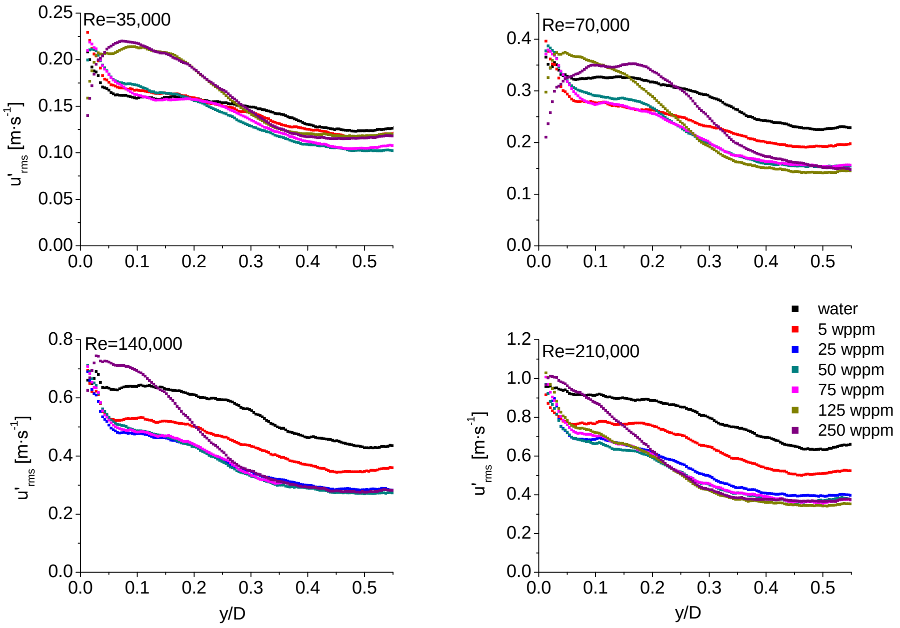

Figure 6.33: Dependence of rms streamwise velocity fluctuations $u'_{\mathrm{rms}}$ on the normalised distance from the wall for PEO8 solutions at various $Re$.

The dependence of the normalised rms streamwise velocity fluctuations at $y/D = 0.015$, 0.1 and 0.5 ($u'_{\mathrm{rms}\,0.015}$, $u'_{\mathrm{rms}\,0.1}$ and $u'_{\mathrm{rms}\,0.5}$) is shown in Figure 6.34. The rms streamwise fluctuations $u'_{\mathrm{rms}}$ was normalised with $u'_{\mathrm{rms}}$ of water at constant $Re$ for a given $y/D$.

$$u'_{\mathrm{rms}\,y/D\,N} = \frac{u'_{\mathrm{rms_i}\,y/D}}{u'_{\mathrm{rms_{water}}\,y/D}}_{Re=\mathrm{const.}} \tag{6.4}$$

The unity value represents the normalised streamwise velocity fluctuation for the pure Newtonian solvent (water) at $Re \sim 35,000 - 210,000$. The first to be noted is that the data became independent of $Re$. For $y/D = 0.015$ the effect of drag reducers on the normalised streamwise velocity fluctuations is negligible except for the highest levels of $DR$ where a decrease can be observed. This decrease is most possibly caused by the shift of the peak $u'_{\mathrm{rms}}$ value away from the wall. The shift of the $u'_{\mathrm{rms}}$ peak can be clearly seen for $y/D = 0.1$ profiles where $u'_{\mathrm{rms}\,0.1\,N}$ decreases down to a minimum situated at $DR \sim 50\%$. After the minimum the values of $u'_{\mathrm{rms}\,0.1\,N}$ sharply increase which signifies the shift of the $u'_{rms}$ peak value away from the wall. It is interesting that the shift of the $u'_{\mathrm{rms}}$ peak value demonstrates itself through the pipe cross-section. An increase of normalised streamwise velocity fluctuations for the highest levels of $DR$ can be seen even at the centre of the pipe $u'_{\mathrm{rms}\,0.5\,N}$. Additionally, the relative intensity of the streamwise velocity fluctuations is almost halved for high levels of $DR$ at the centre of the pipe.

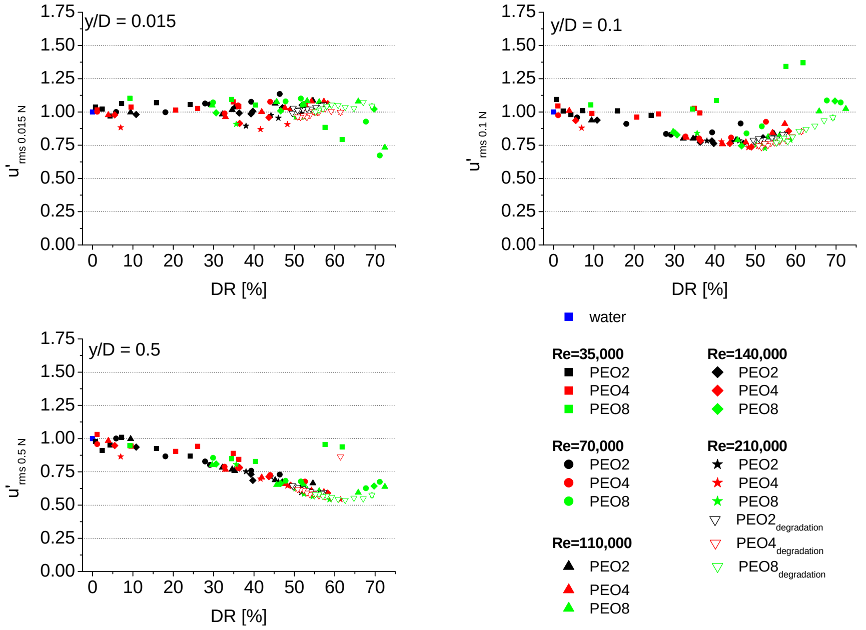

Figure 6.34: Dependence of normalised rms streamwise velocity fluctuations ($u^{'}_{\mathrm{rms}\,y/D\,N}$) on the level of drag reduction at $y/D = 0.015$; $0.1$; and $0.5$ ($u^{'}_{\mathrm{rms}\,0.015\,N}$; $u^{'}_{\mathrm{rms}\,0.1\,N}$ and $u^{'}_{\mathrm{rms}\,0.5\,N}$) .

The presented results indicate that the polymer drag reducing agents modify the streamwise velocity fluctuations over the whole radius of a pipe and that the relative alteration of streamwise velocity fluctuations is independent of $Re$. In the vicinity of the wall only at the highest levels of $DR$ the relative value of $u^{'}_{\mathrm{rms}}$ decreases. It is possible that polymer drag reducers affect $u^{'}_{\mathrm{rms}}$ even in the inner near-wall region, however, the presented results do not contain data for the inner near-wall region due to a lack of resolution. Further from the wall the intensity of the streamwise fluctuations decreased with increasing $DR$ until a given value of $DR$ at which $u^{'}_{\mathrm{rms}}$ starts to increase. The range of minimum values of $u^{'}_{\mathrm{rms}\,0.1\,N}$ and $u^{'}_{\mathrm{rms}\,0.5\,N}$ corresponds approximately to the optimum polymer concentration $c_{\mathrm{opt}}$ after which the measured $DR$ is independent of polymer concentration and can therefore be considered as maximum $DR$ for a given system. The finding indicates that turbulent flow is altered in different way at maximum levels of $DR$ and for $DR$ below $c_{\mathrm{opt}}$.

Similarly to the streamwise velocity fluctuations, the friction velocity normalised spanwise velocity fluctuations $v^{'+}_{\mathrm{rms}}$ as a function of the friction velocity normalised distance from the wall $y^+$ of the presented measurements are compared with data published by den Toonder et al. [4] and White et al. [5] (see Figure 6.35). The data presented here are in good agreement with the published results expect for the three closest points to the wall. Therefore, the first three points will be neglected in the following analysis.

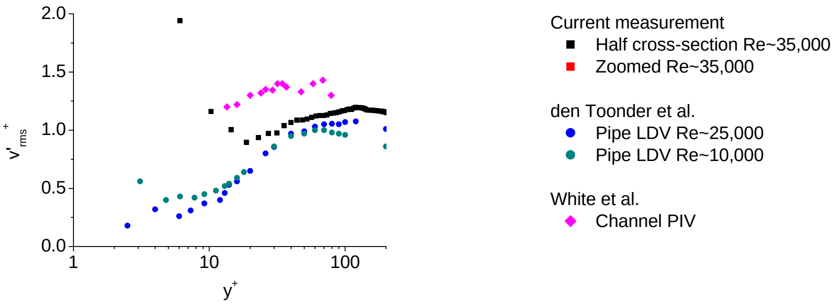

Figure 6.35: Comparison of measured normalised spanwise velocity fluctuations with data published by den Toonder et al. [4] and White et al. [5].

In Figure 6.36 the rms of spanwise velocity fluctuations $v'_{\mathrm{rms}}$ (see Equation 3.32) for PEO8 are reported. The shape of the $v'_{rms}$ profiles of PEO2 and PEO4 are similar to PEO8 (see Appendix A Figures A.6, A.7, A.8 and A.9).. The intensities of $v'_{\mathrm{rms}}$ increased with increasing $Re$. For a constant $Re$ the value of $v'_{\mathrm{rms}}$ profiles peaks at $y/D \sim 0.1 - 0.2$. The height of the peak decreased with increasing polymer concentration and corresponding level of $DR$. Additionally, the position of the peak is shifted towards the outer velocity-defect region with increasing polymer concentration. Both observations are in agreement with published data [4, 87, 5]. Contrary to the streamwise fluctuation $u'_{\mathrm{rms}}$ (see Figure 6.33) there is no difference in the spanwise fluctuation profile trends between the different PEO8 concentrations.

The dependence of the normalised spanwise fluctuation $v'_{\mathrm{rms}\,y/D\,N}$ at $y/D =$ 0.015, 0.1 and 0.5 on the level of $DR$ can be seen in Figure 6.37. The normalisation was made in similar way as for streamwise velocity fluctuations:

$$v'_{\mathrm{rms}\,y/D\,N} = \frac{v'_{\mathrm{rms_i}\,y/D}}{v'_{\mathrm{rms_{water}}\,y/D}}{}_{Re=\mathrm{const.}} \tag{6.5}$$

Similarly to the normalised streamwise velocity fluctuations, the dependence of the normalised spanwise velocity fluctuations on the level of $DR$ is independent on $Re$. The values of $v'_{\mathrm{rms}\,y/D\,N}$ steadily decreased with increasing $DR$ where at maximum measured $DR$ the intensity of normalised spanwise velocity fluctuations is $\sim$ 50% lower compared to water. The similar slope of the

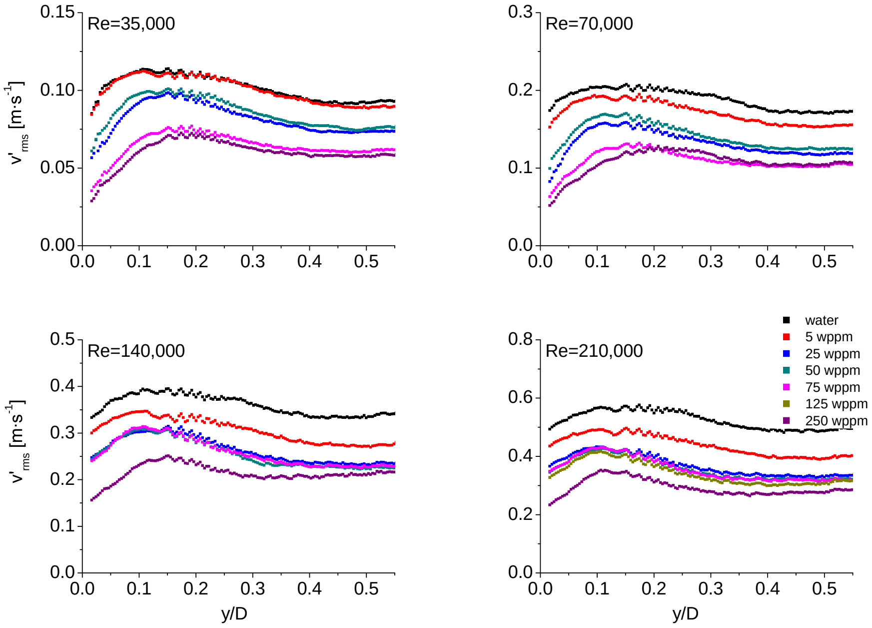

Figure 6.36: Dependence of rms spanwise velocity fluctuations ($v'_{rms}$) on the normalised distance from the wall for PEO8 solutions at various $Re$.

decrease of $v'_{\mathrm{rms}\,y/D\,N} = f\,(DR)$ at various distances from the wall indicates that the intensity of spanwise velocity fluctuations is dumped by polymer drag reducers up to the same extent across the pipe.

An example of the joint probability functions of stream- $u'$ and spanwise $v'$ velocity fluctuations for PEO8 at $Re = 70,000$ and $210,000$ is shown in Figures 6.38 and 6.39. The joint probability function was constructed from 250 bins and the probability of velocity fluctuations is shown by the colour-bar. The polymer additives reduce the intensity of the velocity fluctuations so the highest probability of the velocity fluctuations is shifted towards zero values of velocity fluctuations with increasing polymer concentration. Additionally, the polymer additives reduced more the spanwise fluctuations than the streamwise fluctuations and the joint probability function become more elliptic with increasing polymer concentration. The observation strongly indicates that the polymer additives cause the turbulence to become anisotropic. The anisotropy of the velocity fluctuations was observed for all studied polymers and over the whole range of $Re$ (see Appendix A Figures A.14 - A.16). The results are in agreement with the finding that polymer additives reduced more the spanwise velocity fluctuation than the streamwise velocity fluctuation [165, 5, 98].

The Reynolds stress (see Equation 3.33) as a function of the normalised distance from the wall for PEO8 solutions is shown in Figure 6.40. Similar trends

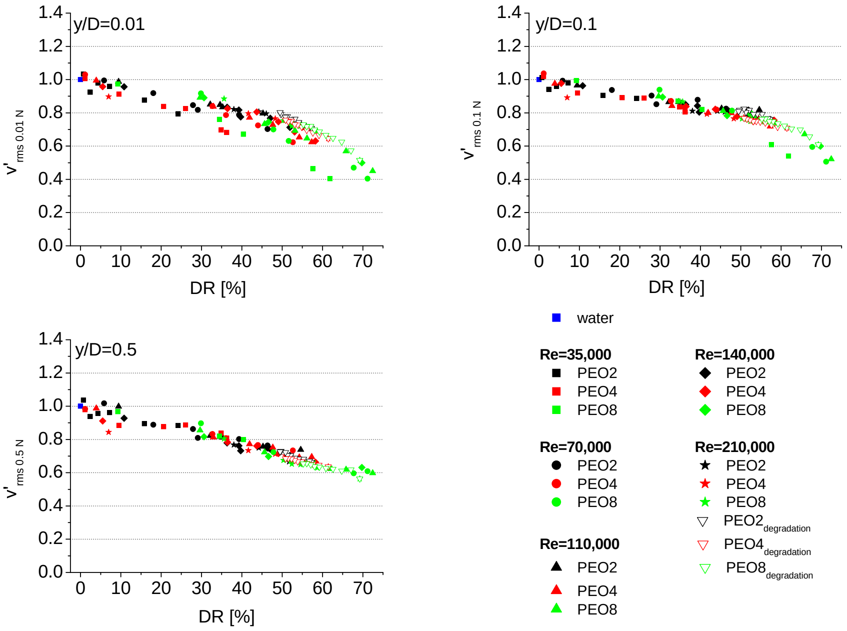

Figure 6.37: Dependence of normalised rms spanwise velocity fluctuations ($v'_{\mathrm{rms}\,y/D\,N}$) on the level of drag reduction at $y/D = 0.015$; 0.1 and 0.5 ($v'_{\mathrm{rms}\,0.015\,N}$; $v'_{\mathrm{rms}\,0.1\,N}$ and $v'_{\mathrm{rms}\,0.5\,N}$).

were observed for PEO2 and PEO4 solutions (see Appendix A Figures A.10 - A.13). All the profiles were smoothed using the adjacent-averaging method over 10 points in order to remove random fluctuations. The Reynolds stress profiles are a function of *Re*; increasing *Re* leads to increased Reynolds stresses. Such a behaviour can be expected from Equation 3.33 and from the streamwise and spanwise velocity fluctuation profiles (e.g. see Figures 6.33 and 6.36). The overall meaning is in the increase of the intensity of turbulences with increasing *Re*. The addition of polymers results in decreased Reynolds stresses. The absolute magnitude of the decrease increased with increasing *Re* for a given polymer concentration. Additionally, the Reynolds stress decreased with increasing polymer molecular weight when all the other parameters were constant. The decrease of Reynolds stress for increasing polymer concentration was previously reported for pipe [4, 87] and channel flow; Warholic et al. [97] found almost zero Reynolds stress for high levels of *DR*. It should be noted that non-zero Reynolds stress profiles were found for pipe flow even for maximum DR [87].

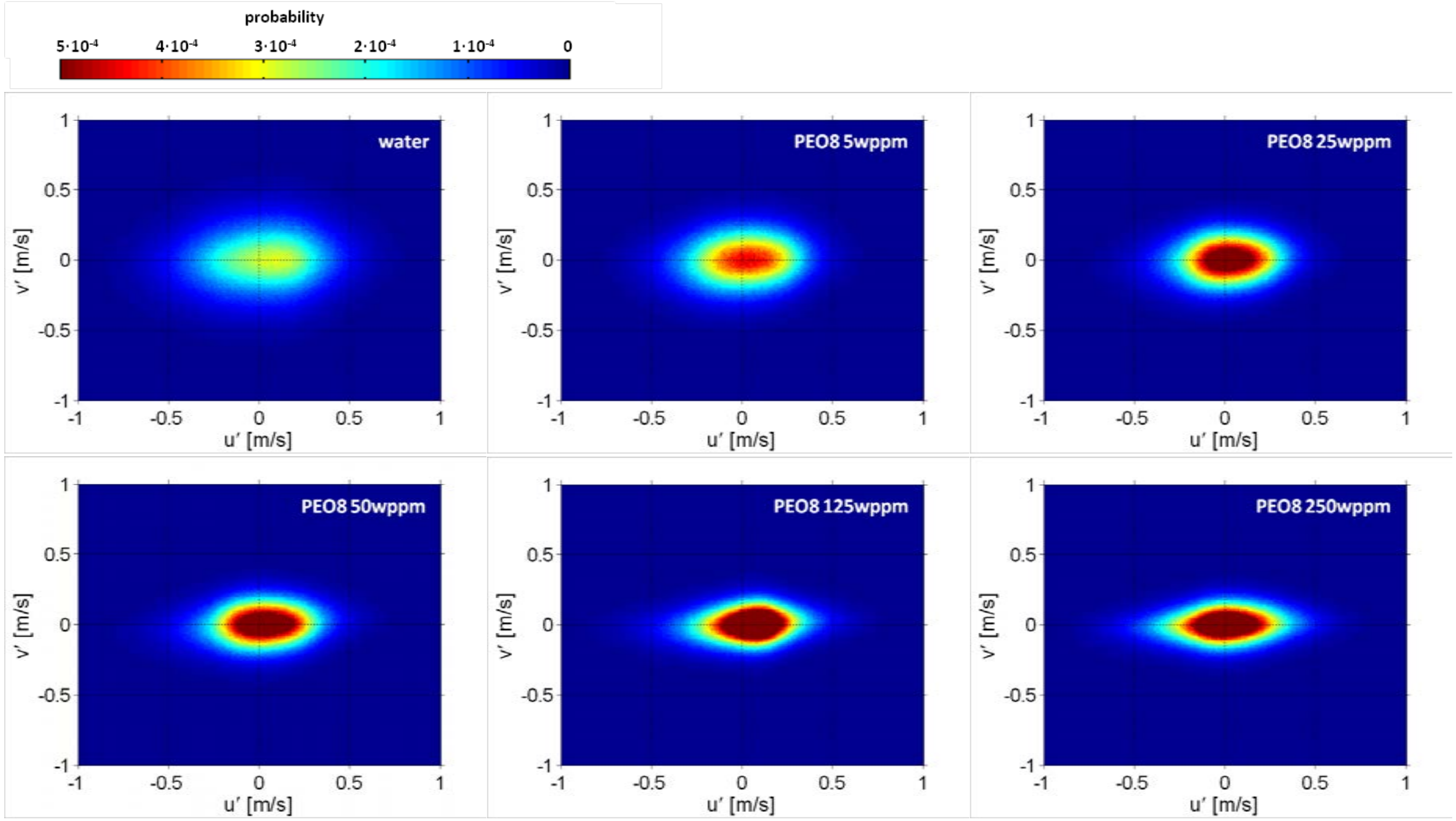

Figure 6.38: Joint probability function of the streamwise and spanwise velocity fluctuations ($u^{'}$ and $v^{'}$) for PEO8 solutions at $Re = 70,000$.

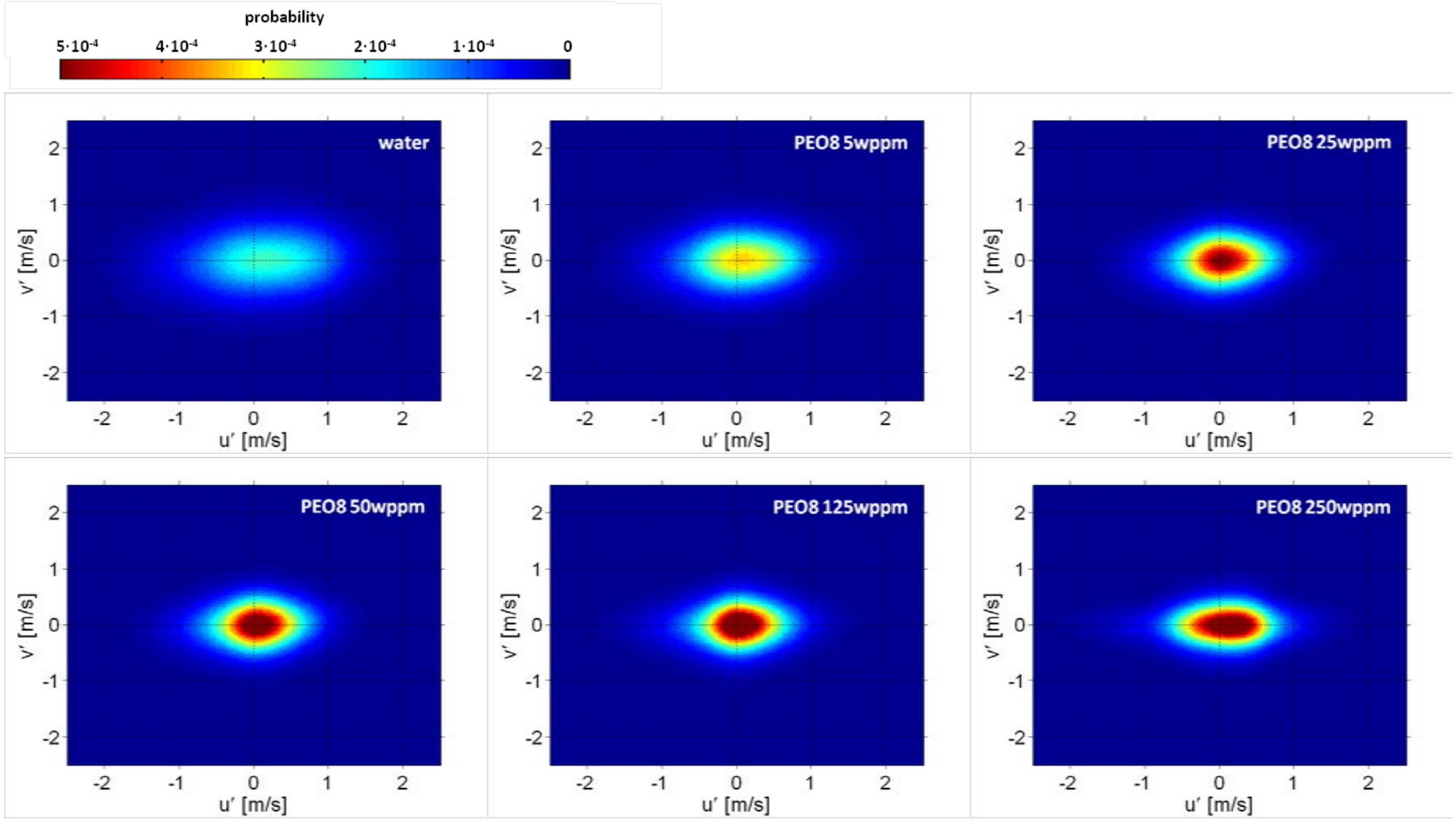

Figure 6.39: Joint probability function of the streamwise and spanwise velocity fluctuations ($u^{'}$ and $v^{'}$) for PEO8 solutions at $Re = 210,000$
.

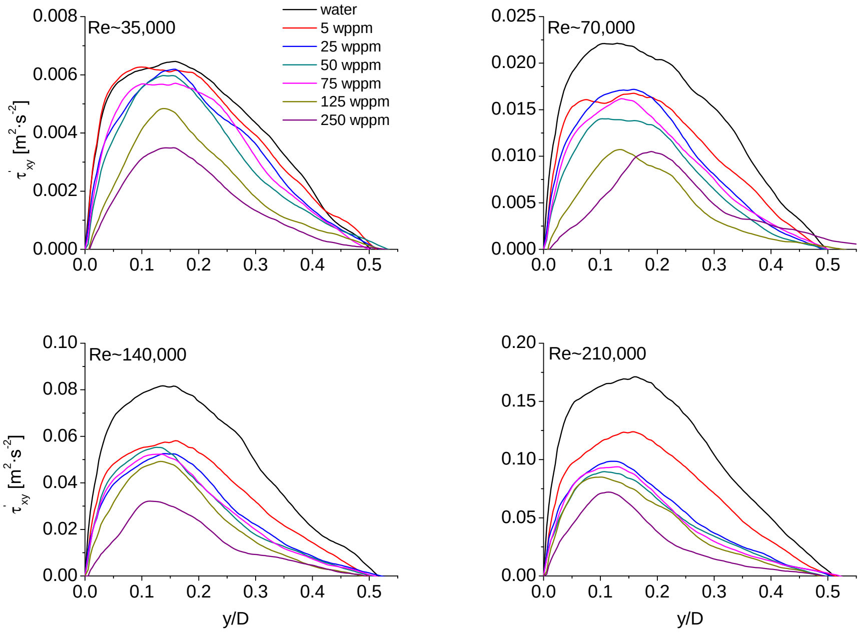

Figure 6.40: Dependence of Reynolds stress $\tau'_{xy}$ on the normalised distance from the wall $y/D$ for PEO8 solutions at various $Re$.

Figure 6.41 shows the dependence of the normalised maximum Reynolds stress and normalised Reynolds stress at $y/D = 0.015$ and 0.4 on the level of $DR$. The Reynolds stress for a given solution at a given location $\tau'_{xy\,y/D_i}$ was normalised with respect to the Reynolds stress at a given location of the pure solvent (water) at constant $Re$:

$$\tau'_{xy\,y/D\,N} = \frac{\tau'_{xy\,y/D_i}}{\tau'_{xy\,y/D_{\text{water}}\;Re=\text{const.}}} \tag{6.6}$$

Figure 6.41 shows that the relative magnitude of the decrease of the Reynolds stress is independent on $Re$ for the maximum value as well as for $y/D = 0.015$ and 0.4. The only factor that affects the normalised Reynolds stress is the level of $DR$. The normalised Reynolds stress at $y/D = 0.015$ and 0.4 was reduced to almost zero at the maximum level of $DR$. However, the normalised maximum Reynolds stress $\tau'_{xy\,\max N}$ was reduced by 60% at maximum $DR$. The decreasing linear trend of the dependency of $\tau'_{xy\,\max N}$ as a function of $DR$ indicated that the absolute value of the maximum Reynolds stress could never drop to zero even for an assumed $DR = 100\%$, which is in contradiction with data reported by Warholic et al. [97] who found almost zero Reynolds stress across a channel at maximum $DR$. It should be noted that the presented results are for pipe flow and Warholic et al. [97] performed the experiments in a channel. It is very possible that the difference between the flow in a channel and in a pipe might be responsible for the contradiction.

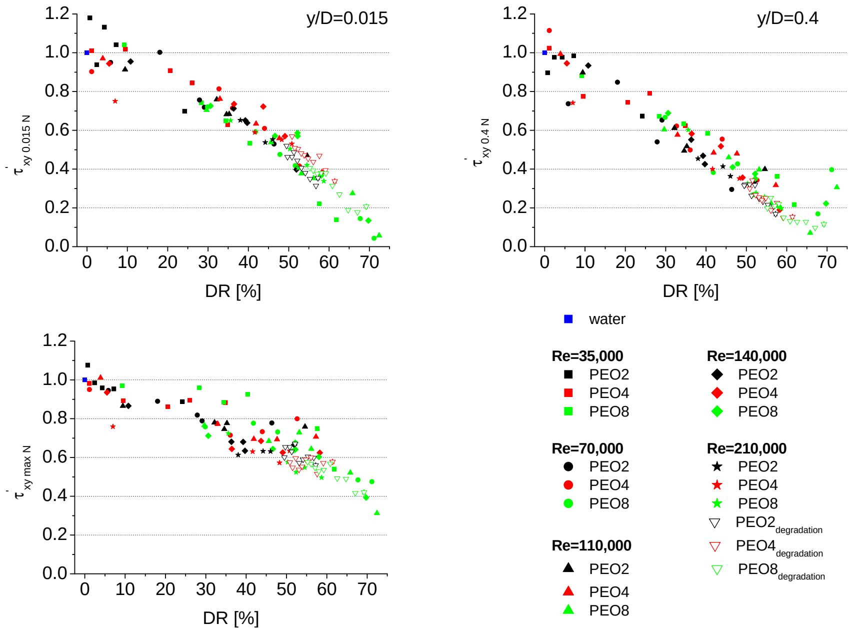

Figure 6.41: Dependence of the normalised maximum peak value of Reynolds stress ($\tau'_{xy\,\max N}$) on the level of drag reduction.

### 6.2.7 Vorticity and Strain Rates

Vorticity is related to the flow rotation domain transformation (see Figure 6.8). The profiles of the mean 2D vorticity of PEO8 solutions are shown in Figure 6.42. The behaviour of PEO2 and PEO4 solutions is very similar to PEO8 (see Appendix A Figures A.17, A.18, A.19 and A.20), excluding the highest PEO8 concentration. The values of mean 2D vorticity have a maximum in the inner near-wall region and exponentially decay with increasing distance from the wall. It was however not possible to analyse the global maximum of the mean 2D vorticity in the inner near-wall region due to lack of resolution in the inner near-wall region. The absolute values of the mean 2D vorticity increase with increasing *Re*. The only area that is affected by the polymer additives is the near-wall region. Measured maximum mean 2D vorticity values increased with polymer concentration. For $y/D \geq 0.05$ the 2D vorticity becomes independent on the polymer concentration with the exception of the highest concentrations of PEO8, which fall on the general 2D vorticity trend at $y/D \geq 0.35$. The higher values of 2D vorticity for the solutions containing 250 wppm of PEO8, and partly even for 125 wppm, can be attributed to the coherent appearance

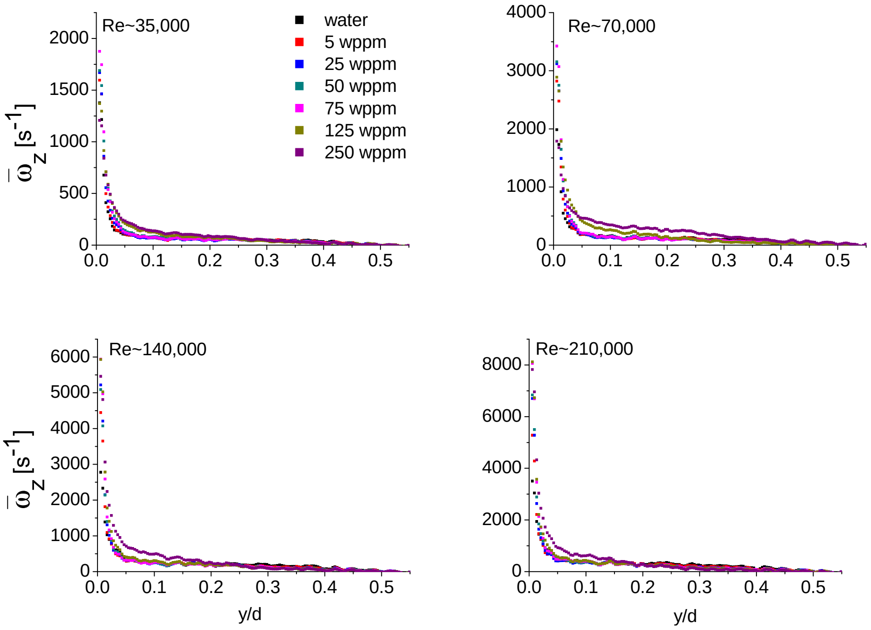

Figure 6.42: Dependence of the mean 2Dt vorticity ($\overline{\omega}_z$) on the normalised distance from the wall for PEO8 solutions at various $Re$.

of the polymer layer (see Figure 6.20), which was bounded by layer of intense instantaneous 2D vorticity. For the other polymer solutions the instantaneous 2D vorticity layers were not so intense and they also appeared mostly in the inner near-wall region (see Figures 6.18, 6.19 and 6.20).

The dependence of the normalised 2D vorticity at $y/D = 0.015$ and 0.1 on the level of $DR$ is shown in Figure 6.43. The values were normalised as follows:

$$\overline{\omega}_{z\,y/D\,N} = \frac{\overline{\omega}_{z_i\,y/D}}{\overline{\omega}_{z_{\text{water}}\,y/D\;Re=\text{const.}}} \tag{6.7}$$

The normalised mean 2D vorticity at $y/D = 0.015$ increases with increasing level of $DR$. The relative increase of 2D vorticity seems to be independent on $Re$, however, the data exhibit significant scatter. It is interesting that the increase of the mean 2D vorticity at $y/D = 0.015$ for maximum recorded $DR$ is almost doubled when compared to water. The increased 2D vorticity in the inner near-wall region can be attributed to the thickening of the buffer layer as demonstrated by the $\Delta B$ parameter (see Section 6.2.5). However, the $\Delta B$ parameter is dependent on $Re$ and the near-wall normalised 2D vorticity seems to be independent on $Re$. Further and more detailed analysis of the flow field especially in the inner near-wall region should be done. One possibility is to process the raw data using the PTV algorithm instead of PIV. During PTV

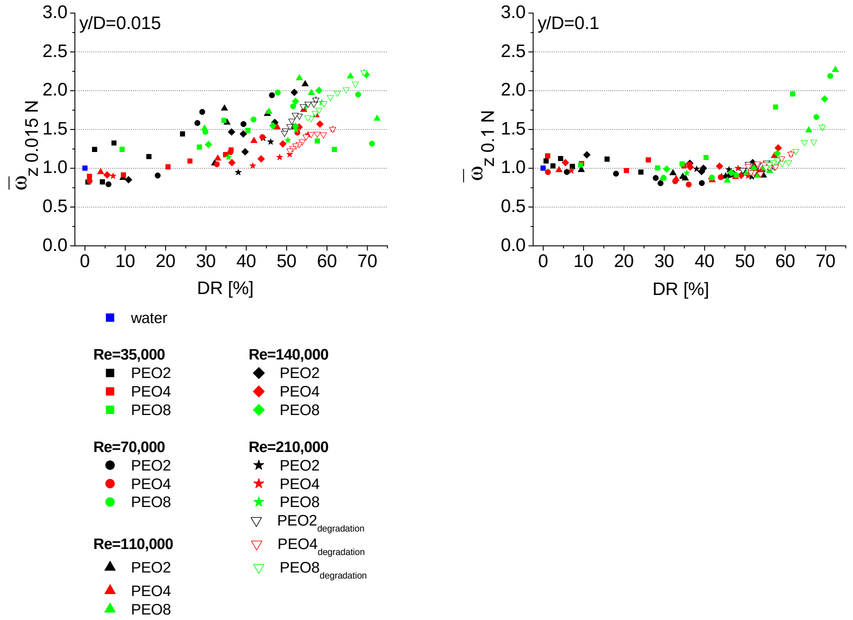

Figure 6.43: Dependence of the normalised mean 2D vorticity ($\overline{\omega}_{z\,y/D\,N}$) on the level of drag reduction at $y/D = 0.015$ and 0.1.

calculation the trajectory of each tracing particle is evaluated and the resulted resolution is theoretically in the order of pixels. Further away from the wall $y/D = 0.1$ the normalised 2D vorticity became independent on $DR$ but only for $DR < 55\%$. Higher levels of $DR$ result in sharp increase of the normalised 2D vorticity. The sharp increase in $\overline{\omega}_{z\,0.1\,N} = f\,(DR)$ at $DR > 55\%$ can be mainly observed for the two highest polymer concentrations of PEO8.

Strain rate values presented below are a measure of the shear transformation of the flow domain (see Figure 6.8). The profiles of the 2D vorticity fluctuations $\omega_z^{'}$ for PEO8 solutions are shown in Figure 6.44. PEO2 and PEO4 solutions show similar trends over the entire pipe cross-section (see Appendix A Figures A.21 - A.24). The 2D vorticity fluctuation has a maximum in the inner near-wall region and then exponentially decays towards the outer velocity-defect region . The polymer additives shift the $\omega_z^{'}$ profiles to lower values which is exactly the opposite trend than that observed for the mean 2D vorticity $\overline{\omega}_z$. According to Sher et al. [109] polymer molecules can be unraveled by centrifugal forces that occur in the pipe regions with high 2D vorticity. Figures 6.42 and 6.44 demonstrate that the region with high mean 2D vorticity and 2D vorticity fluctuations is located near the wall. Additionally, the maximum values of the mean 2D vorticity and the 2D vorticity fluctuations for $Re = 70,000$ are 3530 and 4580 $\mathrm{s}^{-1}$, respectively. The high mean 2D vorticity value indicates that a region with

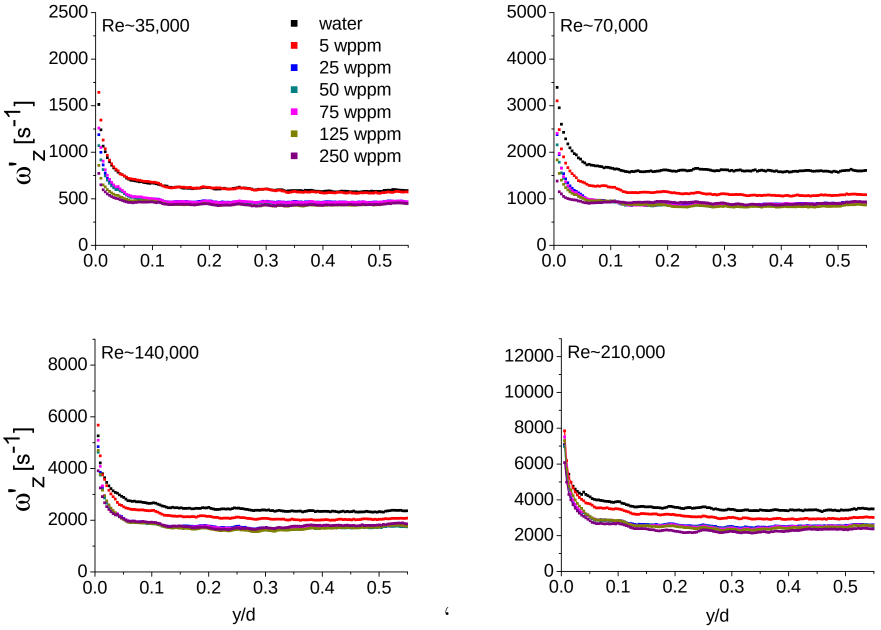

Figure 6.44: Dependence of 2D vorticity fluctuations $(\omega_z^{'})$ on the normalised distance from the wall for PEO8 solutions at various *Re*.

high centrifugal forces indeed exists in the vicinity of the wall where polymer molecules can be entrapped and unraveled.

The dependence of the normalised 2D vorticity fluctuations at $y/D = 0.015$, 0.1 and 0.5 on the level of $DR$ is shown in Figure 6.45. The results were normalised according to the following equation:

$$\omega^{'}_{z\,y/D\,N} = \frac{\omega^{'}_{\mathrm{z_i\,y/D}}}{\omega^{'}_{\mathrm{z_{water}\,y/D}\;\mathrm{Re=const.}}} \tag{6.8}$$

The normalised 2D vorticity fluctuations as a function of $DR$ are independent of *Re*. The relative decrease of the 2D vorticity fluctuations is very similar for all three positions, $y/D = 0.015$, 0.1 and 0.5, however, the results in the inner near-wall region are very scattered. Nevertheless, it can be concluded that the 2D vorticity fluctuations are suppressed by increasing level of $DR$ to the same extent independently on the distance from the wall. At maximum measured $DR$ the 2D vorticity fluctuations are $\sim 25\%$ lower compared to water.

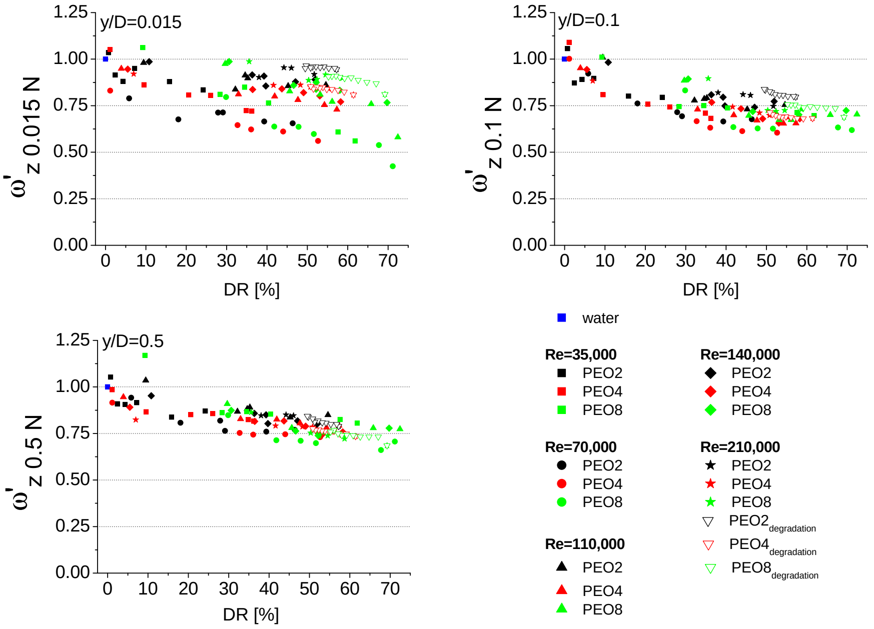

Figure 6.45: Dependence of the normalised 2D vorticity fluctuations $(\omega'_{z\,y/D\,N})$ on the level of drag reduction at $y/D = 0.015$, 0.1 and 0.5.

The average values of the mean streamwise and spanwise shear strain rate $(\overline{\gamma}_{xy},\ \overline{\gamma}_{yx})$ and the mean streamwise and spanwise compression strain rate $(\overline{\gamma}_{xx},\overline{\gamma}_{yy})$ for water at different $Re$ is shown in Figure 6.46. The strain rates $\overline{\gamma}_{xy}$, $\overline{\gamma}_{yx}$, $\overline{\gamma}_{xx}$ and $\overline{\gamma}_{yy}$ are defined by Equations 3.34, 3.35, 3.36 and 3.37, respectively. It is clearly visible that only the mean streamwise shear strain rate reaches non-zero values with its minimum at the inner near-wall region. Therefore, the effect of the polymer additives on the values of $\overline{\gamma}_{yx}$, $\overline{\gamma}_{xx}$ and $\overline{\gamma}_{yx}$ will not be discussed, since the average values are $\sim 0$ across the entire pipe cross-section even for solutions containing polymer additives.

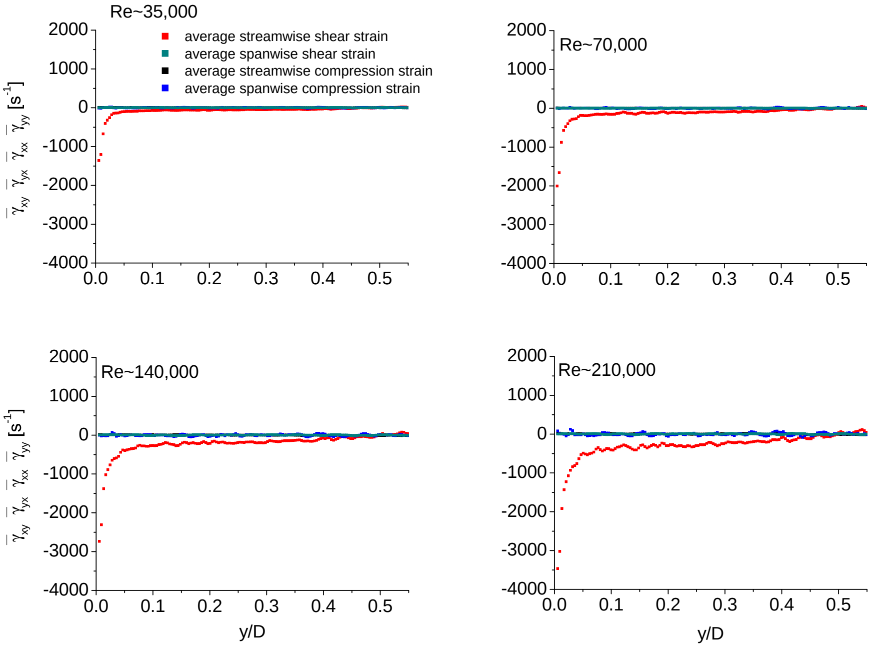

Figure 6.46: Dependence of the mean streamwise shear strain rate ($\overline{\gamma}_{xy}$), the mean streamwise compression strain rate ($\overline{\gamma}_{xx}$), the mean spanwise compression strain rate ($\overline{\gamma}_{yy}$) and the mean spanwise shear strain rate ($\overline{\gamma}_{yx}$) on the normalised distance from the wall for water at different $Re$.

The evolution of the mean streamwise shear strain rate $\overline{\gamma}_{xy}$ for PEO8 solutions is shown in Figure 6.47. The solutions of PEO2 and PEO4 exhibit similar trends (see Appendix A Figures A.25 - A.28). The $\overline{\gamma}_{xy}$ profiles exhibit a minimum in the inner near-wall region. The absolute value of the $\overline{\gamma}_{xy}$ minimum increases with increasing polymer concentration. At $y/D = 0.05 - 0.5$ the average streamwise shear strain rate continuously converges towards zero value. The highest polymer concentrations of PEO8 exhibited a deviation from the trends observed for other polymer-solvent systems at $y/D < 0.3$. The mean streamwise shear strain rate decays more slowly except for the highest studied $Re$, $Re = 210,000$.

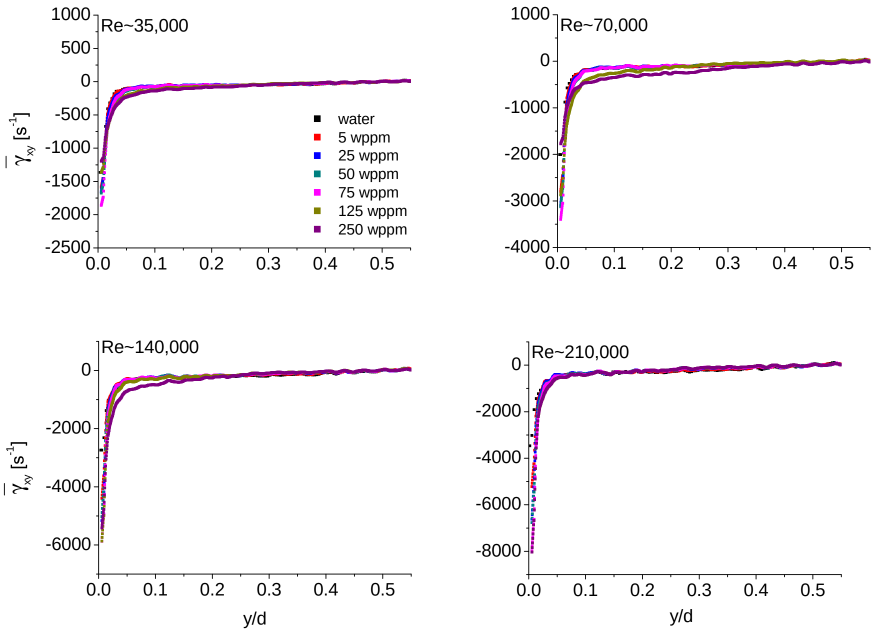

Figure 6.47: Dependence of the mean streamwise shear strain rate ($\overline{\gamma}_{xy}$) on the normalised distance from the wall for PEO8 solutions for various $Re$.

The dependence of the normalised mean streamwise shear strain rate at $y/D = 0.015$ and 0.1 on the level of $DR$ is shown in Figure 6.48. The results were normalised using following expression:

$$\overline{\gamma}_{xy\,y/D\,N} = \frac{\overline{\gamma}_{xy_i\,y/D}}{\overline{\gamma}_{xy_{\text{water}}\,y/D}}{}_{Re=\text{const.}} \tag{6.9}$$

The results of the normalised mean streamwise shear strain rate are almost identical to the results of the normalised 2D vorticity (see Figure 6.43). The similarity is not surprising if the definition of the two variables (Equations 3.34 and 3.38) and the values of mean streamwise and spanwise velocity (see Figures 6.26 and 6.27) are taken in account. The normalised mean streamwise shear strain rate increases with increasing $DR$ in the inner near-wall region, $y/D = 0.015$. However, further away from the wall at $y/D = 0.1$ the values of $\overline{\gamma}_{xy\,0.1\,N}$ become independent on $DR$ for $DR < 50\%$. At the centreline $y/D = 0.5$ the values of the mean streamwise shear strain rate approach zero and became fully independent of $Re$ and the level of $DR$.

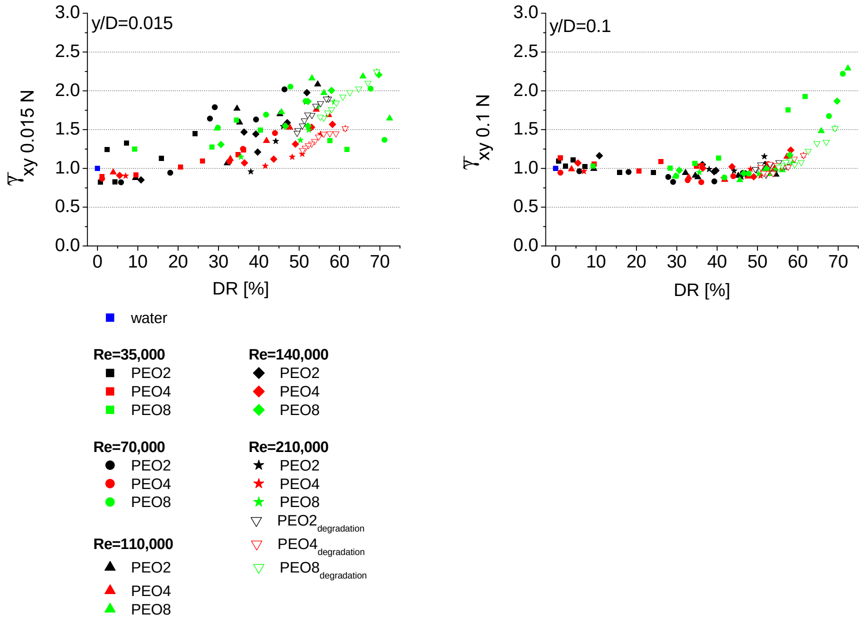

Figure 6.48: Dependence of the normalised mean streamwise shear strain rate $(\overline{\gamma}_{xy\,y/D\,N})$ on the level of drag reduction at $y/D = 0.015$ and 0.1. Increasing trends mean that the minimum value is decreasing.

Figure 6.49 shows the fluctuations of $\gamma_{xy}$, $\gamma_{yx}$, $\gamma_{xx}$ and $\gamma_{yy}$ for PEO8 at $Re = 70,000$. The trends of the fluctuation strain rates are very similar to each other and there is no difference in the trends for various $Re$ and for PEO2 and PEO4 (see Appendix A Figures A.29 - A.44). All the strain rate fluctuations have a maximum in the inner near-wall region. The maximum value increases as follows: $\gamma'_{yx} < \gamma'_{yy} < \gamma'_{xx} < \gamma'_{xy}$. The presented data clearly illustrate that the inner near-wall region is indeed a region of very intense fluctuating strain rates as it is assumed by the common explanation of DR [106] where the strain rate fluctuations in the inner near-wall region are directly linked to the transfer of energy from the turbulent flow to polymer molecules, which is accompanied by polymer elongation. Further from the wall the fluctuating strain rates exponentially decay and they level off for $y/D > 0.15$. The addition of polymer to the flow results in a downward shift of the intensities of the fluctuating strain rates.

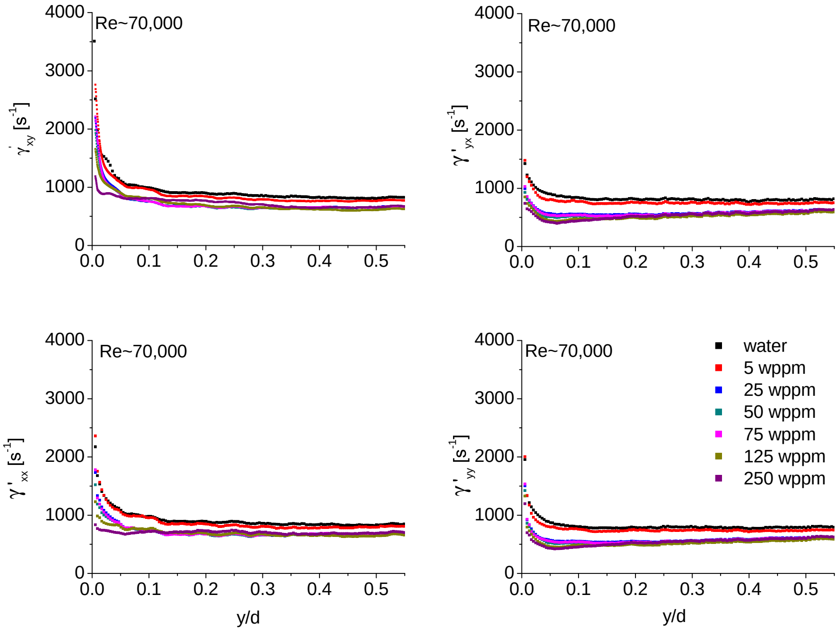

Figure 6.49: The profiles of the fluctuations of streamwise shear strain rate ($\gamma'_{xy}$), spanwise shear strain rate ($\gamma'_{yx}$), streamwise compression strain rate ($\gamma'_{xx}$) and spanwise compression strain rate ($\gamma'_{yy}$) for PEO8 solutions at $Re \sim 70,000$.

The normalised streamwise shear strain rate fluctuations ($\gamma'_{xy\,y/D\,N}$) at $y/D = 0.015$, 0.1 and 0.5 as a function of the level of $DR$ are shown in Figure 6.50. The results were normalised using the following equation:

$$\gamma'_{xy\,y/D\,N} = \frac{\gamma'_{xy_i\,y/D}}{\gamma'_{xy_{\text{water}}\,y/D}}_{Re=\text{const.}} \tag{6.10}$$

The streamwise shear strain rate fluctuation is defined by Equation 3.34 and it is directly proportional to the streamwise velocity fluctuation $u'$. However, the trends of the normalised streamwise shear strain rate fluctuations and the normalised streamwise velocity fluctuations dependency on the level of $DR$ are different (see Figure 6.4). The values of $\gamma'_{xy\,y/D\,N}$ are independent of $Re$. The results in the vicinity of the wall $\gamma'_{xy\,0.015\,N}$ exhibit larger scatter which is caused by low resolution in the inner near-wall region, however, a downward trend is clearly visible. At maximum measured $DR$ the streamwise shear strain rate is $\sim 50\%$ lower when compared to water. The results further from the wall at $y/D = 0.1$ and 0.5 show almost identical trends to each other. Both show a decrease with increasing levels of $DR$ until a threshold, which is situated at $DR \sim 50\%$ after which the values of $\gamma'_{xy\,0.1\,N}$ and $\gamma'_{xy\,0.5\,N}$ level off and become independent of both $Re$ and $DR$. At maximum measured $DR$ the two variables

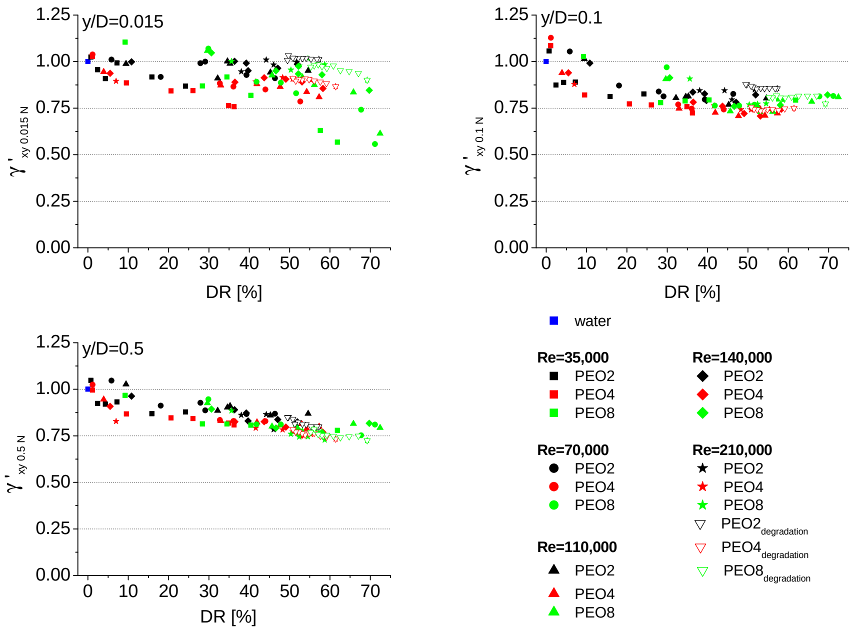

Figure 6.50: Dependence of the normalised streamwise shear strain rate fluctuations ($\gamma^{'}_{xy\,y/D\,N}$) on the level of drag reduction at $y/D = 0.015$, 0.1 and 0.5.

are decreased by 25% when compared to water.

The normalised streamwise compression strain rate fluctuations ($\gamma^{'}_{xx\,y/D\,N}$) at $y/D = 0.015$, 0.1 and 0.5 as a function of the level of $DR$ are shown in Figure 6.50. The results were normalised as follows:

$$\gamma^{'}_{xx\,y/D\,N} = \frac{\gamma^{'}_{xx_i\,y/D}}{\gamma^{'}_{xx_{\text{water}}\,y/D}\,{}_{Re=\text{const.}}} \tag{6.11}$$

The normalised streamwise compression strain rate decreases with increasing level of $DR$ and the relative decrease is independent of $Re$. The results are very similar to the dependency of normalised streamwise shear strain rate on the level of $DR$ (see Figure 6.50). Both variables show different trends in the inner near-wall region, $y/D = 0.015$, and for the region further away from the wall $y/D > 0.1$. In the inner near-wall region the normalised streamwise compression strain rate decreased linearly with increasing $DR$ where at maximum measured $DR$ the $\gamma^{'}_{xx\,0.015\,N}$ is 50% lower when compared to water. In the region further from the wall, $y/D > 0.1$, the normalised streamwise compression strain rate decreased for $DR < 50\%$. After the threshold the normalised streamwise compression strain rates become independent of the level of $DR$.

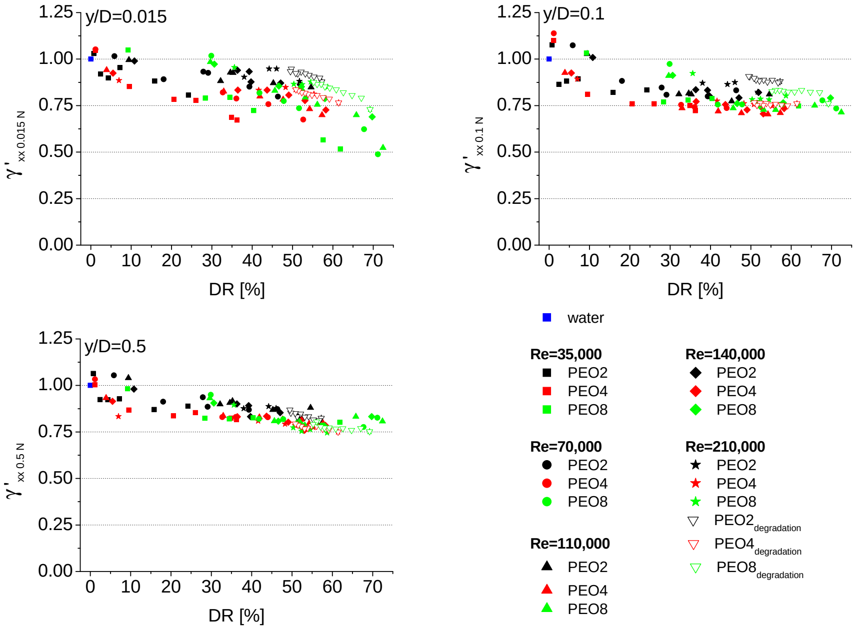

Figure 6.51: Dependence of the normalised streamwise compression strain rate fluctuations ($\gamma'_{xx\,y/D\,N}$) on the level of drag reduction at $y/D = 0.015$, 0.1 and 0.5.

The normalised spanwise shear strain rate fluctuations ($\gamma'_{yx\,y/D\,N}$) at $y/D =$ 0.015, 0.1 and 0.5 as a function of the level of $DR$ are shown in Figure 6.50. The results were normalised as follows:

$$\gamma'_{yx\,y/D\,N} = \frac{\gamma'_{yx_i\,y/D}}{\gamma'_{yx_{\text{water}}\,y/D}}_{Re=\text{const.}} \tag{6.12}$$

The normalised spanwise shear strain rate fluctuation is independent on $Re$ over the whole radius of the pipe. The influence of the drag reducers on the normalised spanwise shear strain rate fluctuations at $y/D = 0.015$ and 0.1 is very similar. At both positions the normalised fluctuations decrease with increasing $DR$ and at the maximum measured $DR$ the fluctuation variables are lowered by $\sim 50\%$ when compared to water. At the centre of the pipe, $y/D = 0.5$, the values of $\gamma'_{xy\,0.5\,N}$ decrease linearly with increasing $DR$ up to $DR \sim 55\%$. After the threshold the values of $\gamma'_{xy\,0.5\,N}$ level off and become independent on both $Re$ and $DR$.

The normalised spanwise compression strain rate fluctuations ($\gamma'_{yy\,y/D\,N}$) at $y/D = 0.015$, 0.1 and 0.5 as a function of the level of $DR$ are shown in Figure 6.50. The results were normalised as follows:

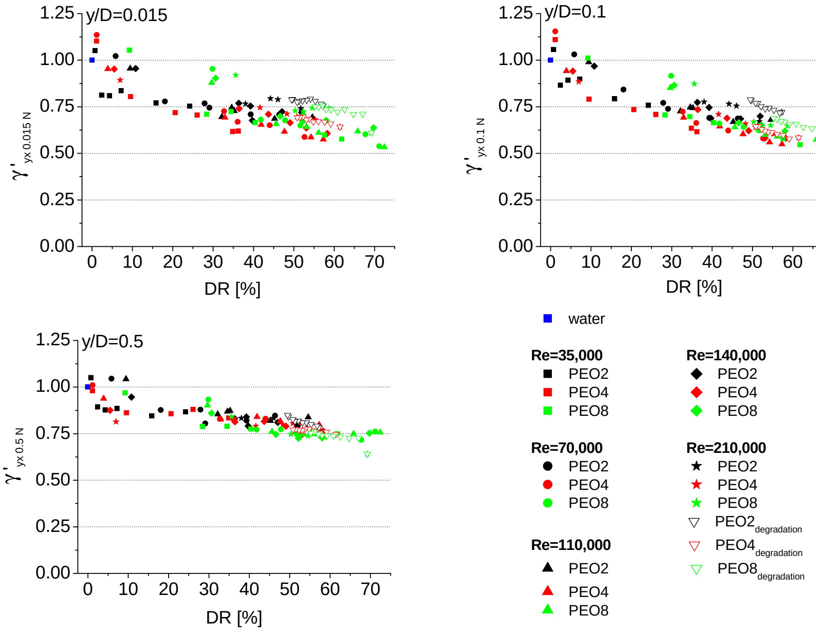

Figure 6.52: Dependence of the normalised spanwise shear strain rate fluctuations ($\gamma'_{yx\,y/D\,N}$) on the level of drag reduction at $y/D = 0.015$, 0.1 and 0.5.

$$\gamma'_{yy\,y/D\,N} = \frac{\gamma'_{yy_i\,y/D}}{\gamma'_{yy_{\text{water}}\,y/D}}_{Re=\text{const.}} \tag{6.13}$$

The dependence of normalised spanwise compression strain rate fluctuations on the level of $DR$ is very similar to the dependence of normalised spanwise shear strain rate fluctuations on $DR$ (see Figure 6.52). Both are independent on $Re$ and both exhibit the same trends for $y/D = 0.015$ and 0.1 where the normalised strain rate values are 50% lower at the maximum measured $DR$. At the centreline the decrease of the normalised strain rate values levels off for $DR > 55\%$ and they are 25% lower when compared to the water.

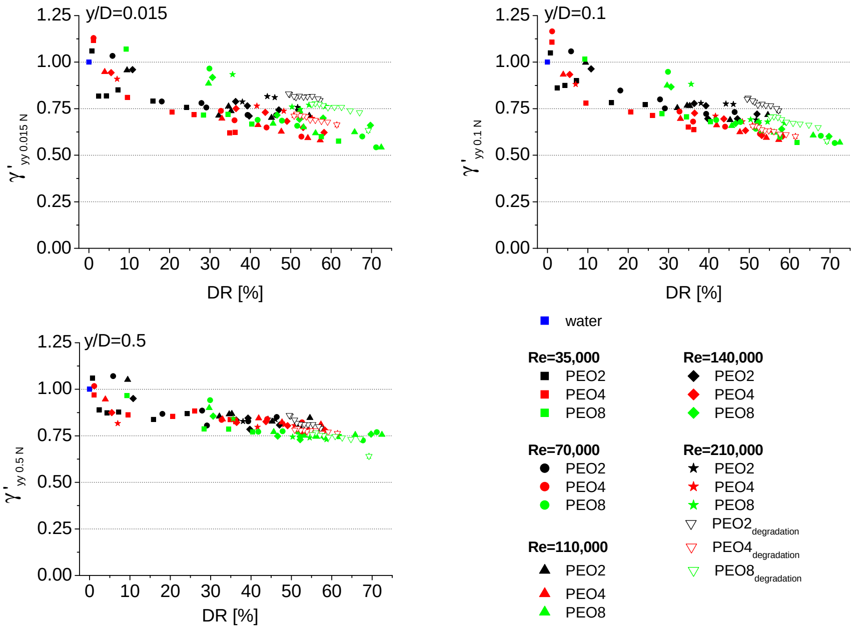

Figure 6.53: Dependence of the normalised streamwise shear strain rate fluctuations $(\gamma'_{yy\,y/D\,N})$ on the level of drag reduction at $y/D = 0.015$, 0.1 and 0.5.

### 6.2.8 Higher Order Statistics - Skewness and Kurtosis

The higher order statistical moments of the velocity fluctuation components, skewness (see Equations 3.39 and 3.40) and kurtosis (see Equations 3.41 and 3.42), are a measure of the asymmetry of the distribution of instantaneous fluctuating velocity components about the mean value. For a Gaussian distribution $S = 0$ and $K = 0$. An example of the shape of distributions with different values of skewness and kurtosis is shown in Figure 6.54.

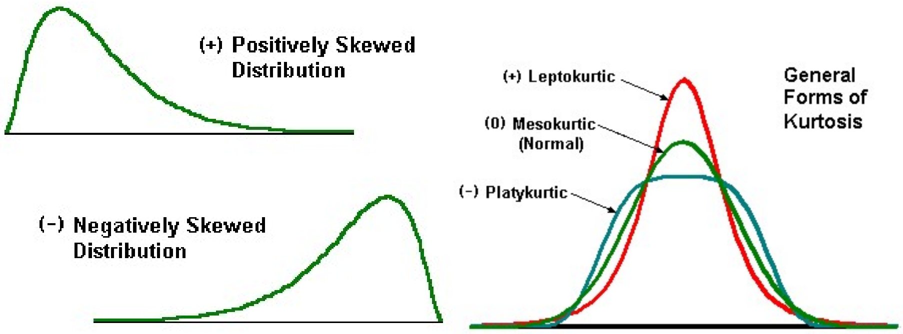

Figure 6.54: Illustration of distributions with different values of skewness and kurtosis [6].

Streamwise skewness results for PEO2, PEO4 and PEO8 are shown in Figures 6.55, 6.56 and 6.57, respectively. An adjacent averaging smoothing over 10 points was used in order to remove the noise from the streamwise skewness data. The streamwise skewness exhibited a dependency on $Re$ at $y/D < 0.25$ where the values of streamwise skewness decrease with increasing $Re$ for water as well as for the polymer solutions. The difference between the Newtonian solvent and the polymer additives is mainly located at $y/D \sim 0.25$ and $y/D > 0.3$. At $y/D \sim 0.25$ the streamwise skewness seems to be a function of polymer concentration; with increasing polymer concentration the streamwise skewness decreased and became a global minimum. The decrease of streamwise skewness is also a function of polymer molecular weight which can be related to the drag reducing efficiency. At $y/D > 0.3$ almost the opposite trend was observed. The streamwise skewness increased with increasing polymer concentration and polymer molecular weight, however the absolute value of the increase is independent on $Re$. Additionally, the increase is not accompanied by a peak value but follows in parallel way the streamwise skewness trends observed for water. The explanation behind the skewness trends is that polymer additives do not only affect the intensity of the turbulent flow but they also affect the entire structure of turbulences. Especially important seems to be $y/D \sim 0.25$ where the increased polymer concentration and polymer molecular weight, which is correlated to the level of $DR$ (see Figure 6.5), resulted in negative very skewed distribution of the streamwise velocity fluctuations. Which means that the probability of intense negative deviations from the average streamwise velocity is much preferred when compared with the positive deviations. Additionally, this event seems to have an effect on the structure of the streamwise fluctuations in the vicinity of the outer velocity-defect region where increasing polymer concentration and polymer molecular weight shifted the distribution of the streamwise fluctuations towards a Gaussian distribution.

Spanwise skewness results as a function of the normalised distance from the wall for PEO8 solutions are shown in Figure 6.58. An adjacent averaging smoothing over 15 points was used in order to remove the noise of the $v'$ skewness data. The PEO2 and PEO4 spanwise skewness results closely follow the spanwise skewness trends observed for water (see Appendix A Figures A.45 and A.46). A very similar behaviour can be seen even for the PEO8 solutions except for the highest concentration (250 wppm) whose profile is slightly shifted to higher skewness values. Based on the results it has to be concluded that the polymer drag reducers do not, or do very little, influence the turbulence structure is the spanwise direction as the structure of the spanwise turbulence is independent on $Re$.

The streamwise kurtosis results for PEO2, PEO4 and PEO8 solutions are

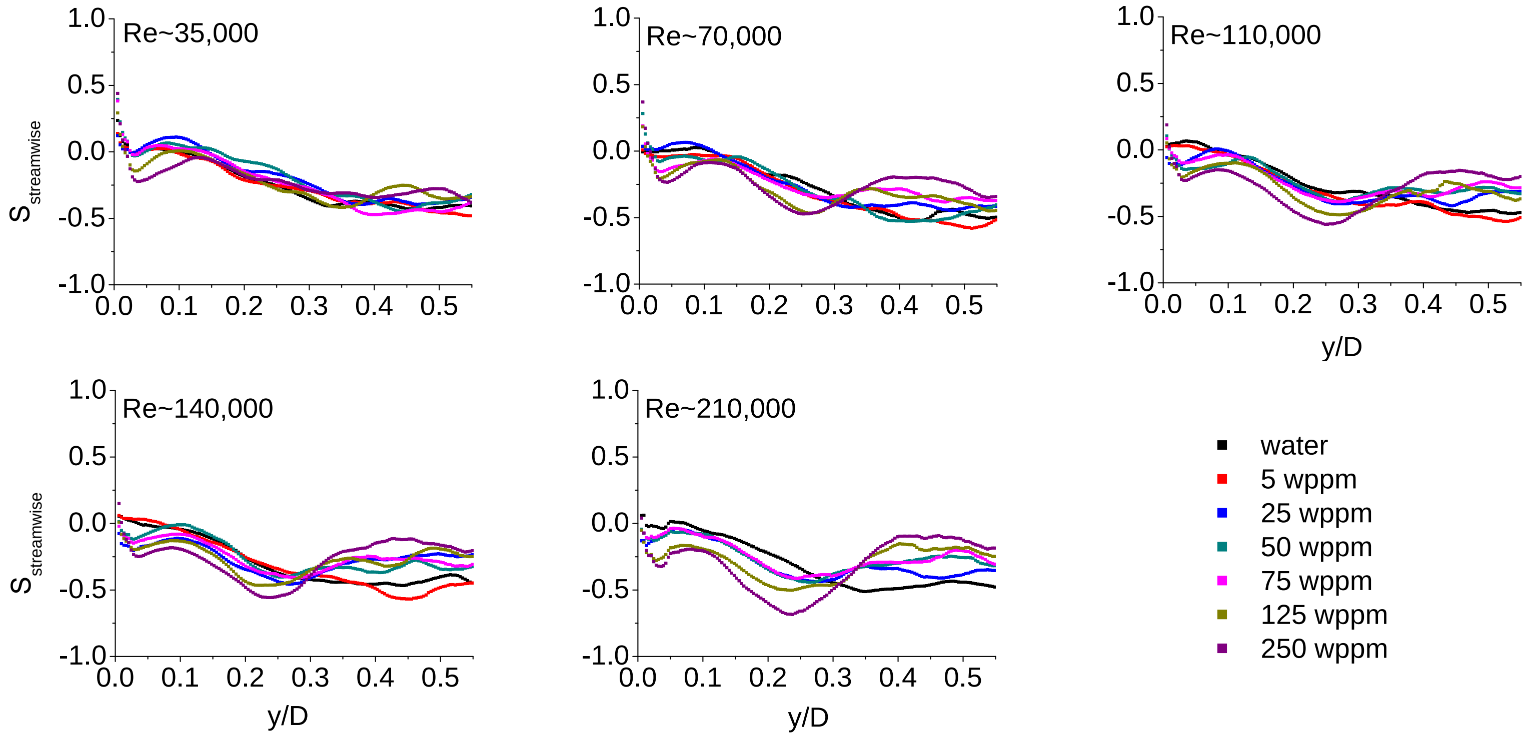

Figure 6.55: Dependence of the streamwise skewness $S_{\mathrm{streamwise}}$ on the normalised distance from the wall for PEO2 solutions at different *Re*.

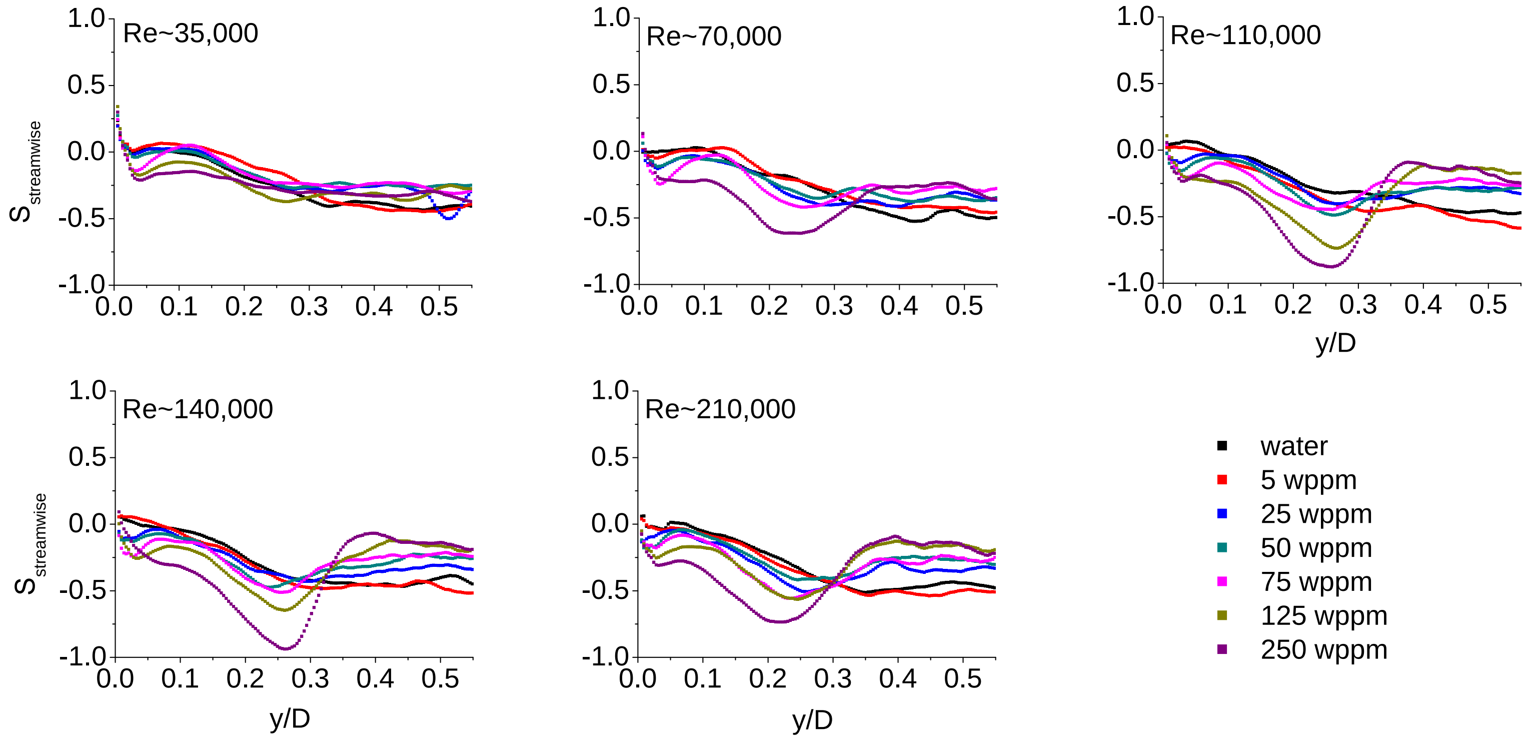

Figure 6.56: Dependence of the streamwise skewness $S_{\text{streamwise}}$ on the normalised distance from the wall for PEO4 solutions at different $Re$.

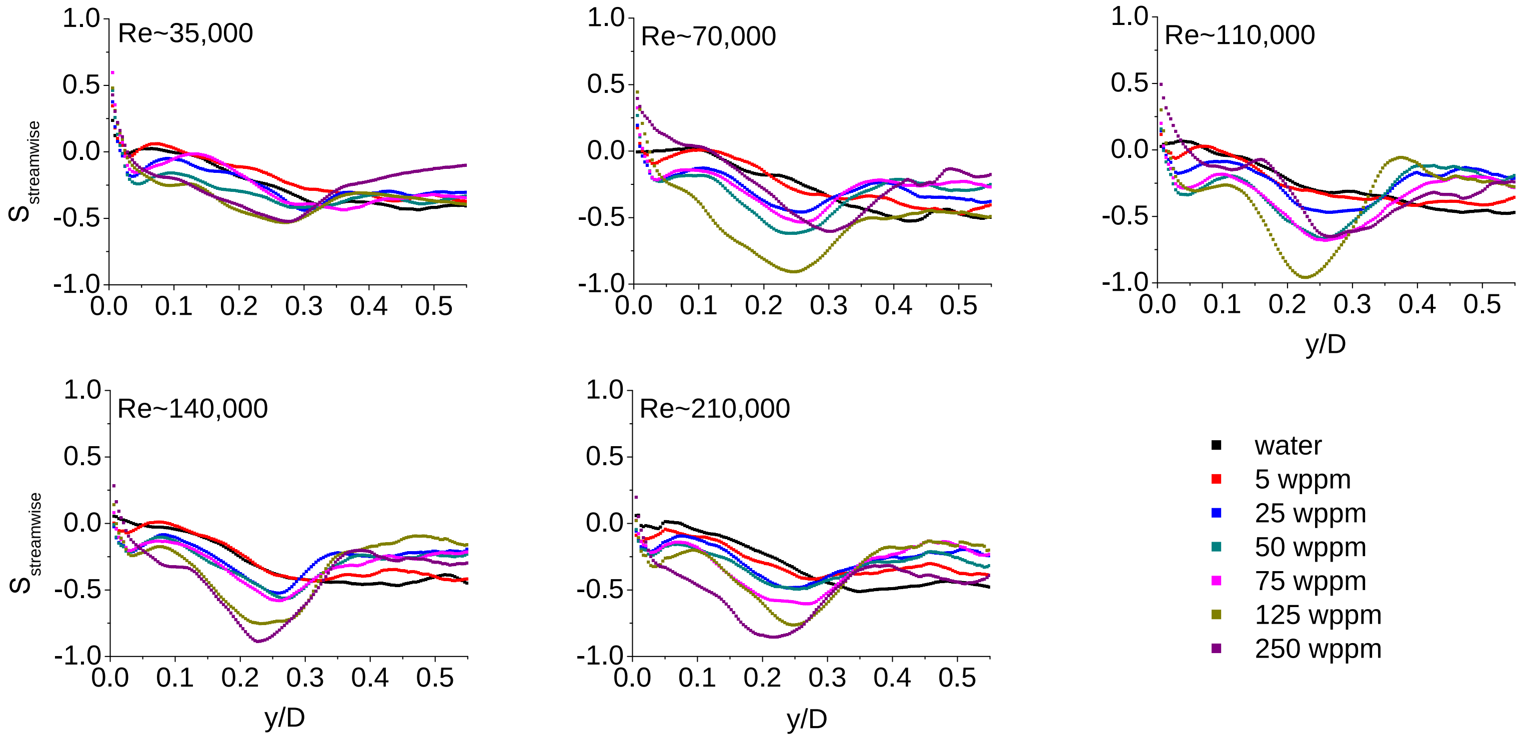

Figure 6.57: Dependence of the streamwise skewness $S_{\text{streamwise}}$ on the normalised distance from the wall for PEO8 solutions at different $Re$.

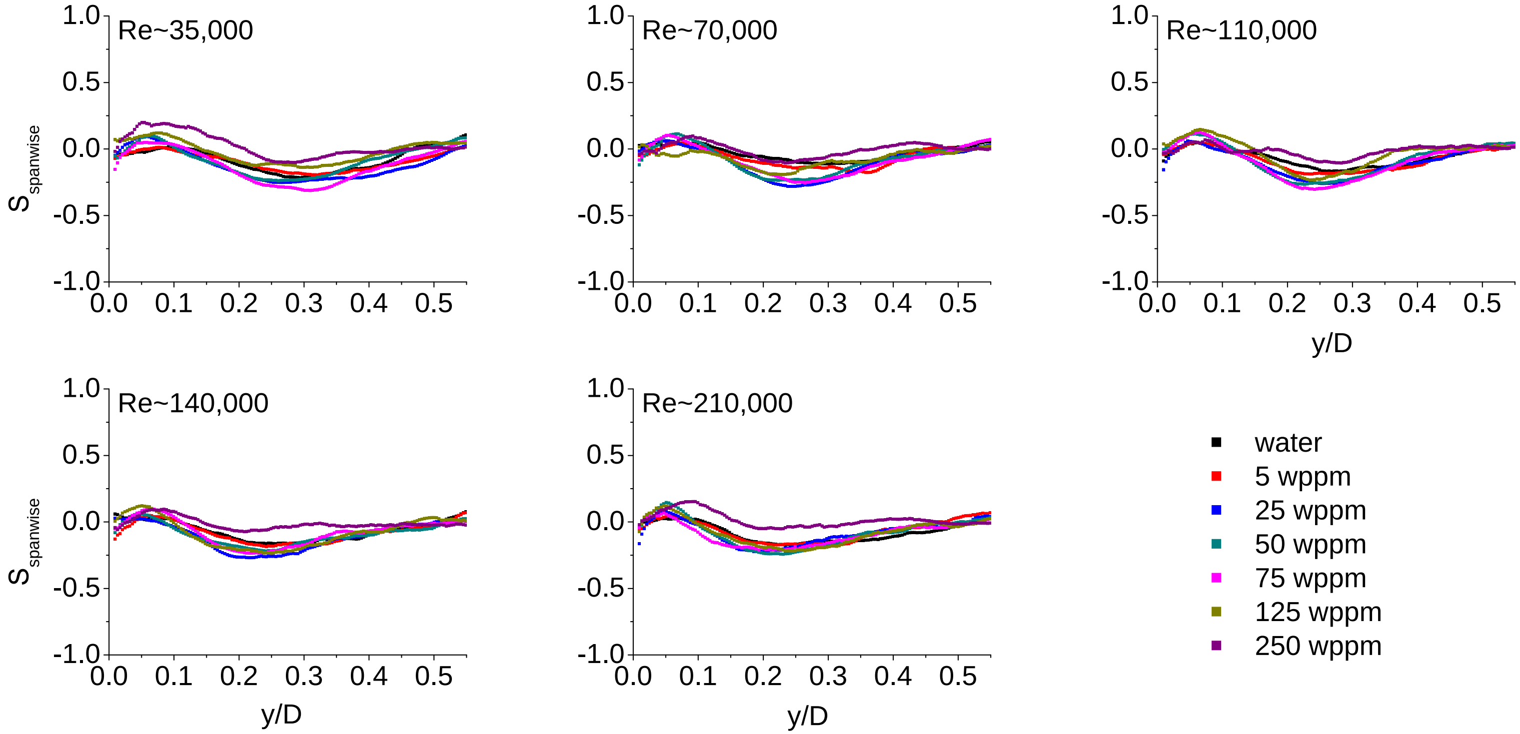

Figure 6.58: Dependence of the spanwise skewness $S_{\mathrm{spanwise}}$ on the distance from the wall for PEO8 solutions at different $Re$.

shown in Figures 6.59, 6.60 and 6.61. The calculated results contained a discrete sharp spike noise in addition to the random noise observed for skewness results. Percentile smoothing over 10 points was used in order to remove the random spikes from the streamwise and spanwise kurtosis data. The disadvantage of the smoothing is that it also removes peak streamwise kurtosis in the inner near-wall region. Therefore the smoothing algorithm was not applied for the data obtained at $y/D \leq 0.025$. The streamwise kurtosis is independent on $Re$ over the whole cross-section of the pipe for water. The streamwise kurtosis has a maximum in the inner near-wall region with no obvious correlation between the height of the maximum and the polymer concentration or the level of $DR$. The polymer additives influence the region of $y/D \sim 0.2 - 0.3$. For low $Re$ ($Re = 35,000$) the effect of polymer additives is negligible. However, with increasing $Re$ the value of streamwise kurtosis increased in the described region. As it was stated above, kurtosis is a measure of narrowness of a distribution. Therefore the increased kurtosis can be ascribed to narrowed distribution of the streamwise velocity fluctuations. Another possible explanation could be that the polymer additives increase the intermittent occurrence of intense streamwise velocity fluctuations in the region of $y/D \sim 0.2 - 0.3$. However, any additional explanation has to be taken as purely speculative. The only valid conclusion is that polymers do alter the structure of the streamwise velocity fluctuations which is demonstrated by the differences in the skewness and kurtosis profiles especially in the region of $y/D \sim 0.2 - 0.3$.

The spanwise kurtosis results for PEO8 solutions are shown in Figure 6.62. The data were smoothed in the same way as the streamwise kurtosis results. The spanwise kurtosis results for PEO2 and PEO4 solutions closely follow the trend observed for water (see Appendix A Figures A.47 and A.48). The spanwise kurtosis profiles are independent on $Re$ and polymer concentration with an exception of the highest concentration of PEO8 (250 wppm). The highest PEO8 concentrations exhibit slightly higher levels of spanwise kurtosis over the whole pipe cross-section. In all cases the spanwise kurtosis has a maximum in the inner near-wall region. Due to the high error of the near-wall measurements it is impossible to define the dependence of the height of the maximum (or even a peak) on the level of $DR$. The origin of the near-wall spanwise kurtosis maximum was explained by Xu et al. [169] who compared DNS simulation data with a detailed near-wall LDV measurements. They link the peak with the regeneration process of the streamwise vortices. The typical value of the near-wall kurtosis for DNS simulations was reported to be $\sim 20$ [169, 170, 168] but the maximum value found here was $\sim 10$. It should be noted that Xu et al. [169] found a spanwise kurtosis peak in the inner near-wall region, however, no peak was observed in the current work due to the problems with resolution

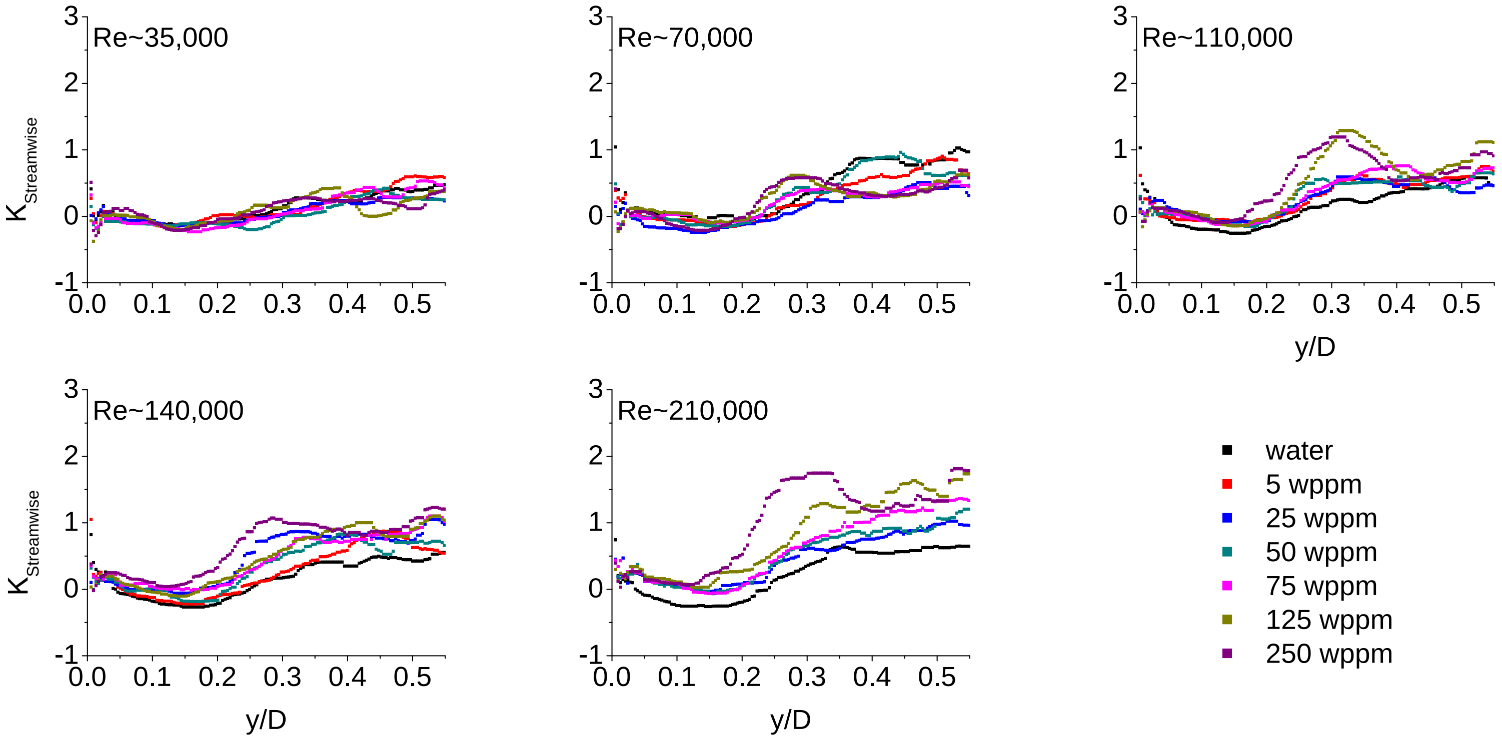

Figure 6.59: Dependence of the streamwise kurtosis $K_{\text{streamwise}}$ on the normalised distance from the wall for PEO2 solutions at different $Re$.

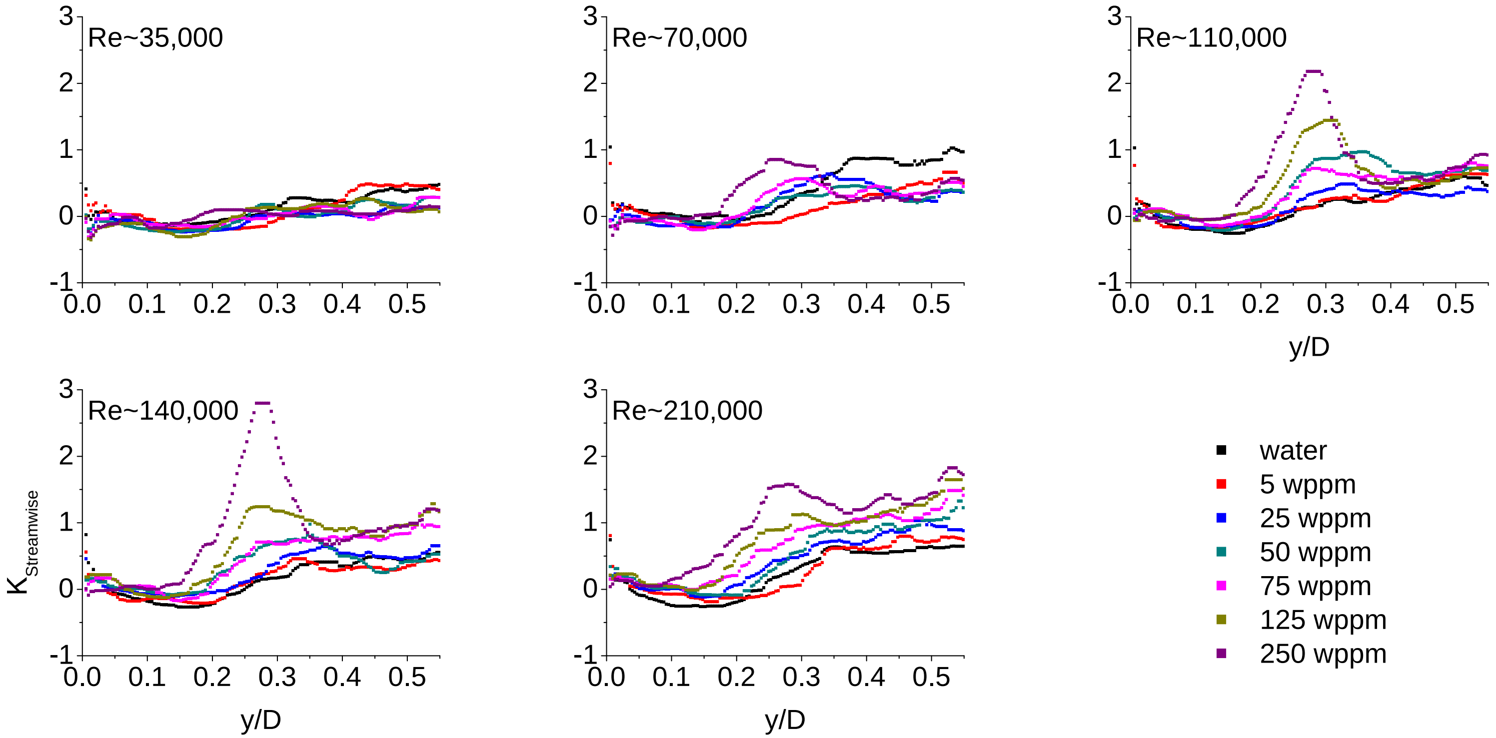

Figure 6.60: Dependence of the streamwise kurtosis $K_{\mathrm{streamwise}}$ on the normalised distance from the wall for PEO4 solutions at different $Re$.

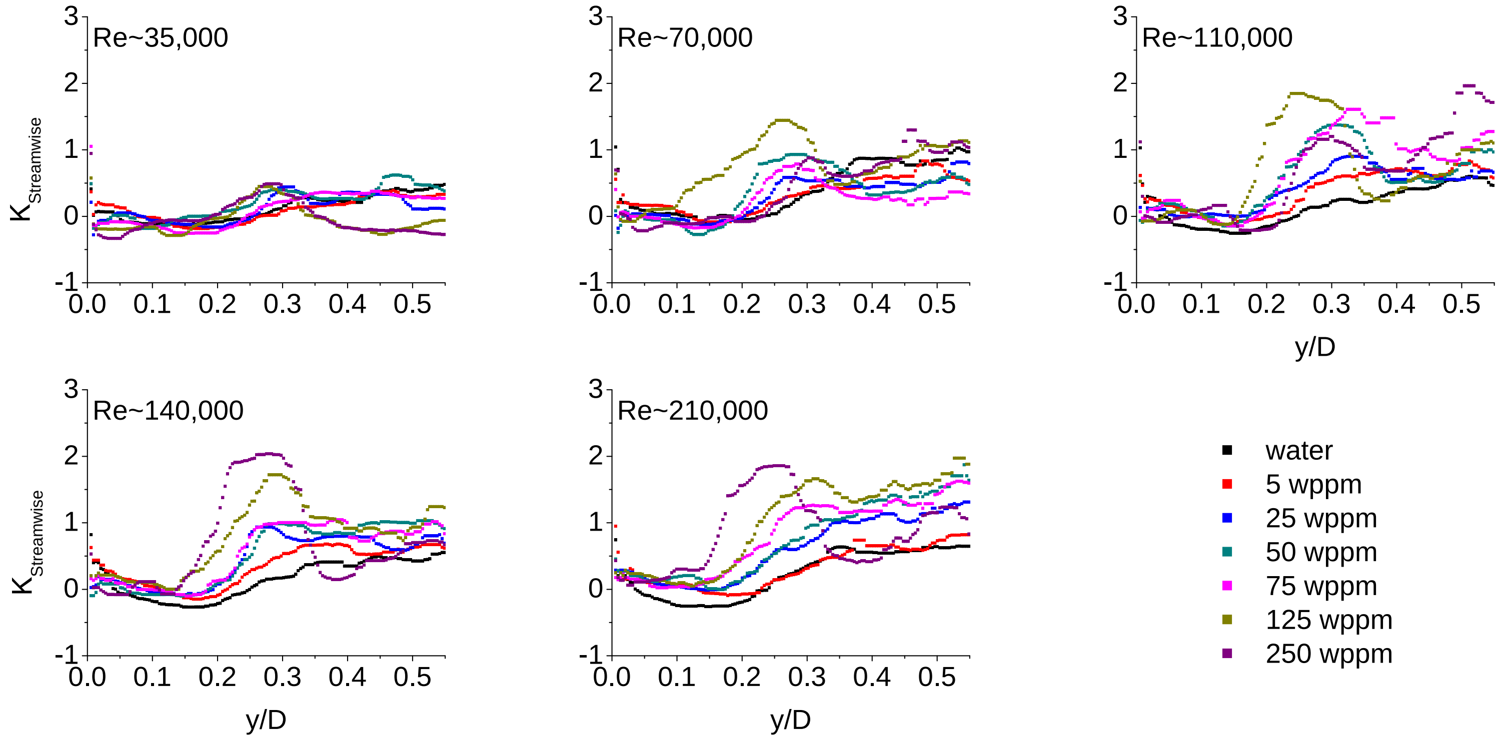

Figure 6.61: Dependence of the streamwise kurtosis $K_{\text{streamwise}}$ on the normalised distance from the wall for PEO8 solutions at different $Re$.

of the data in the inner near-wall region. As stated by Xu et al. [169] the turbulent events responsible for the spanwise kurtosis peak are very difficult to be captured during measurements due to the very intense spikes of spanwise velocities which happen only in the inner near-wall region and they are rare in time and in space.

### 6.2.9 Summary of the Section

In this Chapter the results of 2D particle image velocimetry measurements in turbulent pipe flow of water and dilute polymer solutions of PEO of three different molecular weight averages were presented. The novelty of the measurements with respect to previously reported experimental measurements is: i) the majority of the previous experimental measurements use LDV which is a very precise but one a point technique for the measurement of turbulent flow properties. However, measurements presented in this thesis provide the instantaneous turbulent flow images that are able to capture time dependent turbulent structures and their modification with increasing level of $DR$. ii) The majority of the published results deals with channel flow, with the exception of the work done in Prof Nieuwstadt lab [171], which is of smaller industrial importance but the optical turbulent flow measurements do not suffer of the refraction problems. Measurements presented in this thesis consist of a detailed 2D turbulent flow maps that can be further statistically treated in order to extract variables that are impossible to be measured with one point techniques, such as vorticity. iii) All published work focused only on the analysis of one polymer type, few polymer concentrations or few $Re$. Such results cannot capture the general trends by which the turbulent flow is modified by polymer drag reducing additives. Here measurements were performed using three different molecular weights of PEO, six polymer concentrations for each molecular weight and five $Re$ for each polymer concentration. Simple math gives 90 experiments + five measurements for water for each $Re$ + ten degradation experiments for the highest concentration of each polymer at the highest possible $Re$ (currently achievable), which gives in total 122 data points. Additionally it should be noted that the measurements were done for both half cross-section of the pipe and in the region near the pipe wall (however, the spacial resolution is not as good as for LDV experiments). Comparing the behaviour of different turbulent flow variables with the measured level of $DR$ under different flow condition allowed to find general relationships between DR and turbulent flow that are independent on $Re$. iv) typically the turbulent flow characterisation was performed at moderate $Re$, $Re < 20,000$. In the presented work the turbulent flow statistics is performed up to $Re = 210,000$.

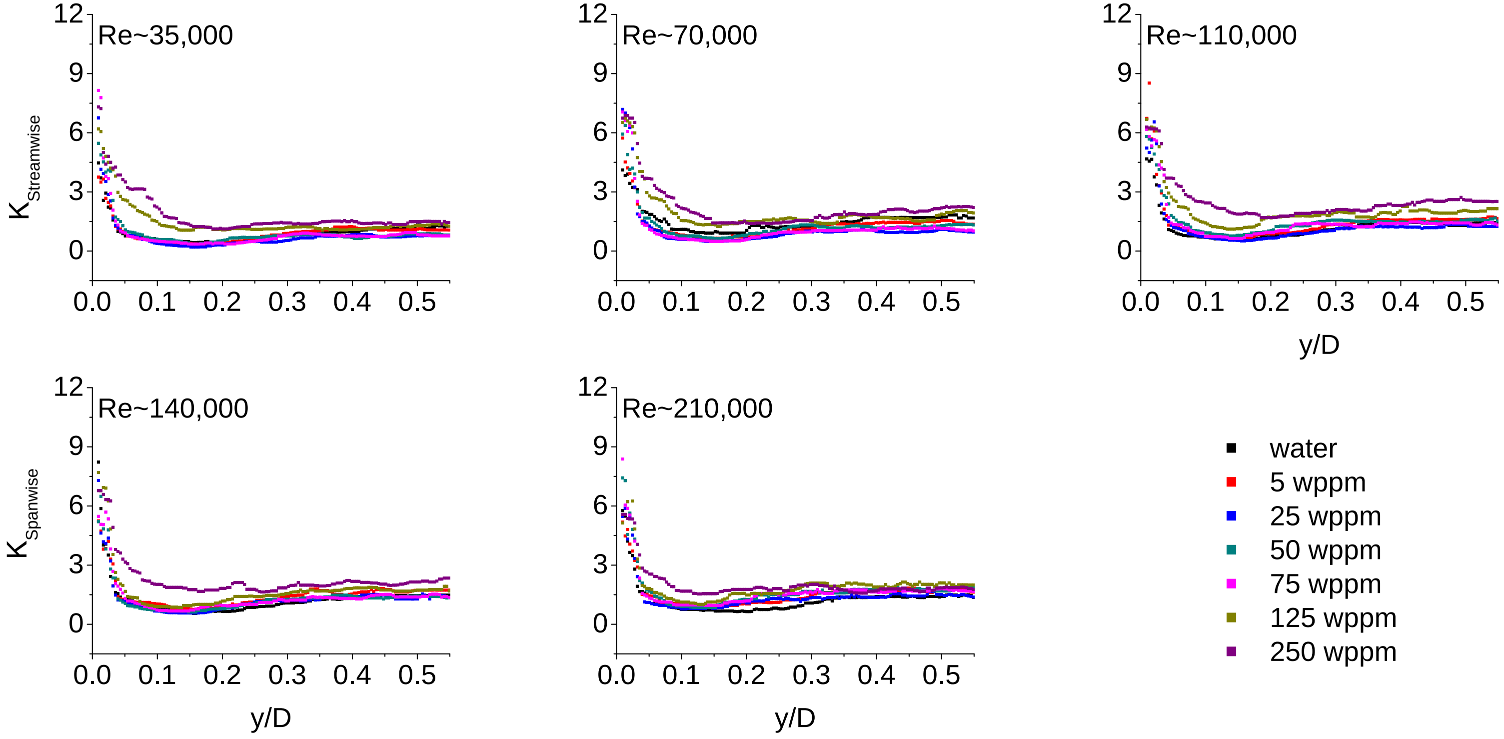

Figure 6.62: Dependence of the spanwise kurtosis $K_{\text{spanwise}}$ on the normalised distance from the wall for PEO8 solutions at different $Re$.

The main findings of this chapter are as follows:

- The instantaneous images of the turbulent flow revealed the presence of regions that contain coherent layers of intense instantaneous streamwise shear strain rate and 2D vorticity. Close inspection showed that the coherent layers are accompanied by a sharp change of the instantaneous streamwise velocity. Such an observation can be, according to the author, linked to the presence of heterogeneous flow that contains two different layers. It was proposed that the layer next to wall is made of elongated and entangled polymer molecules that create a 3D network in the inner near-wall region. Based on the polymer layer observation a new mechanism of polymer induced DR in turbulent flow was proposed. It utilises the classical DR models, where the polymer molecule is unraveled in the inner near-wall region, and adds a spacial component where a network of entangled polymer molecules is created. The typical observations such as: i) increased $DR$ with increasing polymer concentration, ii) the effect of polymer molecular weight, iii) the maximum DR asymptote and iv) the effect of pipe diameter on the level of $DR$ can be explained. Finally, experimental methods that should validate new DR mechanism were proposed.
- The turbulent flow statistics made on 122 experiments revealed general trends by which the turbulent flow is altered by polymer drag reducers. The results are summarised in Table 6.2. The drag reducers in general decrease the intensity of turbulent flow but also change the structure of turbulences. The trends observed for streamwise and spanwise skewness and kurtosis indicate that mainly, or even only, the structure of streamwise velocity fluctuations is changed but not the spanwise velocity fluctuations. Additionally, it was shown that the relative decrease of the intensity of turbulent flow is independent on $Re$. Such a finding, if verified, might help in scaling the DR effect to any $Re$ that can be found in industry and can provide values of turbulent flow variables such as: velocity fluctuation, Reynolds stress, vorticity and strain rate.

Table 6.2: The effect of drag reducers on the turbulent flow

| | Change with increasing drag reduction | | |
|---|---|---|---|
| Variable | How? | Where? | Note |
| $\overline{u}$ | $\sim$ | - | shift towards the laminar profile for the highest concentrations of PEO8 |
| $\overline{v}$ | $\sim$ | - | highly noisy results |
| $u^{'}$ | $\sim\downarrow\uparrow$ | $\sim$ inner near-wall region<br>$\downarrow$ the rest of the pipe | very high $DR$ is accompanied with an increase |
| $v^{'}$ | $\downarrow$ | entire pipe radius | |
| $\tau_{xy}^{'}$ | $\downarrow$ | entire pipe radius | |
| $\overline{\omega}_z$ | $\uparrow$ | inner near-wall region | further from the wall only high levels of $DR$ are accompanied with increase |
| $\omega_z^{'}$ | $\downarrow$ | entire pipe radius | |
| $\overline{\gamma}_{xy}$ | $\downarrow$ | inner near-wall region | the $\overline{\gamma}_{xy}$ values are negative and the absolute value of $\overline{\gamma}_{xy}$ value increases<br>further from the wall only high levels of $DR$ are accompanied with decrease |
| $\gamma_{xy}^{'}$ | $\downarrow$ | entire pipe radius | further from the wall the values level off for $DR > 55\%$ |
| $\overline{\gamma}_{yx}$ | $\sim$ | - | values fluctuate around zero with no visible trend |
| $\gamma_{yx}^{'}$ | $\downarrow$ | entire pipe radius | |
| $\overline{\gamma}_{xx}$ | $\sim$ | - | values fluctuate around zero with no visible trend |
| $\gamma_{xx}^{'}$ | $\downarrow$ | entire pipe radius | further from the wall the values level off for $DR > 55\%$ |
| $\overline{\gamma}_{yy}$ | $\sim$ | - | values fluctuate around zero with no visible trend |
| $\gamma_{yy}^{'}$ | $\downarrow$ | entire pipe radius | |
| $S_{streamwise}$ | $\downarrow_{\uparrow}$ | $y/D \sim 0.25_{y/D>0.3}$ | decrease at $y/D \sim 0.25$ and increase at $y/D > 0.3$ |
| $S_{spanwise}$ | $\sim$ | | PEO8 250 wppm shows slight increase over the entire pipe radius |
| $K_{streamwise}$ | $\uparrow$ | $y/D \sim 0.2 - 0.3$ | |
| $K_{spanwise}$ | $\sim$ | | PEO8 250 wppm shows slight increase over the entire pipe radius |

# Chapter 7

# Conclusions and Future Work

In this final Chapter of the thesis the concluding remarks of the findings presented in this work are presented. The Chapter contains an overall summary as well as suggestions for future work regarding polymer induced DR in turbulent flow.

The thesis was structured into three main parts: i) characterisation of the polymeric systems used in this work in quiescent conditions, ii) polymer characterisation using a commercial rheometer and iii) DR and turbulence characterisation in pipe flow using a flow facility designed by the author.

## 7.1 Conclusions

The use of a commercial rheometer for a DR characterisation was the main topic of the first half of the results part of the thesis. A modification of the analysis of the DR efficiency was proposed, which led to comparable results with those obtained using RDA and flow facilities. Additionally, a time dependent parameter was introduced into the analysis of the data, which allowed for a more precise characterisation of the time dependence of $DR$ in a strong shear flows. The comparison of the $DR$ observed by the rheometer and the flow facility is difficult. The instantaneous levels of $DR$ show very similar trends between the two different measuring techniques. However, the time dependent experiments revealed that the $DR$ results obtained from the rheometer cannot be directly compared to the time dependent tests in a turbulent pipe flow. The main reasons are: i) the level of $DR$ increases in the first few minutes of shearing, especially observed for high polymer concentrations, however the level of $DR$ continuously decreases over time in a turbulent pipe flow. ii) The flow between concentric cylinders exhibits different flow patterns in the range of shear rates that are possible to achieve in a commercial rheometer. The transition between different types of flow are moreover affected by the presence of polymer molecules. Therefore, several flow transitions can occur during the time dependent experiments that are performed in the concentric cylindrical cell. This is in direct contradiction with the flow in a pipe which is always fully turbulent during the time dependent experiments. Nevertheless, the commercial rheometer can be used to analyse the shear stability of polymer solutions. The time dependent behaviour of polymer solutions could be better correlated to the pipe flow when using RDA systems where an exponential decay of $DR$ over time was observed, which is similar to the observations made for the turbulent pipe flow.

Polymer characterisation in quiescent conditions revealed that polymers are present in a solution as individual molecules and also as aggregates containing a number of polymer molecules. It was possible to change the character of the aggregates for PAAm5 by changing the solvent quality. Three different aggregate states were identified: i) no aggregates in a very good solvent (25% v/v formamide water mixture), ii) loosely packed aggregates in a good solvent (water) and iii) tightly packed aggregates in a poor solvent (25% v/v 2-propanol water mixture). The time dependent DR measurements using a commercial rheometer showed that both non-aggregated solutions and solutions that contain loosely packed aggregates behave in the typical manner; where the level of $DR$ decreases over time. However, an unprecedented behaviour was observed for polymer solutions that contain tightly packed aggregates where the level of $DR$ was found to increase over time. The analysis of the molecular weight of fresh and degraded polymer solutions revealed that the polymer molecular weight decreased over time for all three different aggregated systems. To the best of the author's knowledge, this is the first time when an increase in the level of $DR$ during time dependent DR experiments was observed, which was accompanied by decreasing molecular weight. The finding led to a hypothesis that tightly packed polymer aggregates are slowly unraveled by the flow and act as a pool of fresh polymer molecules. It is also possible that the elongated and partially unraveled aggregates do interfere with the vortices and further decrease the frictional drag.

The analysis of the instantaneous images obtained from Particle Image Velocimetry measurements of the turbulent pipe flow revealed the presence of coherent layers of high values of the instantaneous 2D vorticity and low values of the instantaneous streamwise shear strain rate. Also, the instantaneous streamwise velocity sharply increased at the boundary defined by the coherent layer. It was found that the position of the coherent layers is influenced by polymer additives in a very similar way as the polymer additives influence the level of $DR$, which strongly suggests that the coherent layers are linked to the

DR mechanism. Based on the observation, “polymer layer mechanism” of DR was suggested. The idea is that the elongated polymer molecules create a 3D network structure in the inner near-wall region. The concept of the polymer layer was used to explain the common observations made for the DR effect such as: i) increased $DR$ with increasing polymer concentration, ii) the influence of polymer molecular weight on $DR$ and iii) the influence of pipe diameter on the measured level of $DR$. Also, observations that can be experimentally tested and would provide further evidence for the existence of the layer were proposed such as: i) increased viscosity in the inner near-wall region, ii) higher polymer concentration in the inner near-wall region when compared to the outer velocity-defect region and iii) different birefringence pattern in the inner near-wall and the outer velocity-defect region.

The intensity of turbulent flow was investigated in terms of: streamwise and spanwise velocity fluctuations, xy component of the Reynolds stress, 2D vorticity (both mean and fluctuations), streamwise shear strain rate (both mean and fluctuations), spanwise shear strain rate fluctuations, streamwise compression strain rate fluctuations and spanwise compression strain rate fluctuations. The influence of polymer molecular weight, concentration of polymer additives and Reynolds numbers on the mentioned variables was studied. The outcome of the detailed analysis are universal trends of the evolution of each parameter with the level of $DR$. Additionally, it was shown that the polymer additives not only influence the intensity of turbulent flow but also the structure of the turbulences. This conclusion was drawn based on the influence of polymer additives on both streamwise/spanwise skewness and kurtosis. It was found that polymers only influence the structure of the streamwise velocity fluctuations but not the spanwise velocity fluctuations. All the results on the evolution of the parameters mentioned with the level of $DR$ are summarised in Table 6.2.

## 7.2 Recommendations for Future Work

Richard Feynman called turbulence the most important unsolved problem of classical physics. Therefore, the modification of turbulences using polymer additives become even more challenging topic where not many questions are answered up to this date. When both issues are combined we finish with a broad undiscovered area that demands further investigation by theoretical, numerical and experimental techniques. Nevertheless, the current work focused only on the experimental framework of DR and the suggestions for future work will be based on the results and ideas presented in this thesis.

## Polymer Aggregates and Sustainable Drag Reduction

The presented work highlighted the potential of polymer aggregates for DR. It was demonstrated that the level of $DR$ can increase over time even if the polymer molecular weight decreases. The key parameter seems to be the polymer-polymer and polymer-solvent interactions as expressed by the second virial coefficient $A_2$. In polymer solutions with high $A_2$ the solute is present as individual well dissolved and expanded polymer molecules, whilst in solutions with small $A_2$ values polymer molecules tend to be collapsed and contain aggregates. Additionally, when the $A_2$ value approaches $\Theta$ conditions, the polymer aggregates change their packing density from loosely to tightly packed structures. DR characterisation of polymers with different $A_2$ values is therefore needed. Based on these results, an appropriate selection of polymers can be made in order to prepare a polymer blend that, once in a solution, dissolves into a mixture of polymer molecules, and loosely and tightly packed polymer aggregates. The composition of such a mixture can be tailored to obtain and maintain a maximum level of $DR$, even if mechanical degradation of the polymer molecules occurs. The potential application of the described procedure in industrial fields is quite obvious. If the flow conditions are known, the choice of a polymer blend can be tailored to a given time for which the maximum level of $DR$ should be maintained. Finally, the effect of polymer aggregates on the level of $DR$ should be tested within pipe flow in order to verify the results obtained from the measurements done in Taylor flow.

## Upgrades of the Flow Facility

The flow facility was designed in order to achieve $Re \simeq 1,000,000$. A quite simple upgrade that would consist of compressed air gas cylinders connected in a series to the main pressure in the pressure vessel which should provide enough pressure gradient to achieve the extraordinary $Re$ in the test pipe. Such a high $Re$ is not only interesting from the fundamental but also from the industrial point of view.

The other part of the flow facility that should be modified is the test section itself. As described, the test section was not hydrodynamically smooth. Replacement of the present test section with a truly hydrodynamically smooth pipe would certainly improve the quality of the measurements. Additionally, a revolver changer with different pipe diameters or roughness might be considered to be build. Such a changer would make the comparison of the effect of different pipe diameters on DR feasible and would make the flow facility unique.

Finally, the accessory for testing heterogeneous DR should be tested. So far only a centreline injector with variable nozzle diameters was manufactured but different geometries should also be considered such as: wall and near-wall injectors. If DR effect is explained, the explanation should cover both homogeneous and heterogeneous DR.

## Polymer Layer Mechanism

The turbulent flow instantaneous image analysis led to the conclusion that a 3D polymer network exists in the vicinity of the pipe wall. This resulted in the formulation of the "polymer layer mechanism", which can explain most of the experimental observations made in the past and in this work. Methods of verification were already proposed:

- The inner near-wall region should show an increased viscosity. The author is nevertheless not aware of a technique that could test it.
- Higher polymer concentration in the inner near-wall region when compared to the outer velocity-defect region. This prediction can be tested by Laser induced fluorescence when using polymer molecules marked with fluorescein dye. However, new design of visualisation cell should be made that would employ a true refractive index matching technique. One of the possible materials that can be used for the visualisation cell is FEP (fluorinated ethylene propylene) which has almost the same refractive index as water and can be used to produce extruded pipes.
- The birefringence technique can be used in order to distinguish between the near-wall 3D polymer network structure and the outer velocity-defect region that should contain mainly polymer molecules in random coil conformation.

## Universal trends

The PIV measurements performed in this work focused only on one polymer type, PEO. Therefore the trends of turbulent flow variables as a function of the level of $DR$ cannot be considered to be truly universal. The effect of different polymers such as PAAm, xanthan gum, carboxymethylcellulose or guar gum on the structure and intensity of turbulent flow should be analysed. The fundamental and industrial impact of the finding would be enormous if the trends presented in this work are found to be universal.

## Polymer Elongation and Unraveling

The mechanisms explaining the DR effect are linked to polymer extension in the inner near-wall region. However, surprisingly, no experimental finding of such elongation phenomenon has been published yet. Molecular conformations are typically deduced by spectroscopic methods. For instance, IR spectroscopy is able to reveal spectral changes related to different conformations of molecules by virtue of their relevant vibrational modes. Very complex molecules such as proteins have been suitably characterised in terms of their specific structures at different thermodynamic or experimental conditions by using IR or Raman spectroscopy. Experimental set-ups and proper accessories are required in order to perform measurements of polymer solutions under flow conditions. The author expects that statistically treated data from experiments over a long period of time can reveal spectral differences between the inner near-wall region and the outer velocity-defect region of polymer solutions flowing through a pipe that can be interpreted in terms of an elongation of the polymer molecules. Additional perspectives may involve the use of suitable agents (chemicals) able to form specific interactions with the elongated form of the polymer molecule in the inner near-wall region; successive spectroscopic analysis can then be performed under quiescent conditions after extraction of samples from the flow.

# Bibliography

[1] Mungal, G. and Somandepalli, V., Combined PIV and PLIF measurements in a polymer drag reduced boundary layer. Technical report, Thermosciences Division; Mechanical Engineering Department; Stanford (2006).

[2] Virk, P. and Baher, H. (1970) Effect of Polymer Concentration on Drag Reduction. *Chemical Engineering Science,* **25**(7), 1183–1189.

[3] Smith, R. and Tiederman, W. (March, 1991) The Mechanism of Polymer Thread Drag Reduction. *Rheologica Acta,* **30**(2), 103–113.

[4] den Toonder, J., Hulsen, M., Kuiken, G., and Nieuwstadt, F. (April, 1997) Drag Reduction by Polymer Additives in a Turbulent Pipe Flow: Numerical and Laboratory Experiments. *Journal of Fluid Mechanics,* **337**, 193–231.

[5] White, C., Somandepalli, V., and Mungal, M. (January, 2004) The Turbulence Structure of Drag-Reduced Boundary Layer Flow. *Experiments in Fluids,* **36**(1), 62–69.

[6] http://mvpprograms.com/help/P-mvpspc/distributions/SkewnessKurtosis, available: .

[7] Toms, B. (1948) In *Proceedings of the International Congress on Rheology* Proceedings of the International Congress on Rheology in Amsterdam: Vol. 2, pp. 135–141.

[8] Mysels, K. Flow of thickened fluids. (1949).

[9] White, C. and Mungal, M. (2008) Mechanics and Prediction of Turbulent Drag Reduction with Polymer Additives. *Annual Review of Fluid Mechanics,* **40**, 235–256.

[10] Truong, V., Drag Reduction Technologies. Technical report, DSTO Aeoronaoutical and Maritime Research Laboratory (2001).

[11] Choi, K. (May, 2000) European Drag-Reduction Research - Recent Developments and Current Status. *Fluid Dynamics Research,* **26**(5), 325–335.

[12] Virk, P. (1975) Drag Reduction Fundamentals. *AIChE Journal,* **21**(4), 625–656.

[13] Paterson, R. and Abernath, F. (1970) Turbulent Flow Drag Reduction and Degradation with Dilute Polymer Solutions. *Journal of Fluid Mechanics,* **43**, 689–710.

[14] Sung, J., Lim, S., Kim, C., Chung, H., and Choi, Y. (June, 2004) Mechanical Degradation Kinetics of Poly(ethylene oxide) in a Turbulent Flow. *Korea-Australia Rheology Journal,* **16**(2), 57–62.

[15] Vanapalli, S., Islam, M., and Solomon, M. (September, 2005) Scission-Induced Bounds on Maximum Polymer Drag Reduction in Turbulent Flow. *Physics of Fluids,* **17**(9), 2042489 (1–11).

[16] Cox, R. and Dunlop, E. (1977) Influence of Molecular Aggregates on Drag Reduction. *Physics of Fluids,* **20**(10), 203–213.

[17] Kim, C., Kim, J., Lee, K., Choi, H., and Jhon, M. (October, 2000) Mechanical Degradation of Dilute Polymer Solutions Under Turbulent Flow. *Polymer,* **41**(21), 7611–7615.

[18] Vlachogiannis, M., Liberatore, M., Mchugh, A., and Hanratty, T. (December, 2003) Effectiveness of a Drag Reducing Polymer: Relation to Molecular Weight Distribution and Structuring. *Physics of Fluids,* **15**(12), 3786–3794.

[19] Brostow, W., Lobland, H., Reddy, T., Singh, R., and White, L. (January, 2007) Lowering Mechanical Degradation of Drag Reducers in Turbulent Flow. *Journal of Materials Research,* **22**(1), 56–60.

[20] Shetty, A. and Solomon, M. (January, 2009) Aggregation in Dilute Solutions of High Molar Mass Poly(ethylene oxide) and its Effect on Polymer Turbulent Drag Reduction. *Polymer,* **50**(1), 261–270.

[21] Burger, E., Chorn, L., and Perkins, T. (1980) Studies of Drag Reduction Conducted Over A Broad Range of Pipeline Conditions When Flowing Prudhoe Bay Crude-Oil. *Journal of Rheology,* **24**(5), 603–626.

[22] Morgan, S. E. and McCormick, C. L. (1990) Water-Soluble Polymers in Enhanced Oil Recovery. *Progress in Polymer Science,* **15**(1), 103–145.

[23] Lucas, E., Mansur, C., Spinelli, L., and Queiros, Y. (2009) Polymer Science Applied to Petroleum Production. *Pure and Applied Chemistry,* **81**, 473–494.

[24] Singh, R., Singh, J., Deshmukh, S., Kumar, D., and Kumar, A. (1995) Application of Drag-Reducing Polymers in Agriculture. *Current Science,* **68**, 631–641.

[25] Phukan, S., Kumar, P., Panda, J., Nayak, B., Tiwari, K., and Singh, R. (March, 2001) Application of Drag Reducing Commercial and Purified Guargum for Reduction of Energy Requirement of Sprinkler Irrigation and Percolation Rate of the Soil. *Agricultural Water Management,* **47**(2), 101–118.

[26] Sellin, R. and Ollis, M. (1980) Polymer Drag Reduction in Large Pipes and Sewers - Results of Recent Fluid Trials. *Journal of Rheology,* **24**(6), 967–967.

[27] Sellin, R. (1988) Application of Polymer Drag Reduction to Sewer Flow Problems. *AIAA paper,* pp. 88–3666.

[28] Fabula, A. (1971) Fire-Fighting Benefits of Polymeric Friction Reduction. *Journal of Basic Engineering,* **93**(3), 453–455.

[29] Figueredo, R. and Sabadini, E. (March, 2003) Firefighting Foam Stability: the Effect of the Drag Reducer Poly(ethylene oxide). *Colloids and Surfaces A-Physicochemical and Engineering Aspects,* **215**(1-3), 77–86.

[30] Fish, F. (2006) The Myth and Reality of Gray's Pradox: Implication of Dolphin Drag Reduction for Technology. *Bioinspiration & Biomimetics,* **1**, 17–25.

[31] Bushnell, D. (1991) Drag Reduction in Nature. *Annual Review of Fluid Mechanics,* **23**, 65–79.

[32] Kot, E. and Bismarck, A. (2010) Polyacrylamide Containing Weak Temperature Labile Azo Links in the Polymer Backbone. *Macromolecules,* **43**, 6469–6475.

[33] Nadolink, R. and Haigh, W. (1995) Bibliography on Skin Friction Reduction with Polymers and Other Boundary-Layer Additives. *Applied Mechanics Reviews,* **48**(7), 351–459.

[34] Lumley, J. (1969) Drag Reduction by Additives. *Annual Review of Fluid Mechanics,* **1**, 367–384.

[35] Pazwash, H. (1984) Reduction Of Friction Drag In Pipes By Polymers: A Review. *Journal of Transportation Engineering,* **110**(2), 223–234.

[36] Bismarck, A., Chen, L., Griffin, J., Hewitt, G., and Vassilicos, J., Role of Polymers and Surfactants in Drag Reduction in Oil Industry Applications. Technical report, Imperial College Consultants Ltd. (2005).

[37] Brostow, W. (July, 2008) Drag Reduction in Flow: Review of Applications, Mechanism and Prediction. *Journal of Industrial and Engineering Chemistry,* **14**(4), 409–416.

[38] Berman, N. (1978) Drag Reduction By Polymers. *Annual Reviews Fluid Mechanics,* **10**, 47–64.

[39] Morgan, S. and McCormick, C. (1990) Water-Soluble Copolymers .32. - Macromolecular Drag Reduction - A Review of Predictive Theories and the Effects of Polymer Structure. *Progress in Polymer Science,* **15**(3), 507–549.

[40] Lumley, J. and Blossey, P. (1998) Control of Turbulence. *Annual Review of Fluid Mechanics,* **30**, 311–327.

[41] Singh, R. (2004) In *Encyclopedia of polymer science* pp. 519–563 John Wiley & Sons, Inc.

[42] Liberatore, M., Baik, S., Mchugh, A., and Hanratty, T. (November, 2004) Turbulent Drag Reduction of Polyacrylamide Solutions: Effect of Degradation on Molecular Weight Distribution. *Journal of Non-Newtonian Fluid Mechanics,* **123**(2-3), 175–183.

[43] Nakken, T., Tande, M., and Nystrom, B. (January, 2004) Effects of Molar Mass, Concentration and Thermodynamic Conditions on Polymer-Induced Flow Drag Reduction. *European Polymer Journal,* **40**(1), 181–186.

[44] Kim, C., Choi, H., Sung, J., Lee, H., and Jhon, M. (March, 2005) Effect of Solubility Parameter of Polymer-Solvent Pair on Turbulent Drag Reduction. *Macromolecular Symposia,* **222**, 169–174.

[45] Sohn, J., Kim, C., Choi, H., and Jhon, M. (May, 2001) Drag-Reduction Effectiveness of Xanthan Gum in a Rotating Disk Apparatus. *Carbohydrate Polymers,* **45**(1), 61–68.

[46] Kim, C., Lim, S., Choi, H., Sohn, J., and Jhon, M. (March, 2002) Characterization of Drag Reducing Guar Gum in a Rotating Disk Flow. *Journal of Applied Polymer Science,* **83**(13), 2938–2944.

[47] Deshmukh, S., Sudhakar, K., and Singh, R. (September, 1991) Drag-Reduction Efficiency, Shear Stability, and Biodegradation Resistance of Carboxymethyl Cellulose-Based and Starch-Based Graft-Copolymers. *Journal of Applied Polymer Science,* **43**(6), 1091–1101.

[48] Oliver, D. and Bakhtiyarov, S. (1983) Drag Reduction in Exceptionally Dilute Polymer-Solutions. *Journal of Non-Newtonian Fluid Mechanics,* **12**, 113–118.

[49] Hoyt, J. (1986) In *Encyclopedia of Polymer Science and Engineering* Vol. 5, p. 129.

[50] Makogon, B., Pavelko, M., Povkh, I., and Toryanik, A. (1984) Effect of the Temperature on the Hydrodynamic Efficiency and Stability of Polyethylen Oxide and Polyacryl Amide. *Translated from Inzhenerno-Fizicheskii Zhurnal,* **47**(4), 558–565.

[51] Kim, C., Sung, J., Choi, H., Kim, C., Chun, W., and Jhon, M. (December, 1999) Drag Reduction and Mechanical Degradation of Poly(ethylene oxide) in Seawater. *Journal of Chemical Engineering of Japan,* **32**(6), 803–811.

[52] Little, R. (1971) Drag Reduction in Capillary Tubes As A Function of Polymer Concentration and Molecular Weight. *Journal of Colloid and Interface Science,* **37**(4), 811–818.

[53] Virk, P., Merrill, E., Mickley, H., and Smith, K. (1967) The Toms Phenomenon: Turbulent Pipe Flow of Dilute Polymer Solutions. *Journal of Fluid Mechanics,* **30**(2), 305–328.

[54] Gampert, B. and Wagner, P. (1985) The Influence of Polymer Additives on Velocity and Temperature Fields. In Gampert, B., (ed.), *The Influence of Polymer Additives on Velocity and Temperature Fields*, pp. 71–85 Springer-Verlag.

[55] Hunston, D. and Reischman, M. (1975) The Role of Polydispersity in the Mechanism of Drag Reduction. *The Physics of Fluids,* **18**(12), 861080 (1–4).

[56] McCormick, C., Hester, R., Morgan, S., and Safieddine, A. (1990) Water-Soluble Copolymers. 30. Effects of Molecular Structure on Drag Reduction Efficiency. *Macromolecules,* **23**, 2124–2132.

[57] McCormick, C., Hester, R., Morgan, S., and Safieddine, A. (April, 1990) Water-Soluble Copolymers .31. Effects of Molecular-Parameters, Solvation, and Polymer Associations on Drag Reduction Performance. *Macromolecules,* **23**(8), 2132–2139.

[58] McCormick, C., Morgan, S., and Hester, R. (1991) Roles of Molecular-Structure and Solvation on Drag Reduction in Aqueous-Solutions. *Acs Symposium Series,* **467**, 320–337.

[59] Mumick, P., Hester, R., and McCormick, C. (September, 1994) Water-Soluble Copolymers .55. N-Isopropylacrylamide-Co-Acrylamide Copolymers in Drag Reduction - Effect of Molecular-Structure, Hydration, and Flow Geometry on Drag Reduction Performance. *Polymer Engineering and Science,* **34**(18), 1429–1439.

[60] Mumick, P., Welch, P., Salazar, L., and McCormick, C. (January, 1994) Water-Soluble Copolymers .56. Structure and Solvation Effects of Polyampholytes in Drag Reduction. *Macromolecules,* **27**(2), 323–331.

[61] Cowan, M., Garner, C., Hester, R., and McCormick, C. (October, 2001) Water-Soluble Polymers. LXXXIII. Correlation of Drag Experimentally Determined Drag Reduction Efficiency and Extensional Viscosity of High Molecular Weight Polymers in Dilute Aqueous Solution. *Journal of Applied Polymer Science,* **82**(5), 1222–1231.

[62] den Toonder, J., Draad, A., Kuiken, G., and Nieuwstadt, F. (July, 1995) Degradation Effects of Dilute Polymer-Solutions on Turbulent Drag Reduction in Pipe Flows. *Applied Scientific Research,* **55**(1), 63–82.

[63] Bueche, F. (1960) Mechanical Degradation of High Polymers. *Journal of Applied Polymer Science,* **4**, 101–106.

[64] Vanapalli, S., Ceccio, S., and Solomon, M. (November, 2006) Universal Scaling for Polymer Chain Scission in Turbulence. *Proceedings of the National Academy of Sciences of the United States of America,* **103**(45), 16660–16665.

[65] Moussa, T. and Tiu, C. (May, 1994) Factors Affecting Polymer Degradation in Turbulent Pipe-Flow. *Chemical Engineering Science,* **49**(10), 1681–1692.

[66] Nakano, A. and Minoura, Y. (1975) Effects of Solvent and Concentration on Scission of Polymers with High-Speed Stirring. *Journal of Applied Polymer Science,* **19**(8), 2119–2130.

[67] Zakin, J. and Hunston, D. (1978) Effects of Solvent Nature on Mechanical Degradation of High Polymer-Solutions. *Journal of Applied Polymer Science,* **22**(6), 1763–1766.

[68] Moussa, T., Tiu, C., and Sridhar, T. (August, 1993) Effect of Solvent on Polymer Degradation in Turbulent-Flow. *Journal of Non-Newtonian Fluid Mechanics,* **48**(3), 261–284.

[69] Brostow, W. (1983) Drag Reduction and Mechanical Degradation in Polymer-Solutions in Flow. *Polymer,* **24**(5), 631–638.

[70] Sung, J., Kim, C., Choi, H., Hur, B., Kim, J., and Jhon, M. (2004) Turbulent Drag Reduction Efficiency and Mechanical Degradation of Poly(acrylamide). *Journal of Macromolecular Science-Physics,* **B43**(2), 507–518.

[71] Rho, T., Park, J., Kim, C., Yoon, H., and Suh, H. (1996) Degradation of Polyacrylamide in Dilute Solution. *Polymer Degradation and Stability,* **51**(3), 287–293.

[72] Choi, H., Lim, S., Lai, P., and Chan, C. (August, 2002) Turbulent Drag Reduction and Degradation of DNA. *Physical Review Letters,* **89**(8), 088302 (1–4).

[73] Malik, S., Shintre, S., and Mashelkar, R. (January, 1993) Enhancing the Shear Stability in Drag-Reducing Polymers Through Molecular Associations. *Macromolecules,* **26**(1), 55–59.

[74] Khan, M. (November, 2006) Aggregate Formation in Poly(ethylene oxide) Solutions. *Journal of Applied Polymer Science,* **102**(3), 2578–2583.

[75] Polverari, M. and vandeVen, T. (August, 1996) Dilute Aqueous Poly(ethylene oxide) Solutions: Clusters and Single Molecules in Thermodynamic Equilibrium. *Journal of Physical Chemistry,* **100**(32), 13687–13695.

[76] Duval, M. and Boue, F. (November, 2007) Dilute Poly(ethylene oxide) Aqueous Solutions in a Turbulent Flow. *Macromolecules,* **40**(23), 8384–8388.

[77] Gardner, K., Murphy, W., and Geehan, T. (1978) Polyacrylamide Solution Aging. *Journal of Applied Polymer Science,* **22**(3), 881–882.

[78] Kulicke, W., Kniewske, R., and Klein, J. (1982) Propagation, Characterization, Solution Properties and Rheological Behavior of Polyacrylamide. *Progress in Polymer Science,* **8**(4), 373–468.

[79] Muller, G., Laine, J., and Fenyo, J. (1979) High-Molecular-Weight Hydrolyzed Polyacrylamides .1. Characterization - Effect of Salts on the Conformational Properties. *Journal of Polymer Science Part A-Polymer Chemistry,* **17**(3), 659–672.

[80] Liberatore, M., Pollauf, E., and Mchugh, A. (2003) Shear-Induced Structure Formation in Solutions of Drag Reducing Polymers. *Journal of Non-Newtonian Fluid Mechanics,* **113**, 193–208.

[81] Hecker, R., Fawell, P., and Jefferson, A. (December, 1998) The Agglomeration of High Molecular Mass Polyacrylamide in Aqueous Solutions. *Journal of Applied Polymer Science,* **70**(11), 2241–2250.

[82] Gust, G. (1976) Observations on Turbulent-Drag Reduction in a Dilute Suspension of Clay in Sea-Water. *Journal of Fluid Mechanics,* **75**, 29–47.

[83] White, A. (1975) Drag Reduction by Additives Review and Bibliography, , .

[84] Lumley, J. (1973) Drag Reduction in Turbulent flow by Polymer Additives. *Macromol. Rev.,* **7**, 263–290.

[85] McComb, W. (1990) The Physics of Fluid Turbulence - Chapter 14.2.

[86] McComb, W. and Rabie, L. (1982) Local Drag Reduction Due to Injection of Polymer-Solutions Into Turbulent-Flow in A Pipe .2. Laser-Doppler Measurements of Turbulent Structure. *AIChE Journal,* **28**(4), 558–565.

[87] Ptasinski, P., Nieuwstadt, F., Van den Brule, B., and Hulsen, M. (2001) Experiments in Turbulent Pipe Flow with Polymer Additives at Maximum Drag Reduction. *Flow Turbulence and Combustion,* **66**(2), 159–182.

[88] Kim, K. and Sirviente, A. (June, 2005) Turbulence Structure of Polymer Turbulent Channel Flow with and without Macromolecular Polymer Structures. *Experiments in Fluids,* **38**(6), 739–749.

[89] Willert, C. and Gharib, M. (1991) Digital Particle Image Velocimetry. *Experiments in Fluids,* **10**, 181–193.

[90] Mathieu, J. and Scott, J. (2000) An Introduction to Turbulent Flow, Cambridge University Press, .

[91] Kline, S., Reynolds, W., Schraub, F., and Runstadler, P. (1967) The Structure of Turbulent Boundary Layers. *Journal of Fluid Mechanics,* **30**, 741–773.

[92] Robinson, S. (1991) Coherent Motions in the Turbulent Boundary Layer. *Annual Review of Fluid Mechanics,* **23**, 601–639.

[93] Adrian, R., Meinhart, C., and Tomkins, C. (2000) Vortex Organization in the Outer Region of the Turbulent Boundary Layer. *Journal of Fluid Mechanics,* **422**, 1–54.

[94] Ganapathisubramani, B., Hutchins, N., Hambleton, W., Longmire, E., and Marusic, I. (2005) Investigation of Large-Scale Coherence in a Turbulent Boundary Layer Using Two-Point Correlations. *Journal of Fluid Mechanics,* **524**, 57–80.

[95] Bewersdorff, H. (1984) Heterogeneous Drag Reduction in Turbulent Pipe-Flow. *Rheologica Acta,* **23**(5), 522–543.

[96] Pinho, F. and Whitelaw, J. (1990) Flow of Non-Newtonian Fluids in a Pipe. *Journal of Non-Newtonian Fluid Mechanics,* **34**, 129–144.

[97] Warholic, M., Massah, H., and Hanratty, T. (October, 1999) Influence of Drag-Reducing Polymers on Turbulence: Effects of Reynolds Number, Concentration and Mixing. *Experiments in Fluids,* **27**(5), 461–472.

[98] Warholic, M., Heist, D., Katcher, M., and Hanratty, T. (November, 2001) A Study with Particle-Image Velocimetry of the Influence of Drag-Reducing Polymers on the Structure of Turbulence. *Experiments in Fluids,* **31**(5), 474–483.

[99] Vlachogiannis, M. and Hanratty, T. (May, 2004) Influence of Wavy Structured Surfaces and Large Scale Polymer Structures on Drag Reduction. *Experiments in Fluids,* **36**(5), 685–700.

[100] Baik, S., Vlachogiannis, M., and Hanratty, T. (October, 2005) Use of Particle Image Velocimetry to Study Heterogeneous Drag Reduction. *Experiments in Fluids,* **39**(4), 637–650.

[101] Wei, T. and Willmarth, W. (December, 1992) Modifying Turbulent Structure with Drag-Reducing Polymer Additives in Turbulent Channel Flows. *Journal of Fluid Mechanics,* **245**, 619–641.

[102] Oldroyd, J. A Suggested Method of Detecting Wall-Effects in Turbulent Flow Through Tubes. *Proc. 1st Intern. Congr. Rheol. North Holland.,* pp. 130–134.

[103] Elperin, I., Smolskii, B., and Leventhal, L. (1967) Decreasing the Hydrodynamic Resistance of Pipelines.. *Intrnational Chemical Engineering,* **7**, 276–295.

[104] Ryskin, G. (May, 1987) Calculation of the Effect of Polymer Additive in A Converging Flow. *Journal of Fluid Mechanics,* **178**, 423–440.

[105] Ryskin, G. (November, 1987) Turbulent Drag Reduction by Polymers - A Quantitative Theory. *Physical Review Letters,* **59**(18), 2059–2062.

[106] Tabor, M. and de Gennes, P. (October, 1986) A Cascade Theory of Drag Reduction. *Europhysics Letters,* **2**(7), 519–522.

[107] de Gennes, P. (1990) Introduction to Polymer Dynamics, Cambridge University Press, .

[108] L'Vov, V., Pomyalov, A., Procaccia, I., and Tiberkevich, V. (June, 2004) Drag Reduction by Polymers in Wall Bounded Turbulence. *Physical Review Letters,* **92**(24), 244503 (1–4).

[109] Sher, I. and Hetsroni, G. (April, 2008) A Mechanistic Model of Turbulent Drag Reduction by Additives. *Chemical Engineering Science,* **63**(7), 1771–1778.

[110] Choi, H. and Jhon, M. (September, 1996) Polymer-Induced Turbulent Drag Reduction. *Industrial & Engineering Chemistry Research,* **35**(9), 2993–2998.

[111] Kim, C., Choi, H., Kim, C., and Jhon, M. (August, 1998) Drag Reduction Characteristics of Polysaccharide Xanthan Gum. *Macromolecular Rapid Communications,* **19**(8), 419–422.

[112] Cowan, M., Hester, R., and McCormick, C. (October, 2001) Water-Soluble Polymers. LXXXII. Shear Degradation Effects on Drag Reduction Behavior of Dilute Polymer Solutions. *Journal of Applied Polymer Science,* **82**(5), 1211–1221.

[113] Kim, C., Jo, D., Choi, H., Kim, C., and Jhon, M. (2001) A High-Precision Rotating Disk Apparatus for Drag Reduction Characterization. *Polymer Testing,* **20**(1), 43–48.

[114] Andereck, C., Liu, S., and Swinney, H. (March, 1986) Flow Regimes in A Circular Couette System with Independently Rotating Cylinders. *Journal of Fluid Mechanics,* **164**, 155–183.

[115] Keller, A., Kiss, G., and Mackley, M. (1975) Polymer Drag Reduction in Taylor Vortices. *Nature,* **257**(5524), 304–305.

[116] Groisman, A. and Steinberg, V. (August, 1996) Couette-Taylor flow in a dilute polymer solution. *Physical Review Letters,* **77**(8), 1480–1483.

[117] Nakken, T., Tande, M., and Elgsaeter, A. (February, 2001) Measurements of Polymer Induced Drag Reduction and Polymer Dcission in Taylor Flow Using Standard Double-Gap Sample Holders with Axial Symmetry. *Journal of Non-Newtonian Fluid Mechanics,* **97**(1), 1–12.

[118] Coles, D. (1965) Transition in Circular Couette Flow. *Journal of Fluid Mechanics,* **21**, 385–425.

[119] Bizotto, V. and Sabadini, E. (November, 2008) Poly(ethylene oxide) x Polyacrylamide. Which One is More Efficient to Promote Drag Reduction in Aqueous Solution and Less Degradable?. *Journal of Applied Polymer Science,* **110**(3), 1844–1850.

[120] Gasljevic, K., Aguilar, G., and Matthys, E. (January, 2001) On Two Distinct Types of Drag-Reducing Fluids, Diameter Scaling, and Turbulent Profiles. *Journal of Non-Newtonian Fluid Mechanics,* **96**(3), 405–425.

[121] Berman, N. and George, W. (1974) Onset of Drag Reduction in Dilute Polymer-Solutions. *Physics of Fluids,* **17**(1), 250–251.

[122] Sreenivasan, K. and White, C. (April, 2000) The Onset of Drag Reduction by Dilute Polymer Additives, and the Maximum Drag Reduction Asymptote. *Journal of Fluid Mechanics,* **409**, 149–164.

[123] Escudier, M., Presti, F., and Smith, S. (March, 1999) Drag Reduction in the Turbulent Pipe Flow of Polymers. *Journal of Non-Newtonian Fluid Mechanics,* **81**(3), 197–213.

[124] Yu, J., Zakin, J., and Patterson, G. (1979) Mechanical Degradation of High Molecular Weight Polymers in Dilute Solution. *Journal of Applied Polymer Science,* **23**(8), 2493–2512.

[125] Gasljevic, K., Aguilar, G., and Matthys, E. (August, 1999) An Improved Diameter Scaling Correlation for Turbulent Flow of Drag-Reducing Polymer Solutions. *Journal of Non-Newtonian Fluid Mechanics,* **84**(2-3), 131–148.

[126] Vleggaar, J. and Tels, M. (1973) Drag Reduction by Polymer Threads. *Chemical Engineering Science,* **28**(3), 965–968.

[127] Hoyt, J. and Sellin, R. (July, 1991) Polymer Threads and Drag Reduction. *Rheologica Acta,* **30**(4), 307–315.

[128] Saadeh, M. and Strehlow, A. (July, 1993) The Influence of the Injection System on Drag Reduction. *Rheologica Acta,* **32**(4), 398–404.

[129] Kim, K. and Sirviente, A. (January, 2007) Wall Versus Centerline Polymer Injection in Turbulent Channel Flows. *Flow Turbulence and Combustion,* **78**(1), 69–89.

[130] Frings, B. (January, 1988) Heterogeneous Drag Reduction in Turbulent Pipe Flows Using Various Injection Techniques. *Rheologica Acta,* **27**(1), 92–110.

[131] Devanand, K. and Selser, J. (February, 1990) Polyethylene Oxide Does Not Necessarily Aggregate in Water. *Nature,* **343**(6260), 739–741.

[132] Sakai, T. (1968) Huggins Constant k' for Flexible Chain Polymers. *Journal of Polymer Science Part A-2,* **6**, 1535–1549.

[133] Brandrup, J., Immergut, E., and Grulke, E. (1999) Polymer Handbook 4th edition, A Wiley-Interscience publication; John Wiley & Sons, inc., .

[134] Ying, Q. and Chu, B. (1987) Overlap Concentration of Macromolecules in Solution. *Macromolecules,* **20**(2), 362–366.

[135] Kratochvil, P. (1982) Advances in Classical Light Scattering from Polymer Solutions. *Pure and Applied Chemistry,* **54**(2), 379–393.

[136] Chu, B. (2007) Laser Light Scattering : Basic Principles and Practice, Vol. 2nd, Dover Publications, .

[137] Gruber, E. and Schurz, J. (1973) Die Erkennung von Ubermolekularen Gelen in Polymerlosungen mit Hilfe der Lichtstreuung. *Die Angewandte Makromolekulare Chemie,* **29**(30), 121–136.

[138] Wallenfels, K., Sund, H., and Burchard, W. (1962) On the Effect of BZ 55 on the Aggregation of Insulin in the Presence of Zinc Ions. *Biochem Z,* **335**, 315–324.

[139] de Groot, A. and Hamre, W. (1993) Characterization of High-Molecular-Mass Polyethylenes by Gel Permeation Chromatography-Low-Angle Laser-Light Scattering. *Journal of Chromatography,* **648**, 33–39.

[140] Kabátek, Z., Gas, B., and Vohlídal, J. (1997) Gel Permeation Chromatography of Polymers Degrading Randomly in the Column: Theoretical Treatment and Practical Aspects. *Journal of Chromatography A.,* **786**, 209–218.

[141] Mendichi, R. (2009) Encyclopedia of Chromatography, Third Edition Chapter: Polymers: Degradation in GPC/SEC Columns, , .

[142] Zigon, M., The, N., Cheng, S., and GrubisicGallot, Z. (1997) Degradation of High Molecular Weight Polystyrenes During the SEC Separation Process, as Demonstrated by SEC Coupled with LALLS and by Static Light Scattering. *Journal of Liquid Chromatography and Related Technologies,* **20**, 2155–2167.

[143] Striegel, A., Isenberg, S., and Cote, G. (2009) An SEC/MALS Study of Alternan Degradation During Size-Exclusion Chromatographic Analysis. *Analytical and Bioanalytical Chemistry,* **394**, 1887–1893.

[144] Dickerson, J., Flesher, L., and Hester, R. (July, 1994) A High Reynolds-Number Rotating-Disk Rheometer. *Journal of Applied Polymer Science,* **53**(2), 151–159.

[145] Lee, S., Sengupta, S., and Wei, T. (1995) Effect of Polymer Additives on Gortler Vortices in Taylor-Coutte Flow. *Journal of Fluid Mechanics,* **282**, 115–129.

[146] Yi, M. and Kim, C. (October, 1997) Experimental Studies on the Taylor Instability of Dilute Polymer Solutions. *Journal of Non-Newtonian Fluid Mechanics,* **72**(2-3), 113–139.

[147] Camail, M., Margaillan, A., Maesano, J., Thuret, S., and Vernet, J. (June, 1998) Synthesis and Structural Study of New Copolymers, Based on Acrylamide and N-acryloyl Acids, with Persistent Drag Reduction Activity. *Polymer,* **39**(14), 3187–3192.

[148] Dallas, V.; Vassilicos, J. H. G. (2009) Stagnation Point von Karman Coefficient. *Physical Reviewe. E, Statistical, Nonlinear, and Soft Matter Physics,* **80**, 046306 (1–13).

[149] Brostow, W., Ertepinar, H., and Singh, R. (November, 1990) Flow of Dilute Polymer-Solutions - Chain Conformations and Degradation of Drag Reducers. *Macromolecules,* **23**(24), 5109–5118.

[150] Bello, J., Muller, A., and Saez, A. (January, 1996) Effect of Intermolecular Cross Links on Drag Reduction by Polymer Solutions. *Polymer Bulletin,* **36**(1), 111–118.

[151] Wu, S. and Shanks, R. (2003) Conformation of Polyacrylamide in Aqueous Solution with Interactive Additives and Cosolvents. *Journal of Applied Polymer Science,* **89**(11), 3122–3129.

[152] Raos, G. and Allegra, G. (October, 1997) Macromolecular Clusters in Poor-Solvent Polymer Solutions. *Journal of Chemical Physics,* **107**(16), 6479–6490.

[153] Owen, A., Fawell, P., Swift, J., and Farrow, J. (November, 2002) The Impact of Polyacrylamide Flocculant Solution Age on Flocculation Performance. *International Journal of Mineral Processing,* **67**(1-4), 123–144.

[154] Ho, D., Hammouda, B., and Kline, S. (January, 2003) Clustering of Poly(ethylene oxide) in Water Revisited. *Journal of Polymer Science Part B-Polymer Physics,* **41**(1), 135–138.

[155] Nguyen, T. and Kausch, H. (1992) Chain Extension and Degradation in Convergent Flow. *Polymer,* **33**(12), 2611–2621.

[156] Nakagawa, S. and Hanratty, T. (November, 2001) Particle Image Velocimetry Measurements of Flow Over a Wavy Wall. *Physics of Fluids,* **13**(11), 3504–3507.

[157] Kalashnikov, V. and Tsiklauri, M. (December, 1996) Supermolecular Structures and Flow Birefringence in Polymer Solutions. *Colloid and Polymer Science,* **274**(12), 1119–1128.

[158] Interthal, W. and Wilski, H. (1985) Drag Reduction Experiments with Very Large Pipes. *Colloid & Polymer Science,* **263**(3), 1435–1536.

[159] Choi, H., Kim, C., and Jhon, M. (July, 1999) Universal Drag Reduction Characteristics of Polyisobutylene in a Rotating Disk Apparatus. *Polymer,* **40**(16), 4527–4530.

[160] den Toonder, J., Nieuwstadt, F., and Kuiken, G. (March, 1995) The Role of Elongational Viscosity in the Mechanism of Drag Reduction by Polymer Additives. *Applied Scientific Research,* **54**(2), 95–123.

[161] Hoyer, K., Gyr, A., and Tsinober, A. (1995) On the Mechanism of Drag Reduction in Dilute Polymer Solutions. *Applied Scientific Research,* **55**(4), 289–295.

[162] Popper, K. (1963) Conjectures and Refutations: The Growth of Scientific Knowledge, , .

[163] Scrivener, O., Berner, C., Cressely, R., Hocquart, R., Sellin, R., and Vlachos, N. (1979) Dynamical Behavior of Drag-Reducing Polymer-Solutions. *Journal of Non-Newtonian Fluid Mechanics,* **5**(APR), 475–495.

[164] Kim, K., Islam, M., Shen, X., Sirviente, A., and Solomon, M. (November, 2004) Effect of Macromolecular Polymer Structures on Drag Reduction in a Turbulent Channel Flow. *Physics of Fluids,* **16**(11), 4150–4162.

[165] den Toonder, J. Drag Reduction by Polymer Additives in a Turbulent Pipe Flow: Laboratory and Numerical Experiments PhD thesis Technische Universiteit Delft (1995).

[166] Hou, Y., Somandepalli, V., and Mungal, M. (2008) Streamwise Development of Turbulent Boundary-Layer Drag Reduction with Polymer Injection. *Journal of Fluid Mechanics,* **597**, 31–66.

[167] Durst, F., Jovanovic, J., and Sender, J. (1995) LDA Measurements in the Near-Wall Region of a Turbulent Pipe Flow. *Journal of Fluid Mechanics,* **295**, 305–335.

[168] Eggels, J., Unger, F., Weiss, M., Westerweel, J., Adrian, R., Friedrich, R., and Nieuwstadt, F. (1994) Fully Developed Turbulent Pipe Flow: A Comparison Between Direct Numerical Simulation and Experiment. *Journal of Fluid Mechanics,* **268**, 175.

[169] Xu, C., Zhang, Z., den Toonder, J., and Nieuwstadt, F. (1996) Origin of High Kurtosis Levels in the Viscous Sublayer. *Physics of Fluids,* **8**, 1938–1944.

[170] Kim, J., Moin, P., and Moser, R. (1987) Turbulence Statistics in a Fully Developed Channel Flow at Low Reynolds Numbers. *Journal of Fluid Mechanics,* **177**, 133–166.

[171] Westerweel, J. and Boersma, B. (2007) Turbulence Plus. *Flow Turbulence and Combustion,* **79**, 191–206.

# Appendix A

# Additional Results of Chapter 6

## A.1 Gross Flow Measurements

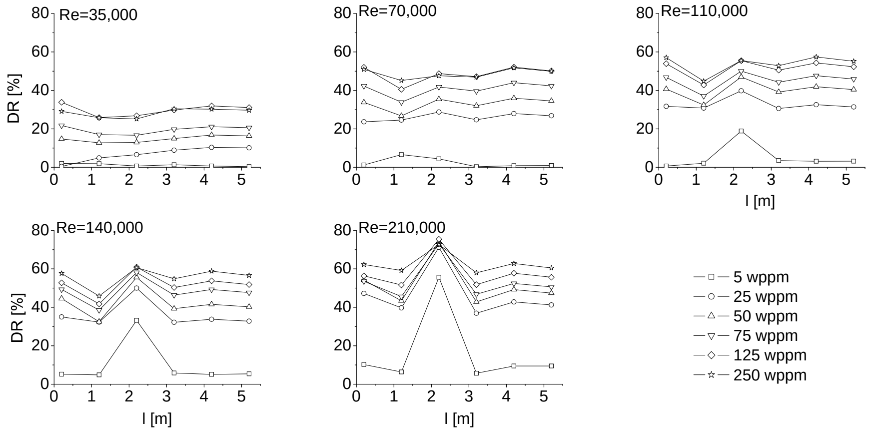

Figure A.1: The evolution of the level of $DR$ with length for PEO4 solutions.

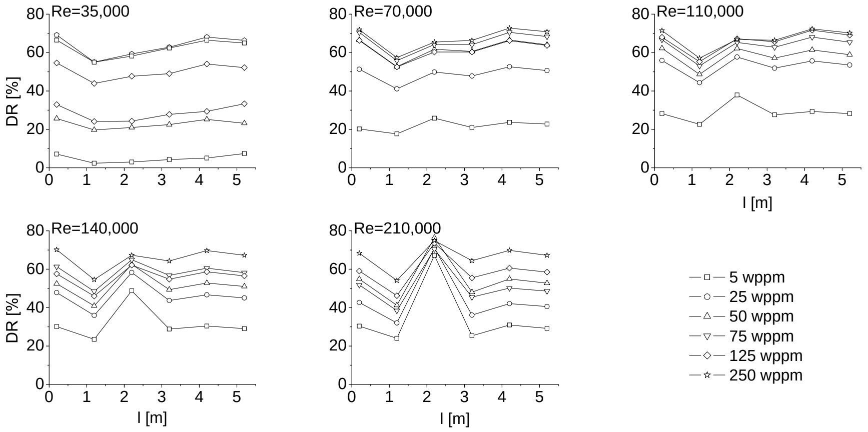

Figure A.2: The evolution of the level of $DR$ with length for PEO8 solutions.

## A.2 Statistics of Velocity Fluctuations

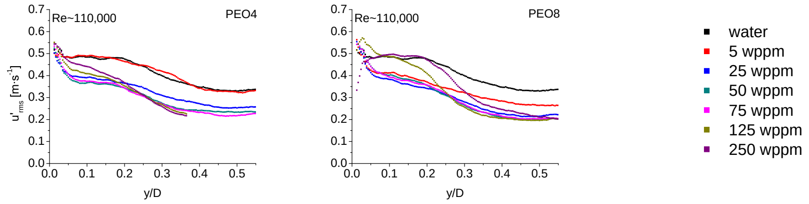

Figure A.4: Dependence of rms streamwise velocity fluctuations ($u'_{\mathrm{rms}}$) on the normalised distance from the wall for PEO4 and PEO8 solutions at $Re = 110,000$.

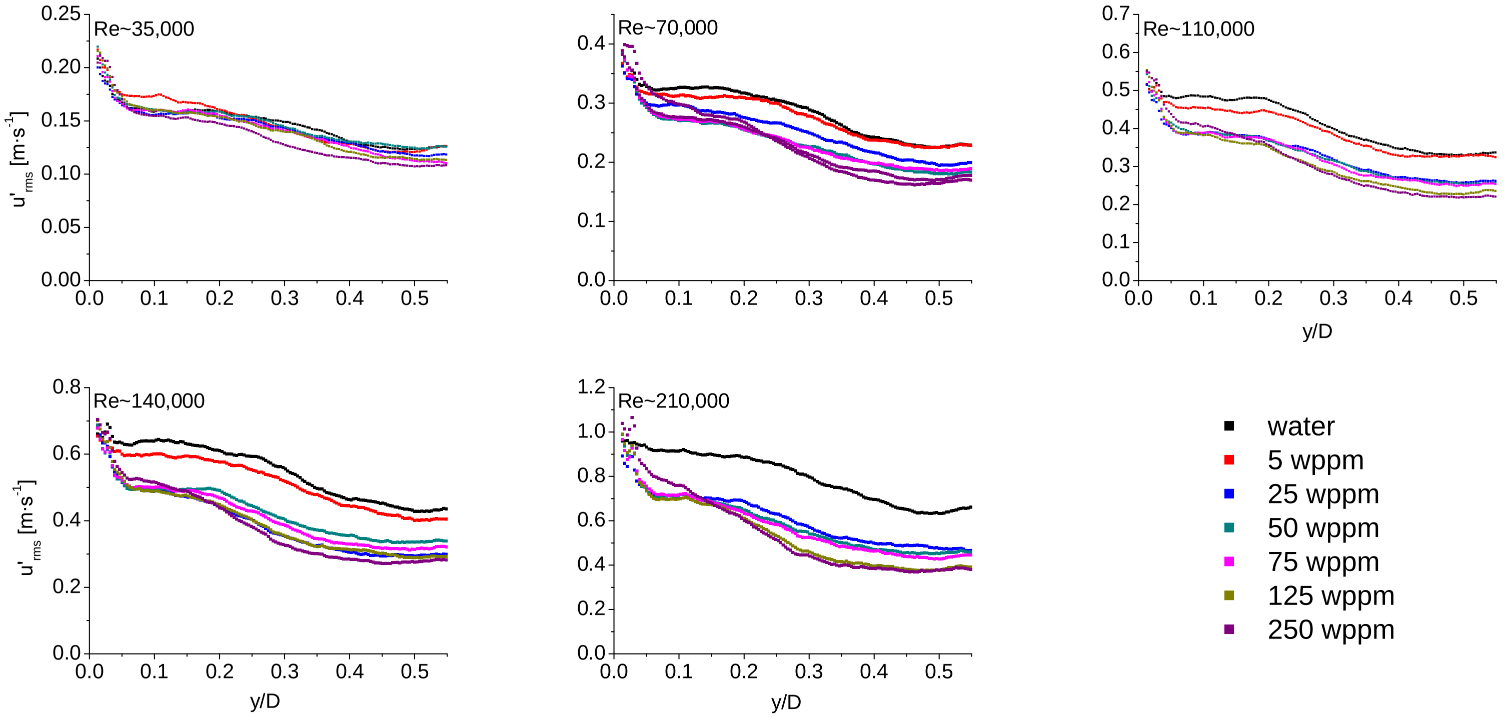

Figure A.3: Dependence of rms streamwise velocity fluctuations ($u'_{\mathrm{rms}}$) on the normalised distance from the wall for PEO2 solutions at various $Re$.

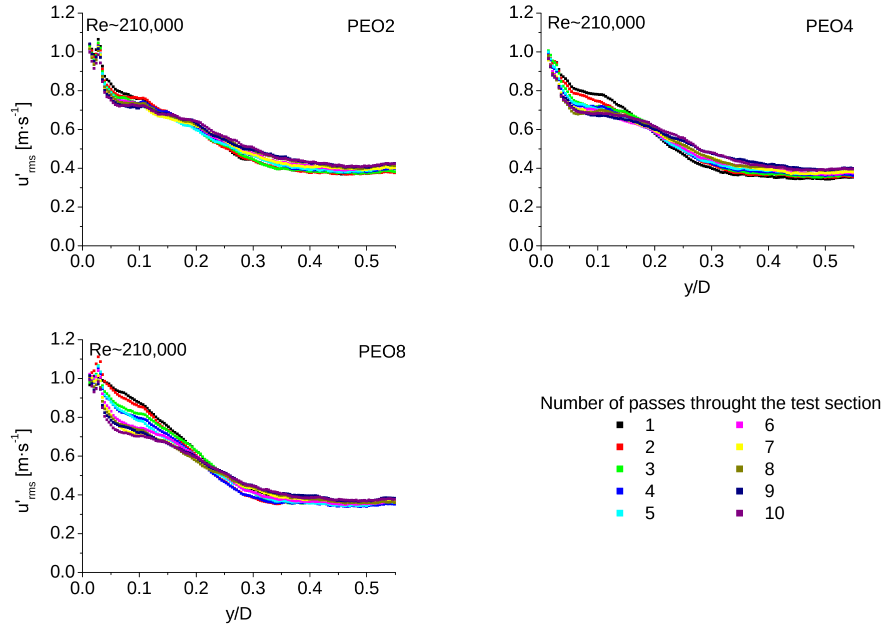

Figure A.5: Dependence of rms streamwise velocity fluctuations ($u'_{\text{rms}}$) on the normalised distance from the wall for degradation experiments of PEO2, PEO4 and PEO8 solutions at $Re = 210,000$.

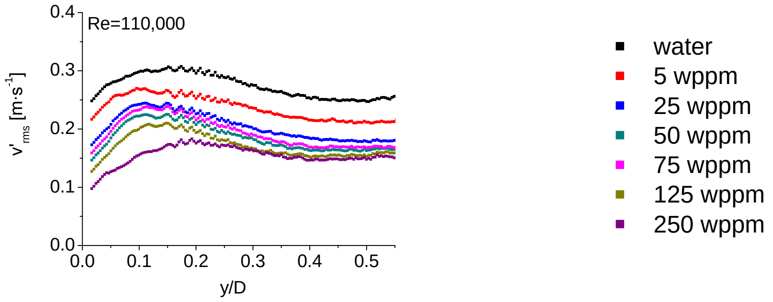

Figure A.8: Dependence of rms spanwise velocity fluctuations ($v'_{\text{rms}}$) on the normalised distance from the wall for PEO8 solutions at $Re = 110,000$.

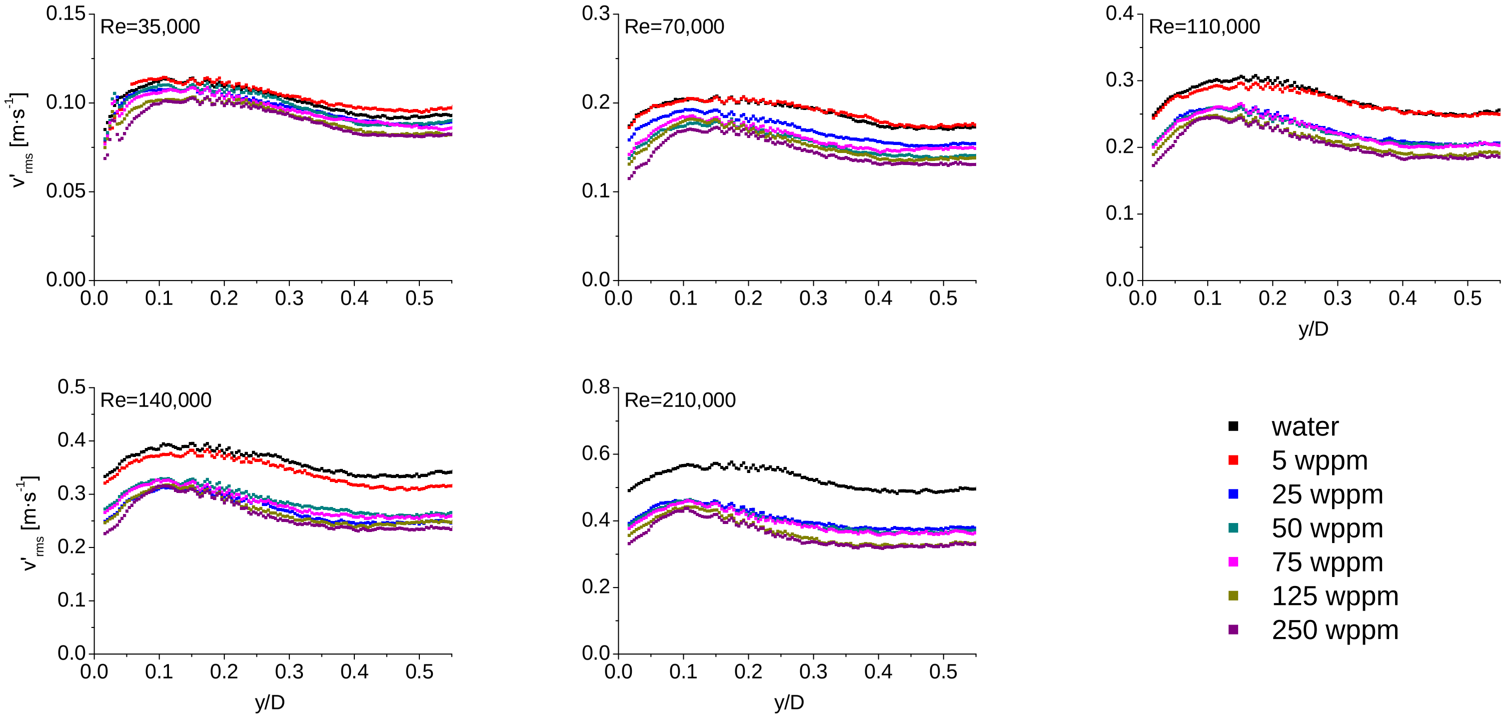

Figure A.6: Dependence of rms spanwise velocity fluctuations ($v'_{\mathrm{rms}}$) on the normalised distance from the wall for PEO2 solutions at various $Re$.

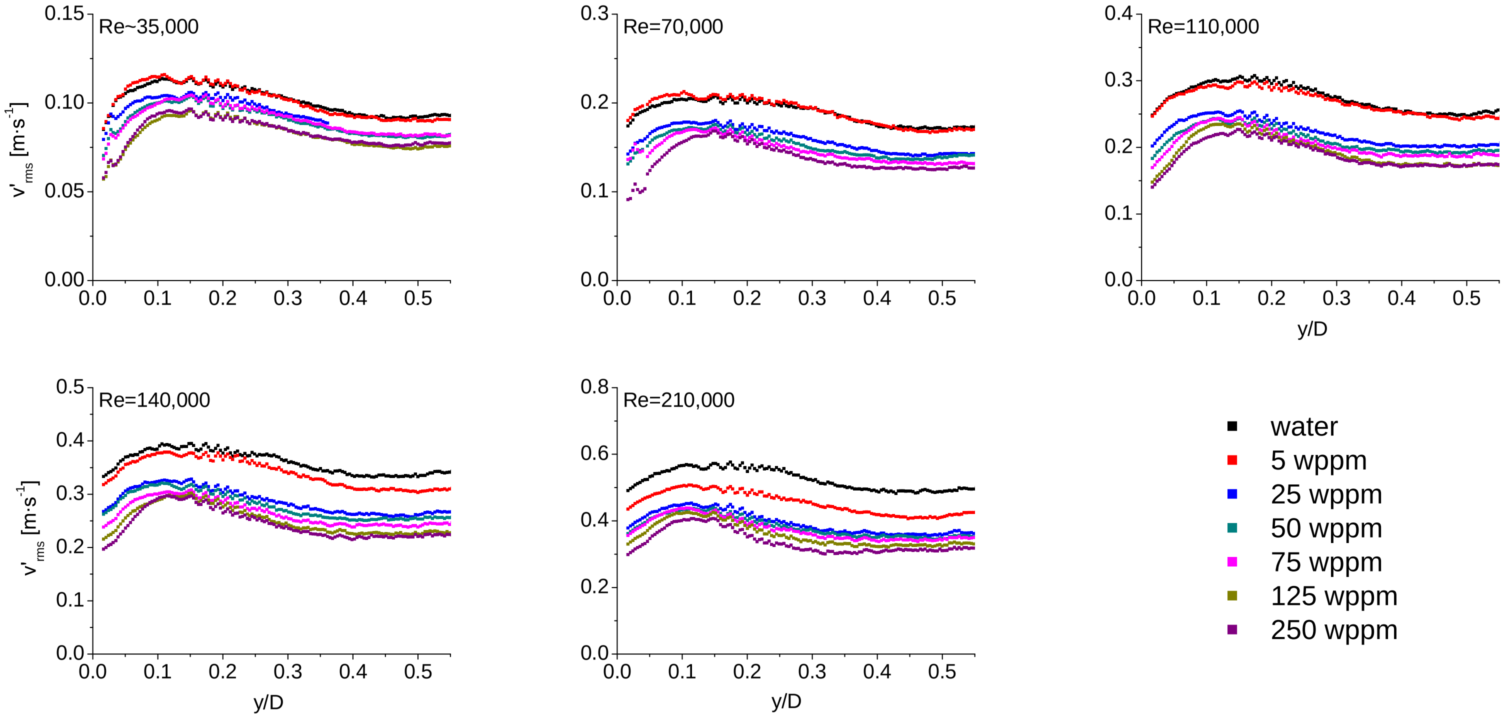

Figure A.7: Dependence of rms spanwise velocity fluctuations ($v'_{\mathrm{rms}}$) on the normalised distance from the wall for PEO4 solutions at various $Re$.

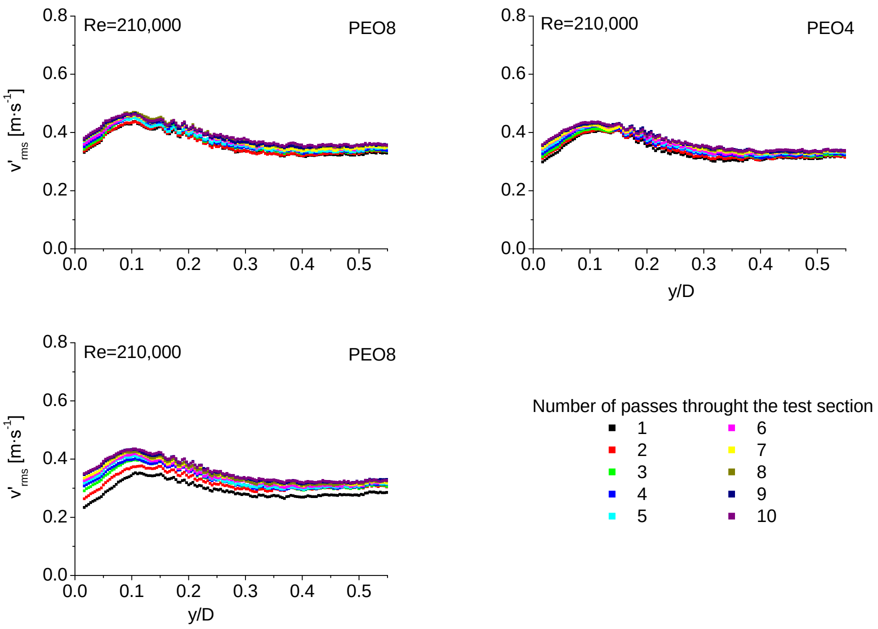

Figure A.9: Dependence of rms streamwise velocity fluctuations ($v'_{\mathrm{rms}}$) on the normalised distance from the wall for degradation experiments of PEO2, PEO4 and PEO8 solutions at $Re = 210,000$.

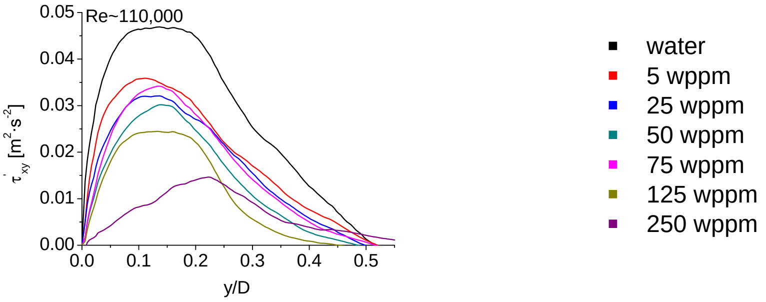

Figure A.12: Dependence of Reynolds stress $\tau'_{xy}$ on the normalised distance from the wall for PEO8 solutions at $Re = 110,000$.

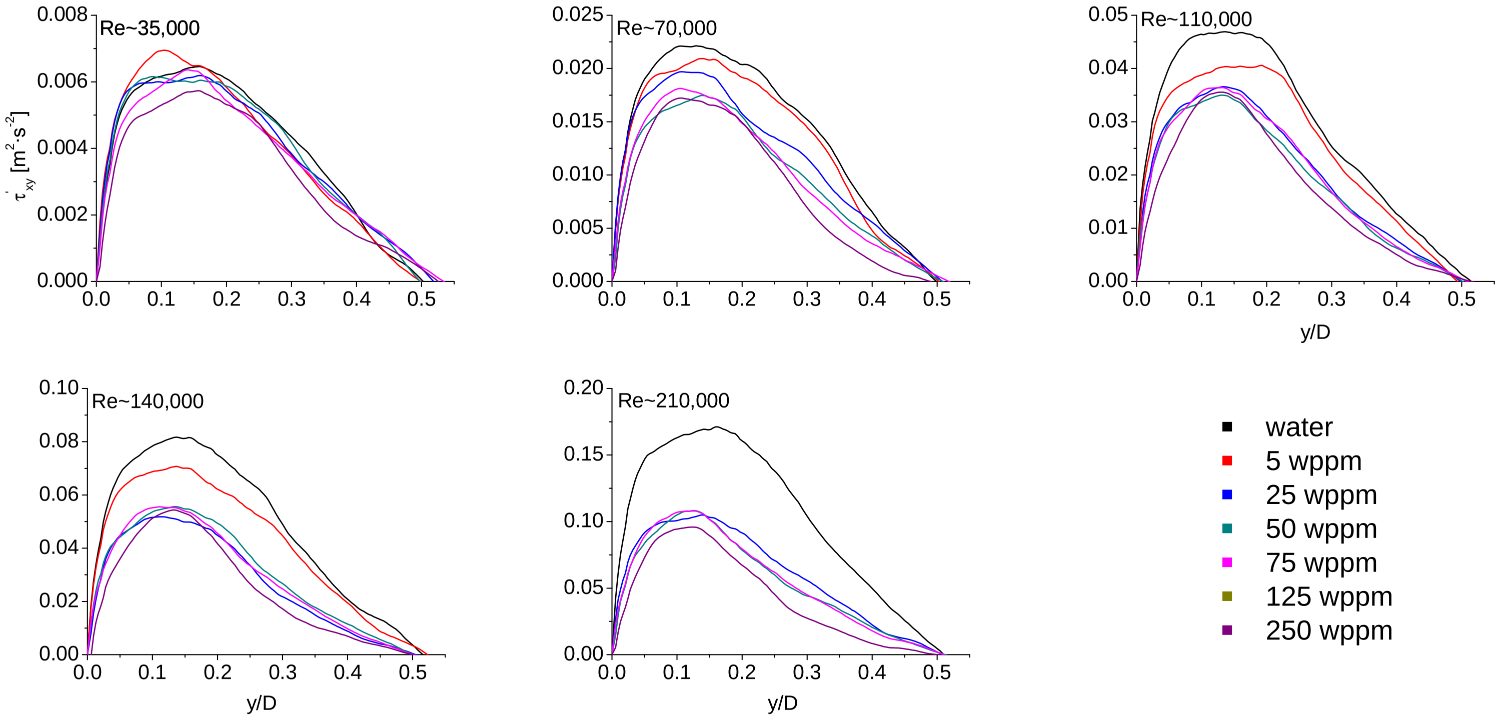

Figure A.10: Dependence of Reynolds stress $\tau'_{xy}$ on the normalised distance from the wall for PEO2 solutions at various $Re$.

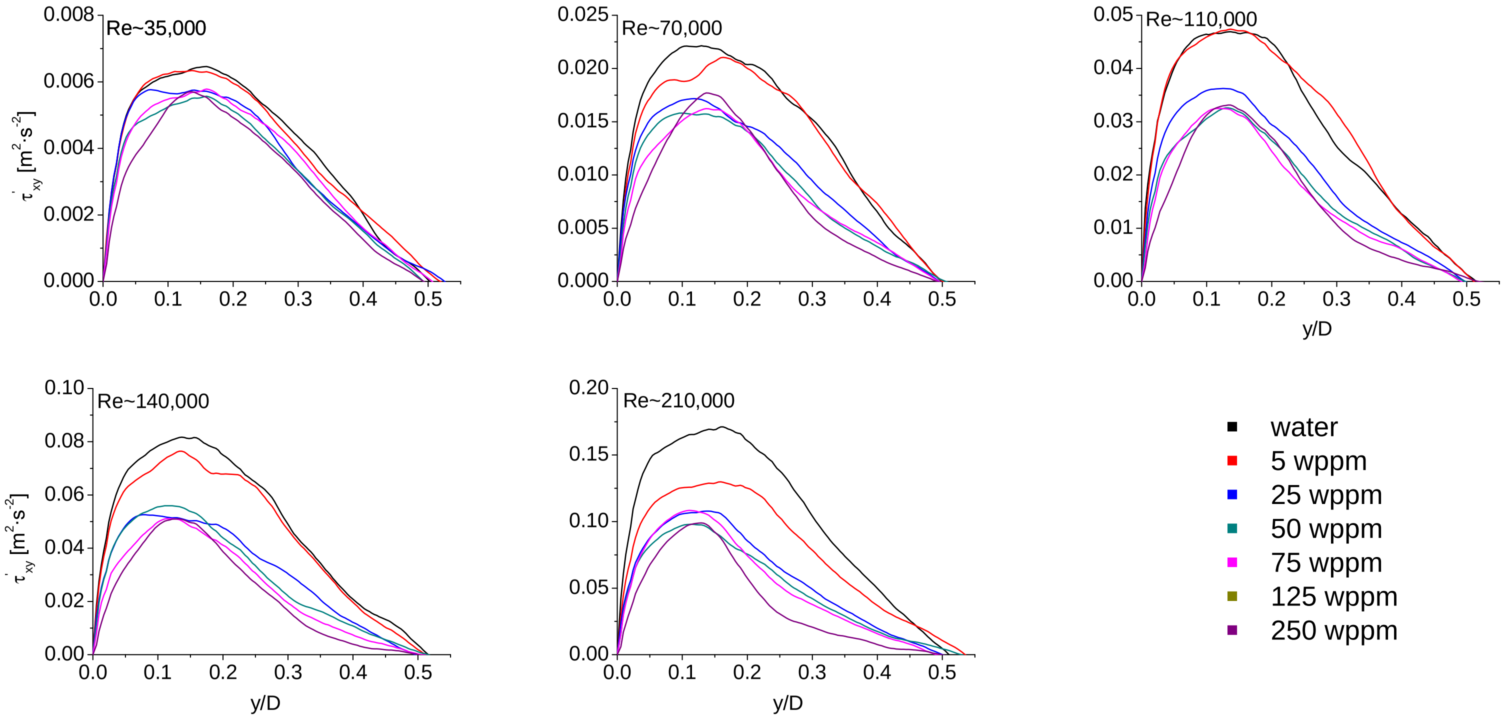

Figure A.11: Dependence of Reynolds stress $\tau_{xy}^{'}$ on the normalised distance from the wall for PEO4 solutions at various *Re*.

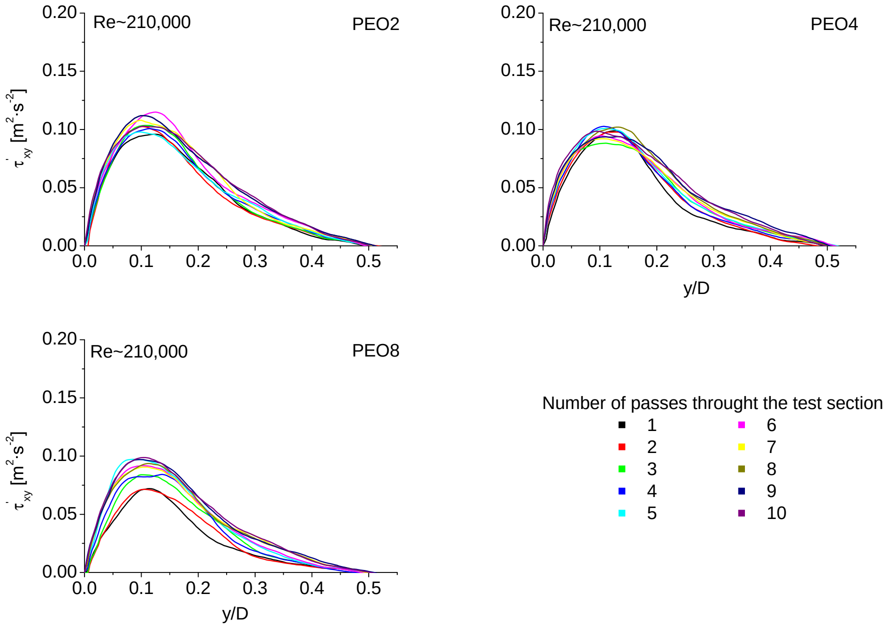

Figure A.13: Dependence of Reynolds stress $\tau'_{xy}$ on the normalised distance from the wall for degradation experiments of PEO2, PEO4 and PEO8 solutions at $Re = 210,000$.

## A.3 Vorticity and Strain Rate

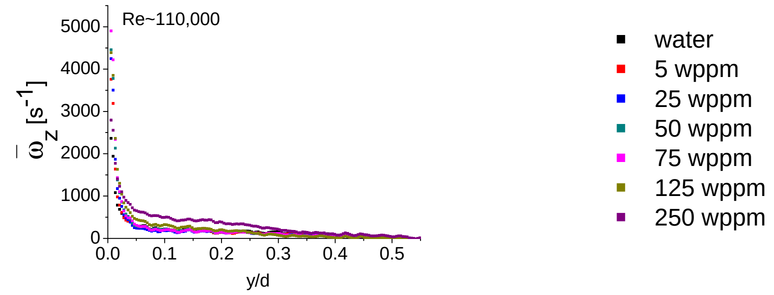

Figure A.19: Dependence of the mean 2D vorticity $\overline{\omega}_z$ on the normalised distance from the wall for PEO8 solutions at $Re$= 110,000.

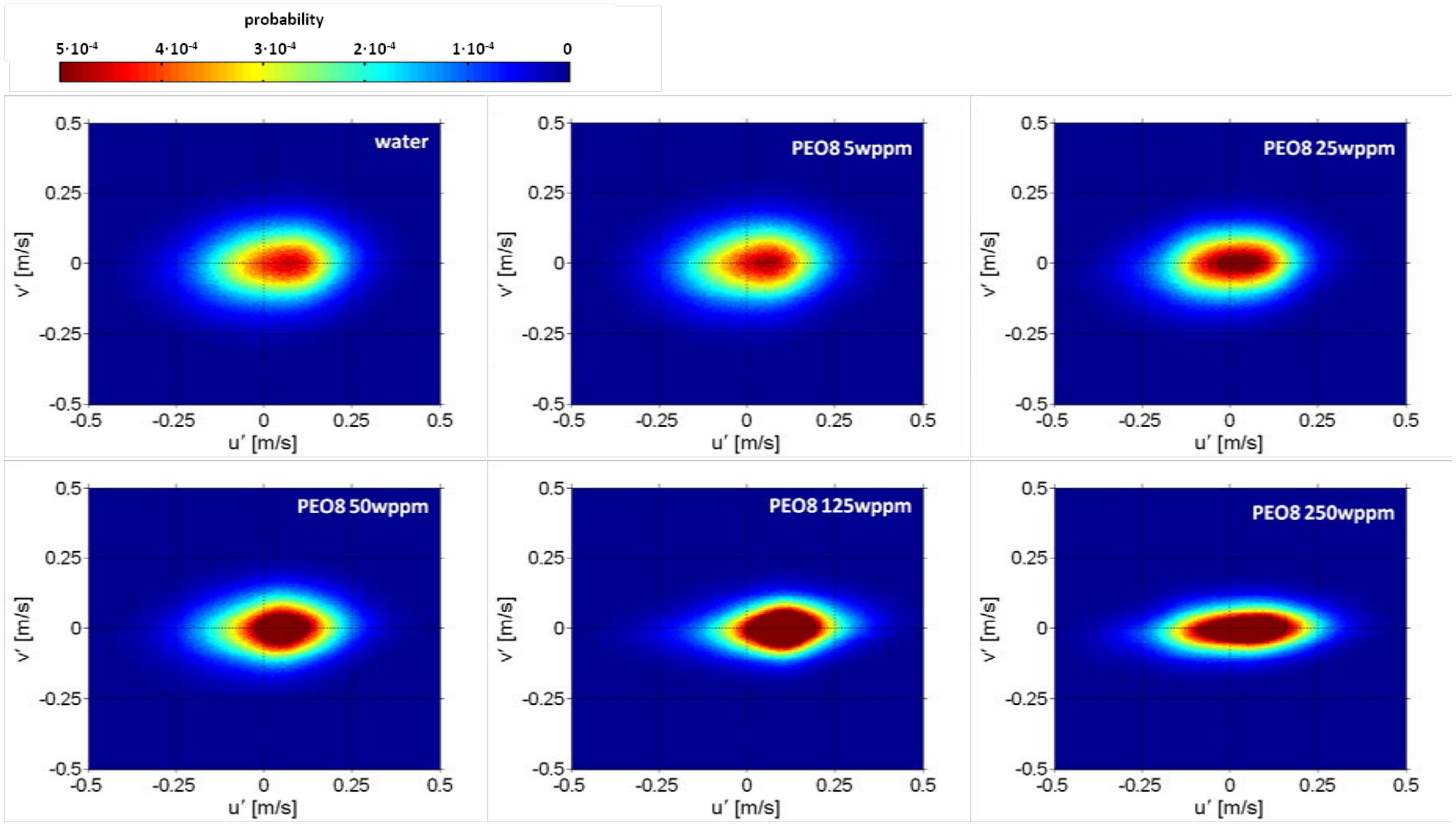

Figure A.14: Joint probability function of the streamwise and spanwise velocity fluctuations ($u^{'}$ and $v^{'}$) for PEO8 solutions at $Re = 35,000$
.

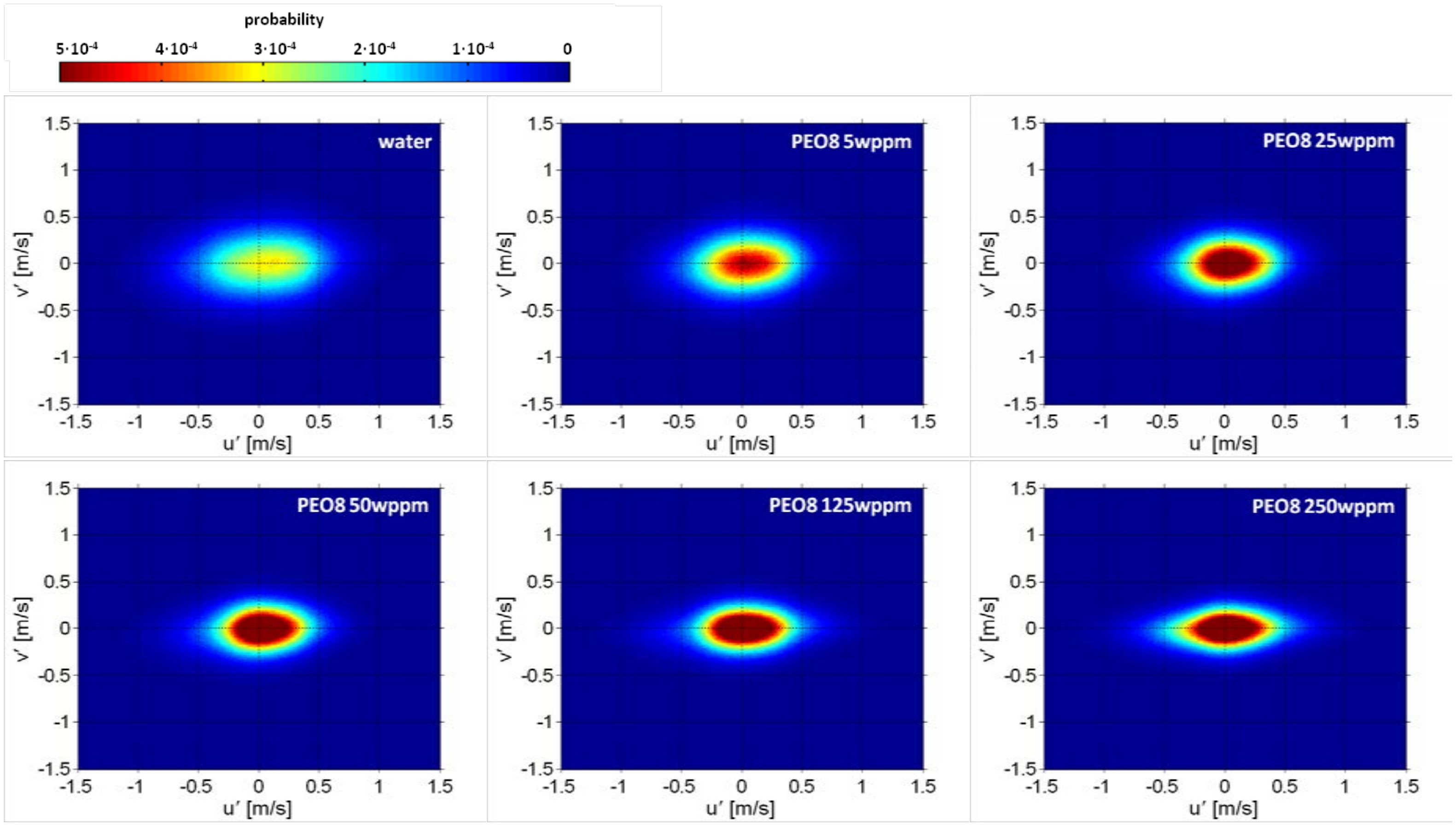

Figure A.15: Joint probability function of the streamwise and spanwise velocity fluctuations ($u^{'}$ and $v^{'}$) for PEO8 solutions at $Re = 110,000$
.

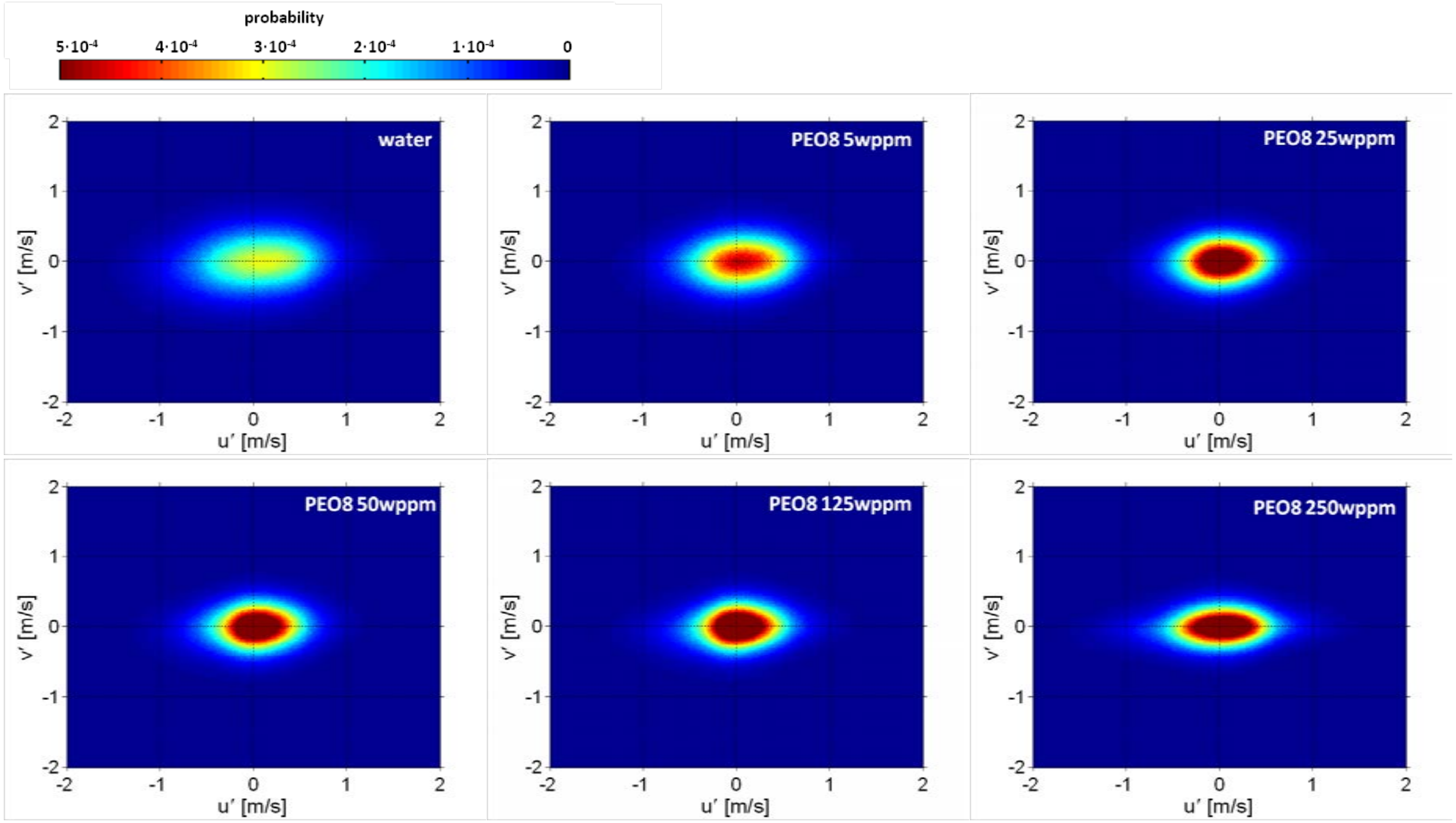

Figure A.16: Joint probability function of the streamwise and spanwise velocity fluctuations ($u^{'}$ and $v^{'}$) for PEO8 solutions at $Re = 140,000$
.

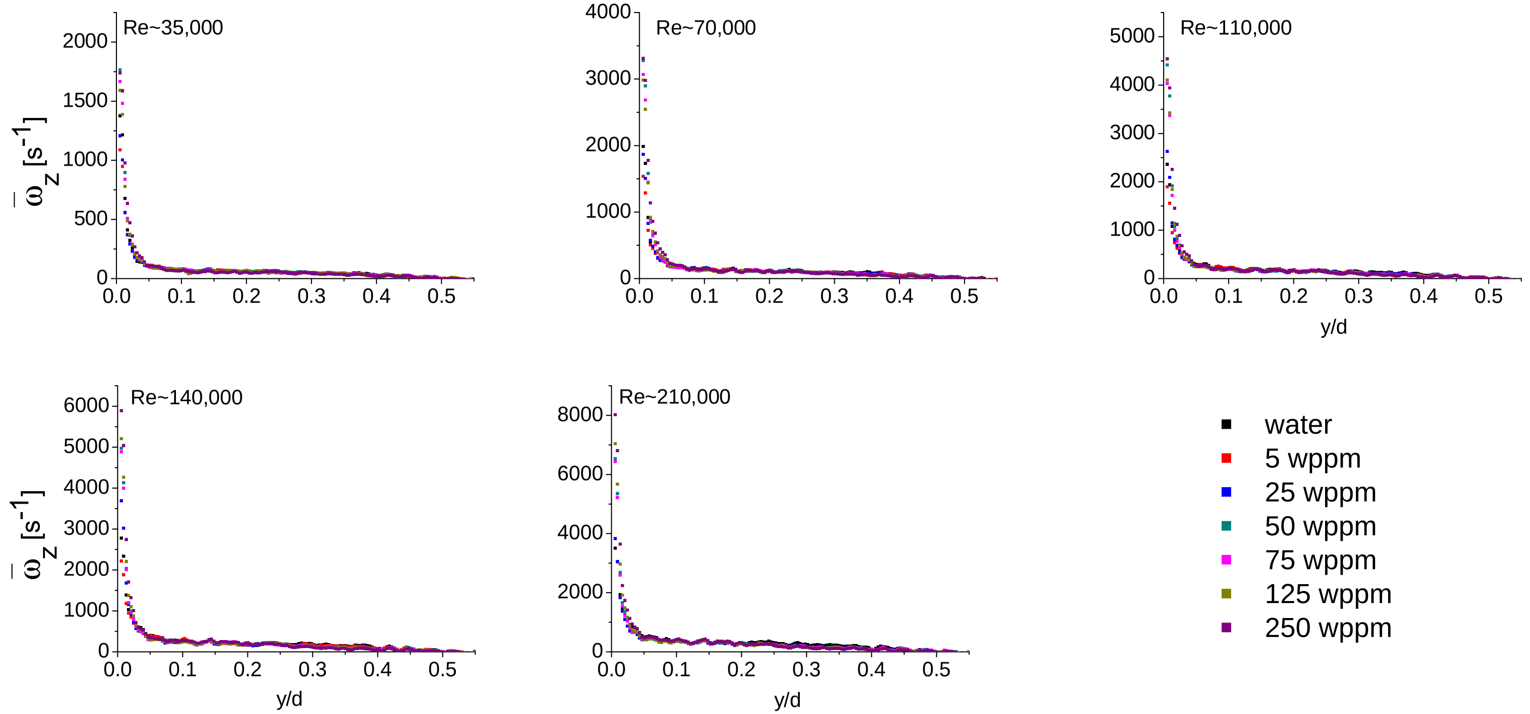

Figure A.17: Dependence of the mean 2D $\overline{\omega}_z$ on the normalised distance from the wall for PEO2 solutions at various $Re$.

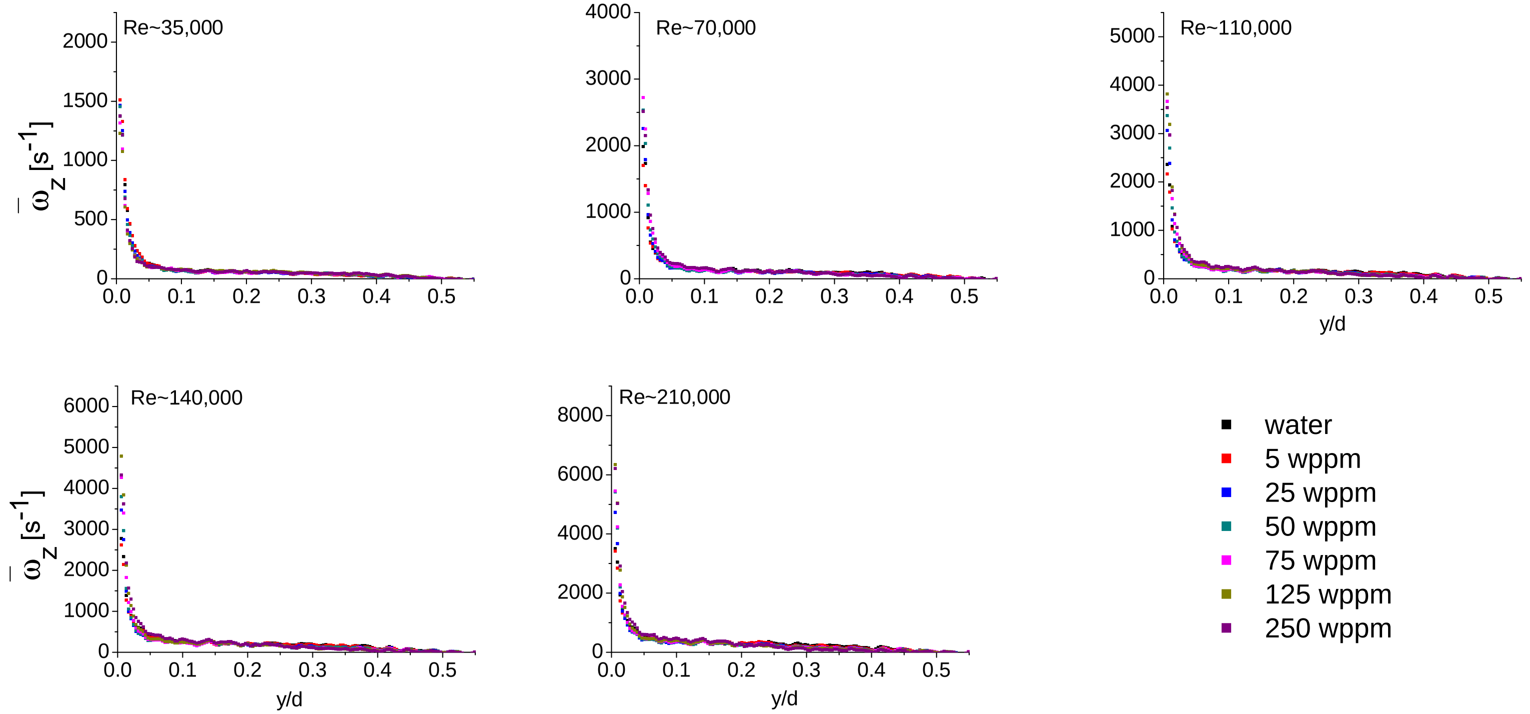

Figure A.18: Dependence of the mean 2D vorticity $\overline{\omega}_z$ on the normalised distance from the wall for PEO4 solutions at various *Re*.

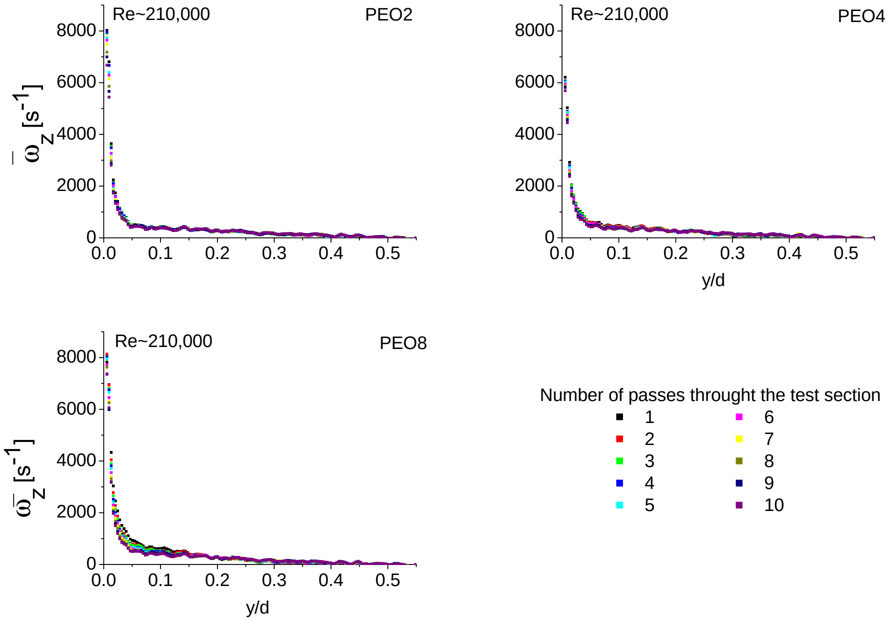

Figure A.20: Dependence of the mean 2D vorticity $\overline{\omega}_z$ on the normalised distance from the wall for degradation experiments of PEO2, PEO4 and PEO8 solutions at $Re = 210,000$.

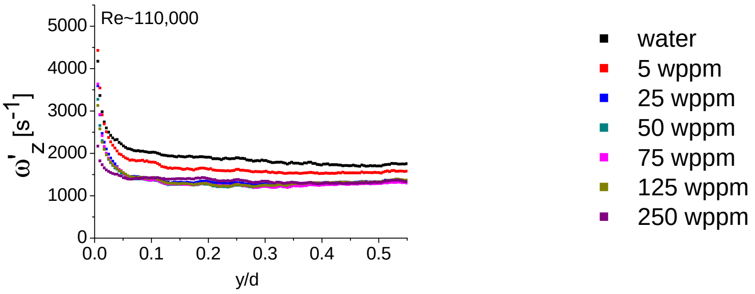

Figure A.23: Dependence of the 2D vorticity fluctuations $\omega_z^{'}$ on the normalised distance from the wall for PEO8 solutions at $Re = 110,000$.

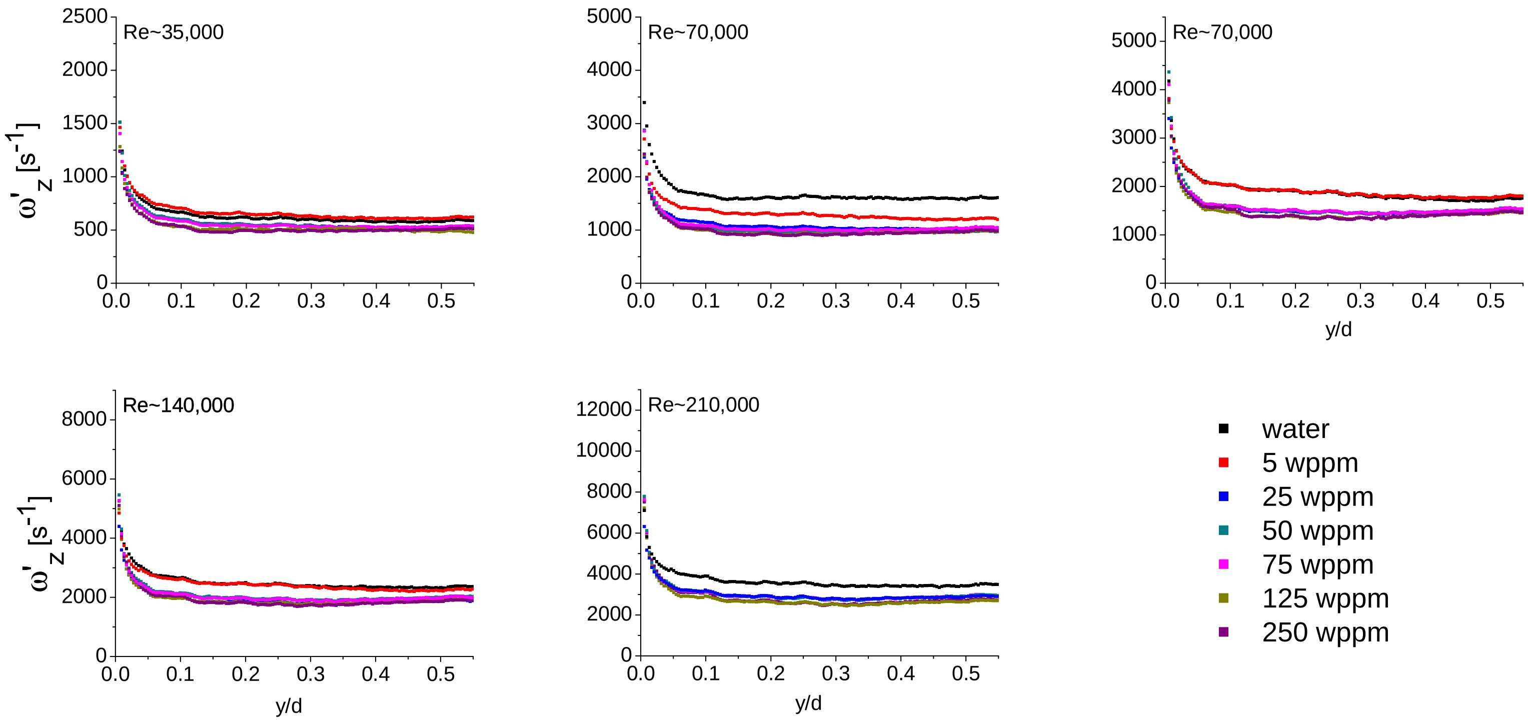

Figure A.21: Dependence of the 2D vorticity fluctuations $\omega_z^{'}$ on the normalised distance from the wall for PEO2 solutions at various $Re$.

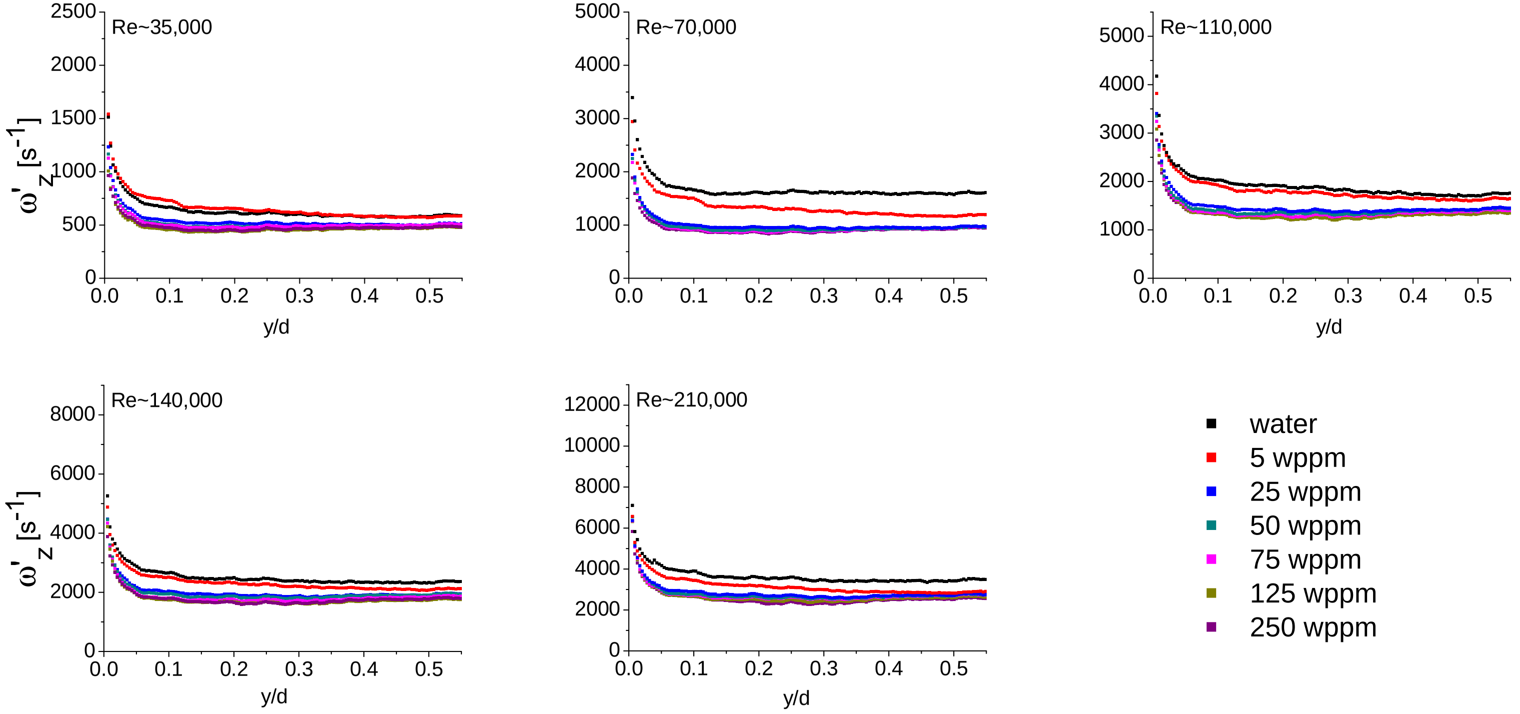

Figure A.22: Dependence of the 2D vorticity fluctuations $\omega_z^{'}$ on the normalised distance from the wall for PEO4 solutions at various $Re$.

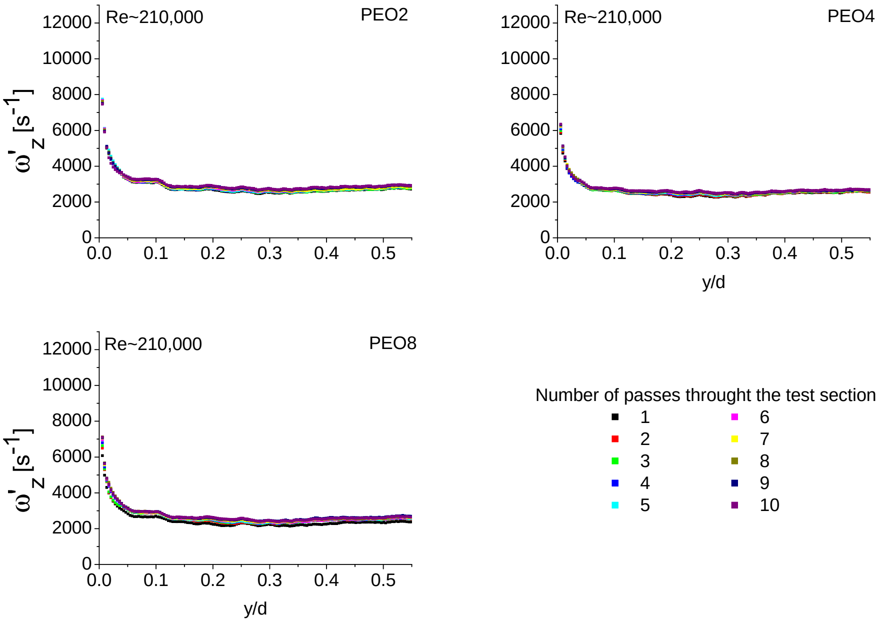

Figure A.24: Dependence of the 2D vorticity fluctuations $\omega_z^{'}$ on the normalised distance from the wall for degradation experiments of PEO2, PEO4 and PEO8 solutions at $Re = 210,000$.

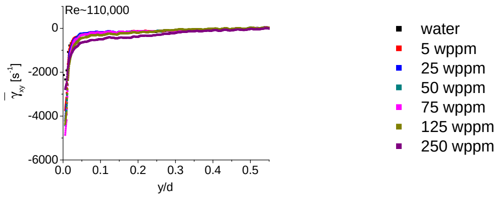

Figure A.27: Dependence of the mean streamwise shear strain rate $\overline{\gamma}_{xy}$ on the normalised distance from the wall for PEO8 solutions $Re = 110,000$.

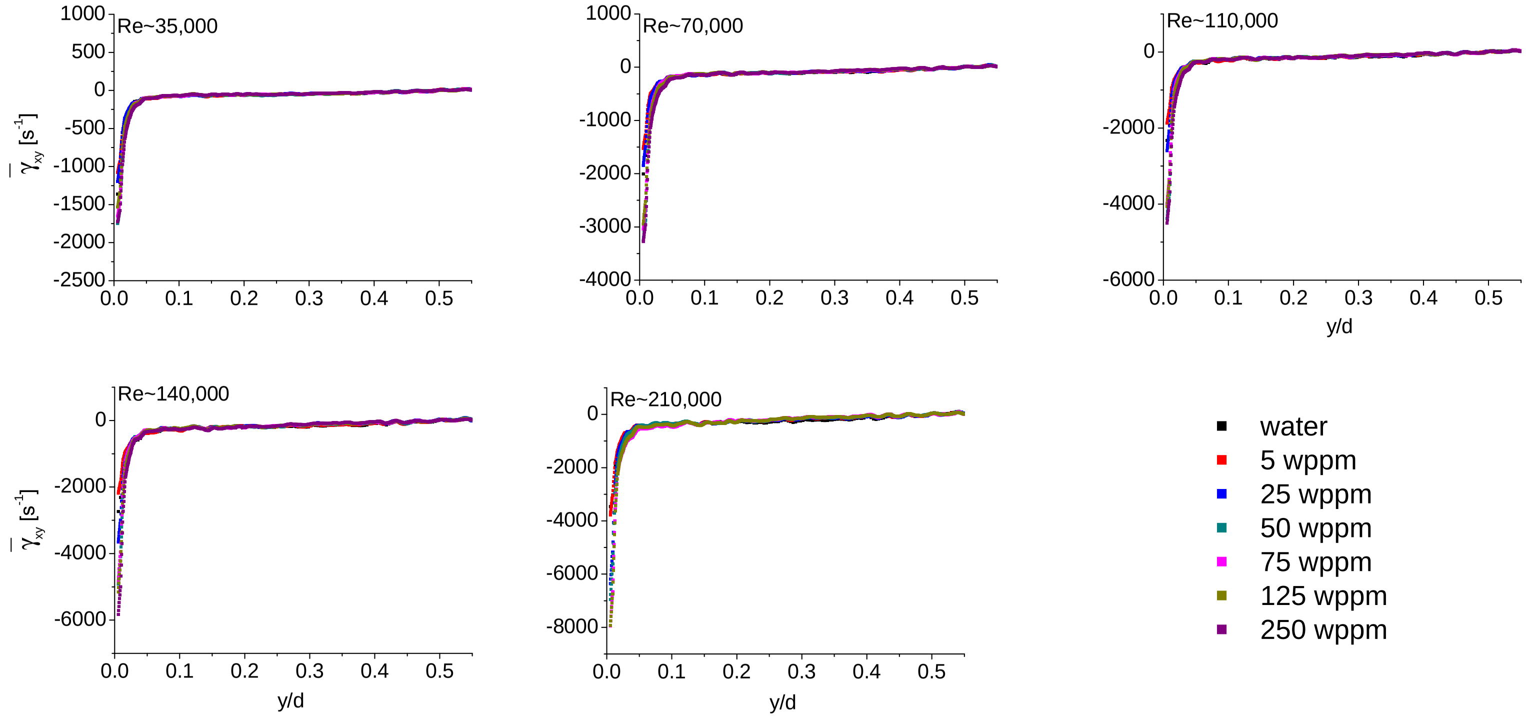

Figure A.25: Dependence of the mean streamwise shear strain rate $\overline{\gamma}_{xy}$ on the normalised distance from the wall for PEO2 solutions at various $Re$.

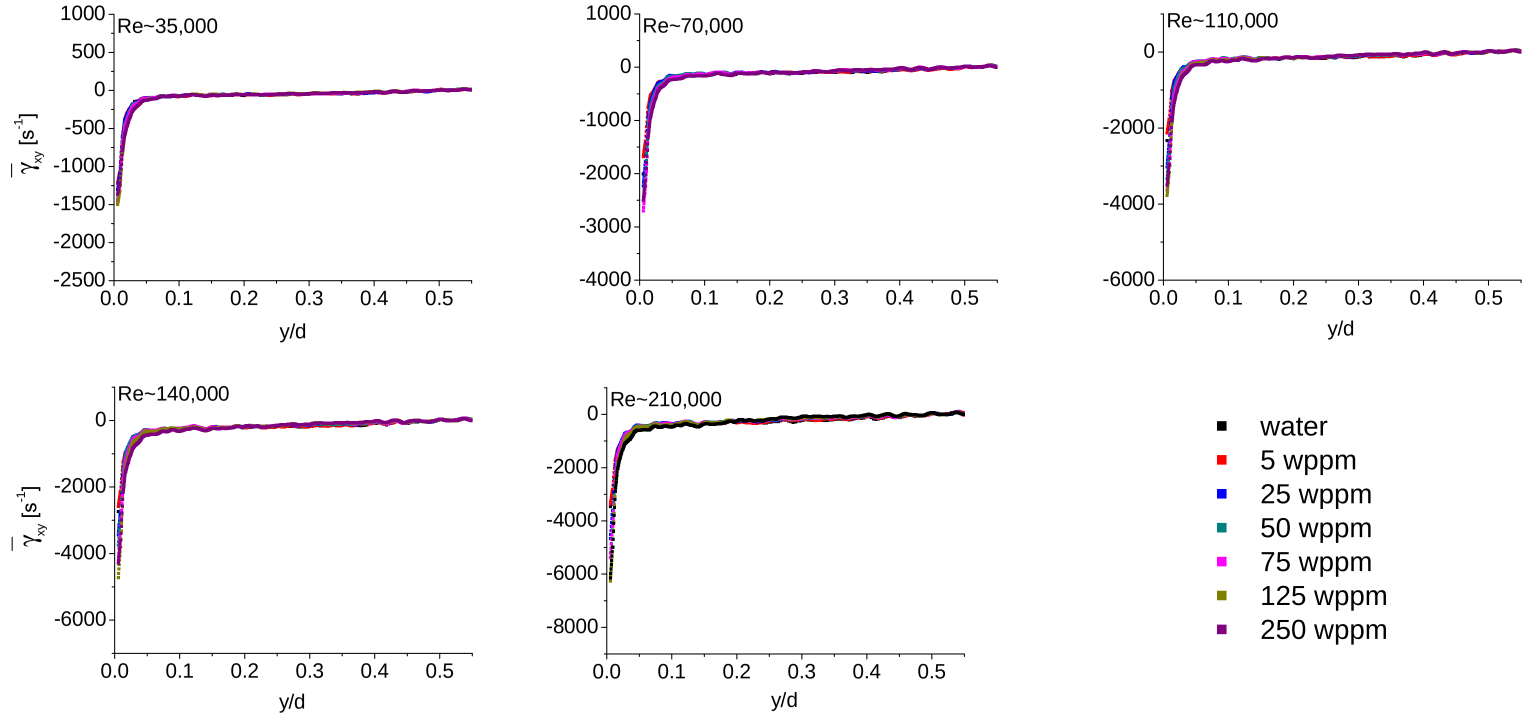

Figure A.26: Dependence of the mean streamwise shear strain rate $\overline{\gamma}_{xy}$ on the normalised distance from the wall for PEO4 solutions at various *Re*.

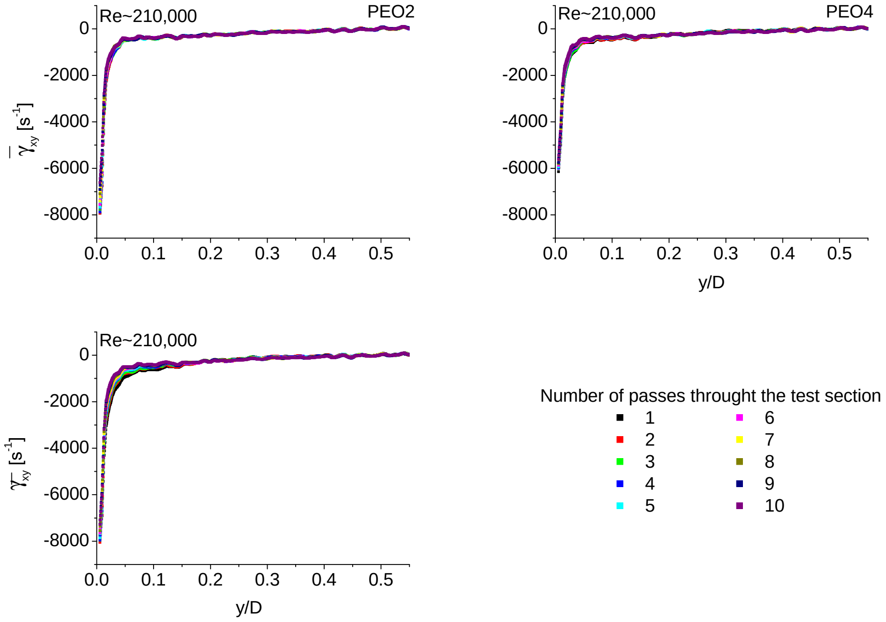

Figure A.28: Dependence of the mean streamwise shear strain rate $\overline{\gamma}_{xy}$ on the normalised distance from the wall for degradation experiments of PEO2, PEO4 and PEO8 solutions at $Re = 210,000$.

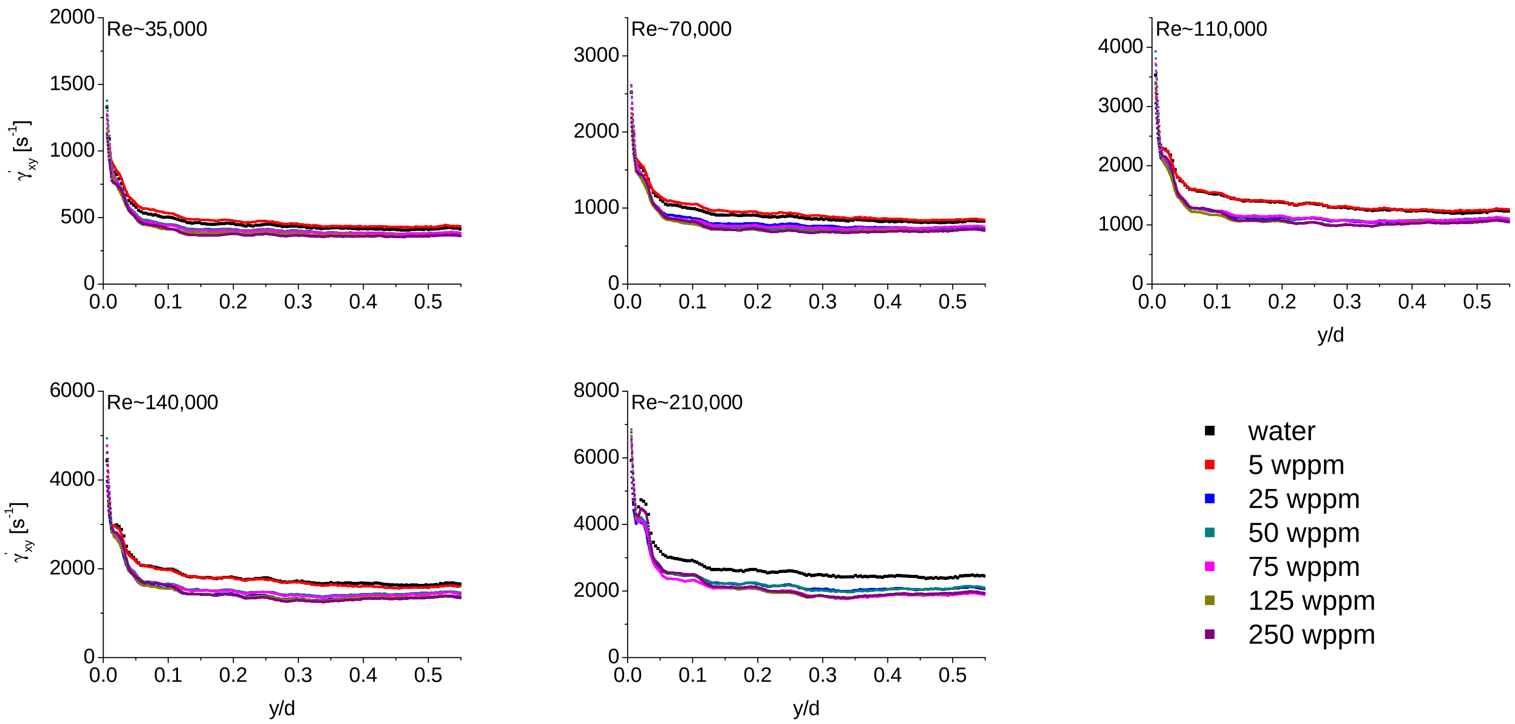

Figure A.29: Dependence of the streamwise shear strain rate fluctuation $\gamma'_{xy}$ on the normalised distance from the wall for PEO2 solutions at various $Re$.

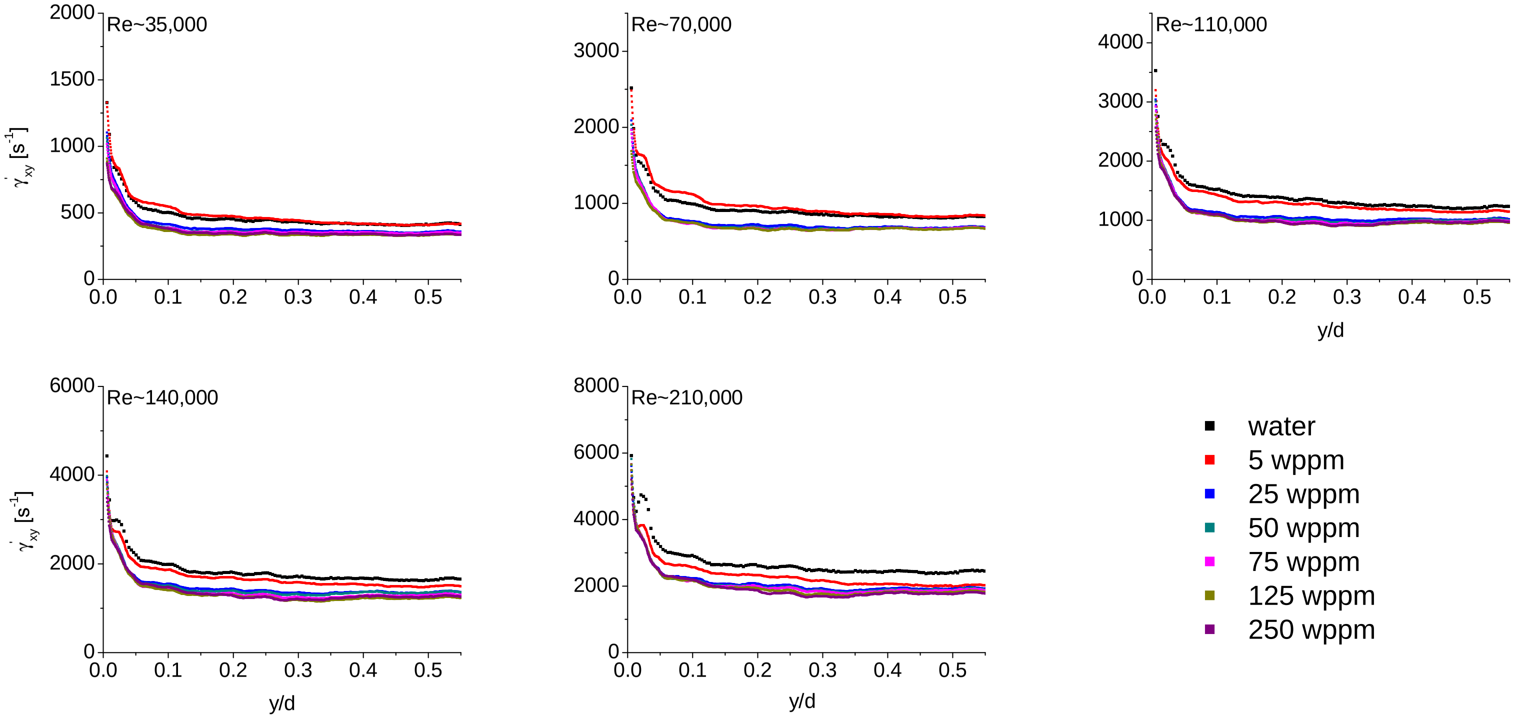

Figure A.30: Dependence of the streamwise shear strain rate fluctuation $\gamma^{'}_{xy}$ on the normalised distance from the wall for PEO4 solutions at various $Re$.

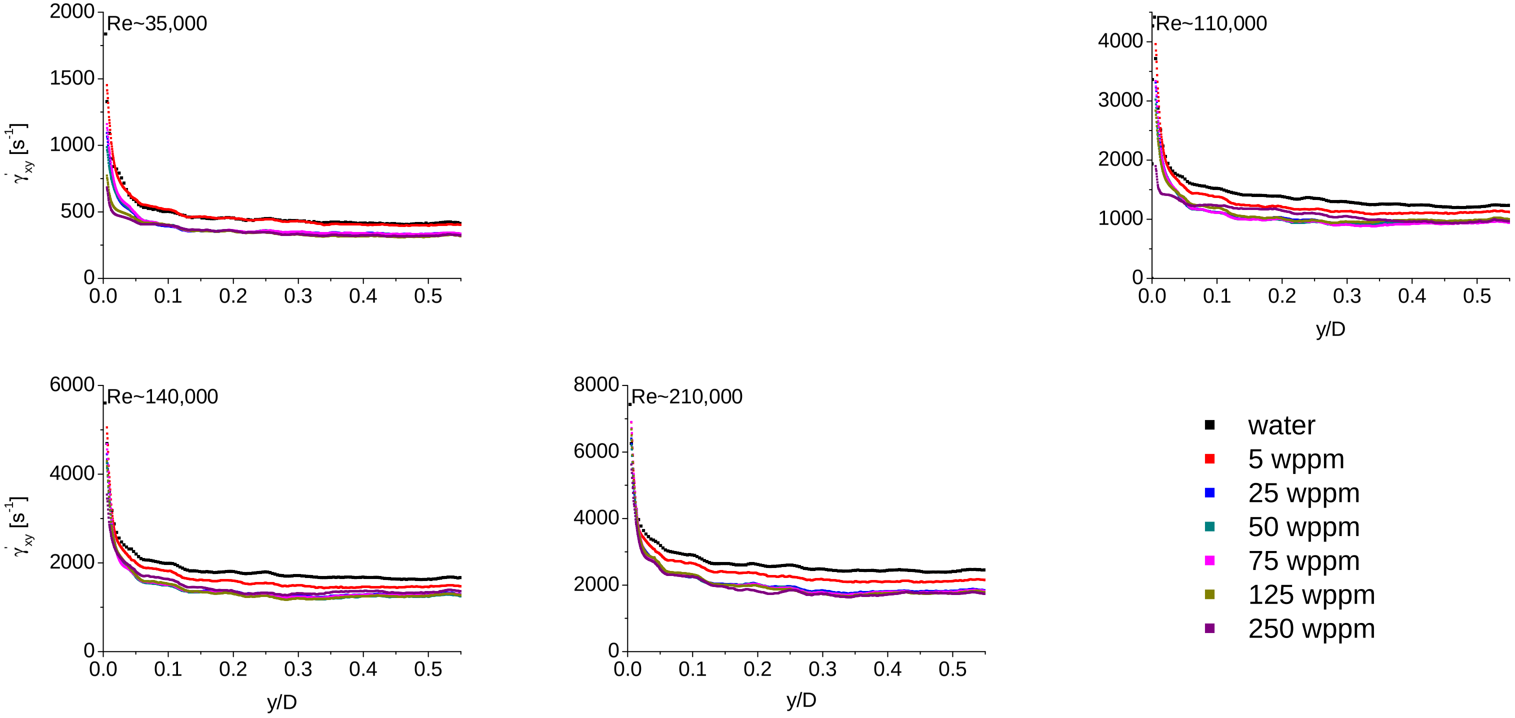

Figure A.31: Dependence of the streamwise shear strain rate fluctuation $\gamma'_{xy}$ on the normalised distance from the wall for PEO8 solutions at various $Re$.

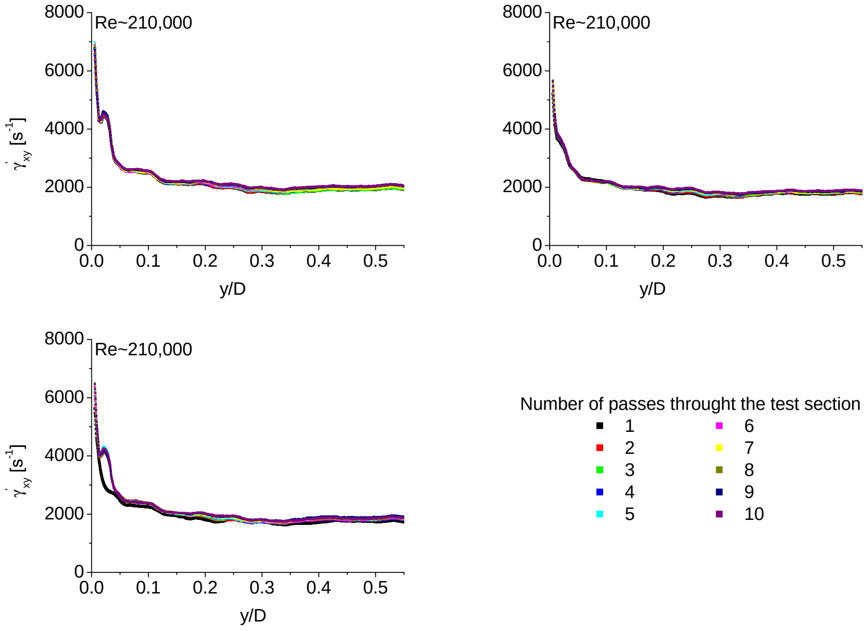

Figure A.32: Dependence of the streamwise shear strain rate fluctuation $\gamma_{xy}^{'}$ on the normalised distance from the wall for degradation experiments of PEO2, PEO4 and PEO8 solutions at $Re = 210,000$.

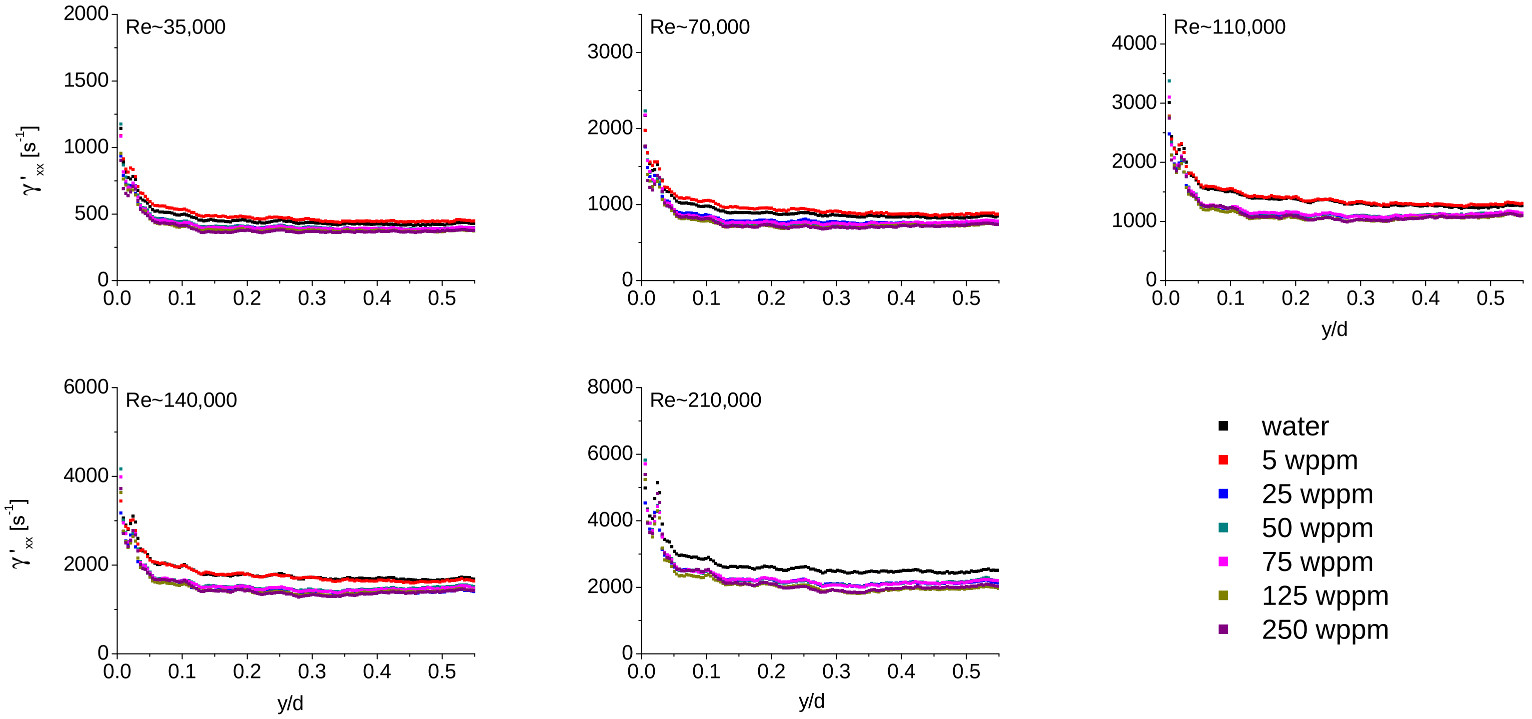

Figure A.33: Dependence of the streamwise compression strain rate fluctuation $\gamma'_{xx}$ on the normalised distance from the wall for PEO2 solutions at various $Re$.

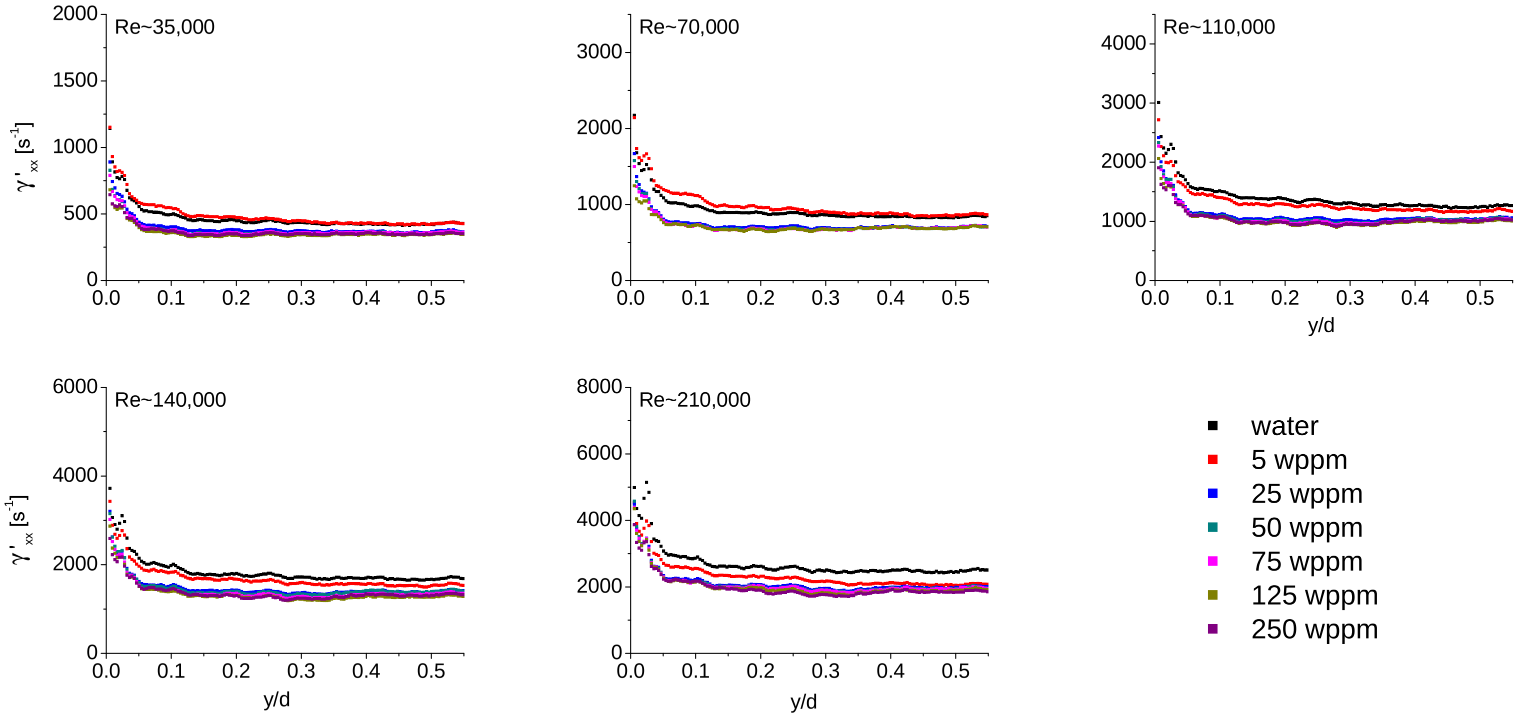

Figure A.34: Dependence of the streamwise compression strain rate fluctuation $\gamma'_{xx}$ on the normalised distance from the wall for PEO4 solutions at various $Re$.

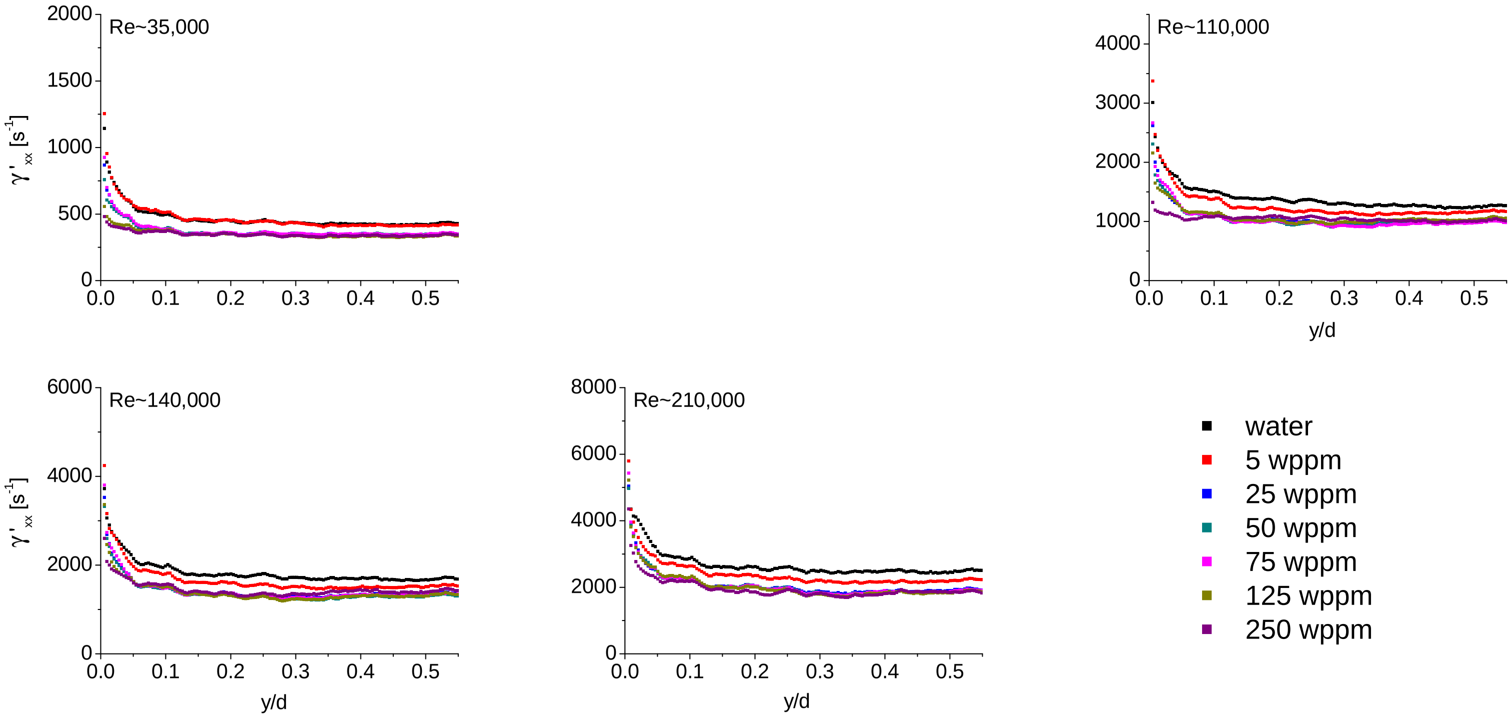

Figure A.35: Dependence of the streamwise compression strain rate fluctuation $\gamma'_{xx}$ on the normalised distance from the wall for PEO8 solutions at various $Re$.

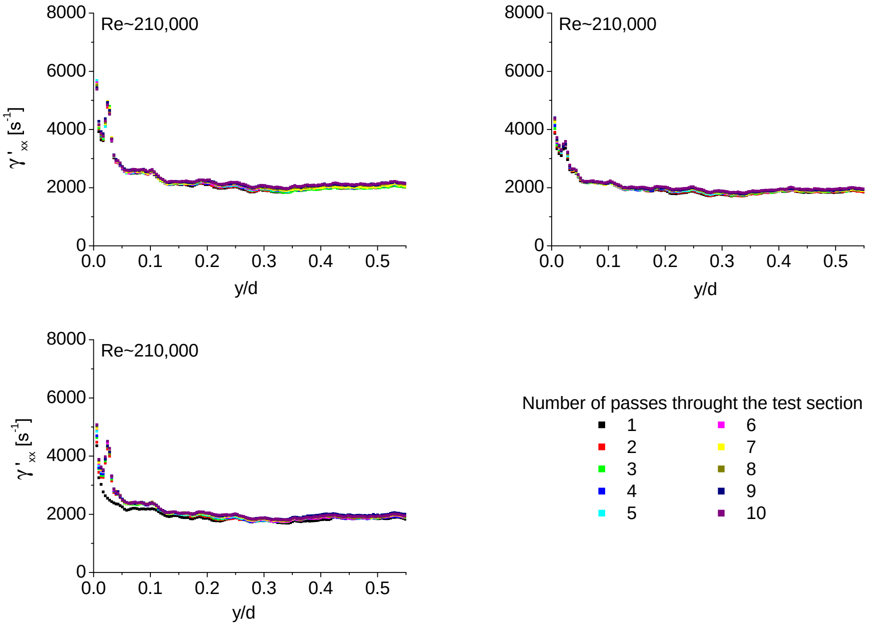

Figure A.36: Dependence of the streamwise shear strain rate fluctuation $\gamma^{'}_{xx}$ on the normalised distance from the wall for degradation experiments of PEO2, PEO4 and PEO8 solutions at $Re = 210,000$.

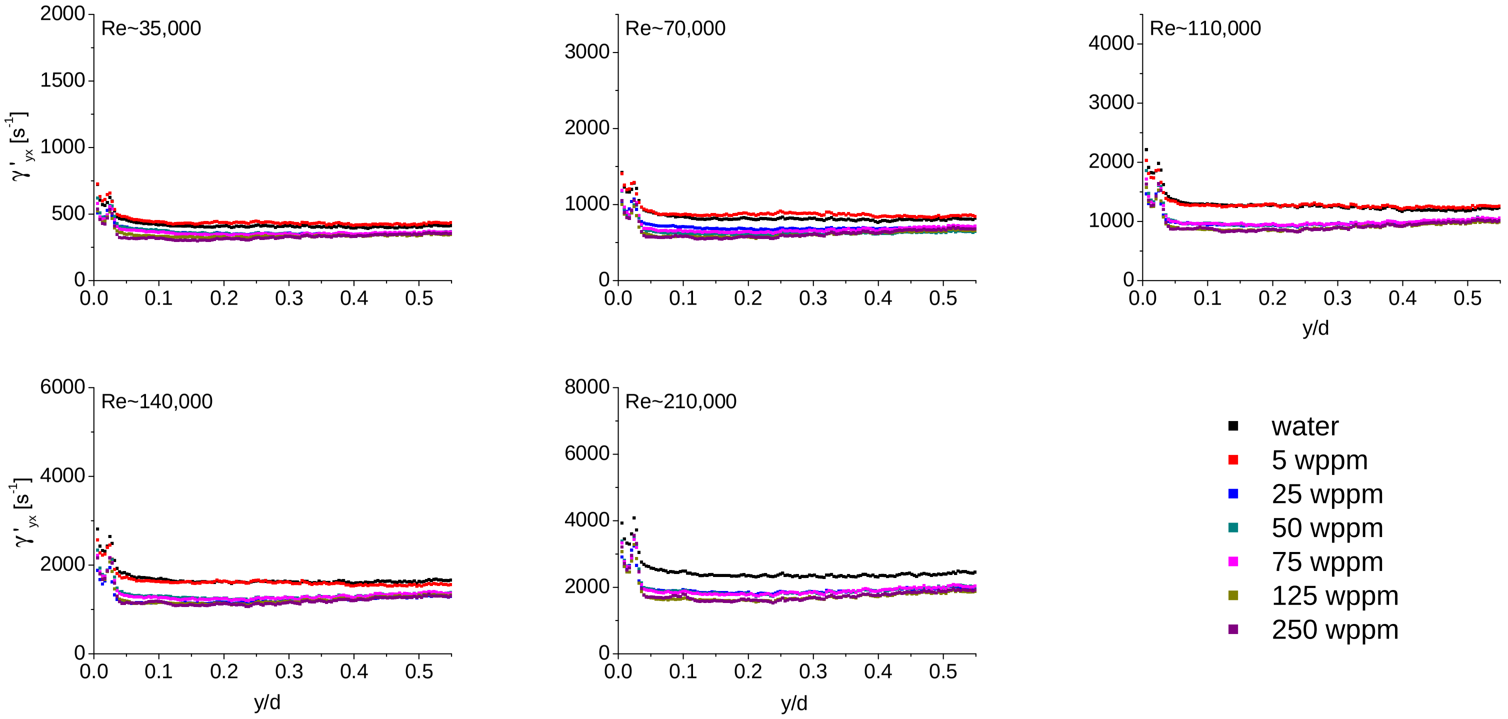

Figure A.37: Dependence of the spanwise shear strain rate fluctuation $\gamma'_{yx}$ on the normalised distance from the wall for PEO2 solutions at various $Re$.

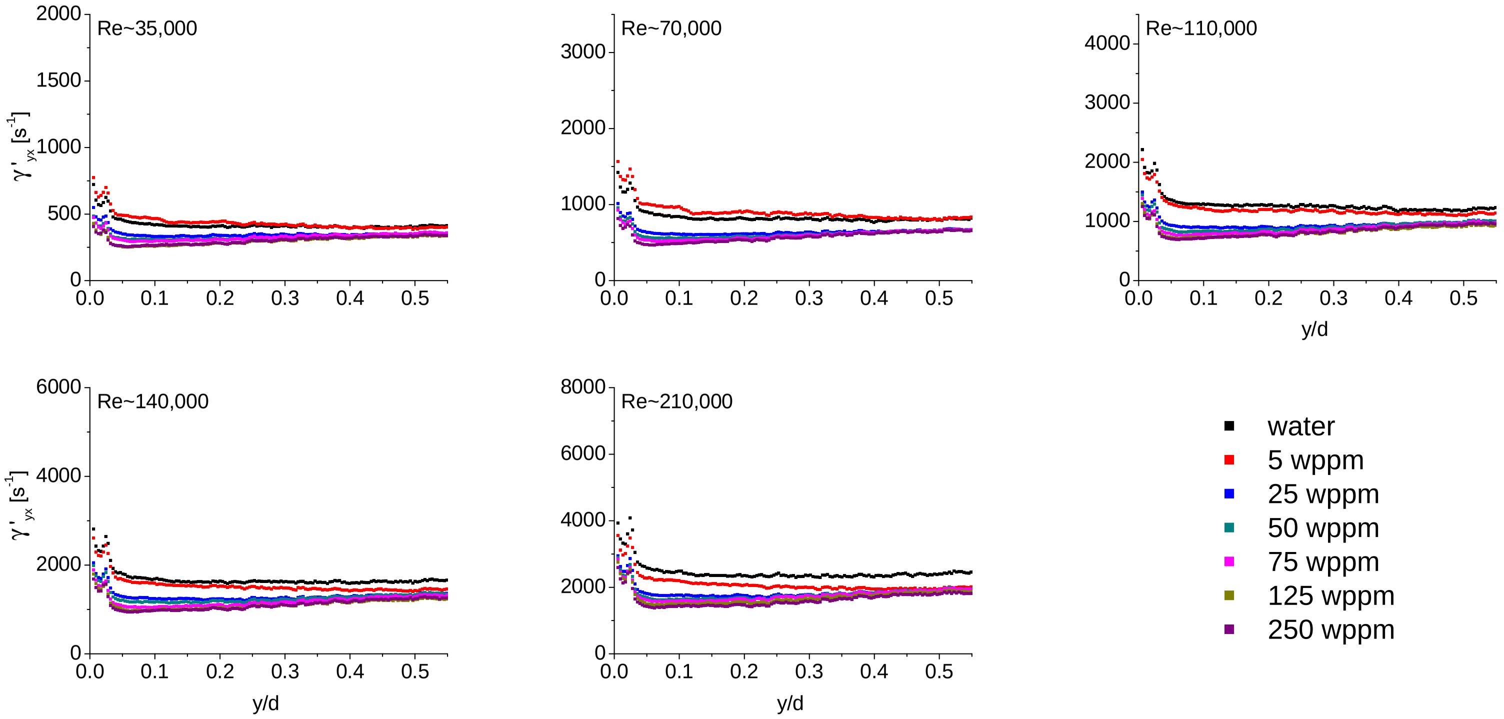

Figure A.38: Dependence of the spanwise shear strain rate fluctuation $\gamma'_{yx}$ on the normalised distance from the wall for PEO4 solutions at various $Re$.

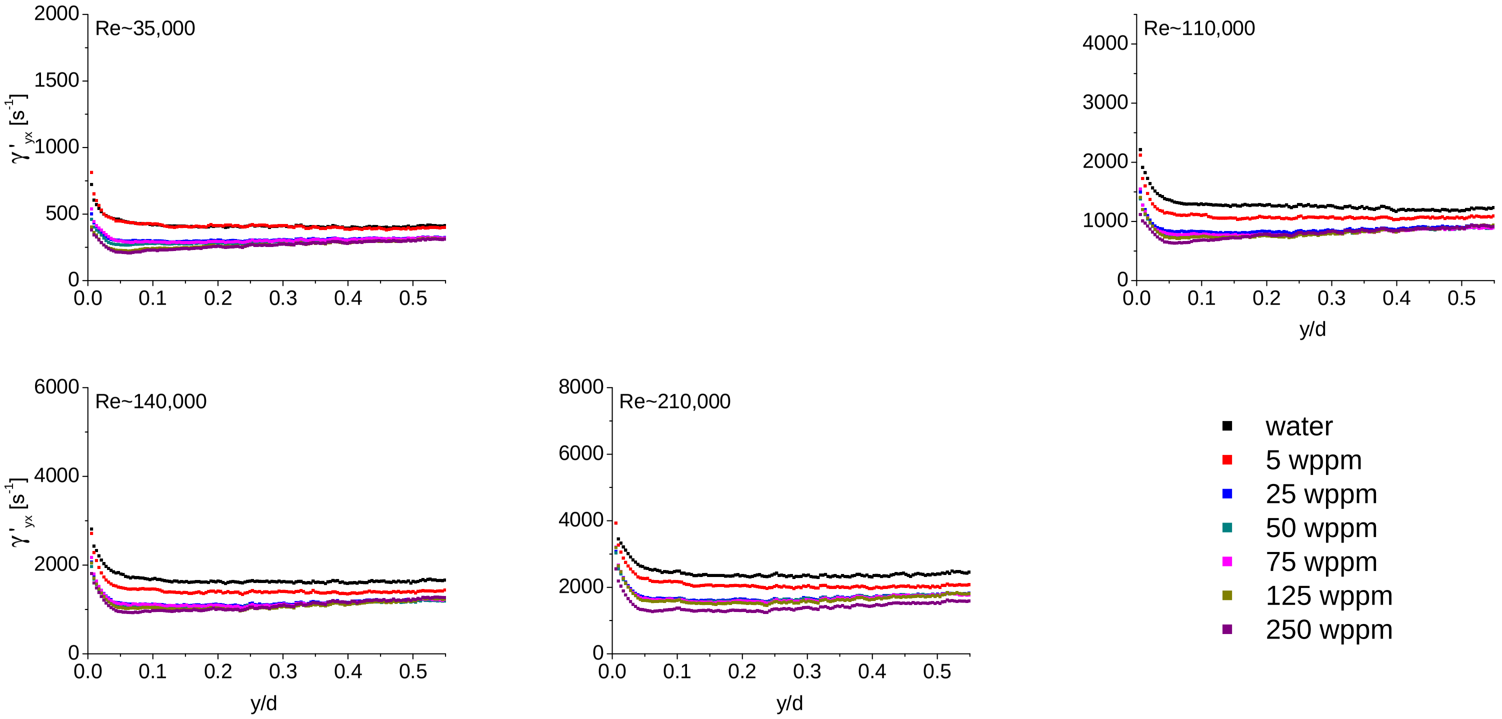

Figure A.39: Dependence of the spanwise shear strain rate fluctuation $\gamma_{yx}^{'}$ on the normalised distance from the wall for PEO8 solutions at various $Re$.

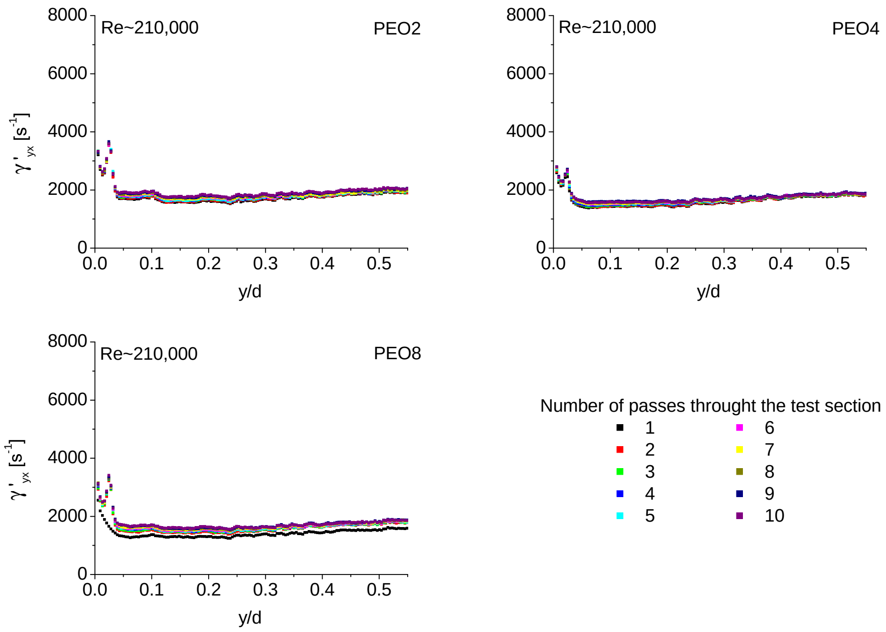

Figure A.40: Dependence of the spanwise shear strain rate fluctuation $\gamma_{yx}^{'}$ on the normalised distance from the wall for degradation experiments of PEO2, PEO4 and PEO8 solutions at $Re = 210,000$.

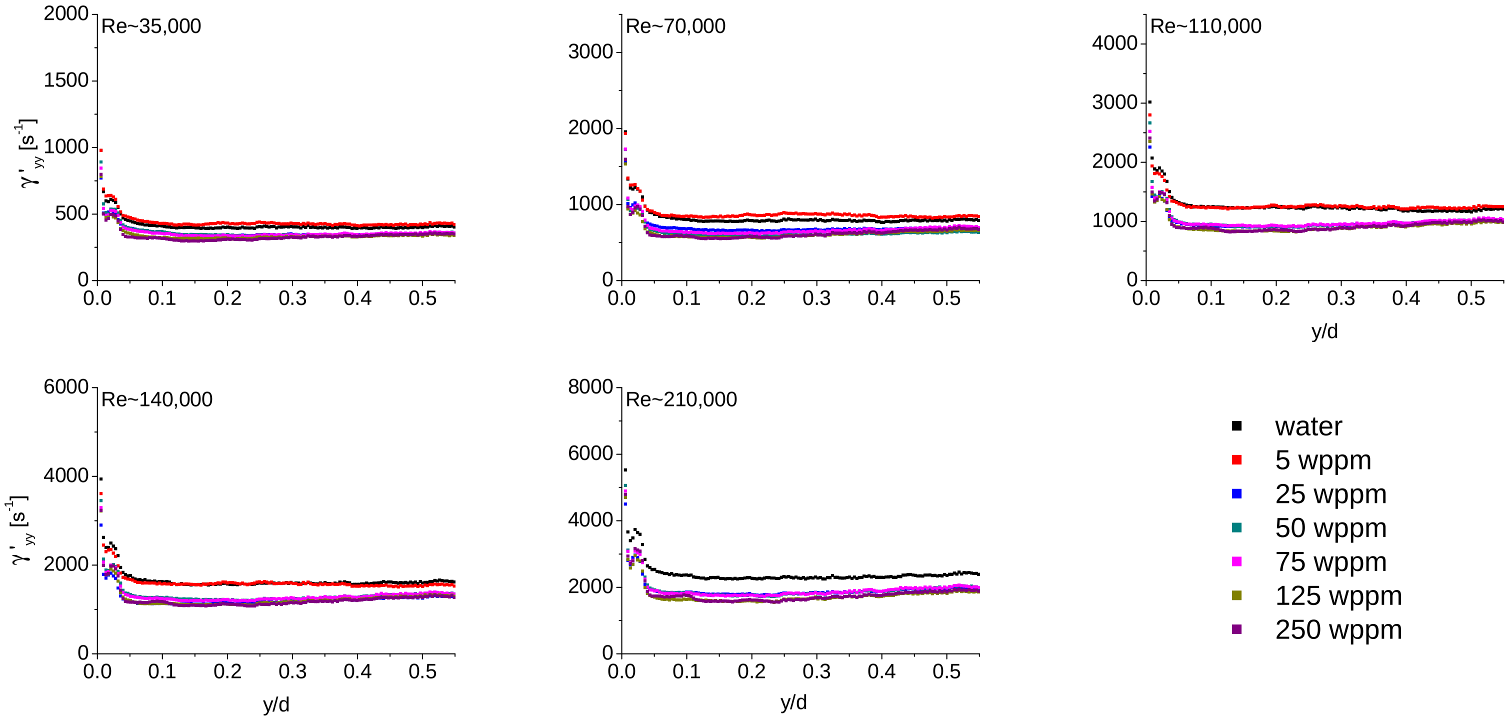

Figure A.41: Dependence of the spanwise compression strain rate fluctuation $\gamma'_{yy}$ on the normalised distance from the wall for PEO2 solutions at various $Re$.

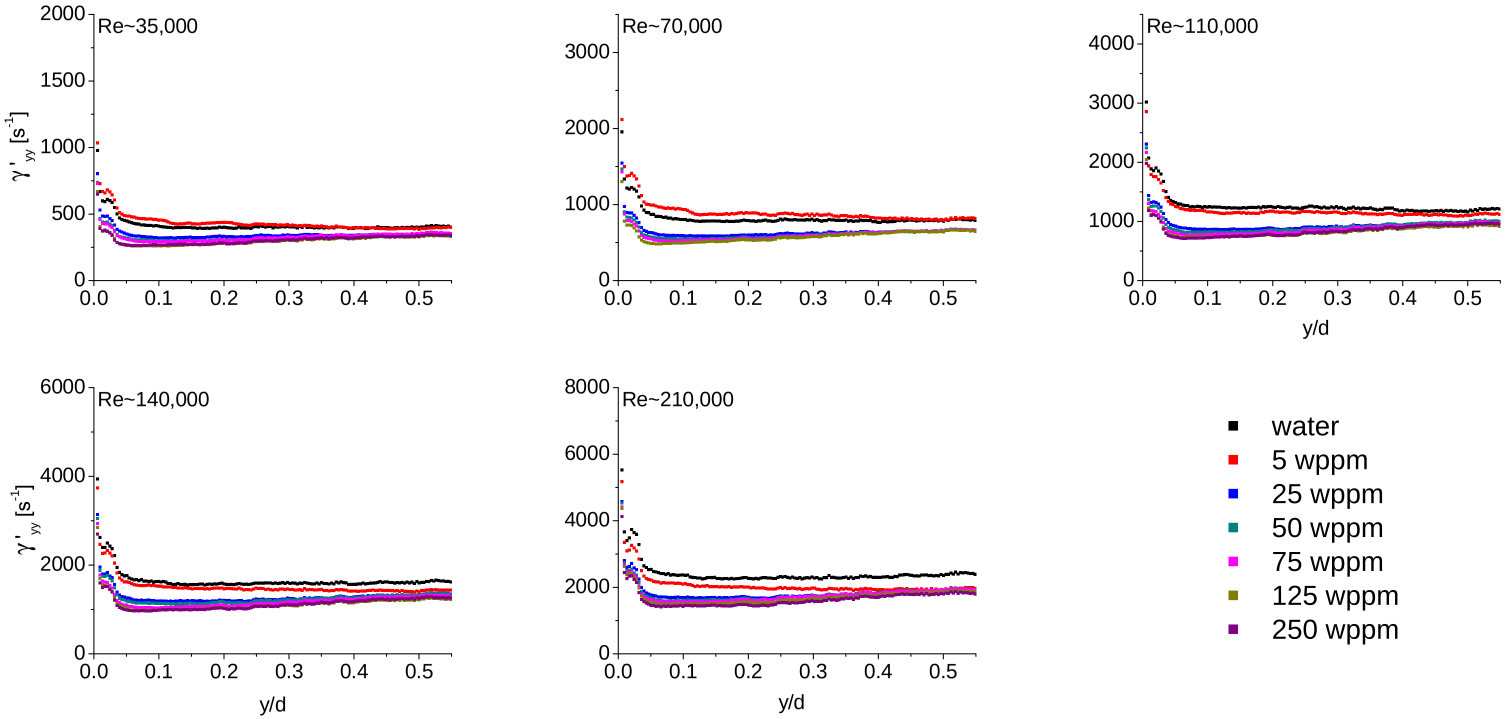

Figure A.42: Dependence of the spanwise compression strain rate fluctuation $\gamma^{'}_{yy}$ on the normalised distance from the wall for PEO4 solutions at various $Re$.

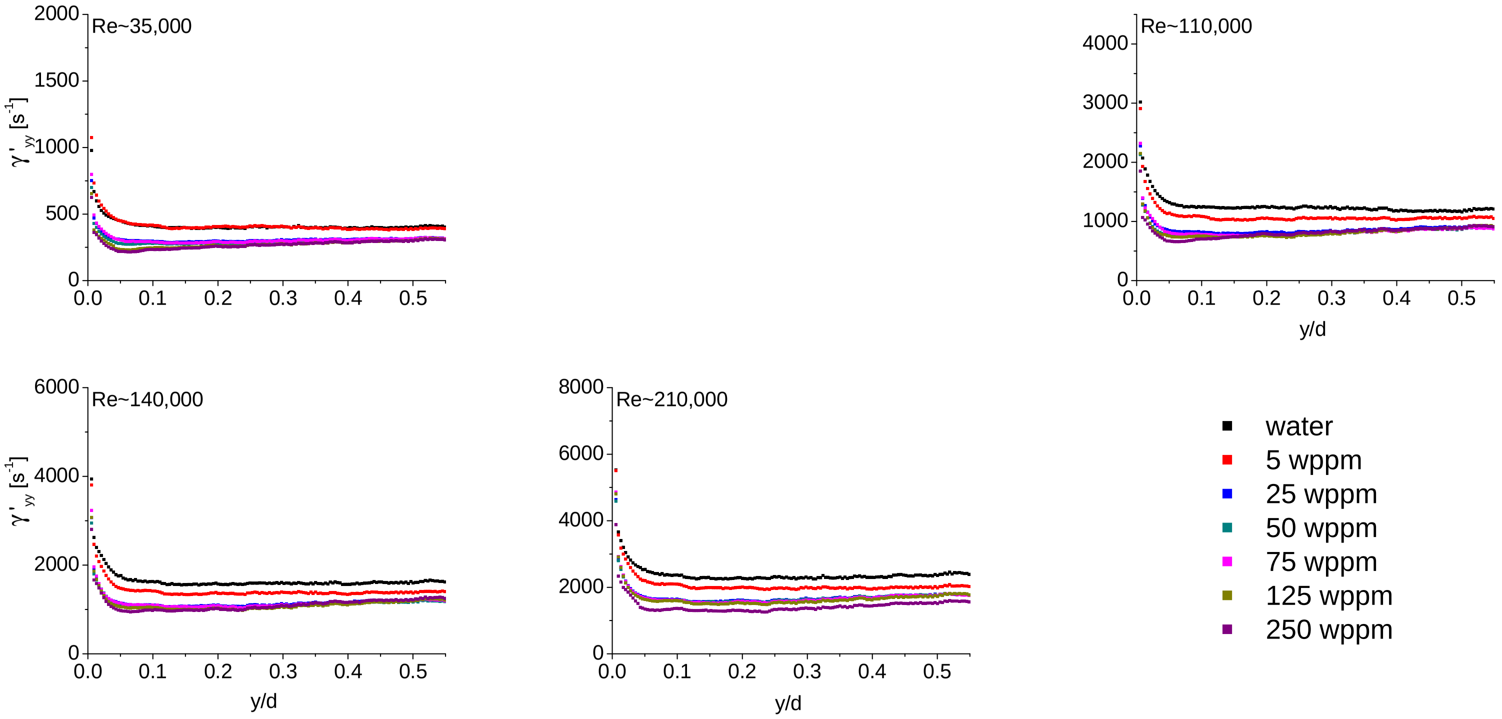

Figure A.43: Dependence of the spanwise compression strain rate fluctuation $\gamma_{yy}^{'}$ on the normalised distance from the wall for PEO8 solutions at various $Re$.

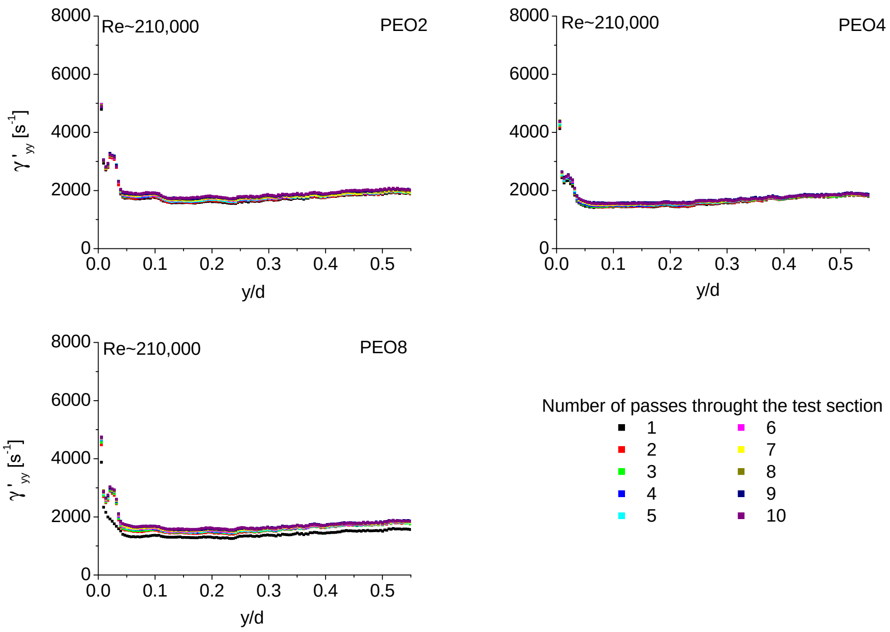

Figure A.44: Dependence of the spanwise compression strain rate fluctuation $\gamma'_{yy}$ on the normalised distance from the wall for degradation experiments of PEO2, PEO4 and PEO8 solutions at $Re = 210,000$.

## A.4 Higher Order Statistics - Skewness and Kurtosis

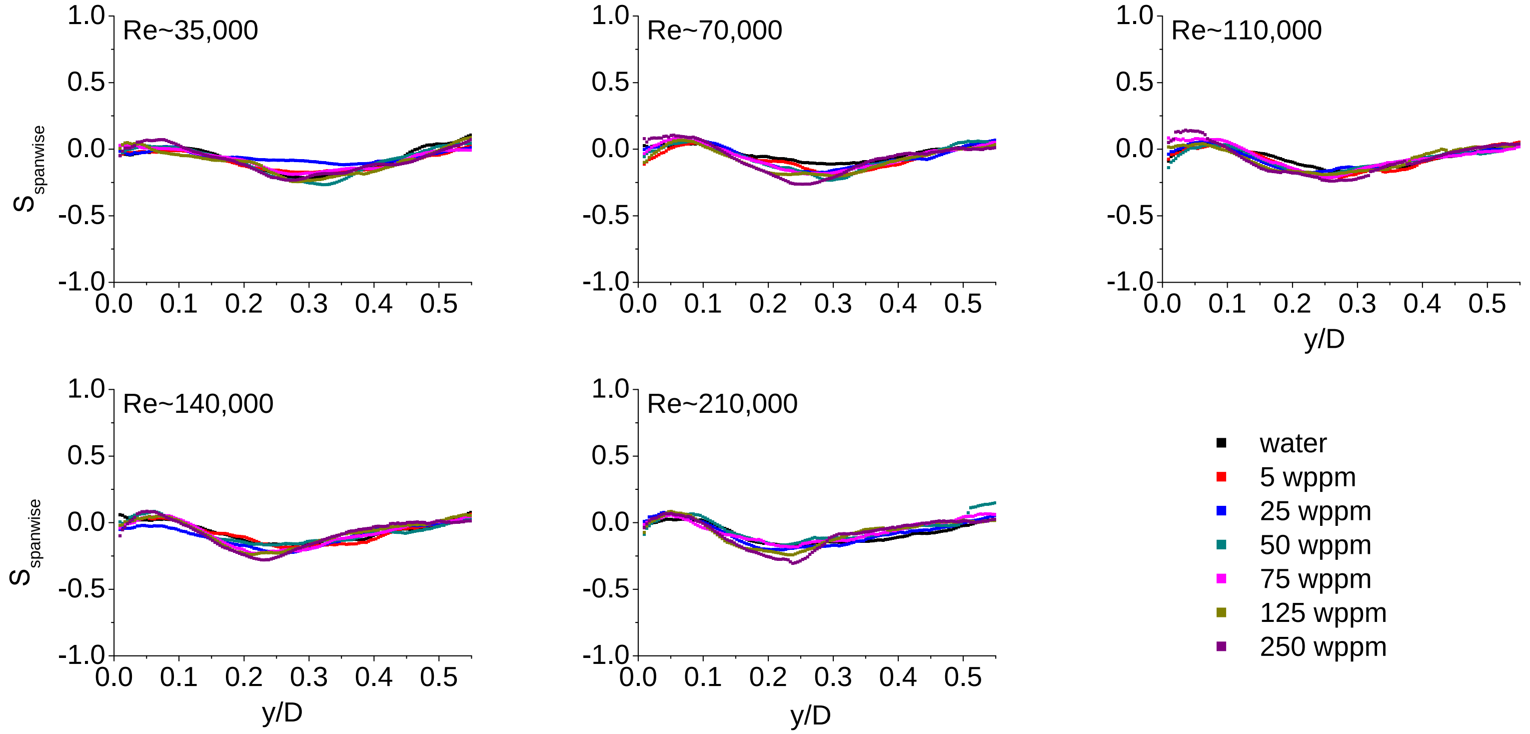

Figure A.45: Dependence of the spanwise skewness $S_{\text{spanwise}}$ on the normalised distance from the wall for PEO2 solutions at various $Re$.

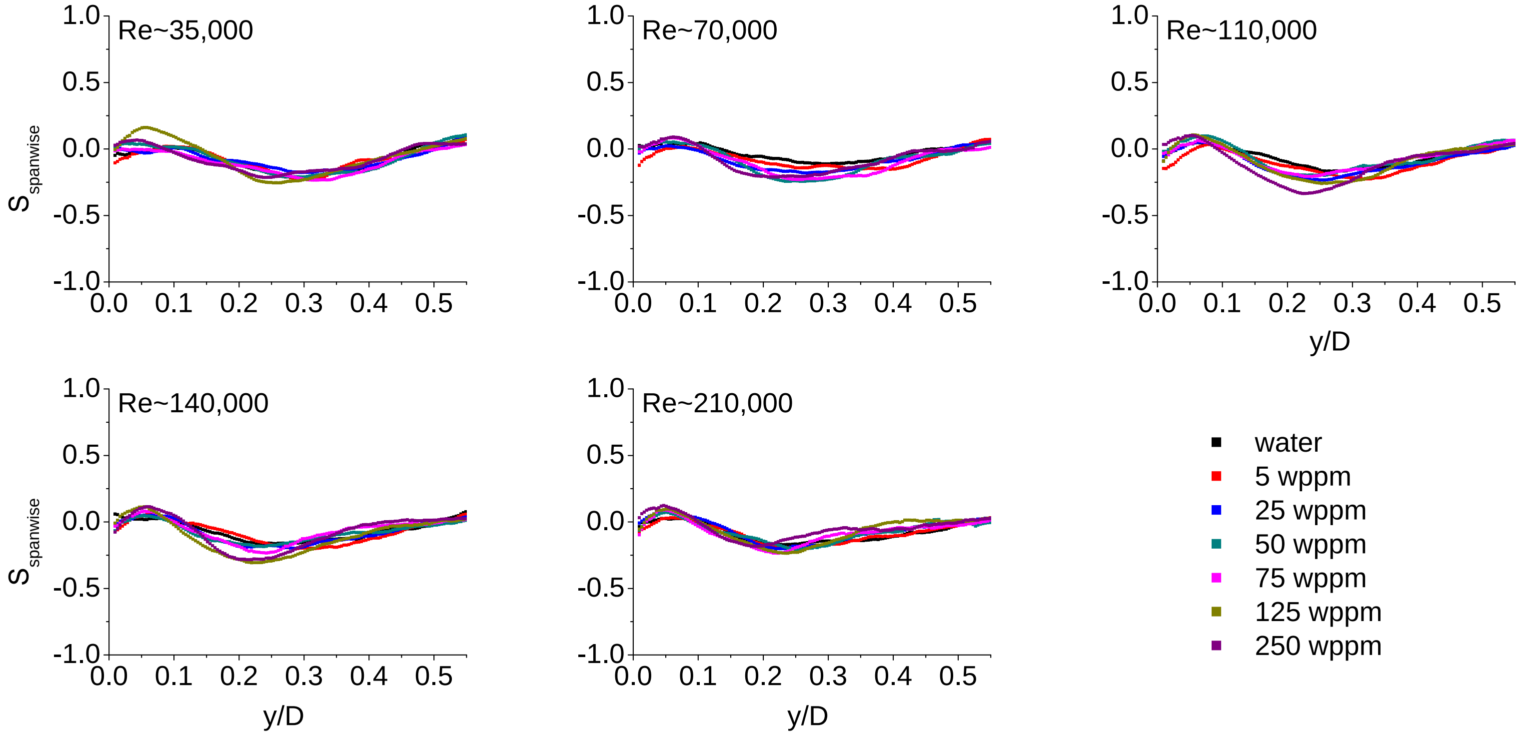

Figure A.46: Dependence of the spanwise skewness $S_{\text{spanwise}}$ on the normalised distance from the wall for PEO4 solutions at various $Re$.

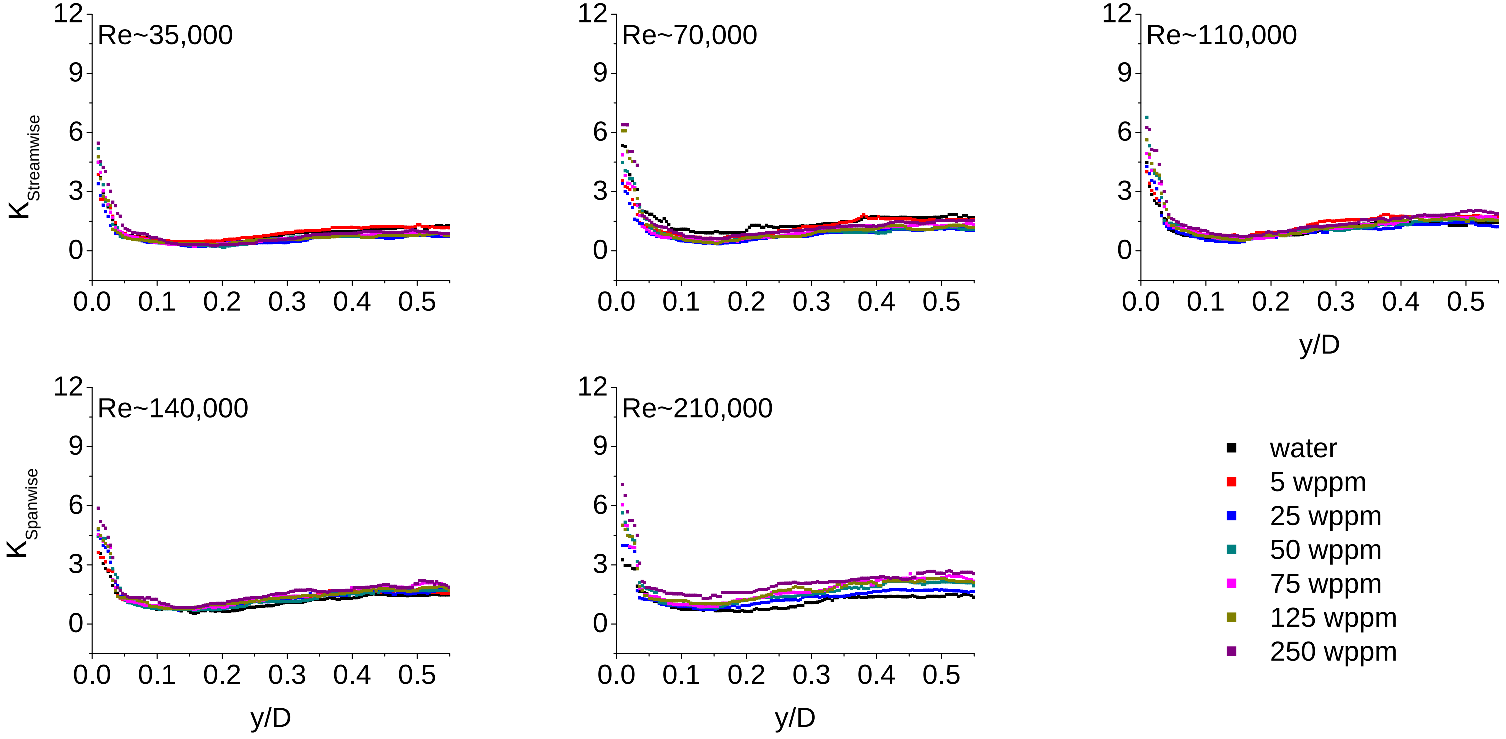

Figure A.47: Dependence of the spanwise kurtosis $K_{\mathrm{spanwise}}$ on the normalised distance from the wall for PEO2 solutions at various $Re$.

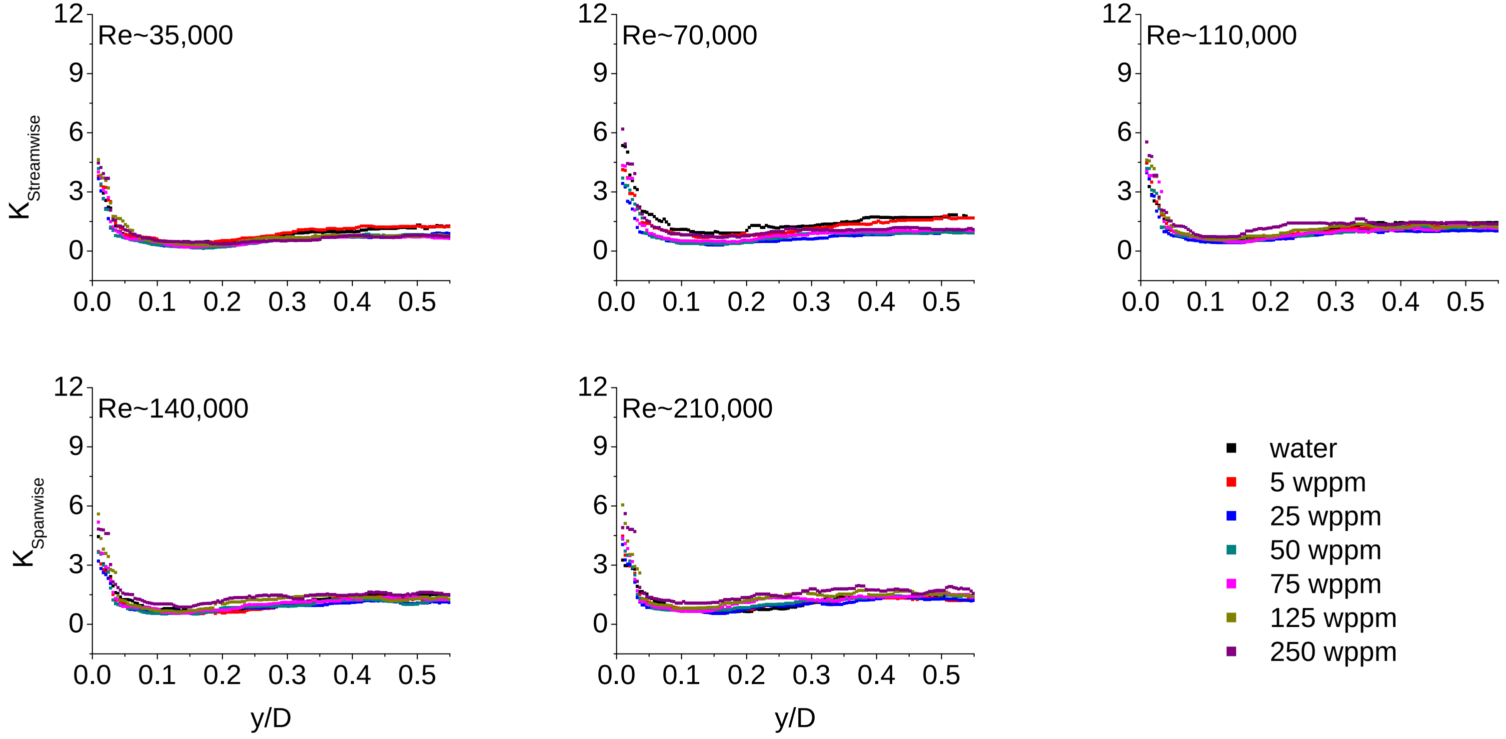

Figure A.48: Dependence of the spanwise kurtosis $K_{\text{spanwise}}$ on the normalised distance from the wall for PEO4 solutions at various $Re$.